International Reviews, Research and Studies in the Field of

MECHANICAL ENGINEERING

EDITOR **PROF. DR. COŞKUN ÖZALP**

SERÜVEN YAYINEVİ

Genel Yayın Yönetmeni / Editor in Chief • C. Cansın Selin Temana

Kapak & İç Tasarım / Cover & Interior Design • Serüven Yayınevi

Birinci Basım / First Edition • © Aralık 2025

ISBN • 978-625-8682-63-2

Serüven Yayınevi / Serüven Publishing
Türkiye Adres / Turkey Address: Kızılay Mah. Fevzi Çakmak 1. Sokak
Ümit Apt No: 22/A Çankaya/ANKARA
Telefon / Phone: 05437675765
web: www.seruvenyayinevi.com
e-mail: seruvenyayinevi@gmail.com

Baskı & Cilt / Printing & Volume
Sertifika / Certificate No: 47083

INTERNATIONAL REVIEWS, RESEARCH AND STUDIES IN THE FIELD OF MECHANICAL ENGINEERING

- DECEMBER 2025 -

EDITOR

PROF. DR. COŞKUN ÖZALP

CONTENTS

Chapter 1

VAPOR CHAMBERS: FUNDAMENTALS, DESIGN PARAMETERS, AND THERMAL PERFORMANCE

Şafak Melih ŞENOCAK [1]

Yasin VAROL [2]

1 Şafak Melih ŞENOCAK, Lecturer, Osmaniye Korkut Ata University, Osmaniye Vocational School e-mail: mlhsnck@gmail.com, ORCID ID: https://orcid.org/0000-0003-0602-2836
2 Prof. Dr. Yasin VAROL, Firat University, Technology Faculty, Elazig
e-mail: yvarol@gmail.com, ORCID ID: https://orcid.org/0000-0003-2989-7125

1. Introduction

With increasing power density in systems such as electronics and batteries, thermal management has become one of the most critical challenges in modern engineering practice. Recent research trends have increasingly favored passive cooling solutions, primarily due to their cost advantages and structural simplicity. Among these, phase change materials, heat pipes, and vapor chambers have emerged as prominent options (Şenocak et al., 2026; Gürgenç et al., 2026; Xie et al., 2021). In components such as microprocessors, power electronic modules, LED lighting systems, battery packs, and fuel cells, heat generation is progressively concentrated over smaller surface areas, making localized hot spots inevitable. The literature clearly indicates that elevated local temperatures not only reduce system efficiency but also lead to material fatigue, performance degradation, and premature failures (Bulut et al., 2019; Egbo, 2022).

Conventional single-phase heat conduction solutions particularly copper or aluminum heat spreader plates may provide adequate performance under low to moderate heat flux conditions; however, their effectiveness becomes limited as power density increases. Because these solutions rely solely on conduction, they can only spread heat to a restricted extent and often fail to ensure temperature uniformity across the surface (Xie et al., 2021). These limitations have intensified interest in passive thermal technologies based on two-phase heat transfer principles consequently, vapor chamber (VC) systems have become one of the leading solutions for electronics cooling in recent years (Bulut et al., 2019; Jiang et al., 2024).

Vapor chambers, as planar two-phase heat spreaders, are distinguished by their ability to redistribute heat from a localized source across a larger area. Their operating principle is based on evaporation in the evaporator region, condensation in the condenser region, and liquid return through a capillary structure (wick). Owing to this cyclic process, vapor chambers can offer substantially lower thermal resistance and higher effective thermal conductivity than solid metal plates of comparable dimensions (Egbo, 2022; Jiang et al., 2024). Numerous experimental studies further demonstrate that vapor chamber implementation improves temperature uniformity and significantly reduces peak surface temperatures (Varol & Oztop, 2025).

The literature shows that a wide range of parameters influence vapor chamber performance. Internal geometry, wick type and microstructural characteristics, working fluid selection, filling ratio, vapor space thickness, and the condenser-to-evaporator area ratio are among the key factors that directly determine system performance (Xie et al., 2021). In particular, the wick structure plays a central role because it governs the balance between

capillary pressure and permeability, which is essential for sustaining two-phase circulation. Comprehensive review studies report in detail that sintered copper powder, wire-mesh (screen), microchannel, and composite wick structures each possess distinct advantages and limitations (Bulut et al., 2019).

Considering real electronic operating conditions, vapor chambers are often subjected to partial heating rather than uniform heating. Nevertheless, for a long time the literature predominantly relied on uniform heating assumptions, and the effects of partial heating were addressed in relatively few studies. In practice, however, components such as processors, power modules, and LED chips generate localized heat loads concentrated over limited areas rather than over the entire surface (Chang et al., 2008; Varol et al., 2025).

Recent experimental findings indicate that the size of the heated area is a decisive factor for vapor chamber thermal performance. Smaller heating areas induce higher local heat fluxes at the evaporator, triggering limiting mechanisms such as capillary limit and dry-out at earlier stages (Chang et al., 2008). Conversely, under larger heating areas, vapor chambers have been reported to exhibit lower thermal resistance and more uniform temperature distributions (Varol et al., 2025; Oztop et al., 2025). Moreover, the geometric compatibility between the heating area and the vapor chamber geometry also affects performance; experimental studies show that square, rectangular, and circular vapor chambers can respond differently under partial heating conditions (Oztop et al., 2025).

Comparative studies between vapor chambers and copper plates provide a clear picture of the advantages enabled by two-phase heat transfer. In many cases, vapor chamber utilization results in lower peak temperatures and improved temperature uniformity (Egbo, 2022; Varol & Oztop, 2025). However, it has also been reported that at high power levels and with large heating areas, the thermal performance of copper plates and vapor chambers may converge (Xie et al., 2021). This observation emphasizes that vapor chamber design must be optimized for the intended application and that no single configuration can be considered universally optimal.

The aim of this book chapter is to examine vapor chamber technology through a comprehensive framework that includes fundamental working principles, thermal behavior under partial heating, the influence of design parameters on performance, and current application trends. Within this scope, the fundamental physical mechanisms governing vapor chambers will be summarized; the effects of partial heating, heating area size, and geometry on thermal performance will be discussed based on the literature; and finally, existing limitations and future research directions will be evaluated.

2. Fundamental Working Principles of Vapor Chambers

Vapor chambers are passive heat spreading devices that operate based on the principles of two-phase heat transfer and can essentially be regarded as planar heat pipes. Unlike conventional cylindrical heat pipes, however, vapor chambers are capable of distributing heat over a two-dimensional plane rather than transporting it along a single direction. This characteristic makes vapor chambers particularly advantageous in electronic applications where localized and high-intensity heat sources are present (Bulut et al., 2019; Egbo, 2022).

The fundamental components of a vapor chamber include a hermetically sealed enclosure, evaporator and condenser surfaces, a capillary structure (wick) covering these surfaces, and a limited amount of working fluid. Thermal energy supplied by the heat source induces evaporation of the working fluid in the evaporator region. During this phase change process, the fluid absorbs a significant amount of latent heat, enabling efficient heat removal from the system. The generated vapor then migrates toward the condenser region due to the pressure gradient between the evaporator and condenser. In the condenser region, the vapor releases its latent heat to the surroundings through condensation. The condensed liquid is subsequently transported back to the evaporator region through the wick structure by capillary forces, thereby sustaining a continuous and stable two-phase circulation cycle (Xie et al., 2021; Jiang et al., 2024). A schematic illustration of the internal structure of a vapor chamber is presented in Figure 1.

Figure 1. Representative internal structure of a vapor chamber (Oztop et al., 2025).

The stable operation of this cycle is directly governed by the internal pressure balance within the vapor chamber. A widely accepted pressure balance criterion in the literature states that the capillary pressure generated by the wick must be greater than or at least equal to the sum of vapor flow

resistance, liquid flow resistance, and gravitational effects (Xie et al., 2021). Consequently, the primary limiting mechanisms governing vapor chamber performance include the capillary limit, vapor flow limit, boiling limit, and dry-out phenomenon. Numerous studies have reported that the capillary limit becomes the dominant constraint particularly under high heat flux conditions and when the heating area is small (Egbo, 2022).

The wick structure constitutes the core component of the vapor chamber operating mechanism. On one hand, the wick facilitates the return of condensed liquid to the evaporator region; on the other hand, it must restrict adverse interactions between the vapor and liquid flows. Sintered copper powder, wire-mesh (screen), microchannel, and composite wick structures are among the most commonly employed configurations reported in the literature (Bulut et al., 2019). While sintered wick structures are capable of generating high capillary pressure, their relatively low permeability may increase liquid flow resistance under high heat load conditions. In contrast, mesh-based wick structures offer higher permeability but are often limited in terms of capillary pressure. This trade-off is frequently described in the literature as the "capillary pressure–permeability balance" problem (Xie et al., 2021).

To address this limitation, composite and hierarchical wick structures have been developed in recent years with the objective of improving this balance. By combining different pore sizes or integrating multiple wick types, it becomes possible to achieve both high capillary pressure and sufficient permeability. This dual functionality becomes even more critical in ultra-thin vapor chamber designs, where a reduction in vapor space thickness leads to a rapid increase in vapor flow resistance, thereby exerting a direct impact on overall system performance (Jiang et al., 2024).

Another key aspect of vapor chamber operation is the size and spatial distribution of the heat source. Under uniform heating conditions, the evaporation region extends over a relatively large area within the vapor chamber. In contrast, under partial heating conditions, evaporation is concentrated within a confined region. This localized evaporation results in significantly higher local heat fluxes at the evaporator, which may cause the capillary limit to be exceeded at earlier stages. Chang et al. (2008) demonstrated that vapor chamber evaporator thermal resistance increases markedly under non-uniform heating conditions. More recent studies have further shown that enlarging the heating area reduces thermal resistance and improves temperature uniformity (Varol et al., 2025; Oztop et al., 2025).

Based on these fundamental physical principles, vapor chamber performance is commonly evaluated using metrics such as thermal resistance, maximum

heat transport capacity, effective thermal conductivity, and surface temperature uniformity. Typical performance ranges reported in the literature for different wick structures and operating conditions are summarized in Table 1.

Table 1. Fundamental performance characteristics of different vapor chamber configurations reported in the literature.

Reference	Wick Structure	Heating Condition	Heat Load (W)	Minimum Thermal Resistance (K/W)
Chang et al. (2008)	Microchannel	Partial heating	20-80	~0.25
Bulut et al. (2019)	Mesh / Sintered	Uniform	30-150	0.15-0.30
Egbo (2022)	Various (review)	-	10-300	0.03-0.40
Varol et al. (2025)	Microchannel	Partial heating	40-150	0.10-0.25
Oztop et al. (2025)	Microchannel	Partial heating	50-200	0.08-0.30

3. Design Parameters, Wick Structures and Performance Limits

Vapor chamber performance is governed not only by the presence of two-phase heat transfer mechanisms, but also by the complex interactions arising from internal geometry, wick structure, and operating conditions. The literature emphasizes that, unless vapor chamber design parameters are carefully optimized, systems that theoretically exhibit high performance potential may encounter significant practical limitations (Xie et al., 2021; Jiang et al., 2024).

3.1. Fundamental Design Parameters

Key parameters in vapor chamber design include vapor space thickness, the evaporator-to-condenser area ratio, heating area size, filling ratio, and the thermophysical properties of the working fluid. In particular, for ultra-thin vapor chamber designs, a reduction in vapor space thickness leads to a dramatic increase in vapor flow resistance, thereby exerting a decisive influence on thermal performance. Huang et al. (2020) demonstrated that when the vapor space thickness decreases below 0.3 mm, the vapor friction coefficient increases sharply, which in turn limits the maximum heat transport capability of the system.

The size of the heating area is a critical parameter for vapor chambers operating under partial heating conditions. Smaller heating areas result in elevated local heat fluxes within the evaporator region, causing the capillary limit to be reached at earlier stages. Experimental studies have shown that thermal resistance increases significantly for small heating areas such as 10 × 10 mm², whereas performance improves when the heating area is expanded (Varol et al., 2025; Oztop et al., 2025).

The filling ratio, defined as the amount of working fluid charged into the vapor chamber, is another key factor affecting the stability of the two-phase circulation. At low filling ratios, the risk of dry-out in the evaporator region increases, while excessive filling reduces the available vapor volume and restricts vapor flow. Numerous studies report that the optimal filling ratio typically lies within the range of 20-40%, outside of which thermal performance deteriorates (Li et al., 2021; Varol et al., 2025).

3.2. Wick Structures and Their Characteristic Features

The wick structure is widely regarded as the core component of a vapor chamber. Its primary function is to return the condensed liquid to the evaporator region while simultaneously generating sufficient capillary pressure to sustain the two-phase cycle. Achieving this function requires a delicate balance between high capillary pressure and low flow resistance, which has motivated the development of various wick design strategies in the literature (Bulut et al., 2019).

Sintered copper powder wicks are capable of producing high capillary pressure due to their small pore sizes; however, their relatively low permeability may restrict liquid return under high heat load conditions. In contrast, mesh-based wicks offer higher permeability but are limited in terms of capillary pressure. Microchannel wick structures partially separate vapor and liquid flow paths, thereby reducing vapor–liquid interaction and improving temperature uniformity (Chang et al., 2008). A schematic representation of the internal structure of a vapor chamber is shown in Figure 2.

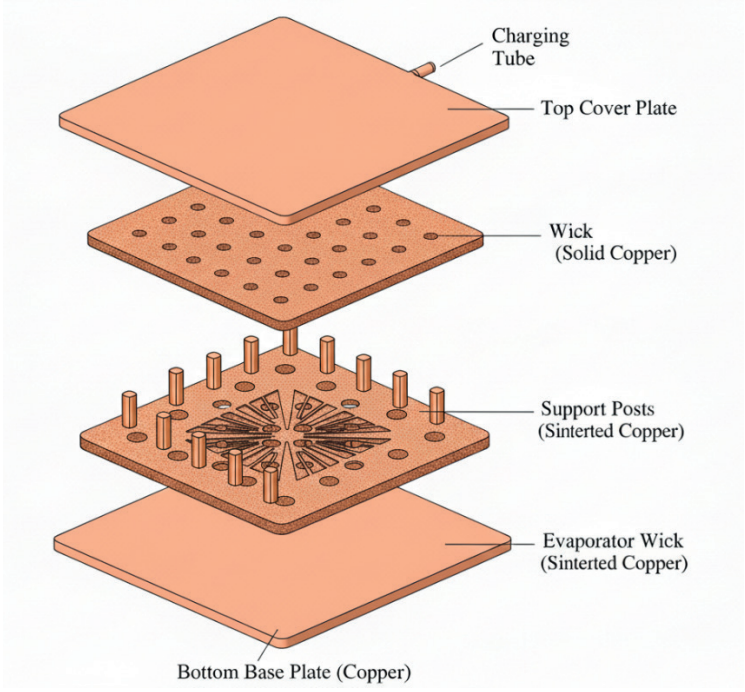

Figure 2. Schematic representation of the internal structure of a vapor chamber.

In recent years, composite and hierarchical wick structures have been developed to overcome the limitations associated with conventional wick designs. The combined use of different pore sizes or multiple wick types enables the simultaneous achievement of high capillary pressure and sufficient permeability. In particular, gradient porous and biomimetic wick designs have demonstrated stable performance even under ultra-high heat flux conditions (Jiang et al., 2024; Zhou et al., 2023).

3.3. Performance Limits and Limiting Mechanisms

Vapor chamber performance is constrained by several fundamental physical limits. In the literature, these limits are commonly classified as the capillary limit, vapor flow limit, boiling limit, and dry-out limit (Egbo, 2022). The capillary limit arises when the maximum capillary pressure generated by the wick is no longer sufficient to overcome the total pressure losses within the system, and it becomes the dominant limiting mechanism particularly under partial heating conditions.

The vapor flow limit is associated with pressure losses resulting from excessive vapor velocity within the vapor space. In ultra-thin vapor chambers, the reduction in vapor space thickness significantly increases vapor flow resistance, causing this limit to be reached at lower heat loads (Huang et al., 2020). The boiling limit, on the other hand, is related to the destabilization of nucleate boiling at the evaporator surface and is typically observed under extremely high heat flux conditions.

The dry-out phenomenon occurs when the liquid film at the evaporator region is completely depleted, leading to a sudden degradation in vapor chamber performance. The literature reports that dry-out is most commonly associated with small heating areas, low filling ratios, and insufficient wick permeability (Chang et al., 2008; Varol et al., 2025).

As summarized in Table 2, the typical performance ranges reported in the literature for different wick structures and design approaches are presented in a comparative manner.

Table 2. Typical performance ranges reported in the literature for different wick structures.

Wick Structure	Typical Heat Load (W)	Minimum Thermal Resistance (K/W)	Dominant Limiting Mechanism	Reference
Sintered copper powder	50-300	0.03-0.20	Capillary limit	Bulut et al. (2019)
Mesh wick	30-150	0.10-0.30	Capillary limit	Egbo (2022)
Microchannel wick	40-200	0.08-0.25	Vapor flow limit	Chang et al. (2008)
Composite / hierarchical wick	100-500	0.02-0.10	Boiling limit	Jiang et al. (2024)
Gradient porous wick	200-500	0.02-0.08	Dry-out delay	Zhou et al. (2023)

4. Manufacturing Approaches and Representative Vapor Chamber Configurations

Vapor chamber performance is determined not only by theoretical design parameters but also by the manufacturing techniques employed and the micro-scale structural characteristics imparted by these processes. The literature

demonstrates that vapor chambers with identical geometric dimensions can exhibit markedly different thermal performance as a result of variations in fabrication methods and wick integration strategies (Bulut et al., 2019; Huang et al., 2020). Consequently, a systematic evaluation of manufacturing approaches is essential for a comprehensive and accurate understanding of vapor chamber technology. Figure 3 illustrates the operating principle of a vapor chamber.

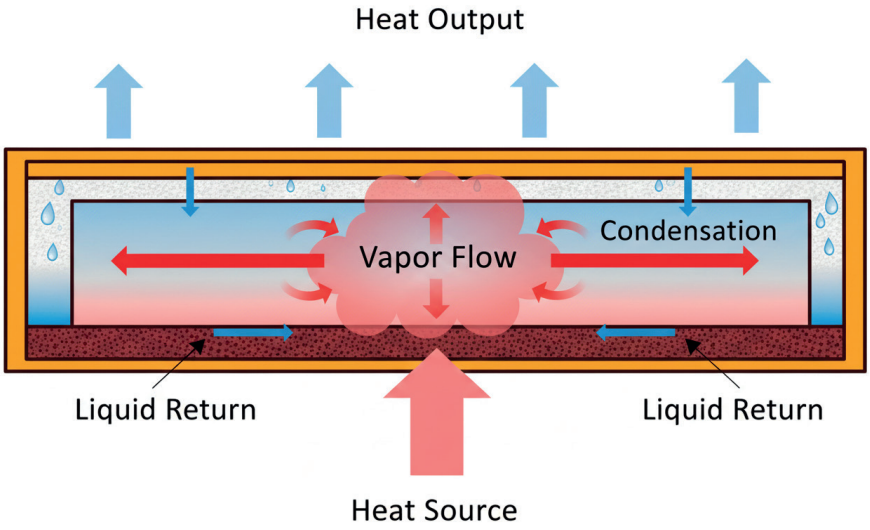

Figure 3. Operating principle of the vapor chamber.

4.1. Conventional Manufacturing Methods

The most widely adopted manufacturing approach for vapor chambers is based on the forming of copper plates combined with the integration of sintered wick structures. In this method, the upper and lower copper plates are typically shaped through stamping or chemical etching processes, after which sintered copper powder or mesh-based wick structures are bonded to the internal surfaces. The plates are subsequently joined under vacuum conditions to form a hermetically sealed enclosure (Li et al., 2016).

Sintered copper powder wicks are particularly favored in applications requiring high capillary pressure. However, their fabrication demands precise control over pore size distribution and inter-particle bonding quality. Previous studies have reported that improper selection of sintering temperature and duration can significantly reduce wick permeability, thereby increasing the risk of dry-out during operation (Li et al., 2016; Meng et al., 2023).

In contrast, mesh-based wick structures offer a simpler and more cost-effective manufacturing route. These wicks are formed by stacking multiple

layers of woven copper mesh, resulting in relatively high permeability but lower capillary pumping capability compared to sintered structures. As a result, mesh wicks are generally preferred for low- to moderate-heat-flux applications (Mochizuki & Nguyen, 2019).

4.2. Micro-Channel and Structurally Supported Designs

In ultra-thin vapor chamber configurations, mechanical integrity becomes a critical design consideration alongside wick performance. Reducing the vapor space thickness increases the susceptibility of the upper and lower plates to structural collapse, necessitating the incorporation of internal support features during fabrication. Micro-pillars (support columns), micro-channels, and periodically distributed support geometries are commonly employed to address this challenge (Huang et al., 2020).

Micro-channel vapor chambers provide a more regulated two-phase transport mechanism by partially guiding both vapor and liquid flow paths. Chang et al. (2008) demonstrated that micro-channeled evaporator surfaces improve temperature uniformity and reduce evaporator thermal resistance under localized heating conditions. Despite these advantages, the fabrication of micro-channel structures is considerably more complex and costly than conventional sintering-based methods.

The geometry and spatial distribution of support columns also exert a direct influence on vapor chamber performance. Numerical investigations have examined the effects of circular, square, and diamond-shaped columns on vapor flow resistance, revealing that small diameter columns arranged in a regular pattern can effectively reduce vapor pressure losses (Huang et al., 2020). This finding is particularly relevant for ultra-thin vapor chamber designs, where a careful balance between mechanical robustness and thermal efficiency must be achieved.

4.3. Advanced and Next-Generation Manufacturing Approaches

In recent years, additive manufacturing and micro-structured printing techniques have emerged as promising alternatives for vapor chamber fabrication. Metal-based additive manufacturing enables the production of porous wick structures with highly complex and optimized geometries that are difficult to achieve using conventional sintering methods. Meng et al. (2023) reported that vapor chambers incorporating additively manufactured porous wicks exhibit improved temperature uniformity compared to their traditionally fabricated counterparts.

Biomimetic designs represent another significant advancement in manufacturing strategies. Wick geometries inspired by leaf venation or vascular flow networks enhance liquid return capability and effectively delay the onset of dry-out. Zhou et al. (2023) demonstrated that vapor chambers equipped with leaf-vein-inspired wick structures maintain low thermal resistance even under high heat load conditions. Despite the increased fabrication complexity, such designs offer substantial potential for applications demanding exceptionally high thermal performance.

4.4. Comparison of Representative Configurations

The characteristic features of vapor chamber configurations employing different manufacturing approaches reported in the literature are summarized in Table 3. This table clearly illustrates the relationship between the applied manufacturing method and the resulting thermal performance.

Table 3. Comparison of vapor chamber configurations employing different manufacturing approaches

Study	Manufacturing Method	Wick Structure	Thickness (mm)	Heat Load (W)	Minimum Thermal Resistance (K/W)
Li et al. (2016)	Sintering	Copper powder	~3.0	60–200	0.12–0.20
Chang et al. (2008)	Micro-channel processing	Micro-channel	~2.5	20–80	~0.25
Huang et al. (2020)	Chemical etching + support columns	Supported structure	<1.0	20–100	0.15–0.30
Meng et al. (2023)	Additive manufacturing	3D-printed porous wick	~2.0	50–150	~0.08
Zhou et al. (2023)	Hybrid (biomimetic)	Gradient wick	~2.0	100–500	0.02–0.05

An examination of Table 3 reveals that vapor chamber performance is determined not only by geometric design parameters but also directly by the manufacturing technique employed and the micro-scale structural features imparted to the internal configuration. In studies based on sintering-driven manufacturing approaches, it is observed that copper powder wick structures

provide high capillary pressure; however, due to relatively high liquid flow resistance, performance may become limited under medium to high heat load conditions (Li et al., 2016). Although such structures offer advantages in terms of reliability and manufacturing repeatability, additional optimization is required for ultra-thin designs and applications involving high heat flux.

In microchannel-based and structurally supported vapor chamber configurations, partial guidance of vapor and liquid flow leads to improved temperature uniformity. Results reported by Chang et al. (2008) and Huang et al. (2020) indicate that, particularly under partial heating and constrained internal cavity conditions, microchannel geometries and support columns are effective in mitigating vapor pressure losses. Nevertheless, it should be noted that the manufacturing complexity and cost of these structures are higher compared to conventional sintering-based approaches.

Vapor chambers produced using additive manufacturing and biomimetic design approaches emerge as the configurations exhibiting the lowest thermal resistance values in the comparison presented in Table 3. In systems incorporating additively manufactured porous and gradient porous wick structures, both high capillary pressure and sufficient permeability can be achieved, enabling stable two-phase operation even at heat loads exceeding 100 W (Meng et al., 2023; Zhou et al., 2023). These findings demonstrate that advanced manufacturing techniques have the potential to significantly extend the performance limits of vapor chambers.

Overall, the data presented in Table 3 indicate that no single manufacturing approach is universally optimal for all vapor chamber applications. While conventional sintering methods provide advantages in terms of cost and manufacturing maturity, micro-structured, additively manufactured, and biomimetic approaches offer superior performance potential for advanced applications requiring high heat flux handling and ultra-thin form factors. Therefore, the selection of a vapor chamber manufacturing method should be made by considering the targeted heat load, geometric constraints, and specific operating conditions.

5. **Applications, Challenges and Future Perspectives**

Vapor chamber technology, owing to its two-phase heat transfer mechanism, has found application across a broad range of thermal management systems. Recent studies demonstrate that vapor chambers are not only effective in conventional electronic cooling applications, but also provide viable solutions in battery systems, power electronics, LED lighting, and data centers. Despite these advantages, several technical and manufacturing-related challenges continue to limit the widespread adoption of this technology.

5.1. Application Areas

Electronic and microprocessor cooling represents the most mature and widely adopted application area for vapor chambers. In high power density CPU and GPU systems, the formation of localized hot spots poses a serious threat to both performance and reliability. By virtue of their two-dimensional heat spreading capability, vapor chambers redistribute these hot spots over a larger surface area, thereby reducing peak surface temperatures. Experimental studies have shown that vapor chamber-integrated cooling solutions achieve better temperature uniformity compared to conventional heat pipes or solid metal heat spreaders (Bulut et al., 2019; Egbo, 2022).

Battery thermal management has emerged as another prominent application area for vapor chambers in recent years. In electric vehicles and energy storage systems, limiting temperature gradients between battery cells is critical for both performance and safety. Li et al. (2021) demonstrated that vapor chamber–assisted liquid cooling systems effectively suppress surface temperature differences in battery modules while providing low thermal resistance at optimal filling ratios. Similarly, Kim et al. (2021) reported that aluminum-based vapor chambers can be successfully implemented in battery packs, while emphasizing that improper filling ratio selection leads to significant performance degradation.

LED and lighting systems constitute another important application domain for vapor chambers. In high-power LED devices, luminous efficiency is directly linked to operating temperature, making thermal control at the LED base essential. Experimental investigations have shown that both three-dimensional and planar vapor chamber designs reduce operating temperatures in LED modules and extend system lifetime (Lu et al., 2019; Zhou et al., 2023).

Power electronics and high heat flux applications represent some of the most demanding operating environments for vapor chambers. Wu et al. (2021) demonstrated that internally cooled vapor chamber (ICVC) designs integrated with liquid cooling can maintain low thermal resistance and excellent temperature uniformity even under extremely high heat flux conditions. Such hybrid systems offer promising solutions for data centers and high-performance computing applications.

5.2. Current Challenges and Limitations

Despite their advantages, several challenges remain unresolved in vapor chamber technology. Among these, manufacturing complexity and cost are the most prominent. Vapor chambers incorporating microchannel, gradient porous, or biomimetic wick structures are considerably more complex and expensive to manufacture than those produced using conventional sintering methods (Huang

et al., 2020; Meng et al., 2023). This poses a significant barrier to large-scale production and industrial scalability. Another major challenge is the increase in vapor flow resistance in ultra-thin vapor chambers. As vapor space thickness decreases, resistance to vapor flow increases, causing the vapor flow limit to be reached at lower heat loads. Wong et al. (2024) highlighted that even the test configuration employed (vapor chamber mode versus heat pipe mode) can significantly influence measured performance in ultra-thin designs, and that improper testing protocols may lead to misleading conclusions. Partial heating and dry-out risk represent additional limitations, particularly in applications involving small heating areas. Numerous studies report that under small heating areas, rapid thinning of the liquid film occurs in the evaporator region, and the onset of dry-out leads to abrupt performance degradation (Chang et al., 2008; Varol et al., 2025). This underscores the importance of carefully considering the interaction between heating area, wick structure, and filling ratio in vapor chamber design. Furthermore, gravity and operating orientation also affect vapor chamber performance. While some wick structures exhibit relatively gravity-insensitive behavior, others suffer substantial performance losses under anti-gravity conditions. This issue is of particular relevance for portable electronics and space applications (Zhou et al., 2023).

5.3. Future Perspectives

Three major trends are expected to shape the future development of vapor chamber technology. First, advanced wick designs and additive manufacturing techniques are anticipated to enable more effective optimization of the capillary pressure–permeability balance. Metal additive manufacturing and micro-structure printing allow the fabrication of complex geometries that are difficult to achieve using conventional methods (Meng et al., 2023).

Second, the adoption of hybrid cooling systems is expected to increase. Combining vapor chambers with liquid cooling, heat sinks, or thermoelectric modules may significantly extend performance limits, particularly in applications involving extremely high heat flux (Wu et al., 2021). This approach holds substantial potential for data centers and power electronics systems.

Finally, application-specific design and optimization will play an increasingly important role. The literature clearly demonstrates that no single vapor chamber design is optimal for all applications. Developing customized designs by considering parameters such as heating area size, geometry, operating orientation, and target heat load will facilitate broader adoption of vapor chamber technology in future thermal management systems (Xie et al., 2021; Jiang et al., 2024). In this context, vapor chambers when supported by appropriate design and manufacturing strategies are expected to continue playing a key role in the thermal management of next-generation electronic and energy systems.

REFERENCES

Bulut, M., Kandlikar, S. G., & Sozbir, N. (2019). A review of vapor chambers. Heat Transfer Engineering, 40(19), 1551–1573. https://doi.org/10.1080/01457632.2018.1480868

Chang, J.-Y., Prasher, R. S., Prstic, S., Cheng, P., & Ma, H. B. (2008). Evaporative thermal performance of vapor chambers under non-uniform heating conditions. Journal of Heat Transfer, 130(12), 121501. https://doi.org/10.1115/1.2976786

Egbo, M. (2022). A review of the thermal performance of vapor chambers and heat sinks. International Journal of Heat and Mass Transfer, 183, 122108. https://doi.org/10.1016/j.ijheatmasstransfer.2021.122108

Gürgenç, E., Öztop, H. F., Şenocak, Ş. M., Aktemur, C., Gürgenç, T., Varol, Y., Yamaç, H. İ., & Gür, M. (2025). Hafnium carbide as a novel nanofiller for RT64HC phase change materials: Enhancing thermal conductivity, heat capacity, and cycling stability. Thermal Science and Engineering Progress, 69, 104257. https://doi.org/10.1016/j.tsep.2025.104257

Huang, G., Liu, W., Luo, Y., Deng, T., Li, Y., & Chen, H. (2020). Research and optimization design of limited internal cavity of ultra-thin vapor chamber. International Journal of Heat and Mass Transfer, 148, 119101. https://doi.org/10.1016/j.ijheatmasstransfer.2019.119101

Jiang, H., Wang, X., Ding, C., Shan, D., Guo, B., Qi, H., & Xu, J. (2024). A review of emerging design and theoretical progress on vapor chamber. International Journal of Heat and Mass Transfer, 231, 125814. https://doi.org/10.1016/j.ijheatmasstransfer.2024.125814

Kim, J. S., Shin, D. H., You, S. M., & Lee, J. (2021). Thermal performance of aluminum vapor chamber for EV battery thermal management. Applied Thermal Engineering, 185, 116337. https://doi.org/10.1016/j.applthermaleng.2020.116337

Li, W., Li, L., Cui, W., & Guo, M. (2021). Experimental investigation on the thermal performance of vapor chamber in a compound liquid cooling system. International Journal of Heat and Mass Transfer, 170, 121026. https://doi.org/10.1016/j.ijheatmasstransfer.2021.121026

Li, Y., Li, Z., Zhou, W., Zeng, Z., Yan, Y., & Li, B. (2016). Experimental investigation of vapor chambers with different wick structures at various parameters. Experimental Thermal and Fluid Science, 77, 132–143. https://doi.org/10.1016/j.expthermflusci.2016.04.017

Lu, Z., Bai, P., Huang, B., Henzen, A., Coehoorn, R., Liao, H., & Zhou, G. (2019). Experimental investigation on the thermal performance of three-dimensional vapor chamber for LED automotive headlamps. Applied Thermal Engineering, 157, 113478. https://doi.org/10.1016/j.applthermaleng.2019.03.049

Meng, X., Tan, S., Yuan, Z., Zhang, Y., & Chen, L. (2023). Experimental study on the heat transfer performance of a vapor chamber with porous wick structures printed via metallic additive anufacturing. International Communications in Heat and Mass Transfer, 140, 106496. https://doi.org/10.1016/j.icheatmasstransfer.2022.106496

Mochizuki, M., & Nguyen, T. (2019). Review of various thin heat spreader vapor chamber designs, performance, lifetime reliability and application. Frontiers in Heat and Mass Transfer, 13. https://doi.org/10.5098/hmt.13.12

Oztop, H. F., Varol, Y., Tamdogan, E., Parlak, M., Senocak, S. M., & Cosanay, H. (2025). Influence of vapor chamber shape on thermal performance under partial heating. International Communications in Heat and Mass Transfer, 167, 109321. https://doi.org/10.1016/j.icheatmasstransfer.2025.109321

Şenocak, Ş. M., Gürgenç, T., Varol, Y., Gürgenç, E., & Öztop, H. F. (2026). Cubic boron nitride enhanced PCM nanocomposites for solar energy storage and thermal management. Solar Energy, 303, 114102. https://doi.org/10.1016/j.solener.2025.114102

Varol, Y., & Oztop, H. F. (2025). Thermal performance investigation of vapor chamber under partial heating. Journal of Heat Transfer, 147(1), 011602. https://doi.org/10.1115/1.4066664

Varol, Y., Oztop, H. F., & Tamdogan, E. (2025). Vapor chamber thermal performance under partial heating with different heating areas. Applied Thermal Engineering, 260, 124978. https://doi.org/10.1016/j.applthermaleng.2024.124978

Wong, S.-C., Huang, L.-Q., & Tang, J.-T. (2024). Straight ultra-thin vapor chambers tested under different modes for different vapor duct thicknesses. Applied Thermal Engineering, 257, 124353.

Wu, G., Luo, Y., Bai, P., Wang, H., Cai, R., Tang, Y., Chen, X., & Zhou, G. (2021). Modeling and experimental analysis of an internally-cooled vapor chamber. Energy Conversion and Management, 235, 114017. https://doi.org/10.1016/j.enconman.2021.114017

Xie, D., Sun, Y., Wang, G., Chen, S., & Ding, G. (2021). Significant factors affecting heat transfer performance of vapor chamber. International Journal of Heat and Mass Transfer, 175, 121132. https://doi.org/10.1016/j.ijheatmasstransfer.2021.121132

Zhou, G., Zhou, J., & Huai, X. (2023). High performance vapor chamber enabled by leaf-vein- inspired wick structure for high-power electronics cooling. Applied Thermal Engineering, 230, 120859. https://doi.org/10.1016/j.applthermaleng.2023.120859

Chapter 2

EFFECT OF WC CONTENT ON PHOTON ATTENUATION PARAMETERS OF AZ61 MAGNESIUM ALLOY COMPOSITES

Hatice VAROL ÖZKAVAK [1]

Kadir GÜNOĞLU [2]

1 Doç. Dr., Isparta Uygulamalı Bilimler Üniversitesi, Teknik Bilimler Meslek Yüksekokulu, haticevarol@isparta.edu.tr, ORCID: 0000-0002-0314-0119.
2 Doç. Dr., Isparta Uygulamalı Bilimler Üniversitesi, Teknik Bilimler Meslek Yüksekokulu, kadirgunoglu@isparta.edu.tr, ORCID: 0000-0002-9008-9162.

1. INTRODUCTION

Ionizing radiation is extensively employed in a wide range of critical fields, including nuclear energy systems, medical imaging and radiotherapy, industrial radiography, space technologies, and defense applications. In such environments, exposure to high-energy gamma rays and X-rays poses significant risks to both living tissues and sensitive electronic components, necessitating the development of effective radiation protection strategies. Radiation protection is fundamentally based on three core principles: minimizing exposure time, increasing the distance from the radiation source, and employing appropriate shielding materials. Within this framework, the development and optimization of advanced shielding materials have become a central research focus in radiation safety studies (Gökçe et al., 2018; Kavaz et al., 2020.

Traditionally, high-density materials such as lead (Pb) and concrete have been widely utilized for gamma radiation shielding due to their strong attenuation capabilities. However, the toxic nature, excessive weight, and limited formability of lead, along with the mechanical and geometrical constraints associated with concrete, have driven increasing interest toward alternative shielding materials (Dong et al., 2021; Almuqrin et al., 2021; Aygün, 2021). In recent years, metal matrix composites (MMCs) have emerged as promising candidates, offering a combination of reduced weight, environmental compatibility, and enhanced mechanical performance compared to conventional shielding materials (Rashed et al., 2021; Rashed et al., 2023).

Among lightweight structural materials, magnesium-based alloys have attracted considerable attention owing to their low density, high specific strength, and excellent castability. The AZ61 magnesium alloy, containing aluminum and zinc as alloying elements, is widely used due to its improved mechanical properties. Nevertheless, the relatively low effective atomic number and density of unreinforced AZ61 alloy result in limited gamma-ray attenuation capability (Majchrowicz et al., 2022; Lee, et al., 2022). This drawback can be effectively mitigated by incorporating ceramic reinforcement phases with high atomic numbers and densities into the magnesium matrix.

In this context, tungsten carbide (WC) was selected as the reinforcement material due to its high tungsten content, elevated density, exceptional hardness, and superior thermal stability. The incorporation of WC particles into the AZ61 matrix increases both the effective atomic number and mass density of the composite, thereby enhancing photon–matter interaction probabilities through photoelectric absorption, Compton scattering, and, at higher photon energies, pair production mechanisms. Consequently, a systematic investigation of the gamma radiation shielding performance of WC-reinforced AZ61 composites is of significant scientific and engineering interest.

The quantitative assessment of radiation shielding performance is commonly conducted using key parameters such as the mass attenuation coefficient (MAC), linear attenuation coefficient (LAC), half-value layer (HVL), tenth-value layer (TVL), mean free path (MFP), the effective atomic number (Zeff) and effective electron density (Neff). These parameters provide comprehensive insight into a material's attenuation efficiency at specific photon energies, the required shielding thickness, and the interaction behavior of photons within the material.

Due to the high cost and time requirements associated with experimental measurements, advanced computational tools such as the Phy-X/PSD software have been increasingly employed for the reliable theoretical evaluation of radiation shielding parameters. Phy-X/PSD is a robust simulation platform capable of accurately calculating photon–matter interaction parameters over a wide energy range based on the chemical composition and density of the investigated materials (Şakar et al., 2020).

The primary objective of this study is to theoretically determine the MAC, LAC, HVL, TVL, MFP, Zeff and Neff values of AZ61-based composites containing 0, 5, 15, and 30 wt.% WC reinforcement using the Phy-X/PSD program, and to comprehensively analyze the influence of WC content on gamma radiation shielding performance.

2. MATERIALS AND METHODS

The reduction in the intensity of ionizing photon radiation (gamma and X-rays) as it passes through a shielding material arises from fundamental photon–matter interaction mechanisms, namely photoelectric absorption, Compton scattering, and pair production at higher photon energies. This attenuation process exhibits a stochastic nature and is commonly described by the Beer–Lambert law (Bashter, 1997). Accordingly, the relationship between the initial intensity I0 of a photon beam and the transmitted intensity I after passing through a homogeneous material of thickness x can be expressed as

$$I = I_0 e^{-\mu x}$$

where μ denotes the LAC.

The LAC, which is measured in cm−1, indicates the likelihood of photon attenuation per unit thickness of the material. The frequency of photon interactions within the shielding medium is directly reflected by this fundamental characteristic. The material density, chemical composition, effective atomic number, and incident photon energy are some of the variables that affect the LAC's magnitude. Increased shielding effectiveness is implied by higher LAC values, which show that photons interact over shorter distances within the material.

The MAC is defined as the ratio of the LAC to the material density and is given by

$$MAC = \frac{\mu}{\rho}$$

where ρ represents the density of the material in g/cm3. Since MAC characterizes the probability of photon–matter interactions per unit mass, it is considered independent of density and is therefore widely used as a comparative parameter for evaluating the shielding performance of materials with different densities. For composite or multi-component materials, the MAC can be calculated using the weight fractions of the constituent elements based on the additive nature of photon interactions, as follows (Gunoglu et al., 2021):

$$(\mu/\rho)_{composite} = \sum_i w_i (\mu/\rho)_i$$

where wi is the weight fraction of the ith component.

The minimal thickness of a shielding material needed to lower the incident photon intensity to 50% of its initial value is known as the HVL. An engineering-friendly and useful metric of shielding performance is HVL. It can be represented quantitatively as follows and is inversely proportional to the linear attenuation coefficient (Gunoglu, 2024):

$$HVL\left(X_{\frac{1}{2}}, cm\right) = \frac{Ln(2)}{\mu}$$

Lower HVL values indicate that effective radiation shielding can be achieved with thinner material layers.

The TVL represents the thickness of a material needed to attenuate the incident photon intensity to 10% of its initial value. TVL is particularly relevant in applications demanding high levels of radiation protection, such as nuclear facilities and medical radiation environments (Gunoglu, 2024). It is larger than the HVL and is defined as

$$TVL\left(X_{\frac{1}{10}}, cm\right) = \frac{Ln(10)}{\mu}$$

The MFP, which characterizes the average distance a photon travels between subsequent contacts within the material, is another crucial shielding characteristic (Gunoglu, 2024). This value, which is equal to the inverse of the linear attenuation coefficient, represents the stochastic character of photon-matter interactions:

$$MFP\ (\lambda, cm) = \frac{1}{\mu}$$

Smaller MFP values indicate more frequent photon interactions and, consequently, superior shielding performance.

When evaluated collectively, these parameters provide a comprehensive and reliable assessment of a material's gamma radiation shielding capability. It is well established that increases in material density and effective atomic number lead to higher LAC and MAC values, while simultaneously reducing HVL, TVL, and MFP values. This behavior highlights the significant potential of composite materials incorporating high-density and high-atomic-number reinforcement phases for advanced radiation shielding applications.

To characterize the probability of photon interactions with matter at both atomic and electronic scales, two fundamental quantities are commonly employed: the total atomic cross section (σt) and the total electronic cross section (σe). The σt represents the interaction probability per individual electron, whereas the σe expresses the overall likelihood of photon interaction with an atom by incorporating all possible interaction mechanisms (Gunoglu et al., 2021). These cross sections form the basis for determining the Zeff and the Neff, which are key parameters for describing the radiation attenuation characteristics of composite and structurally heterogeneous materials.

The Zeff provides a single equivalent value that represents the collective atomic response of a material to incident photon radiation, while the effective electron density quantifies the number of electrons available for photon interactions per unit mass or per unit volume. Both σt and σe, as well as the derived parameters Zeff and Neff, exhibit a strong dependence on photon energy. These quantities are evaluated using the relations given below (Gunoglu et al., 2021; Tekin et al., 2020):

$$\sigma_t = \frac{\mu_m N}{N_A}, \quad \sigma_e = \frac{1}{N_A}\sum_i \frac{f_i N_i}{Z_i}(\mu_m)_i = \frac{\sigma_t}{Z_{eff}} \qquad (3)$$

Where

N : Atomic mass of materials $(N = \sum_i n_i A_i)$

N_A : The Avagadro's number

Z_i : The atomic number of i_{th} element

f_i : The fractional abundance of the element

$$Z_{eff} = \frac{\sigma_t}{\sigma_e}, \quad N_{eff} = \frac{N_A}{N} Z_{eff} \sum_i n_i = \frac{\mu_m}{\sigma_e} \qquad (4)$$

3. RESULTS AND DISCUSSION

The graphs (Figure 1, Figure 2) illustrate the photon energy–dependent variation of the MAC and LAC for the AZ61 alloy and its composites reinforced with 5 wt.%, 15 wt.%, and 30 wt.% WC. A common trend observed in both graphs is that all samples exhibit relatively high attenuation coefficients at low photon energies, followed by a pronounced decrease as the photon energy increases. This behavior is directly associated with the energy-dependent dominance of different photon–matter interaction mechanisms.

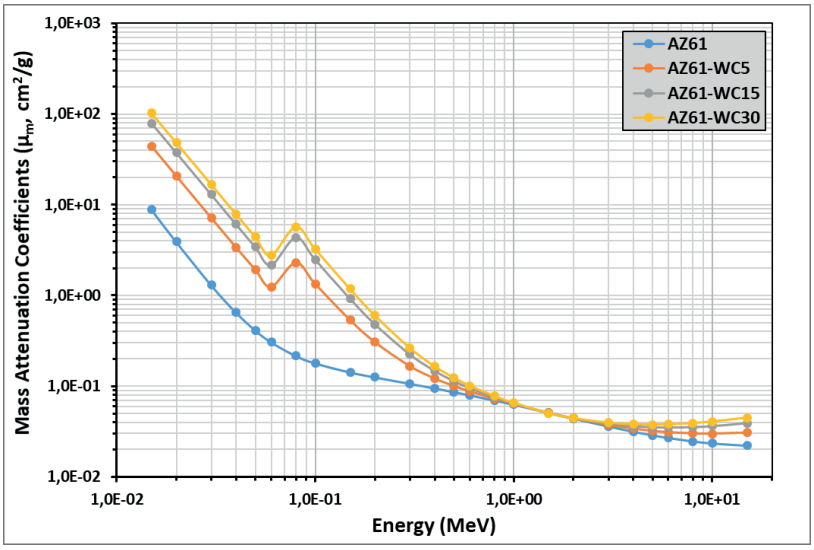

Figure 1. MAC values for the AZ61– WC composites

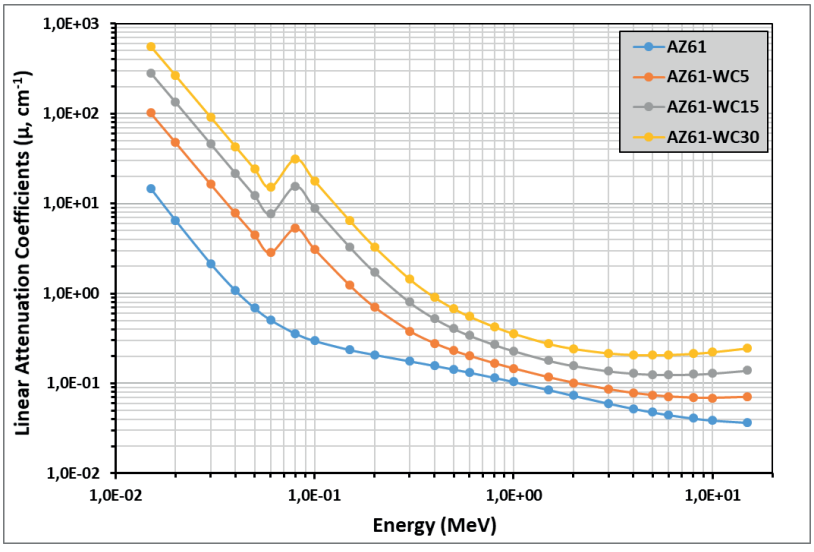

Figure 2. LAC values for the AZ61– WC composites

In the low-energy region (approximately 0.01–0.05 MeV), sharp increases in both MAC and LAC values are observed for all samples. Within this energy range, photoelectric absorption is the prevailing interaction mechanism, and its cross section shows a strong dependence on atomic number, approximately proportional to Z^4–Z^5. Since the base AZ61 alloy is primarily composed of low atomic number elements such as Mg, Al, and Zn, it exhibits the lowest MAC and LAC values in this region. In contrast, the incorporation of WC significantly enhances the attenuation performance, particularly due to the presence of tungsten, which has a high atomic number. As a result, the probability of photoelectric interactions increases substantially, leading to noticeable enhancements in both MAC and LAC. A systematic and pronounced increase in attenuation coefficients is clearly observed as the WC content increases from 5 wt.% to 30 wt.% in the low-energy domain.

For all samples, the attenuation coefficients show a relatively flatter pattern after rapidly decreasing in the intermediate energy range (about 0.05–1 MeV). Compton scattering takes over as the primary contact mechanism in this area. In contrast to the photoelectric effect, Compton scattering is more strongly correlated with electron density and shows very little reliance on atomic number. Consequently, the influence of WC addition is less pronounced than at low energies. Nevertheless, composites containing WC consistently maintain higher MAC and LAC values compared to the unreinforced AZ61 alloy, which can be attributed to the increased effective electron density and overall interaction probability within the composite structure.

At higher photon energies (≈1 MeV and above), the MAC values of all samples converge, and the differences associated with WC content become considerably less significant. In this energy region, pair production starts to contribute to photon attenuation, and material-dependent differences in mass attenuation coefficients tend to diminish. However, the LAC curves still reveal that WC-reinforced composites retain higher attenuation values than the AZ61 alloy even at high energies. This distinction arises because LAC accounts not only for atomic interaction probabilities but also explicitly incorporates the material density.

A comparative examination of the MAC and LAC results highlights the fundamental physical distinction between these two parameters. As a density-independent quantity, MAC primarily reflects the chemical composition and effective atomic number of the material, leading to converging values at higher energies. In contrast, LAC is defined as the product of MAC and material density, and therefore directly reflects density variations. Due to the high density of WC, composites containing 15 wt.% and 30 wt.% WC exhibit significantly elevated LAC values across the entire energy range.

Overall, the graphical analysis clearly demonstrates that WC reinforcement substantially enhances the gamma-ray attenuation capability of the AZ61 alloy over the full photon energy spectrum. At low energies, this improvement is mainly driven by the increased photoelectric absorption associated with the high atomic number of tungsten, while at intermediate and high energies, the increased density and total interaction probability contribute to higher LAC values. These findings indicate that WC-reinforced AZ61 composites represent a promising class of lightweight yet effective gamma radiation shielding materials.

An examination of the HVL (Figure 3), TVL (Figure 4), and MFP (Figure 5) graphs reveals a clear and consistent increase in all three parameters with rising photon energy for every composite system. Higher-energy gamma photons' increased penetrating capacity and the resulting decrease in the likelihood of photon–matter interactions per unit path length are directly linked to this characteristic. Photons are absorbed across very short distances in the low-energy area (≈0.01–0.1 MeV), where photoelectric absorption is the major interaction mechanism, leading to comparatively tiny HVL, TVL, and MFP values. Compton scattering takes over as the dominant interaction process as photon energy rises into the intermediate range (≈0.1–1 MeV), resulting in a smoother and more gradual increase in these parameters with energy. Photons traverse longer average distances within the material at higher energy (≥1 MeV) due to the rising influence of pair creation and the diminishing contribution of Compton scattering. Consequently, the HVL, TVL, and MFP parameters reach their maximum values in this energy domain.

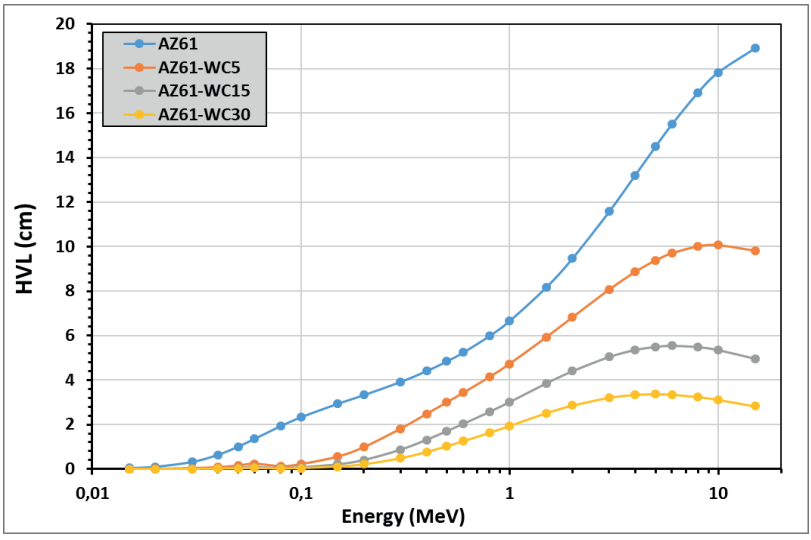

Figure 3. HVLvalues for the AZ61– WC composites

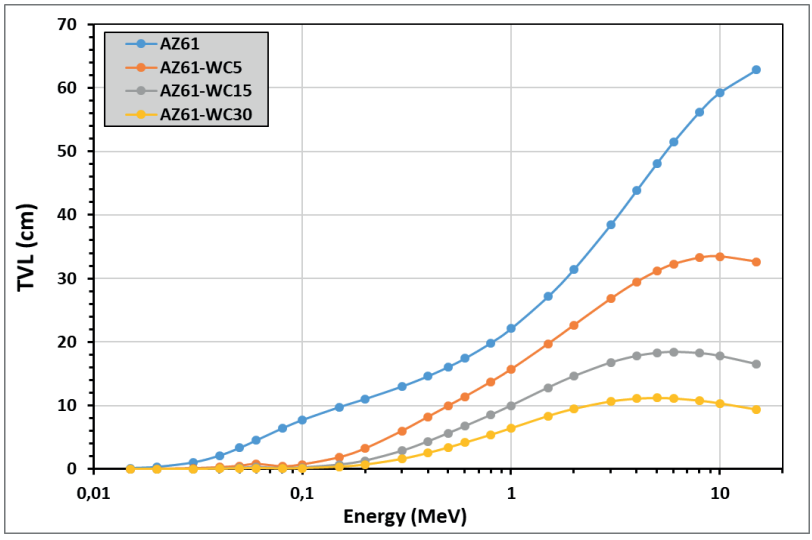

Fikgure 4. TVL values for the AZ61– WC composites

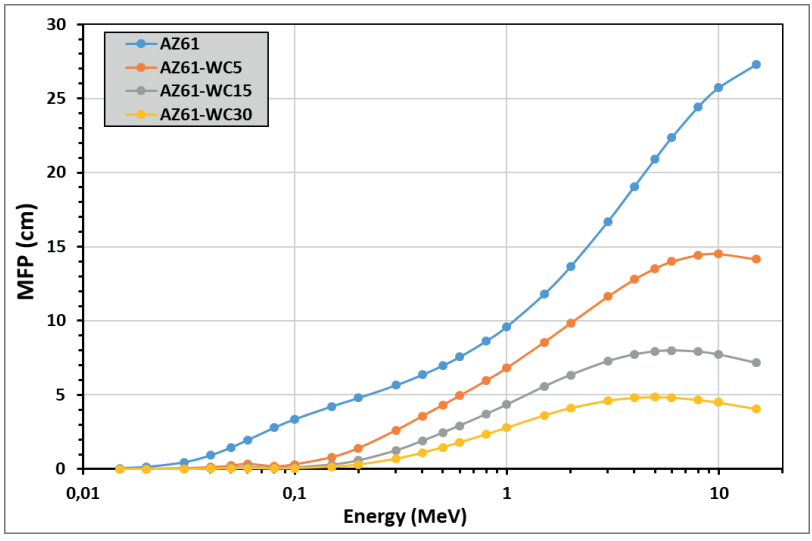

Figure 5. MFP values for the AZ61– WC composites

A comparative evaluation of the composites demonstrates that increasing the WC reinforcement content leads to a systematic reduction in HVL, TVL, and MFP values across the entire energy range. The unreinforced AZ61 alloy exhibits the highest values of these parameters, which can be attributed to its relatively low effective atomic number and density. In contrast, composites containing 5%, 15%, and particularly 30% WC show significantly lower HVL, TVL, and MFP values. The presence of WC, which incorporates

tungsten with a high atomic number and high density, enhances the photon–matter interaction probability and enables more efficient attenuation per unit thickness. As a result, thinner shielding layers and shorter mean free paths are sufficient to achieve the same attenuation levels. The lowest HVL, TVL, and MFP values observed for the AZ61–WC30 sample indicate that higher WC contents provide the most advantageous composite configuration in terms of radiation shielding effectiveness.

Although the energy-dependent trends of HVL, TVL, and MFP are qualitatively similar, notable differences exist in their numerical magnitudes. This distinction arises because, despite all three parameters being derived from the same fundamental quantity—the LAC (μ)—they represent different attenuation criteria. HVL corresponds to the thickness required to reduce the photon intensity to 50% of its initial value, whereas TVL represents the thickness needed for a more stringent reduction to 10%. Consequently, TVL values are inherently larger than HVL values for all energies and compositions. The MFP, on the other hand, characterizes the average distance traveled by a photon between successive interactions, leading to a different scaling behavior compared to HVL and TVL.

With increasing WC content, the decreasing trend in all three parameters remains consistent; however, the relative differences between compositions are more pronounced in the TVL curves than in the HVL curves. This observation suggests that at higher attenuation levels (e.g., 90% intensity reduction), the influence of increased atomic number and density becomes more dominant. In the MFP plots, the sharper rise observed at high photon energies reflects the rapidly decreasing interaction probability of high-energy photons and the corresponding extension of their average free path within the material.

In summary, the similar shapes of the HVL, TVL, and MFP curves originate from their shared dependence on the fundamental attenuation behavior of gamma photons in matter. Nevertheless, differences in their numerical values arise from the distinct attenuation thresholds they represent and from the strong impact of WC addition on both material density and effective atomic number. Overall, the results clearly demonstrate that WC-reinforced AZ61 composites—particularly those with high WC contents—exhibit markedly superior gamma-ray shielding performance compared to the monolithic AZ61 alloy.

The variation of the Zeff of AZ61–WC composites as a function of photon energy is presented in Figure 6. The energy-dependent behavior of Zeff exhibits distinct characteristic trends that are directly governed by the dominant photon–matter interaction mechanisms prevailing in different energy regions.

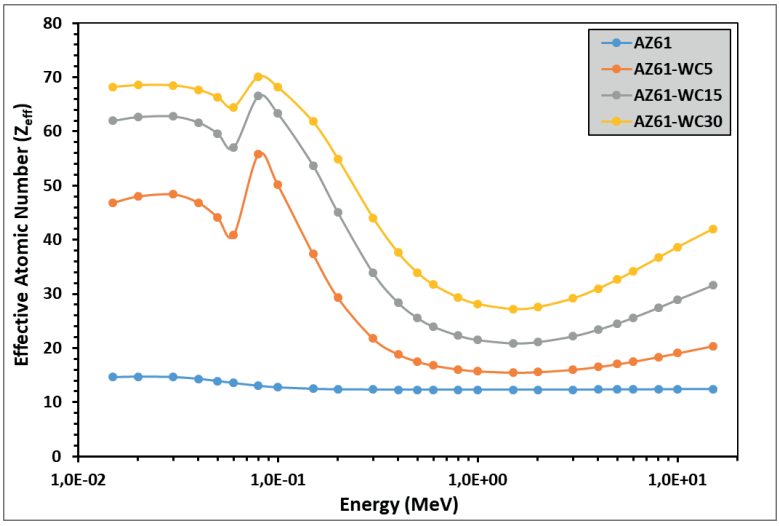

Figure 6. Zeff values for the AZ61– WC composites

In the low-energy range (approximately 0.01–0.1 MeV), all WC-reinforced composites exhibit markedly higher Zeff values compared to the unreinforced AZ61 alloy. This behavior is attributed to the dominance of the photoelectric absorption process in this energy region, which shows a strong dependence on the atomic number, typically proportional to Z4–Z5. The incorporation of WC introduces tungsten (W, Z = 74) into the composite structure, significantly increasing the average atomic number of the material. As a result, a pronounced enhancement in Zeff is observed, with the highest values recorded for the composite containing 30 wt% WC throughout the low-energy region.

The sharp peaks and abrupt variations observed in the Zeff curves at low energies are associated with the characteristic absorption edges (K- and L-edges) of tungsten. These features indicate a substantial increase in the probability of photoelectric interactions in WC-containing composites, reflecting stronger photon interactions with atomic shells. In contrast, the AZ61 alloy, composed primarily of low-Z elements such as Mg, Al, and Zn, displays lower and relatively smoother Zeff values in this region.

As the photon energy increases to the intermediate range (~0.1–1 MeV), a general decreasing trend in Zeff is observed for all samples. In this energy interval, Compton scattering becomes the dominant interaction mechanism, which depends more strongly on electron density than on atomic number. Consequently, the differences in Zeff among samples with varying WC contents become less pronounced, and the corresponding curves converge. Nevertheless, composites with higher WC content still maintain slightly higher Zeff values than the AZ61 alloy, indicating the persistent influence of tungsten's high electron population.

In the high-energy region (>1 MeV), a slight increase in Zeff is observed for all materials, which can be attributed to the onset of pair production. Since this mechanism exhibits an approximate Z2 dependence, composites with higher WC fractions demonstrate enhanced Zeff values. In particular, the AZ61–WC30 composite shows noticeably higher Zeff levels at high photon energies compared to the other samples.

The variation of the Neff of AZ61–WC composites as a function of photon energy is presented in Figure 7. The energy-dependent behavior of Neff exhibits distinct characteristic trends that are directly governed by the dominant photon–matter interaction mechanisms prevailing in different energy regions.

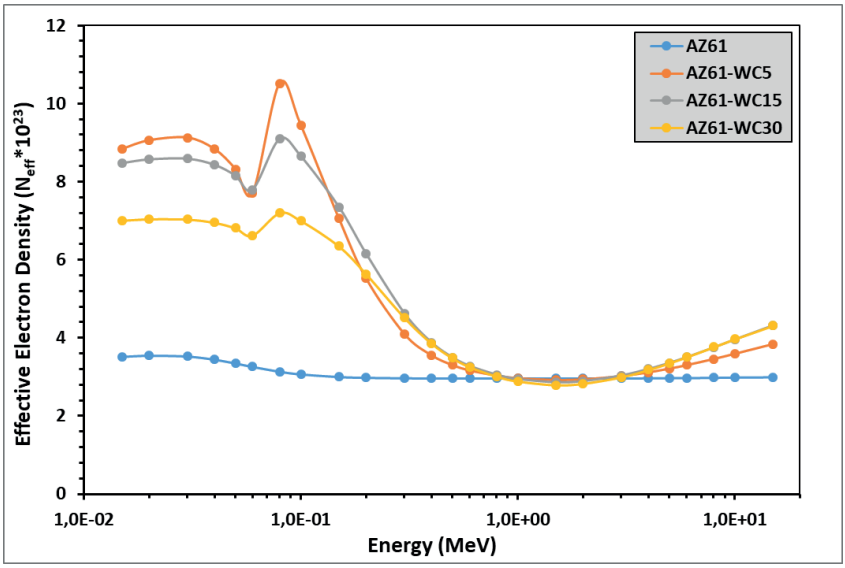

Figure 7. Neff values for the AZ61– WC composites

The trends observed for the Neff generally follow those of Zeff, although the magnitude of variation is comparatively smaller. In the low-energy region, increasing WC content leads to higher Neff values due to the increased total number of electrons contributed by tungsten. However, since Neff is related to the number of electrons per unit mass rather than higher powers of the atomic number, its variation with energy is smoother than that of Zeff.

In the intermediate energy range, the convergence of Neff values for all samples reflects the dominance of Compton scattering, where materials with similar electron densities exhibit comparable interaction behavior. At higher energies, WC-reinforced composites again show a tendency toward increased Neff, which can be linked to the contribution of tungsten to pair production processes.

Overall, increasing the WC reinforcement ratio systematically enhances both Zeff and Neff values of AZ61-based composites across the entire photon energy range, with particularly pronounced effects at low and high energies. These findings clearly demonstrate that WC reinforcement significantly improves the gamma-ray shielding capability of the AZ61 alloy, especially in energy regions dominated by photoelectric absorption and pair production mechanisms.

4. CONCLUSION

This work used the Phy-X/PSD program to theoretically examine the gamma-ray shielding properties of composite materials made by reinforcing an AZ61 magnesium alloy matrix with WC particles at weight fractions of 0, 5, 15, and 30% throughout a photon energy range of 0.015–15 MeV. It is evident from the computed shielding parameters—MAC, LAC, HVL, TVL, MFP, Zeff, and Neff—that WC reinforcement has a significant impact on the behavior of photon–matter interactions.

At low photon energies (≈0.015–0.1 MeV), all samples exhibited relatively high MAC and LAC values, followed by a pronounced decline with increasing energy. This trend is primarily attributed to the dominance of the photoelectric absorption mechanism in the low-energy region. An increase in WC content led to a systematic enhancement of MAC values and, more notably, LAC values across the entire energy spectrum. This improvement arises from the high atomic number of tungsten and the increase in composite density induced by WC addition, both of which significantly elevate the probability of photon absorption. Although the attenuation curves tend to flatten at higher energies (≈1 MeV and above) due to the growing contribution of Compton scattering and pair production, WC-rich composites consistently maintain superior shielding performance compared to the unreinforced AZ61 alloy.

The energy-dependent variations of HVL, TVL, and MFP display similar trends for all samples, with these parameters increasing steadily as photon energy rises. Nevertheless, higher WC reinforcement levels result in a marked reduction in HVL, TVL, and MFP values throughout the investigated energy range. In particular, the AZ61–WC30 composite exhibits the lowest HVL, TVL, and MFP values, indicating that a significantly thinner material layer is sufficient to achieve the same attenuation efficiency. This finding highlights that WC addition not only enhances attenuation coefficients but also enables more compact and lightweight shielding designs.

The analyses of Zeff and Neff provide deeper insight into the underlying interaction mechanisms. In the low-energy region, the elevated and sharply varying Zeff and Neff values reflect the strong dependence of the photoelectric effect on atomic number. Increasing WC content substantially raises Zeff,

thereby markedly improving shielding efficiency against low-energy photons. In the intermediate energy range (≈0.1–1 MeV), the observed reduction in Zeff and Neff is consistent with the predominance of Compton scattering. At higher energies, the renewed increase in these parameters corresponds to the growing contribution of pair production. Among all compositions, the AZ61–WC30 composite consistently exhibits the highest Zeff and Neff values, confirming its superior attenuation capability across all energy regions.

Overall, the results demonstrate that WC reinforcement significantly enhances the gamma-ray shielding performance of AZ61 magnesium alloys. Composites with higher WC content simultaneously achieve lower HVL, TVL, and MFP values and higher MAC, LAC, Zeff, and Neff values, indicating an effective balance between lightweight design and high shielding efficiency. Consequently, AZ61–WC composites emerge as promising, environmentally friendly, and mechanically advantageous alternatives to lead-based materials for applications in nuclear technology, aerospace engineering, medical radiation environments, and portable shielding systems. Future studies are recommended to validate these theoretical findings through experimental measurements and to explore the correlation between mechanical performance and radiation shielding efficiency in greater detail.

REFERENCES

Akkas, A., Tugrul, A. B., Tazegul, O., (2025). Shielding performance of Al–B4C–W composite materials against gamma-ray, beta and neutron radiations. Radiation Physics and Chemistry 232, 112662

Almuqrin, A.H., Sayyed, M.I., (2021). Radiation shielding characterizations and investigation of TeO2– WO3–Bi2O3 and TeO2–WO3–PbO glasses. Appl. Phys. A 127 (3), 1–11.

Asgari, M., Afarideh, H., Ghafoorifard, H., Amirabadi, E.A., (2021). Comparison of nano/ micro lead, bismuth and tungsten on the gamma shielding properties of the flexible composites against photon in wide energy range (40 keV-662 keV), Nucl. Eng. Technol. 53, 4142-4149.

Aygün, B., 2021. Neutron and gamma radiation shielding Ni based new type super alloys development and production by Monte Carlo Simulation technique. Radiat. Phys. Chem. 188, 109630

Bashter, I.I., (1997). Calculation of radiation attenuation coefficients for shielding concretes. Ann. Nucl. Energy 24, 1389.

Dong, M., Zhou, S., Xue, X., Feng, X., Sayyed, M.I., Khandaker, M.U., Bradley, D.A., (2021). The potential use of boron containing resources for protection against nuclear radiation. Radiat. Phys. Chem. 188, 109601.

Gökçe, H.S., Öztürk, B.C., Çam, N.F., Andiç-Çakır, Ö., (2018). Gamma-ray attenuation coefficients and transmission thickness of high consistency heavyweight concrete containing mineral admixture. Cement Concr. Compos. 92, 56–69.

Gunoglu K., (2024). Effect of colemanite mineral on gamma radiation attenuation properties of vinyl ester resin. Journal of Radiation Research and Applied Sciences 17 (2024) 100799, 1-7

Gunoglu, K., Varol Ozkavak, H., Akkurt, I., (2021). Evaluation of gamma ray attenuation properties of boron carbide (B4C) doped AISI 316 stainless steel: Experimental, XCOM and Phy-X/PSD database software. Materials Today Communications 29, 102793, 1-9.

Kavaz, E., Ghanim, E.H., Abouhaswa, A.S., (2020). Optical, structural and nuclear radiation security properties of newly fabricated V2O5-SrO-PbO glass system. J. Non-Cryst. Solids 538, 120045.

Lee, D.H.; Lee, G.M.; Park, S.H. (2022). Difference in extrusion temperature dependences of microstructure and mechanical properties between extruded AZ61 and AZ91 alloys. J. Magnes. Alloy..

Majchrowicz, K.; Adamczyk-Cie´slak, B.; Chromi´ nski, W.; Jó´zwik, P.; Pakieła, Z. (2022).Comparison of Microstructure, Texture, and Mechanical Properties of TZ61 and AZ61 Mg Alloys Processed by Differential Speed Rolling. Materials 2022, 15, 785.

Rashed, G. M., Sadawy, M. M., Kandil, A. A., Abdelkareem, A., Mohrez, W. A., (2023). Corrosion Behavior of AlMg5/10ZrO2 Metal Matrix Composite in 3.5 wt% NaCl Solution. Journal of Bio-and Tribo-Corrosion 9, 36

Rashed, G., Sadawy, M., Kandil, A., Abd Elkarim, A., Mohrez, W., (2021). Influence of ZrO2 particles on the tribological properties of AlMg5 alloy. Journal of Petroleum and Mining Engineering, vol. 23, no. 1, pp. 95-103.

Şakar, E., Özpolat, Ö.F., Alım, B., Sayyed, M.I., Kurudirek, M., (2020). Phy-X/PSD: development of a user friendly online software for calculation of parameters relevant to radiation shielding and dosimetry, Radiat. Phys. Chem. 166, 108496

Tekin, H.O., Abouhaswa, A.S., Kilicoglu, O., Issa, S.A.M., Akkurt, I., Rammah, Y.S., (2020). Fabrication, physical characteristic, and gamma-photon attenuation parameters of newly developed molybdenum reinforced bismuth borate glasses, Phys. Scr. 95, 115703.

Chapter 3

EXPERIMENTAL DESIGN AND OPTIMIZATION METHODS IN ENGINEERING: TAGUCHI METHOD AND RESPONSE SURFACE METHODOLOGY

Salih GÜL [1]

1 Karabuk University, Faculty of Engineering and Natural Sciences, Department of Mechanical Engineering, Karabuk, Türkiye e-mail: msalihgul@karabuk.edu.tr
ORCID ID: 0000-0002-0589-7510

INTRODUCTION

The studies in the fields of engineering do not only focus on attaining targeted performance values regarding the design of products and processes, but today, sustainability goals such as energy efficiency, production cost reduction, optimization of experimental studies and manufacturing processes, hence reduction of carbon emissions and carbon footprint are of greater importance in engineering studies. Since experimental studies carried out in industrial and manufacturing processes are directly related to energy consumption, raw material usage, and environmental impact, it has become necessary for these processes to be planned and efficient at an optimal level. In this context, design of experiments (DOE) has begun to be frequently used in engineering, both in academic research and in industrial applications. DOE methods aim to obtain meaningful and reliable results while minimizing the number of experiments in systems where a large number of input parameters are effective simultaneously. Through DOE methods, unnecessary experimental repetitions are prevented, and costs are reduced by minimizing energy and time losses. In this way, DOE presents a framework for methodological approaches that can be directly associated with a sustainable engineering perspective (Montgomery, 2017).

Among the optimization techniques used within DOE, the Taguchi Method (TM) and Response Surface Methodology (RSM) are among the widely used methods. Both methods aim to increase experimental efficiency and to determine the optimum parameter combination. In the literature, studies in which TM and RSM are applied to the same problems and compared are increasing, and the effects of selecting different methods on the results are being investigated (Asghar, Raman, & Daud, 2014; Said et al., 2013).

TM is an experimental design method developed by Genichi Taguchi and is based on the concept of robust design. The concept of robust design refers to improving not only the average performance of a system but also its stability against environmental effects and uncontrollable variables (Taguchi, Chowdhury, & Wu, 2005). In TM, experiments are prepared using orthogonal arrays, and the obtained results are evaluated using signal-to-noise (S/N) ratios. This approach enables the rapid and systematic acquisition of results with a limited number of experiments in cases where experiments are time-consuming and costly (Titu, Sandu, Pop, Titu, & Ciungu, 2018). However, although TM offers an approach aimed at reducing the number of experiments, it is not intended to model interactions between parameters in detail. This leads TM to determine a more general and approximate optimum method in complex systems (Khuri & Mukhopadhyay, 2010).

RSM is a more detailed optimization method that applies mathematical and statistical regression models to describe the relationship between input

variables and output responses. In this regard, in RSM, the second-order polynomial models are most widely preferred. Response surfaces may be constructed with the help of experimental designs in RSM, such as Central Composite Design and Box–Behnken, thereby allowing the analysis of system behaviour over a wide parameter range (Myers, Montgomery, & Anderson-Cook, 2009). One of the important advantages of RSM over other optimization methods is that the method not only identifies the optimal combinations of parameters but also presents the overall behaviour of the system around these optimal parameters. The usage of three-dimensional response surface plots provides the possibility of visually considering the interaction among parameters when interacting with each other (Khuri & Mukhopadhyay, 2010; Myers et al., 2009).

On the other hand, while considering experimental efficiency, TM uses orthogonal arrays to greatly reduce the number of experiments, and thus it maintains an edge in terms of resource utilization. RSM, though requiring more experiments, provides optimization options that could detail nonlinear behaviours and interactions between parameters that are not available in TM (Asghar et al., 2014; Said et al., 2013). For this reason, the literature recommends using TM for parameter screening and determining initial settings, while using RSM for detailed modelling and precise optimization within a narrowed experimental region (Khuri & Mukhopadhyay, 2010; Sri et al., 2025).

In the present work, the Taguchi Method and Response Surface Methodology are considered only from the point of view of experimental design and optimization. A comparative analysis has been performed based on existing literature, summarizing the basic differences, advantages, and limitations of the two methods. Thus, a general framework will be provided that enables the suitable selection of the experimental design method for engineering applications.

TAGUCHI METHODS (TM)

Experimental studies in engineering applications mostly involve complex structures in which multiple parameters simultaneously affect a process. In such systems, traditional trial-and-error approaches remain limited due to the requirement for a large number of experiments as well as inefficiency in terms of time, cost, and energy. Conducting experiments in a planned and systematic manner has become a necessity in industrial applications. Design of experiments methods enable the investigation of process-influencing parameters with fewer experiments, aiming to achieve reliable results in a shorter time (Karna & Sahai, 2012; Titu et al., 2018). Genichi Taguchi developed TM for this purpose and aims to improve quality at the design stage rather than controlling it after production. In the Taguchi approach,

the primary objective is not only to enhance the performance of a product or process but also to minimize its variability (Fei, Mehat, & Kamaruddin, 2013; Karna & Sahai, 2012). This approach is referred to in the literature as the robust approach. Robust design means that a system yields similar results despite external factors that are difficult to control, such as temperature, humidity, material variations, or measurement uncertainties. One of the main objectives of TM is to minimize the negative effects of such external factors on the experimental process (Karna & Sahai, 2012; Titu et al., 2018).

One of the most important features of TM is that experiments are planned using orthogonal arrays. Orthogonal arrays are designs of experiments that enable the balanced study of the effects of a large number of parameters. They reduce the number of experiments that need to be conducted, often by a great extent, unlike in full factorial designs. The literature indicates that for this reason, TM stands out in engineering applications where time and cost constraints exist (Fei et al., 2013; Taneja, Bector, & Kumar, 2012).

TM utilizes the S/N ratio in evaluating experimental results. In this expression, 'signal' is the desired result, while 'noise' refers to the external factors that affect the result. What is sought here is the realization of more stable results by reducing the effects of external factors. Thus, the TM approach offers a more realistic perspective compared to the interpretations made based on average values only. In TM, ANOVA is also often applied to identify the effects of experimental parameters on the process. Therefore, which parameter is more effective can be detected (Cetin & Kabave Kilincarslan, 2020; Gul, Demirsöz, Kabave Kilincarslan, Polat, & Cetin, 2024; Kabave Kilincarslan, Cetin, Kanbur, Sismanoglu, & Polat, 2023). However, there are studies stating that when the number of parameters is high, TM alone cannot optimize all the interactions in detail; thus, it is advised to use it together with more advanced optimization methods (Fei et al., 2013).

The TM method is a powerful experimental design approach that aims to minimize experimental processes and costs in engineering applications, while also achieving more stable results under variable conditions. The literature used in this study also demonstrates that TM has been reliably applied in different engineering fields.

RESPONSE SURFACE METHODOLOGY (RSM)

Response surface methodology (RSM) is a technique used in engineering applications to examine the relationship between multiple parameters affecting a process and the resulting output. It involves modelling this relationship mathematically and determining appropriate operating conditions. RSM was first developed by Box and Wilson in the 1950s for optimizing chemical

processes. In the subsequent period, it began to be used in many engineering fields (Khuri & Mukhopadhyay, 2010).

The main purpose of RSM is to express the relationship between input variables and output responses within a specific operating range using a mathematical model, rather than to represent the actual behaviour of the optimized system. In this way, system behaviour can be predicted through a simpler equation, rather than complex and costly experimental or numerical analyses (Anderson-Cook, Borror, & Montgomery, 2009; Myers et al., 2009). In RSM, the output is referred to as the 'response' and is assumed to be a function of multiple controllable parameters. In most applications, responses are expressed using low-degree polynomial models. The most commonly used models are linear (first order) and second-order polynomial models. First-order polynomial models are sufficient to determine the linear effects of parameters. In cases where curvature and interactions in the system are pronounced, second-order polynomial models are preferred (Anderson-Cook et al., 2009; Khuri & Mukhopadhyay, 2010).

RSM is used not only to determine the optimum parameters in a system but also to understand how these parameters interact with one another. Through two- or three-dimensional response surface plots, parameter interactions can also be visually examined (Saleem & Somá, 2015; Voss, Dean, & Draguljic, 2017). In order to ensure the validity of RSM, statistical significance tests, error analysis, and model fit are checked. Analysis of variance, residual checks, and confidence intervals are suggested in the literature to check model accuracy (Mäkelä, 2017). Another advantage of the usage of RSM is in systems where computational cost is high. Instead of long analyses, such as finite element methods or Monte Carlo simulations, the system behaviours can be addressed by a response surface created by RSM, which has lower cost and less time (Allaix & Carbone, 2011). RSM is vastly used in engineering applications, such as energy systems and manufacturing methods, to investigate the uncertainties of parameters and find optimum operating conditions (Mäkelä, 2017; Yeten, Castellini, Guyaguler, & Chen, 2005).

RSM is a powerful optimization technique in engineering that can integrate experimental design with mathematical modelling. It is particularly preferred in studies where detailed optimization and an understanding of system behaviours are targeted, especially when parameter interactions are significant.

COMPARISON OF TAGUCHI AND RESPONSE SURFACE METHODS

Design of experiments methods in engineering fields play a crucial role in enhancing product and process performance. Among these design methods, although Taguchi and RSM are directed toward similar objectives, they

employ different statistical approaches. In the literature, numerous studies have applied these methods to the same problems and compared their results (Asghar et al., 2014; Said et al., 2013).

TM is an optimization method that aims to examine the effects of a large number of parameters with a small number of experiments. While the number of experiments is reduced in TM through the use of orthogonal arrays, not only the average performance but also the variability of the outputs is taken into account by using the S/N ratio. In this way, TM is based on the concept of robust design to achieve more stable results under variable operating conditions (Asghar et al., 2014; Khuri & Mukhopadhyay, 2010).

RSM expresses the relationship between input parameters and output results through a mathematical model. In RSM, second-order polynomial mathematical models are generally used. With these models, linear effects, interactions, and curvature behaviours are addressed together. Thus, system behaviour becomes predictable not only at specific experimental points but across the entire investigated parameter range. RSM is preferred in studies where parameter interactions are pronounced, and the determination of optimum conditions is desired (Anderson-Cook et al., 2009; Khuri & Mukhopadhyay, 2010).

When evaluated from the point of view of experimental resource use, TM requires fewer experiments compared to RSM. For that reason, TM is more suitable at the beginning stages of optimization. However, sometimes it becomes difficult to draw fine details about interactions between parameters due to the limited number of experiments in TM. Although RSM requires a larger number of experiments, it gives more detailed information about system behaviour with the obtained regression model (Said et al., 2013). Literature studies have generally observed that optimum conditions revealed by TM usually gave results close to those obtained with RSM, but RSM can explain those results in a more intensive manner. For that reason, literature studies advise obtaining parameter screening and determining initial settings by TM and then performing detailed modelling and precise optimization in the narrowed range of parameters using RSM (Sri et al., 2025).

TM and RSM are complementary methods that meet different needs for optimization problems in engineering. Their choice should be based on consideration of experimental cost, a number of parameters, the level of interactions, and the precision expected from optimization. The effective application of the two discussed optimization methods presented in this study could enable the development of more efficient and reliable engineering solutions.

CONCLUSION

In this study, the basics of experimental design and optimization by using TM and RSM were addressed. TM yields a more practical experimental design for parameter screening and initial optimization since it allows more reduction in the number of experiments. On the other hand, RSM offers more precise optimization since it can model the interaction between parameters and non-linear behaviours. When the literature is also considered, it is observed that these two methods yield more effective results when used appropriately together rather than as alternatives to each other. Therefore, in engineering applications, the selection of the optimization method should be made by considering the complexity of the problem, experimental durations, and costs. If necessary, TM and RSM should be evaluated within the framework of an integrated approach.

REFERENCES

Allaix, D. L., & Carbone, V. I. (2011). An improvement of the response surface method. Structural Safety, 33(2), 165–172. doi:10.1016/J.STRUSAFE.2011.02.001

Anderson-Cook, C. M., Borror, C. M., & Montgomery, D. C. (2009). Response surface design evaluation and comparison. Journal of Statistical Planning and Inference, 139(2), 629–641. doi:10.1016/j.jspi.2008.04.004

Asghar, A., Raman, A. A. A., & Daud, W. M. A. W. (2014). A Comparison of Central Composite Design and Taguchi Method for Optimizing Fenton Process. The Scientific World Journal, 2014(1), 869120. doi:10.1155/2014/869120

Cetin, M. H., & Kabave Kilincarslan, S. (2020). Effects of cutting fluids with nano-silver and borax additives on milling performance of aluminium alloys. Journal of Manufacturing Processes, 50, 170–182. doi:10.1016/j.jmapro.2019.12.042

Fei, N. C., Mehat, N. M., & Kamaruddin, S. (2013). Practical Applications of Taguchi Method for Optimization of Processing Parameters for Plastic Injection Moulding : A Retrospective Review. ISRN Industrial Engineering, 2013, 11. doi:10.1155/2013/462174

Gul, M. S., Demirsöz, R., Kabave Kilincarslan, S., Polat, R., & Cetin, M. H. (2024). Effect of Impact Angle and Speed, and Weight Abrasive Concentration on AISI 1015 and 304 Steel Exposed to Erosive Wear. Journal of Materials Engineering and Performance, 1–19. doi:10.1007/S11665-023-09117-4/FIGURES/11

Kabave Kilincarslan, S., Cetin, M. H., Kanbur, Y., Sismanoglu, S., & Polat, R. (2023). Investigation of the effect of surface modification types on the tribological performance of cow bone powder reinforced polymer materials. Polymer Composites, 44(12), 8403–8430. doi:10.1002/pc.27707

Karna, S. K., & Sahai, R. (2012). An Overview on Taguchi Method. International Journal of Engineering and Mathematical Sciences, 1, 11–17.

Khuri, I., & Mukhopadhyay, S. (2010). Response surface methodology. WIREs Computational Statistics, 2, 128–149. doi:10.1002/wics.73

Mäkelä, M. (2017). Experimental design and response surface methodology in energy applications: A tutorial review. Energy Conversion and Management, 151(May), 630–640. doi:10.1016/j.enconman.2017.09.021

Montgomery, D. C. (2017). Chapter 13: Response Surface Methods and designs. Design and analysis of experiments.

Myers, R. H., Montgomery, D. C., & Anderson-Cook, C. M. (2009). Response Surface Methodology.

Said, M. S., Ghani, J. A., Kassim, M. S., Tomadi, S. H., Hassan, C., Haron, C., & Kedah, K. (2013). Comparison between Taguchi Method and Response Surface Methodology (RSM) In Optimizing Machining Condition Department of Mechanical & Materials Engineering , Faculty of Engineering and Built Environment ,. In International Conference on Robust Quality Engineering (pp. 60–64). Retrieved from https://core.ac.uk/download/pdf/235641908.pdf

Saleem, M. M., & Somá, A. (2015). Design of experiments based factorial design and response surface methodology for MEMS optimization. Microsystem Technologies, 21(1), 263–276. doi:10.1007/s00542-014-2186-8

Sri, D. N., Kottapalli, R., Pavani, A., Ganteda, C., Gouthami, E., Abd-elmonem, A., … Almaliki, A. H. (2025). Comparison between response surface methodology and Taguchi method for dyeing process parameters optimization in fabric manufacturing by empirical planning. Scientific Reports, 15(10209), 1–8.

Taguchi, G., Chowdhury, S., & Wu, Y. (2005). Taguchi's Quality Engineering Handbook. Taguchi's Quality Engineering Handbook. Wiley Blackwell. doi:10.1002/9780470258354

Taneja, J., Bector, M., & Kumar, R. (2012). Application of Taguchi Method for Optimizing Turning Process by the effects of Machining Parameters. International Journal of Engineering and Advanced Technology, 2(1), 263–274.

Titu, A. M., Sandu, A. V., Pop, A. B., Titu, S., & Ciungu, T. C. (2018). The Taguchi Method Application to Improve the Quality of a Sustainable Process. IOP Conference Series: Materials Science and Engineering, 374(1). doi:10.1088/1757-899X/374/1/012054

Voss, D., Dean, A., & Draguljic, D. (2017). Design and Analysis of Experiments Springer Texts in Statistics. Design and Analysis of Experiments Springer Texts in Statistics. doi:10.1016/j.npep.2014.09.004

Yeten, B., Castellini, A., Guyaguler, B., & Chen, W. H. (2005). A comparison study on experimental design and response surface methodologies. SPE Reservoir Simulation Symposium, Proceedings, 465–479. doi:10.2523/93347-ms

Chapter 4

THERMAL AND FLOW MECHANISMS GOVERNING HEAT TRANSFER ENHANCEMENT IN TUBES WITH TWISTED TAPE INSERTS

Fatma OFLAZ [1]

1 Department of Automotive Engineering, Faculty of Technology, Firat University, Elazig, 23119, Turkey. fteber@firat.edu.tr F.Oflaz (0000-0002-9636-5746)

1. Introduction

Enhancing heat transfer efficiency is a key factor in reducing overall energy consumption and operating costs, while also supporting environmentally sustainable practices. In thermal system design, enhancement strategies are widely employed either to increase the effectiveness of heat exchangers or to achieve more compact and lightweight configurations (Ahirwar and kumar 2024). These strategies are generally classified into active and passive approaches. Active methods require auxiliary energy input, whereas passive methods operate solely by modifying flow or surface characteristics without external power consumption (Alam and Kim 2018; Thapa et al. 2021). The present review concentrates on passive enhancement techniques, with particular emphasis on twisted tape inserts due to their structural simplicity and practical applicability in existing heat exchanger systems. When placed inside a tube, twisted tape inserts generate intense rotational flow and continual redirection of the fluid, promoting enhanced cross-sectional mixing and repeatedly interfering with the progression of the thermal boundary layer near the heated wall. (Kadhim et al. 2025). Compared with active enhancement approaches, passive techniques stand out for their operational simplicity, reliability, and energy efficiency. This review synthesizes findings from both experimental investigations and numerical simulations, underscoring the practicality of twisted tape inserts, especially in terms of ease of installation and their suitability for retrofitting conventional tubular heat exchangers.

2. Key Parameters Affecting Heat Exchanger Performance

Heat transfer augmentation methods intensify the coupling between the central flow stream and the wall-adjacent fluid zone. This strengthened interaction enables more effective thermal exchange at the solid fluid interface. As flow intensity increases, momentum change intensifies and convective heat transfer processes become stronger, leading to a significant improvement in overall thermal performance. From an engineering design perspective, the fundamental objective of a heat exchanger is to ensure efficient thermal energy removal or delivery, rather than simply preserving flow continuity. To quantitatively characterize this convective process, a dimensionless metric is necessary. Thus, the Nusselt number is used as the standard metric for convective heat transfer intensity and is determined according to Eq. (1).

$$Nu = \frac{hL}{k} \qquad (1)$$

Another important parameter is the friction factor, expressed by Equation (2):

$$f = \frac{\Delta P}{\frac{1}{2}\rho v^2 \frac{L}{D}} \qquad (2)$$

When evaluating the overall effectiveness of heat transfer enhancement techniques, it is essential to consider hydraulic penalties in addition to thermal improvements. To address this combined effect, the Performance Evaluation Criterion (PEC) is commonly employed. This indicator simultaneously accounts for the extent of heat transfer enhancement together with the corresponding increase in flow resistance, enabling a balanced evaluation of both aspects. By incorporating these opposing influences, the PEC offers a practical framework for comparing enhanced heat exchanger configurations with conventional designs under equal pumping power conditions. The mathematical expression of this criterion is given in Eq. (3).

$$\mathrm{PEC} = \frac{(Nu/Nu_0)}{(f/f_0)^{1/3}} \qquad (3)$$

where Nu and f correspond to the values obtained for the enhanced heat exchanger configuration, whereas Nu_0 and f_0 denote the respective values for the conventional tube (baseline case).

3. Twisted Tape Overview

A twisted tape insert is produced by shaping a thin metal strip into a helical form and positioning it along the tube axis in the flow direction. This simple geometric modification results in a distinct alteration of the internal flow behavior. The insert generates intense rotational motion and secondary flow structures, which promote stronger mixing within the fluid and repeatedly interfere with the formation of the near-wall thermal layer along the tube surface. Consequently, the implementation of twisted tape inserts leads to a noticeable enhancement in convective heat transfer capability.

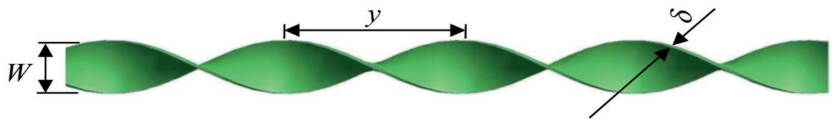

Fig. 1. Geometrical Characteristics of Twisted Tape Inserts (Wijayanta, Mirmanto, and Aziz 2020).

In this configuration, δ corresponds to its thickness, and y refers to the center to center spacing between successive pitches, while w indicates the width (or effective diameter) of the twisted tape. Twisted tape inserts may be produced from metallic materials such as aluminum, copper, and steel, and are available in a wide range of geometrical variants. Numerous configurations have been reported in the literature, including perforated designs, multi twisted tapes, screw type twisted tapes, double cut geometries, spacer integrated tapes,

and helical screw like structures, highlighting the broad diversity of twisted tape modifications developed for heat transfer enhancement (GaneshKumar et al. 2024). The performance of heat transfer systems employing twisted tape inserts is strongly governed by their geometric features. Twist ratio, insert length, and geometric modifications are key factors governing thermal enhancement and flow behavior (Al-Obaidi and Sharif 2021). Fig. 2 illustrates the different parameters that affect the performance of twisted tape inserts.

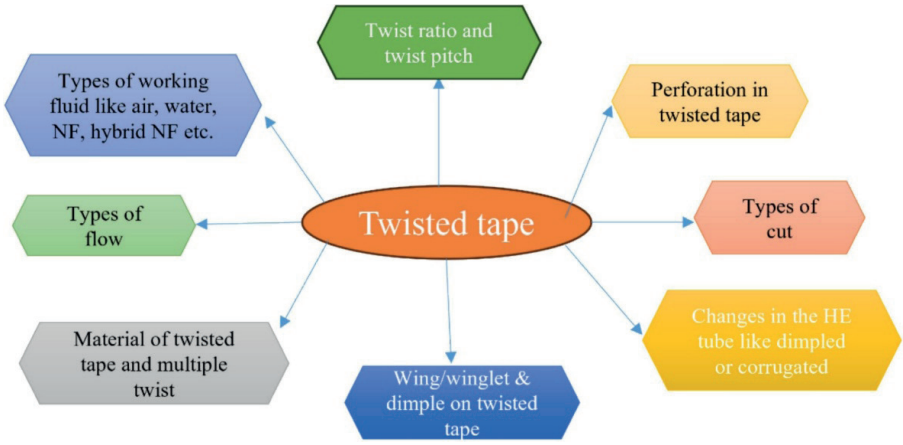

Fig. 2. Parameters Affecting the Performance of Twisted Tape Inserts (Rathaur, Sarviya, and Rajput 2026).

Several geometric descriptors are commonly used to characterize twisted tape inserts and to examine their influence on the internal flow structure. Pitch Length denotes the axial distance along the tube corresponding to a 180° rotation of the insert. Tape Width represents the transverse dimension of the insert and is quantified as the distance between its two side edges measured perpendicular to the longitudinal axis. This geometric parameter governs the fraction of the tube cross section occupied by the insert. The twist ratio is defined as a dimensionless geometric quantity obtained by dividing the pitch length by the tape width. In typical applications, the tape width is selected to be approximately equal to the inner diameter of the tube, allowing the twist ratio to indicate the intensity of flow twisting generated by the insert. The improvement in heat transfer observed with the use of twisted tape inserts (TT) increases from a combination of closely related physical mechanisms(Abolarin, Everts, and Meyer 2019);

• The insertion of a TT effectively modifies the flow passage by reducing the available hydraulic diameter, which increases local flow velocities and enhances streamline curvature. As a consequence, wall shear stress increases and secondary flow structures are more readily generated.

• Due to the partial obstruction created by the TT, fluid acceleration becomes more pronounced in the region adjacent to the wall, limiting the development of the thermal boundary layer and decreasing its overall thickness.

• The twisted configuration of the insert imposes a helicoidal trajectory on the flow along the tube axis, leading to a marked amplification of both axial and tangential velocity components.

• The resulting swirling motion improves fluid mixing by intensifying momentum exchange between the core flow and the near-wall regions, as schematically demonstrated in Fig. 3.

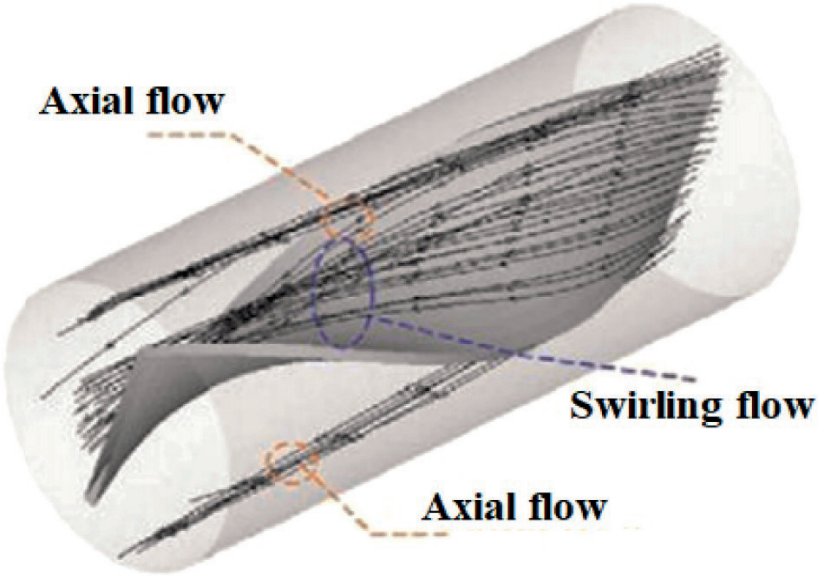

Fig. 3. Flow Characteristics of Twisted Tape Inserts (Hong, Deng, and Zhang 2012).

4. Heat Exchanger Performance Characteristics under Twisted Tape Insertion

Twisted tape inserts have long been employed in tubular configurations as a practical approach to enhancing heat transfer, with reported enhancement levels typically ranging from about 50% to 100%. This improvement primarily originates from the swirling flow induced by the insert, which increases turbulence intensity and repeatedly disturbs the thermal layer formed near the tube surface. Nevertheless, these thermal benefits are inherently accompanied by an increase in pressure losses. Such thermal gains, however, are accompanied by an inevitable rise in pressure losses. The magnitude of

this pressure drop is closely linked to the specific geometry and configuration of the turbulator. In addition, the flow regime has a substantial influence on the overall effectiveness of twisted tape inserts. Their impact is generally more pronounced under turbulent flow conditions, where mixing and flow disturbance are stronger, although measurable heat transfer enhancement can still be observed in laminar regimes (GaneshKumar et al. 2024). Chu et al. (Chu et al. 2020) conducted an experimental study examining the thermo-hydraulic characteristics of tubes equipped with twisted tape inserts over a Reynolds number range of 4000–10,000. For the plain tube configuration, the measured results were found to be consistent with the well-known Gnielinski and Filonenko correlations, with reported deviations of 9.5% for the Nusselt number and 2.8% for the friction factor. Among the various configurations considered, a sequential twisted tape with a twist ratio of 4 yielded the most advantageous combined thermal–hydraulic response, corresponding to a CTP value between 1.08 and 1.10. In addition, the authors reported that increasing the gap ratio from 0.043 to 0.135 led to simultaneous reductions in heat transfer and frictional effects, as reflected by decreases of 6.7% in the Nusselt number and 11.6% in the friction factor. The obtuse V-cut twisted tape configuration exhibited the highest enhancement levels, achieving CTP values in the range of 1.18–1.23. Despite these findings, existing empirical correlations were found to provide limited predictive accuracy for such modified geometries.

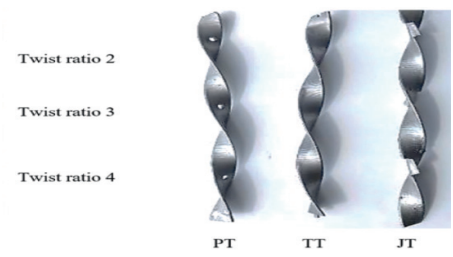

Perforated twisted tape (PT), Typical twisted tape (TT), Jagged twisted tape (JT) (Ashnaaf Abajja et al. 2025)

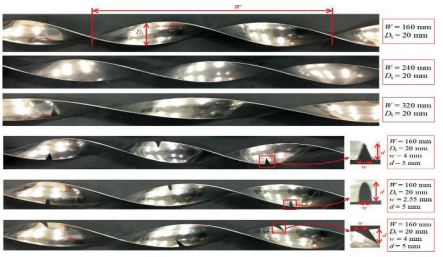

V-cut twisted tape inserts (Chu et al. 2020)

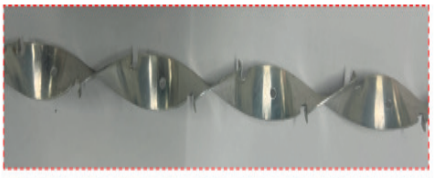

Perforated twisted tape with vortex wing(Mehta et al. 2026)

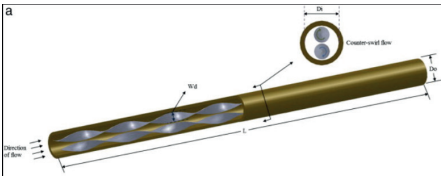

Double counter twisted tape insert (Bhuiya et al. 2014)

Fig. 4. Different types of twisted tapes

Abir et al. (Luo et al. 2024) proposed a twisted tape configuration inspired by DNA geometry, referred to as a special-shaped twisted tape (SSTT), for application in tubular heat exchangers. According to their reported results, a pitch ratio of 2 mm provided the most advantageous thermal response, resulting in an approximate 125% increase in heat transfer when compared with the corresponding plain tube case.

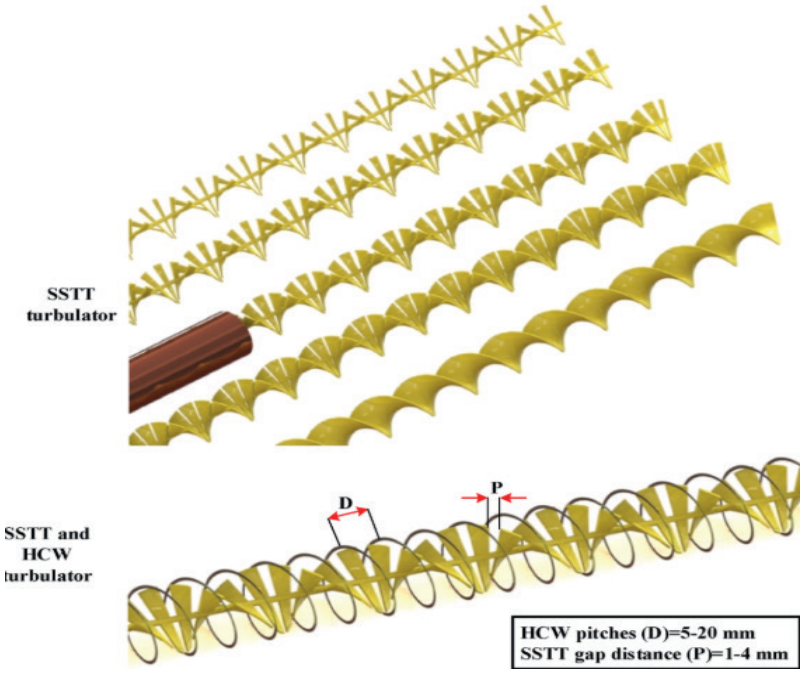

Fig. 5. Schematic illustration of a tube incorporating an SSTT (Luo et al. 2024).

A configuration integrating a twisted tape and a helical coiled wire turbulator has been associated with heat transfer increases on the order of 142%. This gain, however, was associated with a considerable increase in pressure losses, as indicated by an approximate 96% increase in pressure drop. Despite this drawback, the combined arrangement achieved an overall thermal performance factor of 1.31, representing an improvement of nearly 20% compared with a conventional twisted tape configuration.

In a separate experimental investigation (Soltani et al. 2022) analyzed the thermo-hydraulic behavior of a double-pipe heat exchanger incorporating various dimpled twisted tape geometries. Their study considered multiple insert designs, including standard twisted tapes, continuous and winglet-type configurations, as well as discontinuous louvered forms. Each design was examined in both dimpled and smooth versions to evaluate the effect of

surface texturing on heat transfer and pressure drop characteristics.

The experimental study was performed at a Reynolds number of 11,000, while the Reynolds number of the inner pipe was adjusted within the range of 5,000 to 9,500. Compared with the smooth tube case, the use of twisted tape inserts led to increases in both the Nusselt number and the friction factor; however, configurations featuring surface indentations consistently delivered higher levels than their non-indented counterparts. Among the designs examined, the segmented indented louvered twisted tape demonstrated the most favorable thermal response, achieving a maximum thermal performance factor of 1.24 at Re = 5,300.

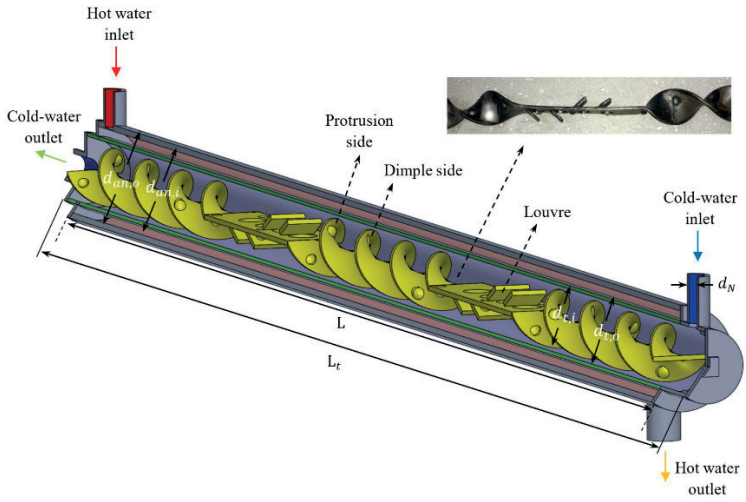

Fig. 6. Schematic of the double pipe heat exchanger with dimpled discontinuous louvered twisted tapes (Soltani et al. 2022).

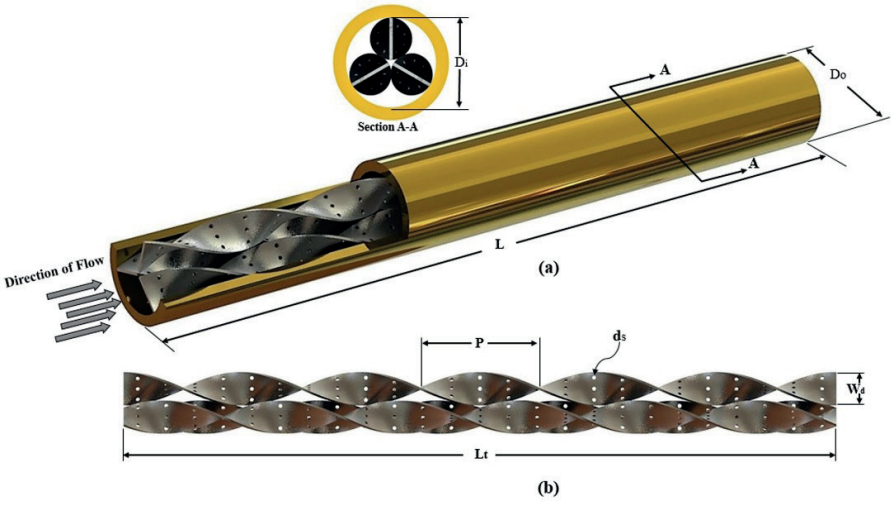

Fig. 7. (a) Schematic of the test section equipped with a PTTT insert; (b) geometrical parameters of the PTTT.(Bhuiya et al. 2020).

Bhuiya et al. (Bhuiya et al. 2020) performed an experimental investigation on a tube heat exchanger fitted with perforated triple twisted tape (PTTT) inserts operating under turbulent flow conditions, covering a Reynolds number range of 7,250–49,800 and porosity values between 1.2% and 18.6%. Their results indicated that the use of PTTT inserts led to substantial increases in the Nusselt number, ranging from 88% to 320%, accompanied by corresponding rises in the friction factor of 112% to 355% relative to a plain tube. Among the configurations examined, a porosity of 4.6% was identified as optimal, yielding a maximum thermal enhancement efficiency of 1.5. In the experimental study conducted by the test facility illustrated in Fig. 8 was used to examine the thermo hydraulic performance of an enhanced tube with water as the working fluid over a Reynolds number range of 3000–21,000 (Mehta et al. 2026). The influence of perforation diameter ratios (d/D = 0.143–0.238) and corresponding vortex generator edge cut ratios (a/D) was analyzed.

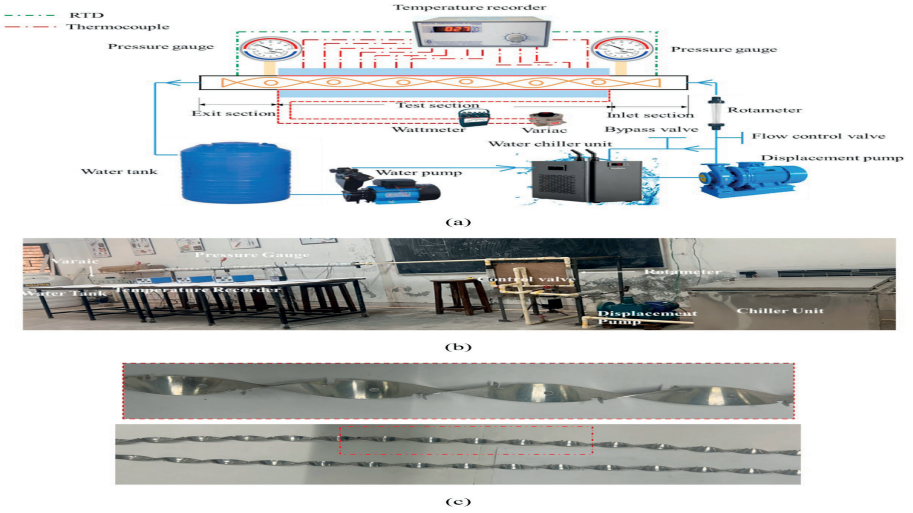

Fig. 8. Experimental Setup for Heat Transfer Measurements (Mehta et al. 2026).

The enhanced tube achieved a maximum Nusselt number improvement of 182.3% and a thermal enhancement factor of 1.68 at Re = 15,000, while the pressure drop increased by up to 345%. Entropy generation and Bejan number analyses indicated a shift toward friction-dominated irreversibility at higher Reynolds numbers and larger perforations.

5. Conclusions

This chapter synthesizes existing knowledge on the application of twisted tape inserts in heat exchanger systems, focusing on their influence on thermal behavior and fluid flow phenomena. By integrating findings from a wide range of published experimental and numerical studies, the role of insert geometry, configuration, and operating conditions in shaping heat transfer behavior is critically examined. Overall, the literature suggests that twisted tape inserts enhance heat transfer mainly by reshaping the internal flow field, while the extent of this enhancement is controlled by geometric characteristics, flow regime, and the properties of the working fluid. The key insights emerging from this synthesis are summarized in the following section.

- The use of twisted tape inserts significantly alters the internal flow structure, leading to enhanced convective heat transfer through intensified fluid mixing and boundary layer disruption. Their influence is particularly pronounced under laminar flow conditions, where the induced flow instabilities promote an early transition toward turbulence, resulting in comparatively higher heat transfer gains than those observed in fully turbulent regimes, where inherent turbulence already exists.

- Geometrical parameters play a decisive role in governing thermal performance. Reducing the pitch length brings the twisted tape closer to the tube wall, increasing the frequency of fluid–surface interactions along the heat transfer surface. This effectively raises the heat transfer surface density per unit length, thereby strengthening convective transport mechanisms.

- Advanced twisted tape configurations further improve performance. Self-rotating twisted tapes outperform stationary inserts by generating dynamic flow structures, such as rotating vortex cores, which intensify fluid mixing and continuously renew the thermal boundary layer. These unsteady flow features enable more effective thermal exchange compared to conventional fixed twisted tapes.

- In addition, modifying twisted tape geometry through cutting, perforation, or segmentation enhances fluid–wall interaction by allowing partial flow penetration through the insert. Such designs increase local turbulence intensity and improve thermal contact at the tube wall, leading to higher convective heat transfer coefficients.

- Finally, the synergistic use of optimized twisted tape geometries with advanced working fluids, including nanofluids and hybrid nanofluids, offers substantial potential for further performance enhancement. This combined approach amplifies the thermal benefits of twisted tape inserts and represents a promising pathway for the development of compact and energy-efficient heat exchangers.

REFERENCES

Abolarin, S. M., M. Everts, and J. P. Meyer. 2019. "Heat Transfer and Pressure Drop Characteristics of Alternating Clockwise and Counter Clockwise Twisted Tape Inserts in the Transitional Flow Regime." International Journal of Heat and Mass Transfer 133:203–17. doi: 10.1016/j.ijheatmasstransfer.2018.12.107.

Ahirwar, Brajesh kumar, and Arvind kumar. 2024. "Review on Different Techniques Used to Enhance the Thermal Performance of Solar Air Heater." International Journal of Heat and Mass Transfer 220(September 2023):124979. doi: 10.1016/j.ijheatmasstransfer.2023.124979.

Al-Obaidi, Ahmed Ramadhan, and Adel Sharif. 2021. "Investigation of the Three-Dimensional Structure, Pressure Drop, and Heat Transfer Characteristics of the Thermohydraulic Flow in a Circular Pipe with Different Twisted-Tape Geometrical Configurations." Journal of Thermal Analysis and Calorimetry 143(5):3533–58. doi: 10.1007/s10973-019-09244-y.

Alam, Tabish, and Man Hoe Kim. 2018. "A Comprehensive Review on Single Phase Heat Transfer Enhancement Techniques in Heat Exchanger Applications." Renewable and Sustainable Energy Reviews 81:813–39. doi: 10.1016/J.RSER.2017.08.060.

Ashnaaf Abajja, Khaled Mohamed, Selcuk Selimli, Abdulmunaem Mohamed Abdullah Shaneb, and Ibrahim Ali M. Eljetlawi. 2025. "Enhancing Heat Transfer for Laminar Flow in Heat Pipes Using Perforated and Jagged-Edged Twisted Tapes: An Experimental Study." Energy 325(April):136141. doi: 10.1016/j.energy.2025.136141.

Bhuiya, M. M. K., A. S. M. Sayem, M. Islam, M. S. U. Chowdhury, and M. Shahabuddin. 2014. "Performance Assessment in a Heat Exchanger Tube Fitted with Double Counter Twisted Tape Inserts." International Communications in Heat and Mass Transfer 50:25–33. doi: 10.1016/j.icheatmasstransfer.2013.11.005.

Bhuiya, Muhammad Mostafa Kamal, Md Mamunur Roshid, Md Mehdi Masud Talukder, Mohammad Golam Rasul, and Prasanjit Das. 2020. "Influence of Perforated Triple Twisted Tape on Thermal Performance Characteristics of a Tube Heat Exchanger." Applied Thermal Engineering 167(November 2019):114769. doi: 10.1016/j.applthermaleng.2019.114769.

Chu, Wen Xiao, Ching An Tsai, Bing Hung Lee, Kai Yueh Cheng, and Chi Chuan Wang. 2020. "Experimental Investigation on Heat Transfer Enhancement with Twisted Tape Having Various V-Cut Configurations." Applied Thermal Engineering 172(December 2019):115148. doi: 10.1016/j.applthermaleng.2020.115148.

GaneshKumar, Poongavanam, S. VinothKumar, V. S. Vigneswaran, Seong Cheol Kim, and Vanaraj Ramkumar. 2024. "Advancing Heat Exchangers for Energy Storage: A Comprehensive Review of Methods and Techniques." Journal of Energy Storage 99(PB):113334. doi: 10.1016/j.est.2024.113334.

Hong, Yuxiang, Xianhe Deng, and Lianshan Zhang. 2012. "3D Numerical Study on Compound Heat Transfer Enhancement of Converging-Diverging Tubes Equipped with Twin Twisted Tapes." Chinese Journal of Chemical Engineering 20(3):589–601. doi: 10.1016/S1004-9541(11)60223-1.

Kadhim, Saif Ali, Karrar A. Hammoodi, Hayder Mohsin Ali, Farhan Lafta Rashid, Hussein Togun, Ahmed Mohsin Alsayah, Ahmed Kadhim Hussein, Hussain Saad Abd, and Issa Omle. 2025. "Influence of the Typical Twisted Tape Inserts into the Inner Tube of Double-Pipe Heat Exchanger: A Limited Review." Results in Engineering 25(February). doi: 10.1016/j.rineng.2025.104386.

Luo, Jie, Ahmed Alghamdi, Fayez Aldawi, Hazim Moria, Abir Mouldi, Hassen Loukil, Ahmed Farouk Deifalla, and S. P. Ghoushchi. 2024. "Thermal-Frictional Behavior of New Special Shape Twisted Tape and Helical Coiled Wire Turbulators in Engine Heat Exchangers System." Case Studies in Thermal Engineering 53(September 2023):103877. doi: 10.1016/j.csite.2023.103877.

Mehta, Rajesh, Anirudh Gupta, Nitin Kumar, Smith Eiamsa-ard, Monsak Pimsarn, and Sunil Chamoli. 2026. "Influence of Perforated Twisted Tapes with Vortex Generator Wings on Heat Transfer Performance and Entropy in a Heat Exchanger Tube." International Journal of Thermal Sciences 219(July 2025):110192. doi: 10.1016/j.ijthermalsci.2025.110192.

Rathaur, Deepak Kumar, R. M. Sarviya, and S. P. S. Rajput. 2026. "International Journal of Heat and Fluid Flow Synergistic Enhancement of Heat Transfer in Tubular Heat Exchangers Using Twisted Tape Inserts and Nanofluids : An Integrated Numerical and Experimental Review." International Journal of Heat and Fluid Flow 118(November 2025):110180. doi: 10.1016/j.ijheatfluidflow.2025.110180.

Soltani, Mohammad Mohsen, Mofid Gorji-Bandpy, Ahmad Vaisi, and Rouhollah Moosavi. 2022. "Heat Transfer Augmentation in a Double-Pipe Heat Exchanger with Dimpled Twisted Tape Inserts: An Experimental Study." Heat and Mass Transfer/Waerme- Und Stoffuebertragung 58(9):1591–1606. doi: 10.1007/s00231-022-03189-z.

Thapa, Sashank, Sushant Samir, Khushmeet Kumar, and Sushma Singh. 2021. "A Review Study on the Active Methods of Heat Transfer Enhancement in Heat Exchangers Using Electroactive and Magnetic Materials." Materials Today: Proceedings 45:4942–47. doi: 10.1016/j.matpr.2021.01.382.

Wijayanta, Agung Tri, Mirmanto, and Muhammad Aziz. 2020. "Heat Transfer Augmentation of Internal Flow Using Twisted Tape Insert in Turbulent Flow." Heat Transfer Engineering 41(14):1288–1300. doi: 10.1080/01457632.2019.1637149.

Chapter 5

ARTIFICIAL INTELLIGENCE METHODOLOGIES IN MECHANICAL DESIGN OPTIMIZATION: THEORY, APPLICATIONS, AND AN INTERDISCIPLINARY PERSPECTIVE

Nilay KÜÇÜKDOĞAN [1]

Savaş ÖZTÜRK [2]

1 Department of Mechatronics Engineering, Faculty of Hasan Ferdi Turgutlu Technology, Manisa Celal Bayar University, Manisa 45160, Türkiye. https://orcid.org/0000-0003-4375-0752
2 Department of Metallurgical and Materials Engineering, Faculty of Engineering and Natural Sciences, Manisa Celal Bayar University, Manisa 45140, Türkiye. https://orcid.org/0000-0003-2661-4556

1. Introduction

Engineering design is fundamentally driven by the objective of maximizing system performance under prescribed constraints, placing optimization at the very core of the design process. The methodologies developed to achieve this objective have evolved substantially in parallel with advancements in technological and computational capabilities. This transformation can be broadly examined across four main eras: the Heuristic/Classical Era, the Age of Numerical Optimization, the Era of Metaheuristic Algorithms, and the Age of Artificial Intelligence–Assisted Optimization (Torta, Casati, Bruni, Mandarino, & Prati, 2025).

The Heuristic and Analytical (Classical) Era, spanning from the Industrial Revolution to the mid-20th century, was characterized by optimization practices largely based on engineers' experience, physical prototyping, and analytical mathematical methods. Gradient-based approaches, such as the method of Lagrange multipliers and the calculus of variations, were effective only for continuous, differentiable, and low-dimensional problems. In complex systems, the "optimal" design was often obtained by comparing a limited number of alternatives or by increasing safety factors. This practice frequently led to material overuse and suboptimal performance, reflecting the inherent limitations of the era (Zelinka, Snasael, & Abraham, 2012).

With the integration of computer technologies into engineering applications, the rise of numerical and computational optimization began during the 1960s–1980s. Advanced simulation techniques such as Finite Element Analysis (FEA) and Computational Fluid Dynamics (CFD) rapidly evolved, enabling design evaluations to be conducted in virtual environments. During the same period, optimization algorithms benefited significantly from increased computational power. Gradient-based methods (e.g., CONMIN) and linear and nonlinear programming techniques became widely adopted. However, these methods often exhibited a strong tendency to converge to local optima, showed high sensitivity to initial conditions, and required computationally expensive simulations to be executed at each design iteration (Haji & Abdulazeez, 2021).

As the demand for solving complex, multimodal problems involving discrete variables increased, nature-inspired metaheuristic algorithms gained widespread acceptance during the 1990s and early 2000s. Methods such as Genetic Algorithms (GA), Simulated Annealing (SA), Ant Colony Optimization (ACO), and Particle Swarm Optimization (PSO) offered significant advantages due to their ability to explore the global search space more effectively and their independence from gradient information. This period also marked the maturation of Multidisciplinary Design Optimization (MDO) and Multi-Objective Optimization approaches from both theoretical and practical perspectives. Nevertheless, a fundamental limitation of these algorithms

remained: achieving optimal solutions typically required thousands or even tens of thousands of function evaluations, and consequently, a large number of high-cost simulations, which continued to represent a dominant constraint (Dépincé, Guédas, & Picard, 2007; Forrester, Sobester, & Keane, 2008).

In the most recent era, artificial intelligence and machine learning–assisted optimization has introduced a paradigm shift in optimization methodologies. The primary driving force behind this transformation is the increased availability of data and the enhanced capability to learn from it. At the core of this approach lies the replacement or augmentation of computationally expensive physics-based simulations with fast and low-cost surrogate models. These surrogate models are trained using a limited number of simulation outputs through machine learning techniques such as Artificial Neural Networks (ANNs), Gaussian Processes (GPs), and Support Vector Machines (SVMs)(Xing & Tong, 2023).

The advantages offered by this new paradigm can be summarized as follows.

Computational Efficiency: Once trained, a surrogate model is capable of evaluating millions of design points at only a small fraction of the computational cost required for a full-scale, high-fidelity simulation.

Complexity Management: Deep learning techniques enable the processing of unstructured engineering data—such as images (e.g., microstructural information), time-series data (sensor measurements), and graph-based representations (e.g., molecular structures)—thereby learning complex relationships that are difficult to capture using conventional modeling approaches.

Inverse Design: Inverse design methodologies, which aim to directly obtain a design configuration that satisfies predefined performance targets, have become practically feasible within this framework.

Real-Time and Lifelong Optimization: Reinforcement learning facilitates continuous learning through interaction with the environment, allowing systems to dynamically improve their performance over time. This capability constitutes a fundamental building block for the development of digital twin technologies and autonomous systems.

In conclusion, optimization in engineering design has undergone a multidimensional evolution over time, progressing from heuristic and analytical methods to numerical algorithms, followed by metaheuristic techniques, and ultimately to contemporary artificial intelligence–assisted models. Each stage of this evolution, shaped by the prevailing technological infrastructure and computational capacity of its era, has contributed significant advances to the solution of design problems (Table 1). Nevertheless, the persistent presence of complex,

high-dimensional, and computationally expensive systems has continually driven the need for more effective optimization strategies. Current AI-based optimization approaches—particularly those leveraging surrogate modeling and reinforcement learning—enhance computational efficiency while rendering design processes more flexible, predictive, and autonomous. This ongoing transformation clearly indicates that the future of engineering design will be built not only upon faster and more accurate methods, but also upon systems that are capable of learning, adapting, and self-optimizing (Rao, 2019; Talbi, 2009).

Table 1 Evolution of optimization paradigms in engineering design

Era / Phase	Core Technologies & Methods	Key Advantages	Primary Limitations / Challenges
Heuristic & Analytical Era (Rao, 2019)	• Engineering intuition & experience • Physical prototyping • Analytical mathematics (Calculus, Lagrange methods)	• Effective for simple problems • Strong physical interpretability	• High cost (prototyping) • Limited to low-dimensional problems • Risk of convergence to local optima
Numerical Optimization Age (Nocedal & Wright, 2006)	• Widespread adoption of computers • Finite Element Analysis (FEA) • Computational Fluid Dynamics (CFD) • Gradient-based algorithms	• Virtual testing capability • Ability to model more complex systems • High repeatability	• Susceptibility to local optima • High computational cost • Requirement of gradient information
Era of Metaheuristic Algorithms (Talbi, 2009)	• Genetic Algorithms (GA) • Particle Swarm Optimization (PSO) • Multidisciplinary Design Optimization (MDO)	• Improved global search capability • Gradient-free optimization • Suitable for discrete and highly nonlinear problems	• Large number of function evaluations • Slow convergence • Sensitivity to parameter tuning
AI-Assisted Optimization Age (Forrester et al., 2008; Goodfellow, 2016)	• Artificial Neural Networks (ANN) • Gaussian Processes / Bayesian Optimization • Reinforcement Learning (RL) • Digital Twins	• Extremely fast evaluations via surrogate models • Capability to process unstructured data • Inverse design & lifelong learning	• Large data requirements • “Black-box” interpretability issues • Complexity of model training

1.1 The Necessity of Interdisciplinary Optimization in Mechanical and Materials Engineering

Traditional engineering practice has predominantly treated system design and material selection as sequential and weakly coupled processes with limited interdisciplinary interaction. Within this framework, mechanical system design is typically finalized first, followed by the selection of a suitable material from existing catalogs to satisfy the resulting requirements. However, the increasingly stringent performance demands of modern engineering—including lightweight design, high strength, cost efficiency, durability, and sustainability—have clearly exposed the limitations of such a sequential and decoupled approach. These challenges necessitate an interdisciplinary design and analysis paradigm in which mechanical system behavior and material properties across multiple length scales are optimized simultaneously within an integrated framework. Such a holistic optimization strategy expands the design space while playing a critical role in maximizing overall system performance (Dépincé et al., 2007; Rao, 2019).

The limitations of traditional approaches become particularly evident when the interaction between design and material behavior is treated in isolation. Independent optimization of mechanical design and material selection often results in suboptimal system-level performance; for instance, a structure optimized solely for weight minimization may fail to achieve the desired service life due to insufficient impact toughness of the selected material. Similarly, the sequential design paradigm hinders the effective integration of advanced materials—such as composites, metallic foams, and shape memory alloys—whose anisotropic or functional characteristics require concurrent consideration during the design stage. Moreover, neglecting manufacturing constraints during design and material selection can either lead to unnecessarily complex and costly production processes or force performance compromises to ensure manufacturability. Collectively, these factors highlight the significant limitations imposed by the lack of interdisciplinary integration in engineering design (Duan, Yan, Lee, Lund, & Wang, 2019; Maleque & Salit, 2013).

The necessity of interdisciplinary optimization becomes even more apparent when considering the multi-objective nature of contemporary engineering problems and the strong coupling between design, material behavior, and manufacturing processes. Lightweighting strategies in the automotive and aerospace sectors, for example, cannot be effectively achieved through geometric optimization or material substitution alone; instead, geometry and material variables must be optimized concurrently. Additive manufacturing technologies further amplify this need by enabling unprecedented geometric freedom while allowing local control of material

properties. Consequently, design problems such as the optimization of heat exchangers involve not only channel geometry but also spatially varying material characteristics, rendering them inherently interdisciplinary. Likewise, accurate prediction of wear, fatigue, and fracture behavior requires the integrated consideration of macroscopic stress distributions and microscopic material features within a unified optimization framework. Sustainability-driven design introduces additional layers of complexity, as minimizing environmental impact demands the simultaneous optimization of mechanical performance, material recyclability, and manufacturing energy consumption (Bendsøe, 2008; Zelinka et al., 2012).

In response to these challenges, the literature increasingly emphasizes integrated frameworks for the simultaneous optimization of materials and mechanical systems. The effective implementation of such approaches relies on three fundamental components: (i) unified modeling strategies capable of representing mechanical behavior and material properties within a common mathematical or computational framework; (ii) advanced optimization algorithms able to handle high-dimensional, multi-objective problems involving geometric, material, and process-related design variables; and (iii) a shared interdisciplinary language that facilitates collaboration among mechanical engineers, materials scientists, and manufacturing engineers. The coordinated integration of these components constitutes the foundation of a new optimization paradigm that is poised to shape the future of mechanical and materials engineering design (Duan et al., 2019; Haji & Abdulazeez, 2021; Zelinka et al., 2012).

2. Theoretical Foundations of Artificial Intelligence–Assisted Optimization

2.1. The Convergence of Machine Learning and Optimization: Fundamental Concepts

At the core of engineering optimization lies the formulation of a problem as the minimization or maximization of an objective function under a given set of constraints. Within this framework, a typical optimization problem is defined as the minimization or maximization of an objective function subject to equality and inequality constraints (Murphy, 2012).

$\boxed{minf(x)}$ veya $\boxed{maxf(x)}$

The objective function is defined by the vector of design variables.

$\boxed{x = [x_1, x_2, \dots, x_n]^T}$

It must satisfy certain inequality and equality constraints:

$\boxed{g_i((x) \leq 0, i = 1,2, \dots, m}$

and

$h_j(x) = 0, j = 1,2,\ldots,p$

In conventional optimization methods, the objective function $f(\mathrm{x})$ and the constraint functions $g_i(\mathrm{x})$ and $h_j(\mathrm{x})$ are defined through explicit mathematical models derived directly from physical laws or experimentally validated principles, such as the differential equations governing the bending behavior of a beam. In contrast, artificial intelligence–assisted optimization introduces a paradigm shift by employing data-driven implicit models that either replace or complement these explicit formulations. This approach is particularly advantageous for modeling complex, nonlinear engineering systems that are difficult to describe in closed analytical form (Murphy, 2012).

To understand this new paradigm, it is essential to clarify how search and learning processes are integrated in the exploration of the design space. Traditional optimization techniques are primarily search-driven, evaluating $f(\mathrm{x})$ at successive design points through iterative procedures. However, each evaluation often requires a computationally expensive simulation or a time-consuming experiment, rendering such methods inefficient for large and complex design spaces. AI-assisted optimization, by contrast, couples search with learning: a surrogate model is constructed from a limited set of input–output samples $(\mathrm{x}, f(\mathrm{x}))$ to approximate the global structure of the design space. Optimization is then performed on this low-cost approximation, or promising regions are identified to selectively guide high-fidelity evaluations. This strategy yields substantial computational efficiency gains, particularly in high-dimensional and expensive-to-evaluate engineering problems (Murphy, 2012; Zelinka et al., 2012).

A surrogate model provides a fast, continuous, and often differentiable approximation of the true objective function produced by high-fidelity physics-based simulations and constitutes a central reasoning component in AI-based optimization. These models are constructed using machine learning algorithms, which learn the underlying functional relationship between the design variables and the system response.

$freal(x) \approx fsurrogated(x \mid \theta)$

where θ denotes the model parameters learned during training (e.g., the weights of an artificial neural network). The accuracy and generalization capability of a surrogate model depend largely on the quality, diversity, and appropriate coverage of the initial training dataset across the design space. Consequently, Design of Experiments (DoE) methodologies, which enable systematic and efficient data acquisition, play a critical role in the success of surrogate-based optimization (Rao, 2019).

Artificial intelligence–based approaches expand the hierarchy of tasks in engineering design, redefining optimization from a pure search problem to a broader framework that also encompasses prediction and inverse analysis. Within this context, forward prediction represents the most fundamental task, aiming to estimate the objective function $f(\mathbf{x})$ or related physical responses (e.g., material properties or stress distributions) for a given design vector $\mathbf{x}$ by capturing complex nonlinear relationships at low computational cost. Optimization or inverse design seeks to identify the design variables that optimize a specified performance metric, a process that is significantly accelerated by the computational efficiency of surrogate models, particularly for high-dimensional and expensive problems. A more challenging class of problems is inverse engineering, in which the objective is to determine the design variables that yield a prescribed target response $f(\mathbf{x})$. Such problems are typically ill-posed, nonlinear, and characterized by multiple feasible solutions. Deep learning–based models provide powerful tools for addressing these inverse problems, especially in complex and high-dimensional design spaces such as material microstructures. This hierarchy of tasks highlights the broader functional scope offered by artificial intelligence in engineering design compared to traditional approaches (Murphy, 2012; Zelinka et al., 2012).

In conventional finite element analysis (FEA) workflows, each design vector $\mathbf{x}$ requires mesh generation, application of boundary conditions, and the solution of large-scale matrix equations, resulting in high computational cost that severely limits large-scale optimization studies. AI-based approaches substantially accelerate this loop by enabling models trained on data from thousands of FEA simulations to predict responses for new design configurations in milliseconds. Similarly, the complex relationship between microstructural design variables (e.g., grain size or phase fraction) and macroscopic mechanical responses, such as yield strength, which is often difficult to express explicitly using physics-based models, can be accurately captured using probabilistic surrogate modeling techniques such as Gaussian processes. These capabilities demonstrate the significant advantages of artificial intelligence in terms of computational efficiency and modeling flexibility in both structural analysis and materials engineering (Rao, 2019; Zelinka et al., 2012).

2.2. Overview of Popular AI-Based Optimization Algorithms

Following the presentation of the theoretical foundations of AI-assisted optimization, it is essential to examine how these concepts are implemented in practical engineering applications. To this end, the algorithmic families most widely adopted in the literature and validated across diverse problem domains are briefly reviewed. These methods provide concrete realizations of surrogate modeling and intelligent sampling strategies, clarifying how the optimization

process is guided in practice. Moreover, each algorithm family offers distinct advantages for problems involving coupled mechanical and material variables and tends to perform more effectively for specific classes of engineering applications (Gadde, 2020; Zelinka et al., 2012).

2.2.1. Gaussian Processes and Bayesian Optimization (for Design of Experiments)

Gaussian Processes (GPs) and Bayesian Optimization constitute a powerful framework for the efficient design of experiments in engineering problems characterized by expensive numerical simulations or physical testing. The central objective of this framework is to systematically answer the question of where the next most informative experiment or simulation should be conducted. In this sense, Bayesian Optimization emerges as a learning-driven search strategy aimed at identifying the global optimum using a minimal number of costly evaluations (Frazier & Wang, 2015; Hebbal, Balesdent, Brevault, Melab, & Talbi, 2023).

At the core of Bayesian Optimization, Gaussian Processes serve as probabilistic surrogate models capable of representing both the predicted mean response and the associated uncertainty. For a given design point x, the objective function is modeled as a random variable,

$$f(x) \sim N(\mu(x), \sigma_2(x))$$

where μ(x) and σ(x) denote the predictive mean and standard deviation, respectively. Unlike classical regression techniques, GP models explicitly capture the covariance structure between data points through kernel functions, such as Radial Basis Function (RBF) or Matérn kernels, thereby enabling simultaneous assessment of prediction accuracy and model confidence (Hebbal et al., 2023).

The decision-making mechanism in Bayesian Optimization is governed by the acquisition function, which exploits the uncertainty information provided by the GP model to select the next evaluation point. Acquisition functions balance exploration and exploitation to improve optimization efficiency. Common strategies include Expected Improvement (EI), which favors regions with high predicted improvement and uncertainty; Upper Confidence Bound (UCB), which combines the predictive mean and uncertainty through a tunable parameter κ; and Probability of Improvement (PI), which prioritizes regions with a high likelihood of outperforming the current best solution. Through these mechanisms, Bayesian Optimization achieves high-quality solutions while minimizing the number of expensive evaluations (Frazier & Wang, 2015; Hebbal et al., 2023).

Bayesian Optimization operates within an iterative loop that tightly integrates learning and search. A typical workflow consists of training a GP model on an initial dataset, $D = (x_i, f(x_i))$, computing the acquisition function over the design space, selecting the next evaluation point as $x_{\text{next}} = \arg\max_x \alpha(x)$, and updating the dataset with the newly evaluated sample. This process is repeated until a predefined stopping criterion is satisfied. Owing to its efficient use of limited data, Bayesian Optimization provides a highly effective strategy for optimization problems involving expensive simulations or experiments (Table 2).

Table 2 Typical Engineering Scenarios Highlighting the Advantages of Bayesian Optimization

Scenario	Contribution of Bayesian Optimization	Example Application
Expensive Evaluations	Enables convergence to the optimum with a minimal number of function evaluations.	Topology optimization of a complex structure where each FEA run requires approximately 24 hours (Schneider, Santiago, Rockstuhl, & Burger, 2017).
Noisy Data	Gaussian Processes naturally model observation noise through a noise variance term (σ_noise).	Data obtained from experimental measurements (e.g., mechanical testing) or partially converged simulations (Ramezani Mayiami et al., 2021).
Mixed Continuous and Categorical Variables	Appropriate kernel design allows simultaneous handling of continuous and discrete variables.	Optimization involving continuous material parameters and categorical material classes (e.g., Alloy A, Composite B) (Garrido-Merchán & Hernández-Lobato, 2020).
Black-Box Optimization	Requires no assumptions regarding functional form, derivatives, or convexity.	Optimization of a closed-source commercial solver (e.g., a CFD package) treated as a black-box (Shangguan, Lin, Wu, & Xu, 2021).

Bayesian Optimization is widely adopted in engineering problems involving expensive evaluations due to its strong computational efficiency and robust global search capability. In many applications, high-quality solutions can be obtained with as few as 50–100 objective function evaluations. Owing to its Gaussian Process–based formulation, Bayesian Optimization provides not only point estimates of the objective function but also quantitative uncertainty information, enabling informed decision-making and improved solution reliability. The probabilistic search strategy systematically balances exploration and exploitation, thereby reducing the risk of premature convergence to local optima. Despite these advantages, the performance of Bayesian Optimization deteriorates in high-dimensional design spaces, typically beyond 15–20 design variables, due to sparsity effects and the reduced effectiveness of kernel-based distance measures. Furthermore, the choice of kernel functions and their associated hyperparameters critically influences model accuracy and optimization performance. The quality of the initial experimental design, such as space-filling strategies including Latin Hypercube Sampling, also plays a decisive role in the overall success of the method (Frazier & Wang, 2015; Hebbal et al., 2023; Schneider et al., 2017).

2.2.2. Deep Learning–Based Surrogate Models

The primary objective of deep learning–based surrogate modeling in engineering optimization is to learn expressive representations capable of capturing complex, high-dimensional, and nonlinear physical behaviors from data. Unlike Gaussian Process–based approaches or metaheuristic algorithms, deep learning models focus on constructing highly accurate and computationally efficient predictors, which are subsequently embedded into optimization or inverse design frameworks. A key advantage of deep neural networks lies in their scalability to high-dimensional problems, where hundreds or even thousands of design variables can be handled without the severe limitations encountered by kernel-based methods. Moreover, deep learning models can directly process diverse data modalities, including images representing material microstructures or geometries, graph-based representations of molecular or lattice systems, and time-series data arising from sensor measurements or loading histories. When trained on sufficiently large datasets, these models can approximate highly nonlinear input–output relationships with high fidelity. Their fully differentiable structure further enables efficient gradient-based optimization through automatic differentiation, making them particularly attractive for large-scale engineering design problems (Table 3) (Frazier & Wang, 2015; Hebbal et al., 2023; Schneider et al., 2017).

Table 3 Major Neural Network Architectures and Their Applications in Engineering

Architecture Type	Primary Data Type	Example in Mechanical–Materials Optimization
Multilayer Perceptron (MLP)	Vector Data (Design Parameters)	**Material Property Prediction:** Alloy composition and heat-treatment parameters → Yield strength, toughness (Tayo, 2020).
Convolutional Neural Networks (CNNs)	Image / Grid Data (2D/3D)	**Microstructure–Property Mapping:** Metallographic images → Mechanical properties. **Geometry–Performance Mapping:** 3D voxelized CAD models → Drag coefficient, stress concentration (Frankel, Safta, Alleman, & Jones, 2022).
Graph Neural Networks (GNNs)	Graph / Structured Data	**Composite Design:** Fiber network topology and properties → Effective composite behavior. **Molecular Design:** Atomic bond graphs → Polymer properties (Inae et al., 2025).
U-Net, Conditional GANs	Input → Image Output	**Inverse Design:** Target stress distribution → Optimal geometry or microstructure. **Cellular Materials:** Target properties → 3D cellular architectures (Li, Ye, Wei, & Zhang, 2024).

Deep learning–based approaches offer a range of application scenarios for engineering optimization problems characterized by different scales and levels of complexity. One prominent application is accelerated Multidisciplinary Design Optimization (MDO), where strongly coupled analyses—such as aerodynamic (CFD), structural (FEA), and thermal simulations—render full high-fidelity evaluations at each iteration computationally prohibitive. In such cases, discipline-specific deep learning surrogate models can be combined into an integrated super-surrogate, enabling rapid prediction of multi-physics performance metrics for a given design vector and significantly reducing computational cost during optimization. Another important class of methods is Physics-Informed Neural Networks (PINNs), which aim to enforce consistency with governing physical laws. By incorporating residuals of partial differential equations (e.g., elasticity or heat conduction) into the training loss function, PINNs ensure that surrogate predictions remain physically plausible, even under limited data availability, thereby improving robustness and reliability. Deep learning also plays a critical role in inverse design, particularly through Variational Autoencoders (VAEs). In this framework, complex geometries are encoded into a low-dimensional latent space, while associated performance metrics are learned simultaneously. Target performance requirements can then be mapped back through the latent space to

generate candidate designs, enabling automated exploration of high-dimensional design spaces. The main advantages of deep learning–based optimization include high representational capacity, flexibility in handling heterogeneous data types, and extremely fast inference once trained. End-to-end learning further allows the integration of feature extraction, prediction, and optimization within a unified framework. However, these benefits come with notable limitations: large training datasets are often required, model interpretability remains limited due to the black-box nature of neural networks, and training demands substantial computational resources. Moreover, insufficient incorporation of physical constraints may lead to non-physical predictions, highlighting the importance of physics-guided learning strategies (Goodfellow, 2016; Hebbal et al., 2023; Ramezani Mayiami et al., 2021).

In summary, Bayesian Optimization and deep learning–based methods should be viewed as complementary components of AI-assisted engineering optimization. Bayesian Optimization excels in low-data, high-cost evaluation settings through uncertainty-aware and sample-efficient search, whereas deep learning surrogate models provide superior scalability and expressive power for high-dimensional and unstructured problems. Effective application in modern engineering design therefore depends not on the isolated strength of a single algorithm, but on selecting and integrating methods in accordance with problem characteristics and available data.

2.2.3. Design Exploration via Reinforcement Learning

Reinforcement Learning (RL) reformulates engineering optimization as a sequential decision-making problem, in which an agent incrementally explores the design space by interacting with an environment and learning from reward-based feedback. Unlike classical optimization methods that treat design as a static parameter selection task, RL models the process as a dynamic and experience-driven evolution of designs over time. In this framework, the agent observes the current system state (e.g., geometry, material distribution, or loading conditions), selects an action that modifies the design, and receives a reward that quantitatively reflects design quality, such as weight reduction or constraint satisfaction. The objective of RL is to learn an optimal policy that maximizes the expected cumulative reward over a sequence of design decisions. A key advantage of RL in engineering optimization lies in its ability to handle constructive and sequential design problems, making it particularly well suited for topology optimization, additive manufacturing, and multi-stage design processes. By explicitly balancing exploration and exploitation, RL can discover non-intuitive design strategies and mitigate entrapment in local optima. Moreover, RL naturally extends to time-dependent and adaptive optimization problems, where system performance must be optimized under varying operational conditions. RL has been successfully applied using different

formulations, including state-based optimization of structural parameters, image-based topology generation, hierarchical policies for multi-scale design, and multi-agent frameworks for cooperative material or composite design. Deep reinforcement learning further enhances these capabilities by leveraging neural networks to represent policies in high-dimensional design spaces. Despite its potential, the effective application of RL depends critically on reward function design, physical fidelity of the simulation environment, and computational efficiency. High-fidelity simulations often render direct RL training prohibitively expensive, motivating the integration of surrogate models to accelerate learning. Consequently, RL is increasingly combined with deep learning–based surrogates and Bayesian optimization to form hybrid frameworks (Brown, Garland, Fadel, & Li, 2022; Goodfellow, 2016).

In summary, reinforcement learning introduces not only a powerful computational tool but also a new optimization paradigm for engineering design. When integrated with surrogate modeling and uncertainty-aware methods, RL provides a foundation for autonomous, adaptive, and data-driven design systems, particularly relevant for future intelligent engineering and materials discovery applications**.**

2.3. Hybrid Approaches: Integration of Genetic Algorithms and Neural Networks

The core philosophy of hybrid optimization lies in combining the global search capability of metaheuristic algorithms with the fast prediction and representation power of deep learning models, thereby exploiting the complementary strengths of both approaches. In this context, the integration of Genetic Algorithms (GA) and Deep Learning (DL) has emerged as an effective paradigm for solving complex and high-dimensional engineering optimization problems. While GAs are well suited for exploring large and multimodal design spaces, their reliance on computationally expensive physics-based simulations for fitness evaluation often limits their practical applicability. Conversely, deep neural networks can act as highly efficient surrogate models but remain reliable only within sufficiently sampled regions of the design space. Hybrid GA–DL frameworks address these limitations by coupling GA-driven exploration with data-driven learning and approximation (Siddique, 2013).

A widely adopted strategy employs deep learning–based surrogate models to replace costly simulations during the GA fitness evaluation. An initial dataset generated via design of experiments is used to train a neural network, which subsequently provides rapid performance predictions. Periodic validation of elite GA solutions using high-fidelity simulations enables active learning and continuous surrogate refinement, significantly reducing the number of expensive evaluations. An alternative strategy enhances genetic operators

using deep learning. Neural networks trained on historical optimization data guide crossover and mutation toward promising design variables, improving convergence speed and reducing randomness. Transfer learning can further accelerate optimization by initializing populations based on prior knowledge from related problems. In a third approach, GAs are used to optimize the architecture and hyperparameters of deep neural networks themselves. Each individual encodes a candidate network configuration, and fitness is evaluated based on validation performance. This automated search replaces heuristic trial-and-error model selection and improves overall robustness. Hybrid GA–DL systems offer substantial gains in computational efficiency, often reducing the number of high-fidelity simulations by several orders of magnitude. The continuous feedback provided by surrogate models enables more directed search and faster convergence. Moreover, the flexibility of GAs in handling discrete and categorical variables complements the ability of deep learning models to capture complex nonlinear relationships. However, these approaches introduce additional challenges, including surrogate model reliability in sparsely sampled regions, increased algorithmic complexity, and sensitivity to initial data quality. Effective hybrid optimization therefore requires careful management of model updates, data selection, and hyperparameter tuning. Hybrid GA–DL frameworks can be viewed as early prototypes of closed-loop, learning-driven engineering design systems. By continuously integrating simulation data, learned representations, and evolutionary search, these methods move beyond traditional digital twins toward adaptive systems capable of autonomous design exploration. Consequently, the synergy between genetic algorithms and deep learning represents one of the most powerful toolsets for modern high-dimensional, multi-objective mechanical and materials optimization (Rao, 2019; Shangguan et al., 2021; Siddique, 2013).

3. Application Scenarios in Mechanical Engineering Design

3.1. Structural Optimization: Neural Networks for Weight Reduction and Strength Maximization

Traditional structural optimization approaches—including topology, shape, and size optimization—require the execution of computationally expensive Finite Element Analysis (FEA) at each design iteration. This requirement becomes particularly restrictive in the presence of complex geometries, multiple loading scenarios, and high-resolution models, leading to significant time and resource demands. The fundamental objective of structural optimization is to obtain a geometry that maximizes stiffness and/or strength under prescribed boundary and loading conditions while minimizing weight or material usage. However, classical iterative solution strategies rely on repeated and costly analysis loops to achieve this goal (Bendsøe, 2008; Nocedal & Wright, 2006).

In this context, deep learning–based end-to-end optimization approaches offer an alternative and innovative framework for structural design problems. Rather than explicitly replicating or iteratively executing traditional FEA-based procedures, this paradigm learns the mechanical behavior of the system directly from data and establishes a direct mapping from design inputs to the final optimized geometry. As a result, the number of high-cost analysis steps can be substantially reduced, enabling structural optimization problems to be solved within significantly shorter time scales (Goodfellow, 2016).

Convolutional Neural Networks (CNNs) provide particularly suitable architecture for topology optimization problems due to their ability to effectively capture spatial correlations in two- and three-dimensional grid-based data. Since the design domain in structural topology optimization is typically represented as a regular cellular grid (pixel- or voxel-based), CNNs naturally align with the problem structure through their capacity for local feature extraction and multi-scale pattern learning (Munk, Vio, & Steven, 2015).

The foundation of CNN-based topology optimization lies in the construction of a large dataset composed of solutions generated by conventional topology optimization methods. Classical algorithms such as SIMP or BESO are employed to produce thousands of optimized designs under varying boundary conditions, loading cases, and target volume fractions. In each sample, these parameters constitute the input to the neural network, while the corresponding optimal material density distribution—defined over a continuous range between 0 and 1—serves as the output. Within this formulation, topology optimization is treated as a supervised learning problem. Using the resulting dataset, a CNN—often based on a U-Net–like encoder–decoder architecture—is trained to learn the mapping between problem definitions and optimal topologies. This architecture enables the network to simultaneously capture global structural behavior and local geometric details, allowing it to directly predict near-optimal topologies for given loading and boundary conditions. Once training is completed, the network can generate an optimized topology for a new design problem within seconds, in stark contrast to the hours or days typically required by conventional iterative optimization methods (Shao, 2020).

The effectiveness of this approach can be illustrated through an industrial-scale example, such as the topology optimization of an aircraft bracket. In a traditional setting, assuming that each FEA iteration requires approximately ten minutes and that around one thousand iterations are needed, the total optimization time amounts to nearly one week of computation. By contrast, in the deep learning–based framework, offline model training requires approximately one day, after which topology optimization for a new bracket

design can be performed in roughly three seconds. The resulting designs preserve stress constraints comparable to those obtained via conventional methods while achieving weight reductions of approximately 35% (Okorie, Perveen, Talamona, & Kostas, 2023).

Such deep learning–based topology optimization approaches reported in the literature are fundamentally based on learning from datasets generated by classical methods such as SIMP and BESO (Figure 1).

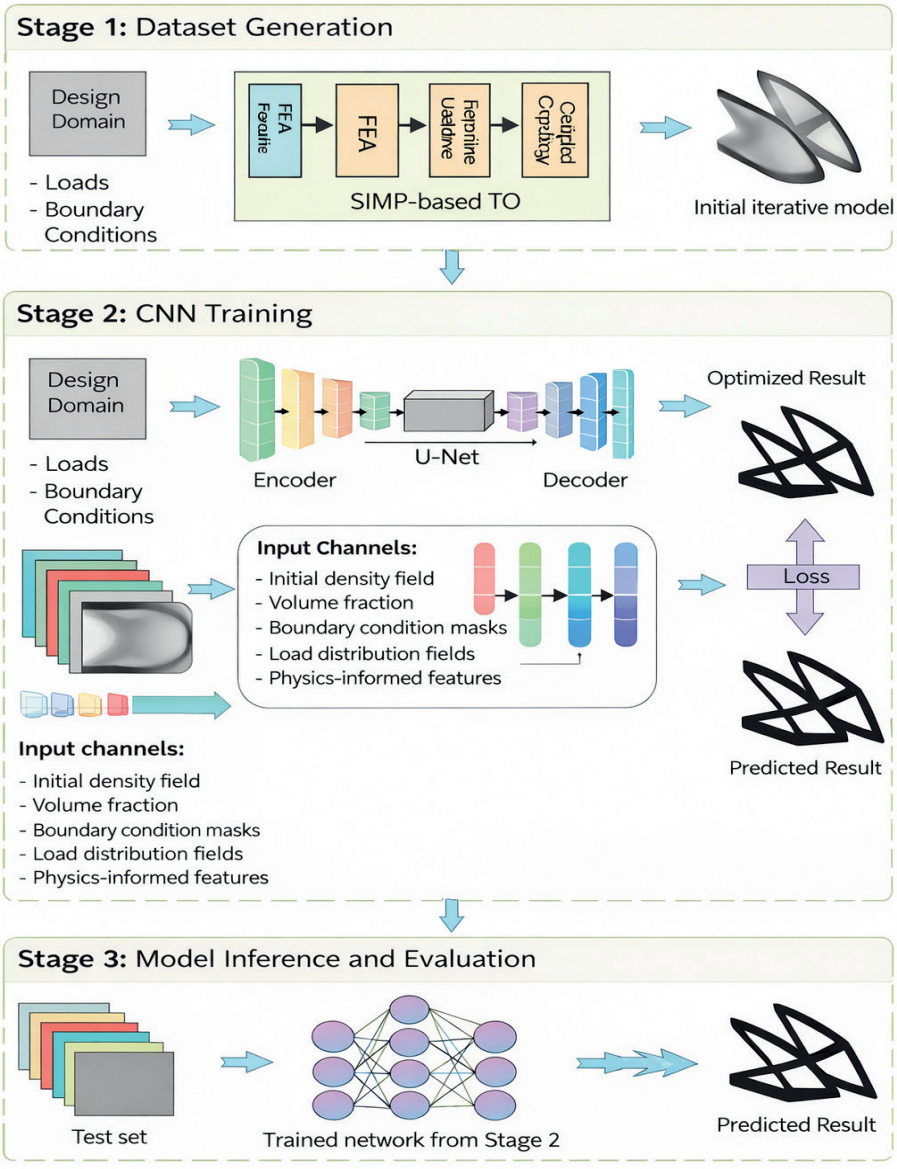

Figure 1. Schematic illustration of the deep learning–based topology optimization framework, including (i) dataset generation using SIMP-based methods, (ii) training of a convolutional neural network (CNN/U-Net) with the generated data, and (iii) inference and performance evaluation of the trained model for new design problems (Bendsøe, 2008; Brunton & Kutz, 2022; Du, Cao, Liang, Chen, & Zhan, 2020; Goodfellow, 2016).

This chapter has examined the methodological transformation introduced by artificial intelligence–based optimization approaches in mechanical and materials engineering design problems. It has been demonstrated that deep learning, reinforcement learning, and hybrid metaheuristic methods significantly accelerate traditional, iterative, and computationally expensive optimization processes, while enabling efficient exploration of high-dimensional design spaces. In particular, through the example of deep learning–based topology optimization, it has been shown that data-driven models trained on physics-based simulations establish an end-to-end design paradigm for engineering applications. Nevertheless, the effectiveness of these approaches strongly depends on factors such as simulation fidelity, data quality, and the proper integration of physical constraints into the learning process. Looking forward, physics-informed artificial intelligence models and autonomous learning loops are expected to play a central role in shaping more adaptive, efficient, and discovery-oriented engineering design workflows.

REFERENCES

Bendsøe, M. P. (2008). Topology optimization. In Encyclopedia of Optimization (pp. 3928-3929): Springer.

Brown, N. K., Garland, A. P., Fadel, G. M., & Li, G. (2022). Deep reinforcement learning for engineering design through topology optimization of elementally discretized design domains. Materials & Design, 218, 110672.

Brunton, S. L., & Kutz, J. N. (2022). Data-driven science and engineering: Machine learning, dynamical systems, and control: Cambridge University Press.

Dépincé, P., Guédas, B., & Picard, J. (2007). Multidisciplinary and multiobjective optimization: Comparison of several methods. Paper presented at the 7th World Congress on Structural and Multidisciplinary Optimization.

Du, G., Cao, X., Liang, J., Chen, X., & Zhan, Y. (2020). Medical image segmentation based on U-net: A review. Journal of Imaging Science & Technology, 64(2).

Duan, Z., Yan, J., Lee, I., Lund, E., & Wang, J. (2019). Discrete material selection and structural topology optimization of composite frames for maximum fundamental frequency with manufacturing constraints. Structural and Multidisciplinary Optimization, 60(5), 1741-1758.

Forrester, A., Sobester, A., & Keane, A. (2008). Engineering design via surrogate modelling: a practical guide: John Wiley & Sons.

Frankel, A. L., Safta, C., Alleman, C., & Jones, R. E. (2022). Mesh-based graph convolutional neural networks for modeling materials with microstructure. Journal of Machine Learning for Modeling and Computing, 3(1).

Frazier, P. I., & Wang, J. (2015). Bayesian optimization for materials design. In Information science for materials discovery and design (pp. 45-75): Springer.

Gadde, H. (2020). AI-Assisted Decision-Making in Database Normalization and Optimization. International Journal of Machine Learning Research in Cybersecurity and Artificial Intelligence, 11(1), 230-259.

Garrido-Merchán, E. C., & Hernández-Lobato, D. (2020). Dealing with categorical and integer-valued variables in bayesian optimization with gaussian processes. Neurocomputing, 380, 20-35.

Goodfellow, I. (2016). Deep learning. In: MIT press.

Haji, S. H., & Abdulazeez, A. M. (2021). Comparison of optimization techniques based on gradient descent algorithm: A review. PalArch's Journal of Archaeology of Egypt/Egyptology, 18(4), 2715-2743.

Hebbal, A., Balesdent, M., Brevault, L., Melab, N., & Talbi, E.-G. (2023). Deep Gaussian process for multi-objective Bayesian optimization. Optimization and Engineering, 24(3), 1809-1848.

Inae, E., Liu, Y., Zhu, Y., Xu, J., Liu, G., Zhang, R., . . . Jiang, M. (2025). Modeling Polymers with Neural Networks: American Chemical Society.

Li, J., Ye, H., Wei, N., & Zhang, X. (2024). ResUNet involved generative adversarial network-based topology optimization for design of 2D microstructure with extreme material properties. Mathematics and Mechanics of Solids, 29(8), 1683-1698.

Maleque, M. A., & Salit, M. S. (2013). Materials selection and design: Springer.

Munk, D. J., Vio, G. A., & Steven, G. P. (2015). Topology and shape optimization methods using evolutionary algorithms: a review. Structural and Multidisciplinary Optimization, 52(3), 613-631.

Murphy, K. P. (2012). Machine learning: a probabilistic perspective: MIT press.

Nocedal, J., & Wright, S. J. (2006). Numerical optimization: Springer.

Okorie, O., Perveen, A., Talamona, D., & Kostas, K. (2023). Topology optimization of an aerospace bracket: Numerical and experimental investigation. Applied Sciences, 13(24), 13218.

Ramezani Mayiami, M., Hajimirsadeghi, M., Skretting, K., Dong, X., Blum, R. S., & Poor, H. V. (2021). Bayesian topology learning and noise removal from network data. Discover Internet of Things, 1(1), 11.

Rao, S. S. (2019). Engineering optimization: theory and practice: John Wiley & Sons.

Schneider, P.-I., Santiago, X. G., Rockstuhl, C., & Burger, S. (2017). Global optimization of complex optical structures using Bayesian optimization based on Gaussian processes. Paper presented at the Digital Optical Technologies 2017.

Shangguan, Z., Lin, L., Wu, W., & Xu, B. (2021). Neural process for black-box model optimization under bayesian framework. arXiv preprint arXiv:2104.02487.

Shao, G. (2020). Comparison of BESO and SIMP to do structural topology optimization in discrete digital design, and then combine them into a hybrid method. Paper presented at the Architectural intelligence: selected papers from the 1st International conference on computational design and robotic fabrication (CDRF 2019).

Siddique, N. (2013). Intelligent control: a hybrid approach based on fuzzy logic, neural networks and genetic algorithms (Vol. 517): Springer.

Talbi, E.-G. (2009). Metaheuristics: from design to implementation: John Wiley & Sons.

Tayo, O. A. (2020). Machine Learning Prediction of Nd: YAG Laser Welded Sintered Metalling Alloy: Mechanical Properties: University of Johannesburg (South Africa).

Torta, P., Casati, R., Bruni, S., Mandarino, A., & Prati, E. (2025). Quantum computing for space applications: a selective review and perspectives. EPJ Quantum Technology, 12(1), 66.

Xing, Y., & Tong, L. (2023). Theory of machine learning assisted structural optimization algorithm and its application. AIAA Journal, 61(10), 4664-4680.

Zelinka, I., Snasael, V., & Abraham, A. (2012). Handbook of optimization: from classical to modern approach (Vol. 38): Springer Science & Business Media.

6

SURFACE MORPHOLOGY OF FDM-PRINTED PLA-BASED PRODUCTS: THE ROLE OF ADDITIVES AND REINFORCEMENTS

Erman ZURNACI[1]

1 Asst. Prof. Dr., Department of Mechanical Engineering, Faculty of Engineering and Architecture, Kastamonu University, Kastamonu 37150, Türkiye, https://orcid.org/0000-0003-1298-4054, ermanzurnaci@kastamonu.edu.tr

1. INTRODUCTION

The increasing demand for low-cost and fast production processes has led to the development of three-dimensional printing technology, and Fused Deposition Modeling (FDM) has become one of the most widely used methods in this technology. This increased demand has also driven the development of more cost-effective production technologies, making 3D printers more economically accessible. Polylactic acid (PLA) is the most commonly used filament type in FDM 3D printers because PLA is a preferred material due to its low cost, ease of processing, and environmentally advantageous structure (Figure 1). Furthermore, its availability from renewable sources, biodegradable nature, and relatively low melting point make it a widely preferred sustainable resource in both industrial and academic studies (Taib et al., 2023; Zurnacı, 2023b; Zurnacı & Özdemir, 2023; Zurnacı & Soran, 2024). Its lower carbon footprint compared to petroleum-derived polymers, combined with its recyclability, makes PLA an attractive material in terms of sustainable production approaches (Figure 2) (Rezvani Ghomi et al., 2021).

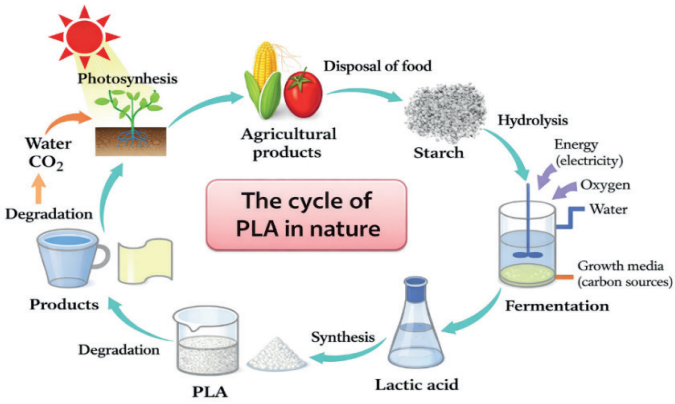

Figure 1. *Production and transformation of PLA material (Xiao et al., 2012)*

Pure PLA offers the most "predictable" surface behavior for FDM due to its low viscosity variation and lack of particles. This is one of the main reasons why PLA is used as a reference material in the literature. PLA does not release harmful chemicals after thermal degradation due to its high melting temperature. In addition, its low shrinkage tendency in FDM systems and its high dimensional stability during printing are among the reasons why PLA is preferred.

While PLA offers these properties, it also has some disadvantages. In particular, PLA's ability to meet specific strength criteria required for engineering applications is limited. This is because PLA's low impact

resistance, brittle structure that develops over time, and tendency to become embrittled restrict its use in applications requiring high strength (Hasan et al., 2024). However, researchers often utilize optimization techniques such as response surface methodology, Taguchi analysis, and fuzzy logic to improve the mechanical strength of products made from PLA material (Zurnacı & Alıcıoğlu, 2026). Furthermore, PLA's tendency to become embrittled over time causes surface wear on products made with PLA, reducing their mechanical performance under thermal and environmental influences (Gigante et al., 2019). To overcome these disadvantages of PLA, new filaments are being produced using different additives. Additives such as natural fibers, synthetic fibers, metal powders, recycled polymers, or polymer blends are commonly used to improve the mechanical properties of PLA (Zurnacı, 2023a). Thanks to the addition of additives, PLA-based filaments can be mechanically strengthened, making them suitable for a broader range of applications.

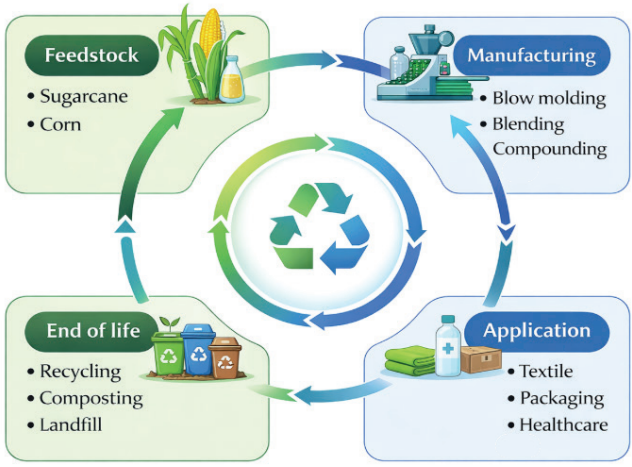

Figure 2. *Schematic representation of the life cycle of bio-based polymers (Rezvani Ghomi et al., 2021)*

Both the type and quantity of additives are essential for meeting engineering criteria. PLA additives are generally added in very low proportions because they alter the natural behavior of PLA and also change its thermal properties, requiring production at higher temperatures. However, while additive additions may provide advantages in terms of mechanical performance, they can negatively affect the surface condition and surface roughness of parts produced with FDM. The presence of fiber, particle, or metal-based additives can disrupt surface homogeneity during layer production, creating micro-protrusions and irregular surface morphologies. Therefore, components produced with additive PLA filaments may have lower surface quality compared to those made with pure PLA. This study, drawing on previous literature, comparatively examines the effects of different additive types on

the surface condition and surface roughness of PLA filaments, and evaluates the relationship between mechanical performance and surface quality.

2. TYPES OF ADDITIVES USED IN PLA FILAMENTS

The types of additives used to improve the mechanical performance of PLA filaments and facilitate their use in different fields alter the microstructure and flow behavior of the material, and also play a decisive role in the surface properties of parts produced with FDM (Ayrilmis, 2018; Pušnik Črešnar et al., 2021; Sakthivel et al., 2020). The reinforced PLA filaments examined in this study were classified according to the types of additives used, as follows:

2.1. PLA Filaments with Natural Fiber Reinforcement

PLA filaments with natural fiber reinforcement are among the most widely used types of reinforced filaments, owing to their sustainable properties, natural appearance, and minimal environmental impact. These filaments contain bio-based and lignocellulosic-based additives such as wood flour, wood fiber, and bamboo fiber. These additives support PLA's sustainability properties while also giving the manufactured products different aesthetic and mechanical characteristics. Natural fiber and filler additives generally increase the rigidity of PLA, while also imparting a natural surface texture to the material (Alpár et al., 2017). The additive ratios in reinforced filaments are not standardized across different brands. Both the additive ratio and the additive sizes can vary between brands. Furthermore, the density and homogeneous distribution of the additives also affect mechanical performance parameters. One of the most significant advantages of naturally reinforced filaments is that they allow for production at low temperatures. The homogeneous distribution of natural fiber additives, fiber size, and fiber-matrix interface compatibility directly affect both mechanical and surface properties (Pickering et al., 2016). Figure 3 shows wood flour-reinforced filaments produced by different brands. Examining the figure, it can be seen that each filament has different color tones. This is due to both the wood flour ratio and the use of wood from other tree species. In PLA filaments with natural fiber reinforcement, the irregular shape and heterogeneous distribution of the fibers can significantly increase surface roughness. In particular, the exposure of fiber ends near the surface during printing leads to the formation of micro-protrusions and voids (Oksman et al., 2003).

Figure 3. *Visual comparison of wood-reinforced filaments from different brands.*

2.2. Synthetic Fiber Reinforced PLA Filaments

Carbon fiber-reinforced PLA (CF-PLA) and glass fiber-reinforced PLA (GF-PLA) filaments have been developed for applications requiring high rigidity and strength. These types of synthetic fiber reinforcements can significantly increase the elastic modulus and load-carrying capacity of PLA. Carbon fibers, while considerably less elastic than PLA, provide the manufactured part with tremendous bending resistance, but can also make products more brittle. Glass fiber-reinforced parts are more flexible than carbon fiber and, therefore, slightly more resistant to impact (Richardson & Wisheart, 1996). The high stiffness and orientation tendency of the fibers have a positive effect on mechanical performance, but can lead to significant changes in layer formation and surface morphology during the printing process. Furthermore, since carbon fiber-reinforced filaments require high production temperatures, thermal degradation can occur during manufacturing, which affects surface roughness (Tekinalp et al., 2014). Both filament types are highly abrasive and can corrode standard brass nozzles. Furthermore, temperature variations during production and the use of high-dimensional additives can cause nozzle clogging, which affects the surface condition. Despite these challenges, synthetic fiber reinforcements enable products to achieve high mechanical performance.

2.3. PLA Filaments with Metal Powder Reinforcement

Metal powder-reinforced PLA filaments are a special type of filament obtained by mixing specific proportions of real metal powders into standard PLA filler. Copper, bronze, aluminum, and steel powders are commonly used as additives (Figure 4). These filaments are used in 3D printing projects focused on aesthetics and high mechanical strength. However, because metals have high melting points, advanced 3D printers and nozzles are required for using these filaments.

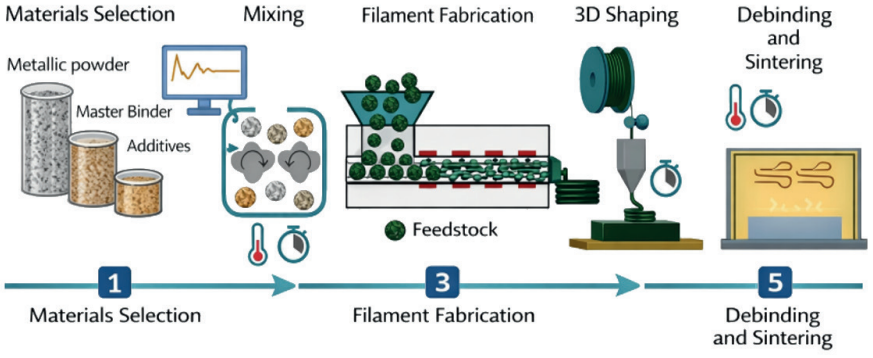

Figure 4. *Production of metallic powder filaments for additive manufacturing (Cerejo et al., 2021)*

Metal powder additives not only impart a metallic appearance to PLA-based filaments but also enhance weight, stiffness, and certain mechanical properties. However, the high density and stiffness of the metal particles significantly affect the filament flow behavior and layer formation mechanism (Ulkir, 2024). Furthermore, products manufactured using these filaments are heavier than those made with

pure PLA. Products made with metal powder-reinforced filaments often require additional processes, such as sanding and polishing, after production to improve surface quality. This increases processing time and cost.

2.4. Sustainable PLA Filaments

The primary filament type considered in this group is RePLA (recycled PLA). These filaments have been developed with a focus on sustainability and cost-effectiveness. Designed to enable the reuse of filaments used in various sectors, including hobbies, toys, modeling, and prototyping, these filaments are highly environmentally friendly. RePLA is produced from recycled PLA raw material. In these types of filaments, material homogeneity and phase compatibility are critical parameters in terms of surface and mechanical properties (Tian et al., 2017). Specifically, reprocessing and reusing filaments at high temperatures can lead to thermal degradation in the PLA material, thereby affecting its surface quality.

3. THE RELATIONSHIP BETWEEN THE MECHANICAL PERFORMANCE CONTRIBUTION OF ADDITIVES AND SURFACE QUALITY

Adding different types of additives to PLA filaments is a widely used method for improving the mechanical performance of parts produced with FDM. Thanks to fiber- and particle-based additives, significant improvements can be achieved in mechanical properties, including elastic modulus, stiffness, bending strength, lightness, and load-carrying capacity, of the produced parts. However, these mechanical gains often come with certain disadvantages in terms of surface condition and surface roughness. In PLA filaments, especially those with natural material reinforcement, the distribution of lignocellulosic structures within the PLA matrix can increase mechanical rigidity (Pickering et al., 2016). However, the irregular geometry of the fibers and the limited interface compatibility with the matrix lead to disruptions in surface homogeneity. The literature indicates that such additives have a positive effect on impact strength and rigidity; however, they also cause a significant increase in surface roughness compared to pure PLA.

Synthetic fiber reinforced PLA filaments (CF-PLA, GF-PLA) are one of the additive groups that yield the most significant improvements in mechanical performance (Liu et al., 2019). Carbon fiber and glass fiber reinforcements can significantly increase the elastic modulus and strength of PLA (Aravind et al., 2023). However, the high stiffness and orientation tendency of the fibers make layer transitions more pronounced during printing, leading to surface roughness. This highlights the need to optimize the relationship between mechanical performance and surface quality. The high stiffness and granular structure of the metal particles lead to the formation of localized protrusions on the surface, thereby increasing surface roughness (Vakharia et al., 2021). Furthermore, the use of these filaments requires high temperatures, which increases energy consumption. The literature emphasizes that these types of filaments are preferred for aesthetic or functional

purposes; however, they show limited suitability for applications requiring high surface quality.

The mechanical performance of Re-PLA filaments varies depending on the quality of the recycled material used and the homogeneity of the mixture. Some studies have reported partial decreases in mechanical properties and increases in surface roughness, despite sustainability and cost advantages (Atakok et al., 2022). This situation reveals that the balance between mechanical gain and surface quality is directly related to the type of additive, as well as production and raw material control.

Overall, while additives to PLA filaments have the potential to improve mechanical performance, it has been shown that surface quality needs to be improved by optimizing production parameters. Therefore, the selection of additive PLA filaments should be made not only based on mechanical requirements but also considering surface quality expectations and application-specific requirements.

4. VISUAL EVALUATION OF THE EFFECT OF ADDITIVE TYPE ON SURFACE MORPHOLOGY

Additives incorporated into PLA filaments significantly affect the surface morphology and roughness characteristics of the manufactured parts. Studies in the literature show that, depending on the type of additive, there is a tendency for either an increase in surface roughness or a deterioration in surface homogeneity. This is because added additives can both alter the production temperature and cause the accumulation of materials that do not sufficiently liquefy on the surface during production as solids. Furthermore, additives that can cause nozzle clogging can create voids during the production process.

Figure 5 shows microscopic images of the filaments used in production. Examination of the filament surfaces reveals that the surface of pure PLA filament is quite smooth, while the surface of CF PLA filament is rougher. Recycled PLA filament also has a rougher surface compared to pure PLA filament.

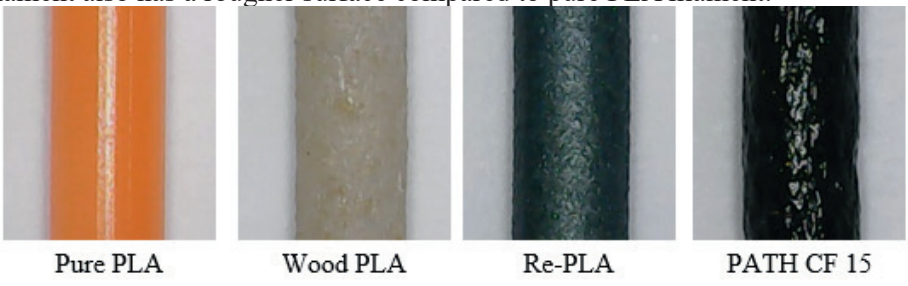

Figure 5. *Microscopic images of different filaments.*

To determine the relationship between the type of additive and surface morphology, samples produced using four different filaments—1) Pure PLA, 2) Wood PLA, 3) Re-PLA, and 4) Carbon Fiber Reinforced PLA—were

morphologically examined using a microscope. A 0.6 mm diameter nozzle was used in the production, and the production speed was kept constant at 250 mm/s (Figure 6).

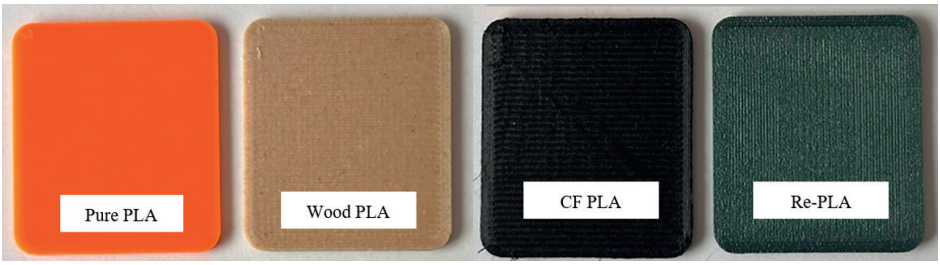

Figure 6. *The test samples produced*

In parts produced with FDM, surface properties are determined by melt flow behavior, interlayer adhesion, the size and distribution of additive particles, and the effect of nozzle diameter. In filaments containing additives, these factors become more complex compared to pure polymers. As shown in Figure 7a, distinct and regular layer traces are observed in the pure PLA sample. The surface exhibits homogeneous melt and smooth flow characteristics due to its additive-free structure. Interlayer transitions are clear and give the impression of low roughness at the micro-scale.

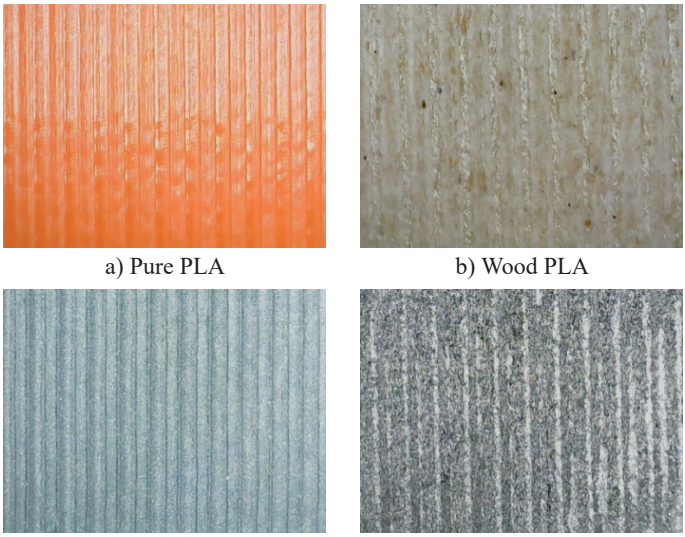

a) Pure PLA b) Wood PLA

c) Re-PLA d) CF PLA

Figure 7. *Surface photographs of products manufactured with different filaments.*

The sample produced with Wood PLA exhibits a heterogeneous structure and irregular micro-voids on its surface (Figure 7b). The presence of wood fibers/particles has resulted in increased localized surface roughness, and the layering lines appear less sharp. While Wood PLA provides an aesthetically

natural/organic texture, the wood-based additives did not fully dissolve within the polymer matrix, creating micro-protrusions.

Flow directions still appear discernible in the Re-PLA sample (Figure 7c). The surface is more matte and irregular at the microscale compared to Pure PLA. Polymer chain shortening and possible contamination effects resulting from the recycling process are more pronounced. Surface quality is slightly reduced compared to pure PLA.

Significantly higher surface roughness is observed in the carbon fiber reinforced PLA-modified sample. Partial protrusions of carbon fibers and more irregular flow directions are seen (Figure 7d). Layer transitions appear sharper and more irregular. Additionally, fiber orientation and micro-protrusions have formed at the nozzle outlet.

5. RESULTS AND DISCUSSIONS

When the studies are evaluated, it is clearly seen that the surface morphology of the samples produced by the FDM printing method is largely affected by the filament composition. While pure PLA exhibits smooth and well-defined layer structures, the addition of wood particles, recycled content, and carbon fibers leads to increased surface heterogeneity and roughness due to the disruption of melt flow behavior and particle-matrix interactions.

In addition to mechanical gains, it is understood that additives often lead to certain differences in surface quality. In PLA filaments with natural fiber reinforcement, increases in surface roughness are observed due to the heterogeneous distribution of fibers and limited interfacial compatibility. In PLA filaments with synthetic fiber reinforcement, the fiber orientation and the exposure of fiber ends in regions close to the surface cause a directional and irregular roughness structure on the surface. In remanufactured filaments such as RePLA, heterogeneity and phase incompatibility originating from the raw material have caused variability in surface quality.

In this context, it becomes clear that when evaluating reinforced PLA filaments, not only improvements in mechanical properties but also their effects on surface quality should be considered. Literature-based comparisons show that a balanced approach between mechanical performance and acceptable surface quality is possible if the type and ratio of the reinforcing compound are appropriately selected. Otherwise, achieving mechanical gains at the expense of surface quality becomes a significant limiting factor, especially in applications with high surface sensitivity.

In conclusion, additives to PLA filaments expand the material's application areas and improve its mechanical performance; however, the effects of these additives on surface condition and surface roughness should not be overlooked. For the effective and sustainable use of additive PLA filaments in engineering applications, the balance between mechanical requirements and surface quality expectations must be carefully evaluated in light of literature findings.

REFERENCES

Alpár, T., Markó, G. & Koroknai, L. (2017). Natural Fiber Reinforced PLA Composites: Effect of Shape of Fiber Elements on Properties of Composites. In *Handbook of Composites from Renewable Materials* (pp. 287–312). Wiley. https://doi.org/10.1002/9781119441632.ch30

Aravind, D., Senthilkumar, K., Rajini, N., Siengchin, S., Yorseng, K., Kumar, T. S. M., Chandrasekar, M., Mohammad, F. & Al-Lohedan, H. A. (2023). Flexural, impact, and dynamic mechanical analysis of glass fiber/ABS and glass fiber/carbon fiber/ABS composites. *Journal of Applied Polymer Science*, *140*(27). https://doi.org/10.1002/app.54007

Atakok, G., Kam, M. & Koc, H. B. (2022). Tensile, three-point bending and impact strength of 3D printed parts using PLA and recycled PLA filaments: A statistical investigation. *Journal of Materials Research and Technology*, *18*, 1542–1554. https://doi.org/10.1016/j.jmrt.2022.03.013

Ayrilmis, N. (2018). Effect of layer thickness on surface properties of 3D printed materials produced from wood flour/PLA filament. *Polymer Testing*, *71*, 163–166. https://doi.org/10.1016/j.polymertesting.2018.09.009

Cerejo, F., Gatões, D. & Vieira, M. T. (2021). Optimization of metallic powder filaments for additive manufacturing extrusion (MEX). *The International Journal of Advanced Manufacturing Technology*, *115*(7–8), 2449–2464. https://doi.org/10.1007/s00170-021-07043-0

Gigante, V., Canesi, I., Cinelli, P., Coltelli, M. B. & Lazzeri, A. (2019). Rubber Toughening of Polylactic Acid (PLA) with Poly(butylene adipate-co-terephthalate) (PBAT): Mechanical Properties, Fracture Mechanics and Analysis of Ductile-to-Brittle Behavior while Varying Temperature and Test Speed. *European Polymer Journal*, *115*, 125–137. https://doi.org/10.1016/j.eurpolymj.2019.03.015

Hasan, M. R., Davies, I. J., Pramanik, A., John, M. & Biswas, W. K. (2024). Potential of recycled PLA in 3D printing: A review. *Sustainable Manufacturing and Service Economics*, *3*, 100020. https://doi.org/10.1016/j.smse.2024.100020

Liu, J., Chen, W., Hao, H. & Wang, Z. (2019). Numerical study of low-speed impact response of sandwich panel with tube filled honeycomb core. *Composite Structures*, *220*, 736–748. https://doi.org/10.1016/J.COMPSTRUCT.2019.04.023

Oksman, K., Skrifvars, M. & Selin, J.-F. (2003). Natural fibres as reinforcement in polylactic acid (PLA) composites. *Composites Science and Technology*, *63*(9), 1317–1324. https://doi.org/10.1016/S0266-3538(03)00103-9

Pickering, K. L., Efendy, M. G. A. & Le, T. M. (2016). A review of recent developments in natural fibre composites and their mechanical performance. *Composites Part A: Applied Science and Manufacturing*, *83*, 98–112. https://doi.org/10.1016/j.compositesa.2015.08.038

Pušnik Črešnar, K., Aulova, A., Bikiaris, D. N., Lambropoulou, D., Kuzmič, K. & Fras Zemljič, L. (2021). Incorporation of Metal-Based Nanoadditives into the PLA

Matrix: Effect of Surface Properties on Antibacterial Activity and Mechanical Performance of PLA Nanoadditive Films. *Molecules*, *26*(14), 4161. https://doi.org/10.3390/molecules26144161

Rezvani Ghomi, E. R., Khosravi, F., Saedi Ardahaei, A. S., Dai, Y., Neisiany, R. E., Foroughi, F., Wu, M., Das, O. & Ramakrishna, S. (2021). The Life Cycle Assessment for Polylactic Acid (PLA) to Make It a Low-Carbon Material. *Polymers*, *13*(11), 1854. https://doi.org/10.3390/polym13111854

Richardson, M. O. W. & Wisheart, M. J. (1996). Review of low-velocity impact properties of composite materials. *Composites Part A: Applied Science and Manufacturing*, *27*(12), 1123–1131. https://doi.org/10.1016/1359-835X(96)00074-7

Sakthivel, N., Bramsch, J., Voung, P., Swink, I., Averick, S. & Vora, H. D. (2020). Investigation of 3D-printed PLA–stainless-steel polymeric composite through fused deposition modelling-based additive manufacturing process for biomedical applications. *MEDICAL DEVICES & SENSORS*, *3*(6). https://doi.org/10.1002/mds3.10080

Taib, N.-A. A. B., Rahman, M. R., Huda, D., Kuok, K. K., Hamdan, S., Bakri, M. K. Bin, Julaihi, M. R. M. Bin & Khan, A. (2023). A review on poly lactic acid (PLA) as a biodegradable polymer. *Polymer Bulletin*, *80*(2), 1179–1213. https://doi.org/10.1007/s00289-022-04160-y

Tekinalp, H. L., Kunc, V., Velez-Garcia, G. M., Duty, C. E., Love, L. J., Naskar, A. K., Blue, C. A. & Ozcan, S. (2014). Highly oriented carbon fiber–polymer composites via additive manufacturing. *Composites Science and Technology*, *105*, 144–150. https://doi.org/10.1016/j.compscitech.2014.10.009

Tian, X., Liu, T., Wang, Q., Dilmurat, A., Li, D. & Ziegmann, G. (2017). Recycling and remanufacturing of 3D printed continuous carbon fiber reinforced PLA composites. *Journal of Cleaner Production*, *142*, 1609–1618. https://doi.org/10.1016/j.jclepro.2016.11.139

Ulkir, O. (2024). Investigation on the mechanical and thermal properties of metal-PLA composites fabricated by FDM. *Rapid Prototyping Journal*, *30*(10), 2113–2122. https://doi.org/10.1108/RPJ-01-2024-0007

Vakharia, V. S., Kuentz, L., Salem, A., Halbig, M. C., Salem, J. A. & Singh, M. (2021). Additive Manufacturing and Characterization of Metal Particulate Reinforced Polylactic Acid (PLA) Polymer Composites. *Polymers*, *13*(20), 3545. https://doi.org/10.3390/polym13203545

Xiao, L., Wang, B., Yang, G. & Gauthier, M. (2012). Poly(Lactic Acid)-Based Biomaterials: Synthesis, Modification and Applications. In *Biomedical Science, Engineering and Technology*. InTech. https://doi.org/10.5772/23927

Zurnacı, E. (2023). Optimization of 3D Printing Parameters to Mechanical Strength Improvement of Sustainable Printing Material Using RSM. *International Journal of 3D Printing Technologies and Digital Industry*, *7*(1), 38–46. https://doi.org/10.46519/ij3dptdi.1231076

Zurnacı, E. (2023). Parametric Optimization of Fracture Resistance of Multilayer 3D

Printed Parts. *International Conference on Advances and Innovations in Engineering*, 63–64.

Zurnacı, E. & Alıcıoğlu, F. C. (2026). Mechanical strength of PLA parts manufactured by FDM using RSM and fuzzy logic. *Materials Testing*, *68*(1), 50–66. https://doi.org/10.1515/mt-2025-0307

Zurnacı, E. & Özdemir, H. K. (2023). Investigation of the Compressive Strength, Energy Absorption Properties and Deformation Modes of the Reinforced Core Cell Produced by the FDM Method. *Gazi Journal of Engineering Sciences*, *9*(1), 1–11. https://doi.org/10.30855/gmbd.0705047

Zurnacı, E. & Soran, İ. İ. (2024). Parametric Design and 3D Production of Door Hinges for Electric Vehicles. *International Conference on Multidisciplinary Sciences and Technological Developments*, 109–116.

Chapter 7

HYDROGEN STORAGE TECHNOLOGIES: FUNDAMENTALS, MATERIALS, APPLICATIONS AND SYSTEM-LEVEL PERSPECTIVES

Şafak Melih ŞENOCAK [1]

Yasin VAROL [2]

1 Şafak Melih ŞENOCAK, Lecturer, Osmaniye Korkut Ata University, Osmaniye Vocational School e-mail: mlhsnck@gmail.com, ORCID ID: https://orcid.org/0000-0003-0602-2836
2 Prof. Dr. Yasin VAROL, Firat University, Technology Faculty, Elazig
e-mail: yvarol@gmail.com, ORCID ID: https://orcid.org/0000-0003-2989-7125

1. Introduction

Global energy systems have faced significant pressure since the mid twentieth century due to rapidly increasing consumption, the dominance of fossil fuels and the persistence of carbon intensive production pathways (Öztürk et al., 2024). The literature emphasizes that climate change, global warming, energy supply insecurity and the sharp rise in greenhouse gas emissions driven by fossil fuel use have become principal factors compelling the development of alternative options and a transition toward modern energy structures (Ellabban et al., 2014; Omer, 2008; Liu et al., 2020; Firat et al., 2023). This situation has stimulated broader deployment of renewable energy sources and intensified research on advanced energy storage systems (Şenocak et al., 2026; Gürgenç et al., 2025). Studies indicate that sustainable development goals and the carbon reduction commitments of the Paris Agreement have strengthened the pressure on countries to decarbonize, which has increased the need for low carbon energy carriers more than ever before. Within this transition, hydrogen emerges as a strategic energy carrier due to its high specific energy content, its production potential from diverse resources, its only emission being water vapor and its inherently carbon free nature. Figure 1 illustrates the pathway of hydrogen from production to end use and highlights its relevance for future energy planning.

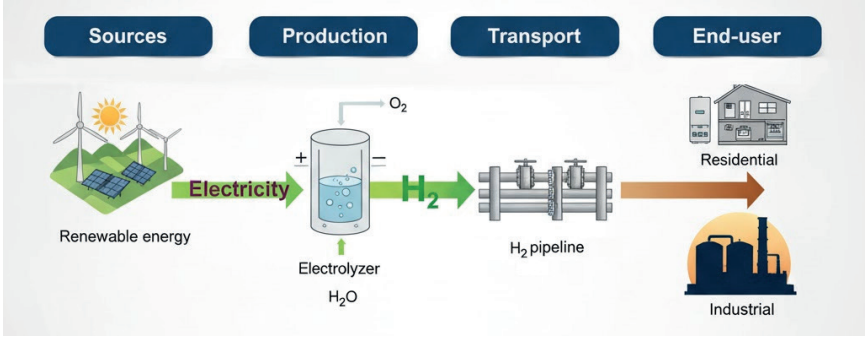

Figure 1. Schematic representation of hydrogen production and delivery to the end user.

The literature clearly indicates that the gravimetric energy density of hydrogen is almost three times higher than that of conventional fossil fuels (Bosu & Rajamohan, 2024). However, its low volumetric energy density, high diffusion coefficient, wide flammability range and the tendency to cause hydrogen embrittlement in metallic materials make well engineered storage solutions indispensable for its safe and efficient integration into energy systems (Li et al., 2022; Moradi & Groth, 2019). Figure 2 presents data on globally announced flagship hydrogen initiatives and provides an overview of current and planned large scale hydrogen deployment efforts.

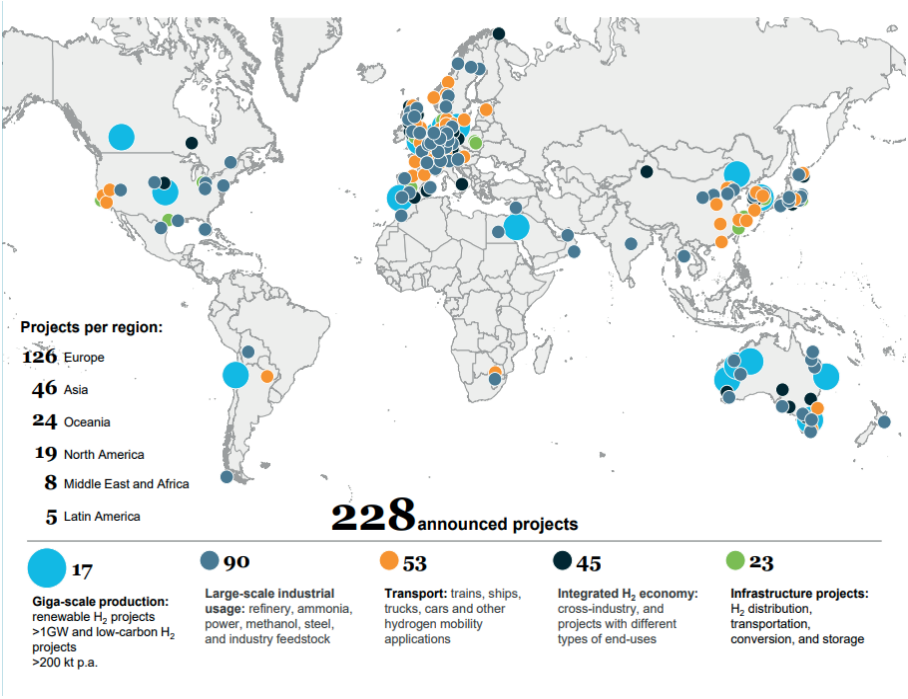

Figure 2. Globally announced flagship hydrogen initiatives, adapted from data compiled by the Hydrogen Council (Hydrogen Council, 2021).

The foremost technical challenge associated with hydrogen is its storage. The density of hydrogen in the gas phase under atmospheric conditions is extremely low and this limits the practical use of the advantageous properties that make hydrogen an attractive energy carrier. Safe and economically viable storage therefore requires one of three fundamental approaches that rely on high pressure containment, low temperature liquefaction or material based storage media (Moradi & Groth, 2019; Tarkowski & Uliasz-Misiak, 2022). In this context, the current literature classifies hydrogen storage technologies into two principal categories:

(1) physical storage methods, which include compressed gas, liquid hydrogen, cryo compressed hydrogen and underground storage, and

(2) material based storage methods, which include metal hydrides, complex hydrides, porous carbons and metal organic frameworks, liquid organic hydrogen carriers and ammonia based carriers (Bosu & Rajamohan, 2024; Rivard et al., 2019).

Compressed gas storage is currently the most widely used method in the transport sector. For example, composite Type IV tanks that can withstand pressures of 70 MPa are regarded as the only practically viable on board solution for modern fuel cell vehicles (Rivard et al., 2019). Despite this, compressed storage systems raise significant engineering concerns related to safety, fatigue life and material integrity due to the high operating pressures involved. Liquid hydrogen storage offers much higher volumetric energy density, yet the extremely low temperature required, around -253 degrees Celsius, the need for multi layer vacuum insulation in tank design and the high energy consumption of the liquefaction process impose serious economic and technical limitations. The literature clearly states that liquefaction requires about 30 percent more energy than compression (Aziz, 2021; Denton & Nicholls, 1965). Underground hydrogen storage has recently attracted growing attention as a research field because of its potential to overcome the scale limitations of above ground options. Salt caverns are considered among the most promising configurations due to their large storage capacity, fast injection and withdrawal capability and low leakage risk (Liu et al., 2020). In contrast, aquifer storage is reported to be the most expensive option because of the large cushion gas requirement, with some studies indicating that up to 42 percent of the total capital cost may arise solely from the need for cushion gas (Tarkowski & Uliasz Misiak, 2022). Depleted oil and gas reservoirs, on the other hand, can provide an economic advantage of about 5 to 24 percent by reusing existing hydrocarbon infrastructure.

In the field of material based storage, a wide range of technologies has been investigated. Metal hydrides accommodate hydrogen atoms in interstitial sites of the metal lattice and thereby provide high volumetric density, yet their relatively low gravimetric capacity and limited heat transfer performance tend to restrict their use in vehicular applications (Huot, 2009; Muthukumar et al., 2023). Complex hydrides such as $NaAlH_4$ and $LiBH_4$ can theoretically meet Department of Energy storage targets, although slow reaction kinetics, high desorption temperatures and challenges in reversibility have so far prevented their deployment at commercial scale (Muthukumar et al., 2023). Porous carbons and metal organic frameworks are regarded as promising because of their high surface areas, but their weak interaction energy with hydrogen at ambient temperature implies that effective storage generally requires cryogenic operation near 77 Kelvin (Mohan, 2019). Beyond the performance of individual technologies, safety remains one of the most critical dimensions of hydrogen storage. The high diffusion coefficient of hydrogen, its wide flammability range and its propensity for spontaneous ignition in the case of high pressure leaks necessitate comprehensive safety strategies at system level (Li et al., 2022). Variations in shock wave behaviour with pipeline geometry and changes in ignition thresholds in different configurations also play a decisive role in engineering design and risk assessment.

This broad body of literature demonstrates that hydrogen storage is one of the most complex and critical components of the emerging hydrogen economy. None of the existing technological options can satisfy all requirements on their own and each technology exhibits distinct advantages and limitations depending on operating conditions and application context. For this reason, the scientific foundations, performance metrics, engineering challenges and application domains of hydrogen storage technologies must be assessed through an integrated framework. Such a holistic evaluation is essential for the development of a sustainable and resilient hydrogen infrastructure.

2. Fundamentals and classification of hydrogen storage

In order to understand the scientific and engineering foundations of hydrogen storage technologies, it is first necessary to examine in detail the physical properties of hydrogen, the performance metrics relevant to storage systems and the influence of these metrics on technology selection. Storage methods differ significantly from those used for other energy carriers because hydrogen exhibits very low volumetric density, a high diffusion coefficient and thermodynamic behaviour that is complex from the standpoint of practical implementation (Li et al., 2022; Bosu & Rajamohan, 2024). This section presents the basic scientific framework of hydrogen storage, the key performance criteria and the classification approaches that are widely accepted in the literature within a comprehensive and comparative perspective.

2.1. Critical physical and thermodynamic properties of hydrogen for storage

The physical behaviour of hydrogen plays a decisive role in the choice of storage method. The molecular mass of hydrogen is very low at 2 g mol^{-1} and this leads to high diffusivity, low density and unstable volumetric behaviour over a wide temperature range in the gas phase. The low volumetric energy density of hydrogen in the gas phase, about 9.9 MJ m^{-3} on a lower heating value basis, is very limited compared with conventional fuels. As a result, storage at high pressure, storage at low temperature or storage in suitable materials becomes essential (Moradi & Groth, 2019).

The cryogenic properties of hydrogen are also noteworthy from a storage perspective. Since its critical temperature is around -240 degrees Celsius, liquefaction requires cooling to very low temperatures close to minus degrees Celsius. This implies that liquid hydrogen storage demands complex cryogenic insulation, multi layer vacuum insulated tanks and radiation shields (Aziz, 2021). The interaction of hydrogen with materials directly affects the design

of storage systems. In particular, steel alloys are susceptible to hydrogen embrittlement under high pressure, which increases the risk of crack initiation and growth. This phenomenon weakens the structural integrity of pipelines and storage vessels by accelerating crack propagation in the metallic matrix (Li et al., 2022). In addition, hydrogen gas can combine with shock waves at microstructural discontinuities on the inner surfaces of pipes, which may lead to sudden temperature rises and self ignition events. These physical and thermodynamic characteristics show that hydrogen storage requires a much higher level of engineering rigor than storage of other energy carriers. Table 1 summarizes the main physical properties of hydrogen and the associated engineering challenges.

Table 1. Principal physical properties of hydrogen relevant to storage and associated engineering implications (Li et al., 2022; Moradi & Groth, 2019; Aziz, 2021; Li et al., 2022)

Property	Value or behaviour	Engineering implication
Molecular mass	2 g mol^{-1}	Very high diffusion, strong propensity for leakage
Volumetric energy density (gas)	9.9 MJ m^{-3}	Necessitates high pressure and or low temperature
Liquefaction temperature	-253 °C	Requires cryogenic storage tanks
Diffusion coefficient	Very high	Increases leakage and ignition risk
Interaction with metals	Embrittlement	Promotes crack initiation and growth in steels and alloys
Shock wave interaction	High temperature rise	Possibility of spontaneous ignition

2.2. Success criteria, performance metrics and international targets in hydrogen storage

The performance evaluation of hydrogen storage systems must consider not only storage capacity but also gravimetric and volumetric performance, energy efficiency, cycle life, filling and discharging rates and safety related parameters in an integrated manner. The United States Department of Energy (DOE) has set system level targets for light duty vehicles for 2025 as 55 g H_2 per kilogram of system on a gravimetric basis and 40 g H_2 per litre of system on a volumetric basis (Muthukumar et al., 2023). These targets indicate that

most current technologies still fail to reach these values at the system level. For example, seven hundred bar Type IV tanks provide a system gravimetric capacity of approximately 5.7 wt% which is very close to the DOE target of 5.5 wt% (Rivard et al., 2019). In contrast, metal hydrides generally remain below 3 wt% at the system level due to their high mass despite their high volumetric capacity (Huot, 2009). Although some complex hydrides can theoretically meet DOE targets, slow kinetics, high desorption temperatures and issues with reversibility hinder their deployment (Muthukumar et al., 2023). Metal organic frameworks and carbon based adsorbents can achieve 5 to 7 wt% at 77 K, whereas their performance decreases sharply at room temperature (Mohan, 2019). Furthermore, filling time constitutes another critical indicator for storage systems. For hydrogen vehicles, the target is to fill 5 to 6 kg of hydrogen in about 3 to 5 minutes. This requires rapid heat transfer and effective management of pressure shocks in the tank, which creates a significant engineering challenge from the standpoint of tank safety (Li et al., 2019).

From an efficiency perspective, gas compression consumes energy on the order of 10 percent of the lower heating value of hydrogen (Moradi & Groth, 2019). Liquefaction requires roughly 30 percent more energy than compression (Denton & Nicholls, 1965). In liquid organic hydrogen carrier technologies, substantial heat input is required in both hydrogenation and dehydrogenation steps and this generally leads to low round trip efficiency (Muthukumar et al., 2023). Table 2 summarizes hydrogen storage technologies and their typical performance metrics.

Table 2. Principal performance metrics and typical values for hydrogen storage systems

Metric	Typical value or range	Technology	Source
Gravimetric capacity	Approximately 5.7 wt%	700 bar Type IV tank	Rivard et al., (2019)
Gravimetric capacity	Below 3 wt%	Metal hydrides	Huot, (2009)
Volumetric capacity	Approximately 40 g L^{-1}	DOE system level target	Muthukumar., (2023)
Liquefaction energy	Very high, about 30 percent higher than compression	Liquid H_2	Denton & Nicholls, (1965)
Adsorption capacity	5 to 7 wt% at 77 K	MOFs and activated carbons	Mohan et al., (2019)
Filling time	3 to 5 minutes	Vehicle tank	Li et al., (2019)

2.3. Classification of hydrogen storage technologies in the literature

The current literature examines hydrogen storage methods under two main categories (Bosu & Rajamohan, 2024; Moradi & Groth, 2019).

1. **Physical storage**

- Compressed gas storage at 350 to 700 bar
- Liquid hydrogenf at approximately -253 °C
- Cryo compressed hydrogen at 20 to 150 K and 200 to 350 bar
- Underground hydrogen storage in salt caverns, depleted reservoirs and aquifers

2. **Material based storage**

- Metal hydrides
- Complex hydrides
- Adsorption based systems employing carbons and metal organic frameworks
- Liquid organic hydrogen carrier systems
- Ammonia and other chemical carriers

Moradi and Groth (2019) emphasize that these two main classes face different challenges in terms of safety, efficiency and scalability. Physical methods are more technologically mature but are associated with high costs. Material based methods in contrast possess high potential yet remain under development due to kinetic and thermodynamic limitations. Figure 3 presents a schematic representation of hydrogen storage systems.

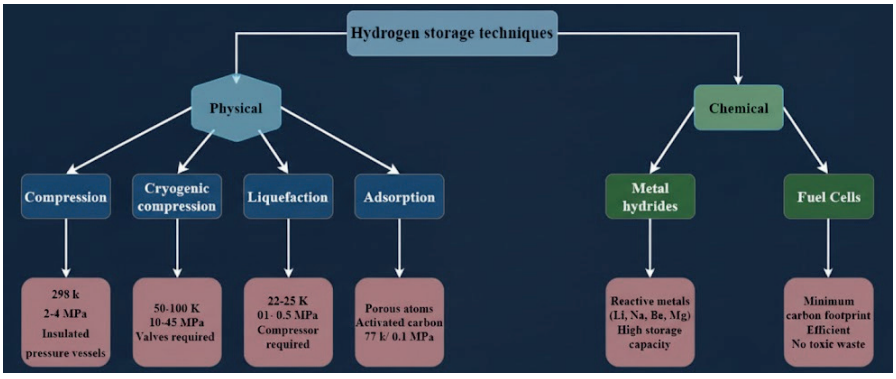

Figure 3. Modes of hydrogen storage
(Bosu, S., & Rajamohan, N., 2024)

3. Physical hydrogen storage technologies

The common objective of physical storage approaches is to increase the volumetric density of hydrogen through pressure, temperature or a combination of both. The contemporary literature highlights four main sub methods under this heading. These are compressed gaseous hydrogen (CGH_2), liquid hydrogen (LH_2), cryo compressed hydrogen and underground hydrogen storage (UHS). These methods exhibit distinct infrastructure and safety requirements, energy inputs and scale related economics. In particular, 700 bar composite tanks represent the only technically mature on board option for transport applications, whereas cryogenic systems and underground storage solutions become advantageous for refuelling stations, stationary applications and large scale systems (Muthukumar et al., 2023; Bosu & Rajamohan, 2024; Rivard et al., 2019).

3.1. Compressed hydrogen (CGH_2)

Compressed gas storage is currently the only practically viable on board method, especially in light duty vehicles. Composite pressure vessels of Type IV that can withstand pressures of 70 MPa, that is about 700 bar, are used in both prototype and commercial vehicles (Rivard et al., 2019; Muthukumar et al., 2023). The composite vessel structure consists of a polymer liner such as HDPE that provides tightness, a carbon fibre and resin composite shell that carries the mechanical load and an outer protective layer (Rivard et al., 2019). In terms of capacity and performance, the seven hundred bar Type IV tank architecture offers a system gravimetric capacity of approximately 5.7 wt% in vehicle applications as exemplified by the Mirai and combines high allowable pressure in the range of 700 to 750 bar with low mass. Type V vessels that do not employ a liner are lighter, yet in practice they are limited to pressures below 15 bar and are therefore not suitable for on board storage (Muthukumar et al., 2023).

The literature indicates that Type I to Type IV vessels differ significantly in cost, mass and allowable pressure. Type I vessels made entirely of metal are the least expensive but also the heaviest. Type II vessels with a metal liner and partial composite overwrap reduce mass by about 30 to 40 percent at the expense of approximately 50 percent higher cost. Type III vessels with a metal liner and full composite overwrap provide mature performance in the range of 350 to 700 bar. Type IV vessels that combine a polymer liner with a full carbon fibre reinforced polymer overwrap represent the most suitable compromise between mass and performance up to 700 bar for on board applications (Muthukumar et al., 2023, comparison table or scheme). These findings are consistent with earlier studies that classify vessel types and compare pressure

resistance and capacity per unit mass (Moradi & Groth, 2019).

From the perspective of refuelling, fast filling targets of 3 to 5 minutes require advanced filling strategies due to Joule Thomson heating, pressure fluctuations and material safety considerations. This necessitates sophisticated fast fill control, thermal management and appropriate pressure relief device configurations (Li et al., 2019). In addition, the work of compression and the required pumping power are higher than those of natural gas because of the low molar mass and low volumetric energy density of hydrogen. This leads to higher tip speeds and more demanding lubrication and maintenance regimes in compressors (Moradi & Groth, 2019). Table 3 summarizes the main characteristics of compressed hydrogen vessel types.

Table 3. Summary comparison of compressed hydrogen vessels (Type I to V) (Moradi & Groth, 2019; Muthukumar et al., 2023)

Vessel type	Material and structure	Typical pressure	Mass and characteristics	Main features
Type I	All metal steel or aluminium	Up to 200 bar	Heaviest, lowest cost	Industrial use, too heavy for on board applications
Type II	Metal liner plus partial composite	Up to 300 bar	About 30 to 40 percent lighter, cost about 50 percent higher	Compromise between mass and cost
Type III	Metal liner plus full composite	350 to 700 bar	Reliable, composite shell carries the load	Mature at 45 MPa, challenges at 70 MPa testing
Type IV	Polymer liner plus full CFRP	700 to 750 bar	Lightest, system capacity approximately 5.7 wt%	Standard for fuel cell electric vehicles
Type V	All composite without liner	Typically below 15 bar	Very light, limited allowable pressure	Pre commercial stage

3.2. Liquid hydrogen and cryogenic systems

In terms of liquefaction and storage, liquid hydrogen at approximately -253

°C provides high volumetric density. However, liquefaction cycles such as Linde Hampson and Claude require high energy input as well as multilayer vacuum insulation and radiation shields for storage tanks (Aziz, 2021). Although the design of cryogenic tanks is technically feasible, both capital and operating costs are high and the energy consumed for liquefaction is about 30 percent higher than that required for gas compression and cannot be recovered in operation (Rivard et al., 2019). Moreover, boil off losses arising from structural heat ingress in cryogenic systems are among the most critical issues in operational design. Large scale LH_2 spill experiments conducted historically at sites such as NASA Whitesands and subsequent studies have shown that liquid hydrogen exhibits more intense and irregular boiling and a faster upward rise of the vapor cloud compared with liquid nitrogen. This implies that spill and atmospheric dispersion behaviour of LH_2 must be treated specifically in safety analyses (Li et al., 2022). Cryo compressed hydrogen tanks combine low temperature with intermediate or high pressure with the aim of achieving higher effective density and improved dormancy and boil off management inside the vessel. In the literature, this approach is represented as a sub class of cryogenic compression typically operated in the range of 50 to 100 K and 10 to 45 MPa (Bosu & Rajamohan, 2024). Although automotive prototypes have been demonstrated, the complexity of the system and the requirement for an insulated pressure vessel remain major obstacles to widespread adoption (Rivard et al., 2019). Table 4 presents a comparative overview of the performance and operating characteristics of physical storage methods.

Table 4. Performance and operating characteristics of physical hydrogen storage methods

Criterion	Compressed H_2	Liquid H_2 (LH_2)	Cryo compressed hydrogen
Typical operating condition	350 to 700 bar	Approximately 20 K and about 1 bar with vacuum insulation	50 to 100 K and 10 to 45 MPa
Density and main advantage	Mature infrastructure and fast refuelling	High volumetric density	Higher effective density and improved boil off management
Energy input	Work of compression	Liquefaction energy about 30 percent higher than compression	Combined cooling and compression
Main limitation	Tank cost and mass	Boil off, cryogenic safety and high cost	Complexity of insulated pressure vessel
References	Rivard 2019, Muthukumar 2023	Rivard 2019, Aziz 2021, Li 2022	Bosu & Rajamohan 2024, Rivard 2019

3.3. Underground hydrogen storage (UHS)

Underground hydrogen storage in geological formations such as salt caverns, depleted oil and gas reservoirs and aquifers offers the possibility of seasonal and very large scale energy storage. The general consensus in the literature is that salt caverns are technically and economically favourable, whereas aquifers represent capital intensive solutions because of the need for cushion gas (Navaid, Emadi & Watson, 2023). Cost assessments report that the cushion gas requirement in aquifers can reach up to 42 percent of the total capital cost. More effective injection and withdrawal strategies and appropriate selection of cushion gas can improve recoverability and thereby reduce costs indirectly (Navaid et al., 2023). Depleted reservoirs can provide a cost advantage in the range of approximately 4.7 to 23.6 percent relative to aquifers and salt caverns through the reuse of existing infrastructure. In addition, the displacement of residual hydrocarbons by cushion gas offers potential for additional hydrocarbon recovery. On the other hand, gas mobility, caprock integrity and gas purity are decisive factors in terms of both safety and economics. Site specific characterization of porosity, permeability and

capillary entry pressure is unavoidable and constitutes a fixed cost component that also extends the project timeline (Navaid et al., 2023). Table 5 summarizes the comparative characteristics of underground storage environments.

Table 5. Comparison of underground hydrogen storage environments (Navaid et al., 2023)

Environment	Strengths	Weaknesses and risks	Economic note
Salt cavern	High integrity, low leakage risk, fast injection and withdrawal	Limited geographical availability	In most scenarios the least cost option according to the literature
Depleted reservoir	Reuse of existing infrastructure	Management of hydrogen mobility and purity	Potential cost advantage of approximately 4.7 to 23.6 percent
Aquifer	Wide availability	Cushion gas may reach around 42 percent of capital cost, heavy characterization requirements	High operational costs for dehydration, separation and desalination

4. **Material based hydrogen storage technologies**

Storing hydrogen within a solid or liquid carrier requires a system design that balances storage capacity with heat management, reversibility, cycle life and safety. In this context, research has focused on intermetallic metal hydrides, complex or chemical hydrides, porous adsorbents such as carbons and metal organic frameworks and liquid organic hydrogen carriers together with ammonia. The literature shows that metal hydrides provide high volumetric density, that complex hydrides can exhibit improved reversibility through doping, that carbon and MOF adsorbents can deliver significant gravimetric capacities under cryogenic conditions and that liquid organic hydrogen carriers offer practical storage and transport solutions due to their compatibility with existing liquid fuel logistics (Mohan, 2019; Usman, 2022; Rivard, Trudeau & Zaghib, 2019). Figure 4 presents a schematic classification of solid state hydrogen storage systems.

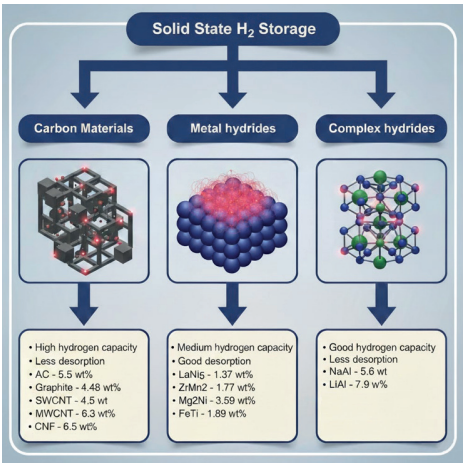

Figure 4. Classification diagram of solid state hydrogen storage systems (Mohan, 2019)

In metal hydrides, hydrogen is accommodated in the metal lattice through chemical absorption and the equilibrium behaviour is described by pressure composition temperature diagrams. Typical systems include AB_5 such as $LaNi_5$, AB_2 such as $ZrMn_2$, AB such as FeTi and A_2B such as Mg_2Ni. It has been reported that capacities in the range of 1 to 3.5 wt% can be achieved at pressures close to ambient at room temperature, while Mg based systems can provide higher gravimetric capacities at the expense of higher desorption temperatures (Mohan, 2019). This overall picture has motivated efforts to improve performance through nanostructuring and catalysis. In particular, doping with Ti and other transition metals has been shown to accelerate hydride kinetics and to reduce equilibrium temperatures. Reversible hydrogen release from $NaAlH_4$ after doping with Ti compounds was first demonstrated by Bogdanović and Schwickardi (1997) and this effect has been confirmed in many subsequent studies (Bogdanović & Schwickardi, 1997; summary in Usman, 2022). The advantages of metal hydrides at the system level are high volumetric density and inherent safety, while mass and heat management remain major limiting factors (Usman, 2022; Muthukumar et al., 2023). Table 6 lists typical properties of selected intermetallic hydrides.

Table 6. Typical properties of selected intermetallic hydrides (Mohan, 2019)

System	Structure	Approximate capacity wt%	Typical equilibrium condition example
$LaNi_5$ (AB_5)	Intermetallic	1.37	2 bar and 298 K
$ZrMn_2$ (AB_2)	Intermetallic	1.77	1 bar and 298 K
Mg_2Ni (A_2B)	Intermetallic	3.59	555 K
FeTi (AB)	Intermetallic	1.89	303 K

In complex or chemical hydrides including alanates, borohydrides and ammonium derivatives, high theoretical gravimetric capacities have been reported. However, the temperature and pressure requirements and slow kinetics associated with rehydrogenation remain major obstacles in most systems. For $NaAlH_4$, reversible hydrogen release up to about 5.5 to 5.6 wt% has been reported and doping with $TiCl_3$ or TiF_3 can reduce desorption temperature by roughly 80 to 85 °C (Usman, 2022; Bogdanović & Schwickardi, 1997). For $LiAlH_4$ and similar systems, rehydrogenation requires demanding conditions in the range of 200 to 400 °C and 10 to 40 MPa and this significantly limits their practical applicability (Usman, 2022). In summary, complex hydrides exhibit high storage potential, yet their requirement for high heat input and specific reactor designs remains decisive at the engineering scale (Usman, 2022; Muthukumar et al., 2023).

In physical adsorption, hydrogen is retained through van der Waals interactions and capacity is strongly influenced by specific surface area and micropore volume. Extensive studies have been conducted on activated carbons, carbon nanofibres, nanotubes and graphene derivatives. For activated carbons such as AX 21 and Maxsorb, capacities of approximately 5 to 6 wt% at 77 K have been achieved, whereas capacities at 298 K drop below 1 wt% (Mohan, 2019; Chahine & Bose, 1994; Xu et al., 1999). These results indicate that physisorption based solutions cannot meet DOE targets at room temperature and that cryogenic operation is therefore required (Mohan, 2019). Metal organic frameworks in contrast present a stronger picture under cryogenic conditions due to their very high specific surface area and tunable pore structure. Hydrogen storage of approximately 4.5 wt% at 77 K has been reported for MOF 5 and about 9 wt% at 77 K and 56 bar for NU 100, whereas most MOFs remain below 1 wt% at room temperature (Li et al., 2009; Farha et al., 2010; Langmi et al., 2014; numerical values summarized in Usman,

2022). In the engineering design of adsorbent based tanks, heat removal during desorption becomes a key issue and for filling times in the range of 3 to 5 minutes measures such as heat exchanger integration and compaction with expanded natural graphite have been proposed (Broom et al., 2016; Mohan, 2019).

In liquid organic hydrogen carrier systems, hydrogen is chemically bound to a hydrogen lean organic molecule through a hydrogenation reaction and released when needed via dehydrogenation. In the methylcyclohexane to toluene cycle, a gravimetric capacity of 6.2 wt% corresponding to an energy density of approximately 5.5 MJ L^{-1} has been reported and operation around 325 °C is possible with reforming derived catalysts such as Pt on Al_2O_3. A conceptual scheme of this system is provided by Usman (2022). For dodecahydro N ethylcarbazole, reversible hydrogen content of 5.8 wt%, a dehydrogenation temperature of about 170 °C and an enthalpy of around 51 kJ mol^{-1} H_2 have been reported. A theoretical content of 8.5 wt% and an equivalent energy density of about 7 MJ L^{-1} make this system attractive particularly for stationary applications (Rivard, Trudeau & Zaghib, 2019). It has also been emphasized that LOHC processes are strongly dependent on catalysis. Precious metals such as Pt, Pd, Rh, Au and Ru are widely used, which is a decisive factor for both cost and sustainability (Rivard, Trudeau & Zaghib, 2019; Usman, 2022). At industrial scale, demonstration plants have been established by companies such as Hydrogenious and Chiyoda and logistic concepts have been developed using systems such as dibenzyltoluene and perhydro dibenzyltoluene (Muthukumar et al., 2023).

When ammonia is considered as a hydrogen carrier, it offers advantages for large scale maritime transport and storage. In scenarios where NH_3 is used directly, the overall chain efficiency remains relatively high, whereas an additional efficiency penalty arises when reconversion to hydrogen is required. For ship transport, methylcyclohexane, methanol and ammonia have been shown to be competitive in terms of cost and energy density per unit transported hydrogen kilometre and the final choice depends on infrastructure, toxicity and regulatory conditions (Muthukumar et al., 2023).

In this overall framework, metal hydrides stand out in terms of safety and volumetric density, complex hydrides in terms of potential gravimetric capacity, adsorbents in terms of cryogenic performance and LOHC and NH_3 systems in terms of logistics and infrastructure compatibility. No single option can satisfy all criteria simultaneously and technology selection must therefore be made according to the specific application context (Usman, 2022; Mohan, 2019; Rivard, Trudeau & Zaghib, 2019).

5. Applications, safety, economics and future perspectives

The engineering feasibility of hydrogen storage technologies depends strongly on the use context, safety requirements, economic scalability and the capability to integrate with energy systems. The real world role of storage strategies must therefore be evaluated not only in terms of theoretical capacity or operating pressure but also in relation to their applicability in transport, stationary systems, grid scale storage, emergency power systems, logistics chains and conversion between different energy carriers (Rivard, Trudeau & Zaghib, 2019; Muthukumar et al., 2023). This section explores the current and medium term positioning of hydrogen storage technologies in a multidimensional manner.

5.1. Storage requirements by application domain

5.1.1. Transport and mobility systems

Transport applications are among the fields with the most stringent requirements for hydrogen storage. For light duty fuel cell electric vehicles, the most critical parameters are gravimetric capacity, volumetric density, filling time, safety and cost. The literature indicates that to date only 70 MPa composite tanks of Type IV have been implemented in commercial vehicles. For example, system level values of approximately 5.7 wt% have been reported for vehicles such as the Toyota Mirai (Rivard et al., 2019). In this context, material based solutions such as $NaAlH_4$, MgH_2 or MOF based systems have not yet been able to meet the strict targets associated with these applications (Farha et al., 2010; Langmi et al., 2014).

In sectors shaped by the trade off between range and payload such as heavy duty transport, maritime shipping and aviation, physical storage options become more prominent. Liquid hydrogen tanks provide significant advantages for long range requirements. For instance, in aviation applications storing hydrogen at approximately -253 °C in the liquid phase offers higher volumetric energy density than carbon fibre composite tanks at compressed conditions (Aziz, 2021).

5.1.2. Stationary and distributed energy systems

In stationary systems, mass is not a primary limitation and therefore metal hydride tanks, LOHC systems or medium pressure cylindrical storage solutions in the range of 20 to 50 MPa are considered more feasible. In particular, the ability of metal hydrides to operate safely at low pressure is regarded as an advantage in backup power systems used for telecommunications, hospitals

and data centres (Broom et al., 2016). LOHC based solutions have been tested in stationary microgrids and hybrid solar hydrogen plants. Integrated PV LOHC electrolyser test units reported by Usman (2022) demonstrate that the dibenzyltoluene or perhydro dibenzyltoluene cycle can be implemented practically in systems at the scale of a few kilowatts. Figure 5 presents a photograph of an LOHC test station.

Figure 5. LOHC test station photograph (Muthukumar et al., 2023)

5.1.3. Large scale and grid level storage

Grid level storage is one of the most complex components of energy systems, as capacity requirements can reach the GWh to TWh scale. It is generally recognized that only underground hydrogen storage systems can reach such capacities. Previous studies show that salt caverns are the most suitable option, while aquifers may account for up to 42 percent of total capital cost due to the requirement for cushion gas (Navaid, Emadi & Watson, 2023). Depleted reservoirs can provide cost advantages in the range of approximately 4.7 to 23.6 percent through reuse of existing infrastructure.

The sustainability of underground hydrogen storage depends on rock integrity, capillary entry pressure, microbial interactions and hydrogen purity and therefore its integration into energy systems requires coordination between geology, chemistry and materials engineering disciplines (Tarkowski & Uliasz-Misiak, 2022). In addition, safety considerations are recognized as one of the most decisive factors in the widespread adoption of hydrogen storage technologies. The wide flammability range of hydrogen, its low minimum ignition energy, high diffusion coefficient and its tendency to induce hydrogen embrittlement in materials are parameters that must be continuously monitored in system design (Li et al., 2022). In high pressure storage, the most critical risk is that sudden leaks can combine with shock waves and lead to spontaneous ignition.

5.2. Economic assessment and efficiency perspective

Economic assessment of storage technologies must address not only equipment costs but also energy input, round trip efficiency, operation and maintenance requirements and life cycle characteristics. Considering the DOE system targets:

- Compressed gas storage is often seen as advantageous in terms of cost and performance particularly in mobility applications, since the work of compression is on the order of 10 percent of the lower heating value of hydrogen (Rivard et al., 2019).

- Liquid hydrogen approaches economic viability only in applications that require very long range due to its high energy input, which is around 30 percent greater than that of compression (Aziz, 2021).

- Although metal hydrides provide high volumetric density, they are not economically attractive for transport because of high cost per kilogram of hydrogen, tank mass and heat management requirements.

- MOF and other adsorbent systems entail high operating costs due to the need for 77 K cryogenic conditions, yet they occupy niche roles in sensors, drones and military applications.

- The cost of LOHC systems is largely determined by the catalyst and heat input, although their liquid phase logistics make them one of the least expensive options in terms of transport and storage infrastructure (Rivard et al., 2019).

- Underground hydrogen storage offers the lowest specific cost for large scale storage and no alternative currently exists for systems at the TWh scale (Navaid et al., 2023).

5.4. Future perspectives

The contemporary literature suggests that hydrogen storage technologies will not converge on a single universal solution in the near future but will rather be shaped by multiple and hybrid approaches. Research is underway on nano catalysis in metal hydrides, reduction of reaction enthalpy in complex hydrides, high capacity operation near room temperature in MOFs, new catalyst alloys that lower cost in LOHC systems and less toxic transport scenarios for ammonia (Farha et al., 2010; Langmi et al., 2014; Usman, 2022).

Infrastructure is also among the most critical factors in the development of a large scale hydrogen economy. As the distance between hydrogen production and consumption sites increases, it is expected that derivative energy carriers such as LOHCs, NH_3, methanol or borohydrides will become more prominent than direct gaseous hydrogen transport. This will require multi step storage, transport and conversion chains in energy systems. In conclusion, both physical and material based technologies exhibit distinct strengths and weaknesses. In a future scenario where hydrogen is integrated across all sectors, a multimodal storage infrastructure will be required in which different storage methods are used simultaneously according to application specific needs.

6. Conclusions

This study has examined the multidimensional structure of hydrogen storage technologies from a holistic perspective, covering a spectrum that ranges from physical methods to material based solutions and from underground storage to liquid organic carriers. The findings indicate that hydrogen is likely to play an increasingly strategic role in energy systems while storage infrastructure remains the most complex and decisive component of this transformation. Physical storage methods currently address short and medium term needs of the transport sector through their high power density, fast refuelling capability and mature technology readiness. However, the energy input and safety requirements of liquid hydrogen and cryogenic systems make them economically meaningful only at specific scale and in certain applications.

Material based storage solutions are particularly attractive in the long term due to their potential to provide high gravimetric and volumetric capacities. Nevertheless, mass and heat management issues in metal hydrides, reversibility and rehydrogenation requirements in complex hydrides and low capacity at room temperature in MOF and carbon adsorbents indicate that these technologies have not yet reached the desired system level performance. LOHC and ammonia based chemical carriers offer significant advantages in terms of logistics, safety and infrastructure compatibility and emerge as strong candidates especially for intercontinental transport and long term storage.

From a safety perspective, a common picture emerges across all storage methods. The physical properties of hydrogen including its wide flammability range, high diffusion capability and tendency to cause material embrittlement make multi layer protection strategies mandatory in storage system design. The commercialization of storage technologies is therefore linked not only to capacity or cost optimisation but also to parallel advances in risk assessment, material durability and operational safety.

In light of these considerations, it is not realistic to expect a single storage method to meet all requirements in the development of the hydrogen economy. Instead, it is anticipated that a multimodal storage portfolio composed of methods selected according to application context and integrated with each other will become a core component of future energy infrastructure. In the medium and long term, advances in nanotechnology, catalysis, improvement of cryogenic efficiency, geological integrity assessment and system integration are expected to significantly extend the technical limits of hydrogen storage.

In this regard, hydrogen storage technologies can be regarded as one of the most critical and dynamic domains of the energy transition and as scientific progress, infrastructure investment and policy support move forward in parallel, hydrogen is expected to assume a central role in low carbon global energy systems.

REFERENCES

Aziz, M. (2021). Liquid hydrogen: A review on liquefaction, storage, transportation, and safety. Energies, 14, 5917. https://doi.org/10.3390/en14185917

Bogdanović, B., & Schwickardi, M. (1997). Ti doped alkali metal aluminium hydrides as potential novel reversible hydrogen storage materials. Journal of Alloys and Compounds, 253–254, 1–9. https://doi.org/10.1016/S0925-8388(96)03049-6

Broom, D. P., Webb, C. J., Hurst, K. E., Parilla, P. A., Gennett, T., Brown, C. M., … Ben, T. (2016). Outlook and challenges for hydrogen storage in nanoporous materials. Applied Physics A, 126(10), 1–42. https://doi.org/10.1007/s00339-016-9651-4

Bosu, S., & Rajamohan, N. (2024). Recent advancements in hydrogen storage – Comparative review on methods, operating conditions and challenges. International Journal of Hydrogen Energy, 52, 352–370. https://doi.org/10.1016/j.ijhydene.2023.01.344

Chahine, R., & Bose, T. K. (1994). Low pressure adsorption storage of hydrogen. International Journal of Hydrogen Energy, 19(2), 161–164. https://doi.org/10.1016/0360-3199(94)90121-X

Denton, W. H., & Nicholls, C. M. (1965). Technology and uses of liquid hydrogen. Physics Bulletin, 16(4), 137. https://doi.org/10.1088/0031-9112/16/4/008

Farha, O. K., Yazaydin, A. O., Eryazici, I., Malliakas, C. D., Hauser, B. G., Kanatzidis, M. G., & Hupp, J. T. (2010). De novo synthesis of a MOF with ultrahigh surface area and gas storage capacities (NU-100). Nature Chemistry, 2(11), 944–948. https://doi.org/10.1038/nchem.834

Fırat, M., Şenocak, Ş. M., Okcu, M., Varol, Y., & Altun, Ş. (2023). Ozone-assisted combustion and emission control in RCCI engines: A comprehensive study. Energy, 202, 129247. https://doi.org/10.1016/j.energy.2023.129247

Huot, J. (2009). Metal hydrides. In M. Hirscher (Ed.), Handbook of Hydrogen Storage. Weinheim: Wiley-VCH.

Hydrogen Council. (2021). Hydrogen insights: A perspective on hydrogen investment, market development and cost competitiveness. Hydrogen Council.

Gürgenç, E., Öztop, H. F., Yamaç, H. İ., Aksu Canbay, C., Şenocak, Ş. M., Özabacı, M., Gürgenç, T., & Gür, M. (2025). B4C-based nanoenhancement on the thermophysical and stability performance of solar salt: A novel approach for high-temperature TES applications. Case Studies in Thermal Engineering, 75, 107257. https://doi.org/10.1016/j.csite.2025.107257

Langmi, H. W., Ren, J., North, B. C., Mathe, M., & Bessarabov, D. (2014). Hydrogen storage in metal–organic frameworks: A review. Electrochimica Acta, 128, 368–392. https://doi.org/10.1016/j.electacta.2013.10.190

Li, H., Cao, X., Liu, Y., Shao, Y., Nan, Z., Teng, L., … Bian, J. (2022). Safety of hydrogen storage and transportation: An overview on mechanisms, techniques, and challenges. Energy Reports, 8, 6258–6269. https://doi.org/10.1016/j.egyr.2022.04.067

Li, J.-R., Kuppler, R. J., & Zhou, H.-C. (2009). Selective gas adsorption and separation in metal–organic frameworks. Chemical Society Reviews, 38(5), 1477–1504. https://doi.org/10.1039/B802426J

Li, M., Bai, Y., Zhang, C., & Song, Y. (2019). Review on the research of hydrogen storage system fast refueling in fuel cell vehicle. International Journal of Hydrogen Energy, 44, 10677–10693. https://doi.org/10.1016/j.ijhydene.2019.02.208

Liu, W., Zhang, Z., Chen, J., Jiang, D., Wu, F., Fan, J., et al. (2020). Feasibility evaluation of large-scale underground hydrogen storage in bedded salt rocks of China: A case study in Jiangsu province. Energy, 198, 117348. https://doi.org/10.1016/j.energy.2020.117348

Mohan, M., Sharma, V. K., Kumar, E. A., & Gayathri, V. (2019). Hydrogen storage in carbon materials—A review. Energy Storage, 1(2), e35. https://doi.org/10.1002/est2.35

Moradi, R., & Groth, K. M. (2019). Hydrogen storage and delivery: Review of the state of the art technologies and risk and reliability analysis. International Journal of Hydrogen Energy, 44(23), 12254–12269. https://doi.org/10.1016/j.ijhydene.2019.03.041

Muthukumar, P., Kumar, A., Afzal, M., Bhogilla, S., Sharma, P., Parida, A., … Jain, I. P. (2023). Review on large-scale hydrogen storage systems for better sustainability. International Journal of Hydrogen Energy, 48, 33223–33259.https://doi.org/10.1016/j.ijhydene.2023.04.304

Navaid, H. B., Emadi, H., & Watson, M. (2023). A comprehensive literature review on the challenges associated with underground hydrogen storage. International Journal of Hydrogen Energy, 48, 10603–10635. https://doi.org/10.1016/j.ijhydene.2022.11.225

Öztürk, G., Şenocak, Ş. M., Şenocak, N., & Fırat, M. (2024). An experimental investigation of 1,2-dimethoxy ethane as a fuel additive in biodiesel-fueled diesel engine. Journal of the Energy Institute, 117, 101824. https://doi.org/10.1016/j.joei.2024.101824

Rivard, E., Trudeau, M., & Zaghib, K. (2019). Hydrogen storage for mobility: A review. Materials, 12(1973), 1–26. https://doi.org/10.3390/ma12121973

Tarkowski, R., & Uliasz-Misiak, B. (2022). Towards underground hydrogen storage: A review of barriers. Renewable and Sustainable Energy Reviews, 162, 112451. https://doi.org/10.1016/j.rser.2022.112451

Usman, M. R. (2022). Hydrogen storage methods: Review and current status. Renewable and Sustainable Energy Reviews, 167, 112743. https://doi.org/10.1016/j.rser.2022.112743

Şenocak, Ş. M., Gürgenç, T., Varol, Y., Gürgenç, E., & Öztop, H. F. (2026). Cubic boron nitride enhanced PCM nanocomposites for solar energy storage and thermal management. Solar Energy, 303, 114102. https://doi.org/10.1016/j.solener.2025.114102

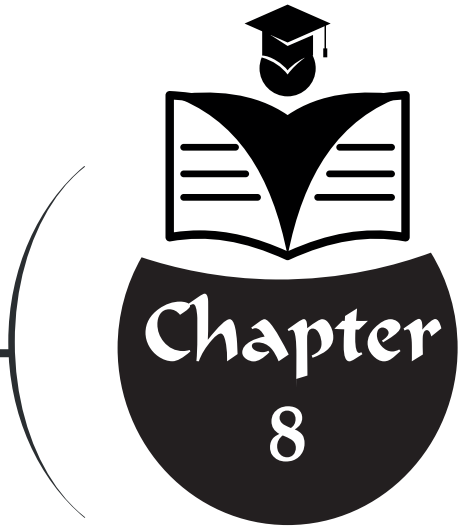

EFFICIENT STRUCTURAL ANALYSIS USING PROJECTION-BASED REDUCED ORDER MODELS

Okan DUYMAZLAR [1]

1 Lecturer, Ege University, Ege Vocational School, Mechatronics, okan.duymazlar@ege.edu.tr, ORCID: 0000-0002-1327-7493.

1. INTRODUCTION

One of the most popular methods in structural mechanics, Finite Element Analysis (FEA), is a key numerical method used to predict the mechanical response of structures when subjected to loads, boundary conditions, and external influences. In this approach, a continuous physical field is divided into a finite number of smaller subfields called elements, which are connected to each other via nodes (Kim, 2015). Rules derived from continuum mechanics—typically equilibrium equations and constitutive material laws—are approximated over these elements and converted into a global system of algebraic equations. Solving this system yields quantities of interest such as node displacements, strains, stresses, and reaction forces. FEA is widely used because it can handle complex geometries, heterogeneous materials, and realistic boundary conditions that are analytically unsolvable (GÖNENLİ, 2022; Gonenli & Das, 2021; Kim, 2015; Reddy & Arciniega, 2004; Santana, Ferreira, Gomes, & Tita, 2024).

Although it is accurate and used as an industry standard, one of the major limitations of finite element analysis is the computational cost, which varies depending on the geometry, problem type, and hardware used (Yadav & Suresh, 2014; Yu, Lou, Dong, Li, & Jin, 2023). As model complexity increases through finer meshes, three-dimensional solid elements, nonlinear material behavior, large deformations, or contact interactions, the number of degrees of freedom, pre-conditions, and constraints rapidly increases. This leads to large, sparse linear or nonlinear systems that require significant memory and computation time to solve. In static analyses, the solution time is determined by matrix assembly and solving large linear systems, while in dynamic or transient analyses, iterative time integration further increases the computational load. For applications requiring thousands of finite element analysis evaluations, such as design optimization, uncertainty estimation, real-time simulation, or controller design, these computational costs become a critical bottleneck (Yadav & Suresh, 2014).

To overcome this challenge, "reduced-order models (ROMs)" have been proposed as a way to significantly reduce computational load while retaining the fundamental physical behavior of the original high-fidelity model (Hijazi, Freitag, & Landwehr, 2023; Stabile, Hijazi, Mola, Lorenzi, & Rozza, 2017). The basic idea behind model order reduction is to map the governing equations onto a low-dimensional subspace that captures the dominant features of the system response. Classical techniques such as Proper Orthogonal Decomposition (POD), reduced basis methods, and modal reduction typically determine a set of basis vectors that capture the most vigorous or relevant deformation modes, often extracted from snapshots of full-order FEA solutions. The original high-dimensional problem is then approximated using only a small number of generalized coordinates. This reduction leads to orders-of-magnitude gains

in computational efficiency, making near real-time simulation possible for problems that would otherwise be computationally infeasible.

Reduced-order models are typically derived directly from the fundamental equations and have a strong connection to the governing physics, while surrogate models represent a more data-driven approach. A surrogate model aims to learn a direct mapping between inputs (such as loads, boundary conditions, material parameters, or geometric features) and outputs (such as displacements, stresses, or failure criteria) without explicitly solving the governing equations (Das, Gonenli, & Das, 2023). These models are typically built using regression techniques, machine learning methods, or neural networks trained on data obtained from high-fidelity finite element analysis (FEA) simulations (Das et al., 2023; Wu, Zhang, Nielsen, & Chen, 2023). Once trained, surrogate models can generate predictions almost instantaneously, making them particularly attractive for optimization loops, sensitivity studies, and real-time decision-making. However, in most cases, they require thousands of simulation data points under the same loading and boundary conditions. Even then, it cannot be fully guaranteed that their predictions will be made with an acceptable margin of error.

Fundamental difference between reduced-order models and surrogate models are in how physical knowledge gets factored in. Reduced-order models are based on physics and typically rely on projections of the original equations; which helps preserve stability, consistency, and interpretability. In contrast, surrogate models are primarily data-driven and may not explicitly apply physical laws unless additional constraints or hybrid approaches are used. Although this can provide excellent prediction performance within the range of training data, it may also introduce risks when extrapolating beyond this range. Consequently, surrogate models typically require careful data set design, validation, and uncertainty assessment (Meng, Yao, & Liu, 2025; Yamaguchi & Okuda, 2021).

In this study, a Proper Orthogonal Decomposition (POD)-Galerkin-based reduced-order modeling approach is demonstrated in a static structural analysis problem and systematically evaluated against a high-accuracy finite element solution used as the ground truth. The benchmark problem is defined as a three-dimensional cantilever beam, a classic but representative example of structural mechanics; this cantilever beam allows for clear interpretation of displacement and stress fields while also exhibiting non-negligible spatial response characteristics. Rather than a single deterministic case, the beam was subjected to multiple point loads applied at randomly selected points along its span with varying load magnitudes to mimic a wide range of loading scenarios. This setup allows the reduced model to be tested under various excitation conditions and prevents it from being overly tailored to a specific load configuration.

The POD basis is constructed using snapshots obtained from fully ranked finite element simulations corresponding to different loading conditions and amplitudes. These snapshots capture the dominant deformation patterns of the structure and form a low-dimensional subspace in which the governing balance equations are reflected using the Galerkin formulation. Once the reduced system is assembled, solutions can be computed at a significantly lower computational cost compared to the original finite element model. The reduced model predictions are then directly compared with the exact FEA results in terms of node displacement fields and derived quantities, allowing for a detailed quantification of the approximation quality.

Several performance metrics are considered to provide a comprehensive and objective comparison. The computation time is used to measure the efficiency gain achieved by the reduced-order model compared to the full finite element solution. Accuracy is measured by comparing the reduced and full-order displacement fields, while average error metrics calculated across all nodes and loading scenarios are used to summarize overall model accuracy. These metrics collectively highlight the balance between computational cost and numerical accuracy that lies at the heart of reduced-order modeling strategies.

This comparative study demonstrates that POD-Galerkin-based reduced-order models can significantly reduce computation time while maintaining high accuracy in static structural analysis problems with variable load conditions. Although the current research environment is largely influenced by neural network-based surrogate modeling approaches, the results of this study demonstrate that classical projection-based methods are still highly competitive. In particular, they offer strong physical interpretability, predictable behavior, and robust performance without requiring large training datasets. In conclusion, this study reinforces the importance of POD-based reduced-order modeling as a powerful and reliable alternative for efficient structural analysis, particularly in scenarios where physical consistence and computational efficiency are of primary concern.

2. MATERIAL AND METHOD

In this study, a projection-based reduced-order model (ROM) was developed for static structural analysis within the framework of linear elasticity and evaluated by comparing it with reference exact solutions (Stabile et al., 2017). The reference solution was obtained using traditional finite element analysis (FEA), which served as the ground truth for accuracy assessment.

2.1. Problem Definition and Modeling Assumptions

The following assumptions are adopted throughout the modeling and reduction process:

- Linear elastic material behavior
- Small strain and small displacement hypothesis
- Static equilibrium (no inertial or damping effects)
- No geometric nonlinearity, contact, or material nonlinearity
- Loads applied as nodal point forces

These assumptions ensure that the governing equations remain linear, making the problem well suited for Proper Orthogonal Decomposition (POD)–Galerkin model order reduction.

2.2 Geometry Discretization and Material Model

The benchmark problem considered in this study is a three-dimensional cantilever beam, which is a classical example in structural mechanics due to its well-understood deformation behavior and sensitivity to external loading. The beam geometry is defined by:

$$L_x = 2000, L_y = 100, L_z = 100$$

Let N denote the total number of nodes. The total number of degrees of freedom is therefore:

$N_{\text{dof}} = 3N$ The beam is modeled as a homogeneous, isotropic, linear elastic material characterized by:

$$E = 206000, \nu = 0.3$$

where E is Young's modulus and ν is Poisson's ratio. Under these assumptions, the constitutive relation is governed by Hooke's law.

2.3 Boundary Conditions

A clamped boundary condition is imposed on the left end of the beam. All displacement components are constrained to zero for nodes satisfying: $x \approx 0$ with another saying $\mathbf{u} = \mathbf{0}$ on Γ_{fixed}

2.4 Governing Equation of the Full-Order Model

After finite element discretization and assembly, the static equilibrium equation of the system is given by:

$\mathrm{Ku} = \mathrm{f}$ where:

- $\mathbf{K} \in \mathbb{R}^{N_{\text{dof}} \times N_{\text{dof}}}$ is the global stiffness matrix,
- $\mathbf{u} \in \mathbb{R}^{N_{\text{dof}}}$ is the displacement vector,
- $\mathbf{f} \in \mathbb{R}^{N_{\text{dof}}}$ is the external force vector.

2.5. Snapshot Generation for POD

To construct a reduced basis capable of representing a wide range of structural responses, the training dataset is generated using randomized point-load configurations. For each snapshot, a random number of load application nodes is selected:

$$N_p \in [1, N_p^{\max}]$$

Load nodes are chosen excluding constrained nodes and forces are applied in the z-direction only, with random sign and magnitude:

$$F_z \sim \mathcal{U}(-F_{\max}, F_{\max})$$

This approach ensures that the snapshot set spans diverse deformation modes and load locations. For each load configuration, a full static FEA solve is performed, yielding a displacement vector:

$$\mathbf{u}^{(i)} \in \mathbb{R}^{N_{\text{dof}}}$$

All snapshots are assembled into a snapshot matrix where N_s is the total number of snapshots :

$$\mathbf{X} = [\mathbf{u}^{(1)} \quad \mathbf{u}^{(2)} \quad \dots \quad \mathbf{u}^{(N_s)}] \in \mathbb{R}^{N_{\text{dof}} \times N_s}$$

To properly enforce boundary conditions, the displacement vector is partitioned into free and constrained degrees of freedom:

$$\mathbf{u} = \begin{bmatrix} \mathbf{u}_f \\ \mathbf{u}_c \end{bmatrix}$$

Only the free DOFs are retained for POD analysis and mean of the snapshot data is computed as follows:

$$\mathbf{X}_f = \mathbf{X}[\text{free DOFs}, :]$$

$$\bar{\mathbf{x}}_f = \frac{1}{N_s} \sum_{i=1}^{N_s} \mathbf{u}_f^{(i)}$$ Mean-centered snapshots are obtained and singular value decomposition (SVD) is then applied. After SVD, the POD basis is defined by retaining the first r left singular vectors:

$$\mathbf{X}_{fc} = \mathbf{X}_f - \bar{\mathbf{x}}_f \mathbf{1}^T$$

$$\mathbf{X}_{fc} = \mathbf{U}\boldsymbol{\Sigma}\mathbf{V}^T$$

$$\boldsymbol{\Phi}_f = \mathbf{U}_{(:,1:r)}$$

2.5. Galerkin Projection and Reduced System

The displacement field is approximated as:

$$\mathbf{u}_f \approx \bar{\mathbf{x}}_f + \mathbf{\Phi}_f \mathbf{q}$$

where $\mathbf{q} \in \mathbb{R}^r$ is the vector of reduced coordinates. Substituting the reduced approximation into the full equilibrium equation and applying Galerkin projection yields:

$$\mathbf{K}_r \mathbf{q} = \mathbf{\Phi}_f^T (\mathbf{f}_f - \mathbf{K}_f \bar{\mathbf{x}}_f)$$

where the reduced stiffness matrix is defined as the following equation which ensures consistency when mean subtraction is used.

$$\mathbf{K}_r = \mathbf{\Phi}_f^T \mathbf{K}_f \mathbf{\Phi}_f$$

2.7. ROM Inference and Reconstruction

For a new load case, the global force vector f is assembled, forces are restricted to free DOFs: f_fand reduced coordinates are computed by solving:

$$\mathbf{K}_r \mathbf{q} = \mathbf{f}_r$$

Then, the full displacement field is reconstructed:

$$\mathbf{u} = \begin{bmatrix} \bar{\mathbf{x}}_f + \mathbf{\Phi}_f \mathbf{q} \\ \mathbf{0} \end{bmatrix}$$

3. RESULTS

The reduced-order model (ROM) was evaluated using ten independent random loading scenarios. For each test, the full-order finite element analysis (FEA) solution was computed and compared against the ROM prediction. The performance of the proposed ROM was compared with the full-order FEA model by quantifying the increase in computational speed and evaluating numerical accuracy through Relative L2, RMS, and Maximum Absolute Error norms; this provided an assessment of both efficiency and accuracy. The results demonstrate a significant computational speed-up while maintaining acceptable accuracy.

Relative L2 error, maximum absolute displacement error, RMS error are used as:

$$\varepsilon_{\text{rel}} = \frac{\| \mathbf{u}_{\text{FEA}} - \mathbf{u}_{\text{ROM}} \|_2}{\| \mathbf{u}_{\text{FEA}} \|_2}$$

$$\varepsilon_{\text{RMS}} = \sqrt{\frac{1}{N_{\text{dof}}} \sum_{j=1}^{N_{\text{dof}}} (u_{\text{FEA},j} - u_{\text{ROM},j})^2}$$

$$\varepsilon_{\max} = \max_j \; | u_{\text{FEA},j} - u_{\text{ROM},j} |$$

Random and stochastic experiments, in other words, independent and discrete experiments, were conducted for performance comparison. Ten randomly selected experiments from the conducted experiments are shared in Table 1 below.

Test	Load Points Number	L2 Relative Error (%)	Max Absolute Error	RMS Error	FEA Time (s)	ROM Time (s)
1	1	7.125	6.7539e-02	2.4716e-02	2.7039	0.0010
2	10	8.881	1.1320e-01	4.3872e-02	2.6980	0.0001
3	1	7.799	5.5235e-02	2.0886e-02	2.6600	0.0001
4	6	0.394	3.4132e-03	9.6931e-04	2.6793	0.0010
5	9	6.397	7.1398e-02	3.0759e-02	2.7518	0.0001
6	1	14.828	4.7542e-02	1.8092e-02	2.7395	0.0010
7	1	9.036	9.7192e-03	3.6627e-03	2.7101	0.0011
8	10	60.053	3.7343e-02	1.3548e-02	2.7276	0.0013
9	3	11.923	5.3962e-02	2.0562e-02	2.7129	0.0001
10	9	4.614	1.2445e-01	4.7158e-02	2.6674	0.0012

Table 1 ROM and FEA Comparisons

As seen from the Table 1, proposed physics-based ROM provided an enormous increase in computational speed of approximately 4510 times compared to the fully ordered finite element analysis (FEA) model. While the average L2 error is approximately 13%, the absolute RMS error remains at the 10^{-2} mm level; this is an acceptable value for rapid design iterations where real-time feedback is prioritized over high-precision final verification.

As shown in Table 1, the proposed physics-based reduced-order model (ROM) provides an average improvement of approximately 4,510 times in computational efficiency compared to the full-order finite element analysis

(FEA) model. This dramatic reduction in computational cost highlights the effectiveness of the projection-based ROM approach for scenarios where rapid solutions are required.

Although the average relative L2 displacement error is around 13%, the corresponding absolute root-mean-square (RMS) error remains at the 10^{-2} mm scale; this proves that the deviation between ROM and FEA solutions is small in terms of absolute value. Such error levels are typically acceptable in early-stage engineering tasks focused on capturing global structural response and not requiring highly localized accuracy, including parametric studies, design exploration, and real-time decision support systems.

These results indicate that the proposed ROM provides an appropriate balance between accuracy and computational efficiency, making it highly suitable for applications requiring fast, physically consistent predictions. While the full-order FEA model may continue to be used for final validation and detailed stress analysis, the ROM serves as an efficient alternative for rapid evaluations during iterative design processes.

The strength of the developed ROM is clearly evident in 10 stochastic load scenarios. While the average relative L2 error is calculated as 13.1%, a closer look at the Root Mean Square (RMS) errors reveals consistently high accuracy, with deviations remaining below 0.05 mm in 90% of cases. The highest error observed in Case 8 is attributed to the beam's low total displacement magnitude; this increases the relative error percentage despite a small absolute deviation. Computational efficiency gains are extraordinary; ROM provides a 4500-fold increase in performance by omitting the dense assembly and inverting steps of the global stiffness matrix. This confirms that Physics-Based ROM provides an optimal balance between near-instantaneous execution and physical accuracy for high-fidelity structural problems.

Metric	Value
Average FEA Time (s)	2.7051
Average ROM Time (s)	0.0006
Average Speed-up	4509.8
Average L2 Relative Error (%)	13.105

Table 2 Mean Values of the Performance Criteria

The average performance metrics shown in Table 2 demonstrate the overall accuracy and computational efficiency of the reduced-order model (ROM) across ten independent random loading scenarios. The average finite element analysis (FEA) computation time of 2.7051 s represents the computational

cost of solving the full-order finite element model, while the average ROM computation time of 0.0006 s demonstrates the extremely low computational load of the reduced model. This results in an average acceleration factor of approximately 4500, highlighting the suitability of the ROM for real-time or interactive applications.

The presented methodology establishes a fully physics-based, projection-driven reduced order modeling pipeline for static structural analysis. By constructing the reduced basis from high-fidelity FEA snapshots and employing a Galerkin projection, the resulting ROM achieves significant computational speedup while preserving accuracy.

For reference and demonstration purposes, two representative loading conditions were selected from the test set to demonstrate the predictive capability of the proposed reduced-order model. Figures 1 and 2 provide a detailed visual comparison between the full-order finite element analysis (FEA) results and the corresponding reduced-order model (ROM) predictions for a cantilever beam configuration. In each figure, the actual FEA displacement field, the displacement field predicted by the ROM, and the absolute displacement error distribution are shown side by side. The close agreement observed between the FEA and ROM displacement contours confirms that the ROM accurately captures the global deformation behavior of the structure under different loading conditions; the error plots show that inconsistencies remain spatially uniform and limited in magnitude. These representative cases visually support the quantitative error metrics reported in Table 1 and demonstrate the robustness of the ROM in reproducing the structural response of the cantilever beam under varying load scenarios.

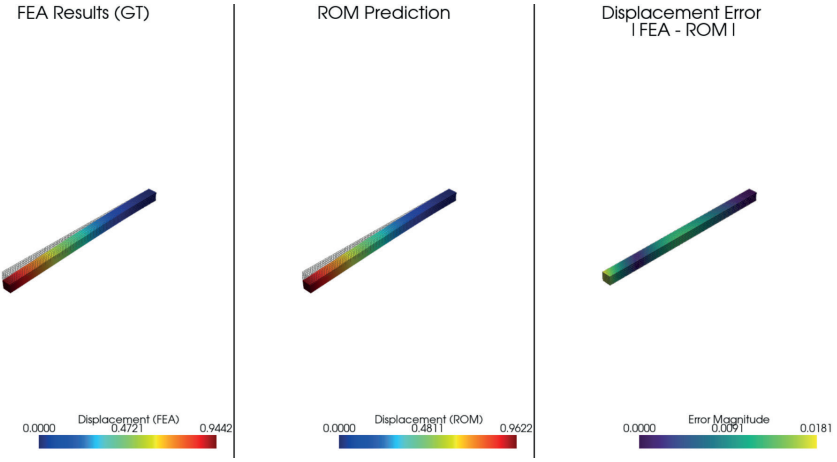

Figure 1 *Randomly applied 5 nodal force and comparison*

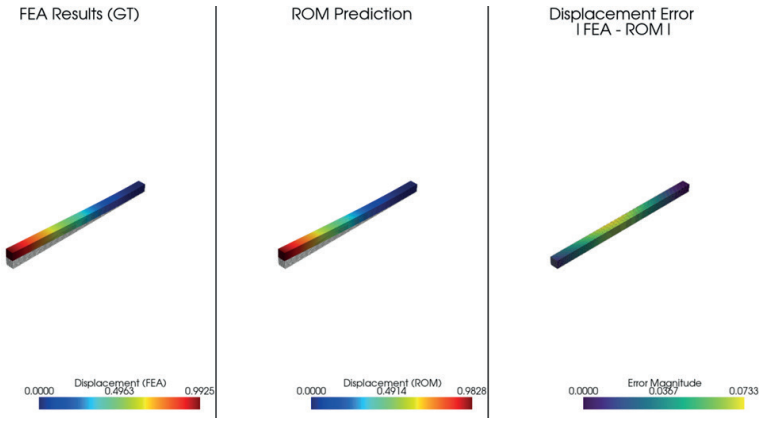

Figure 2 *Randomly applied 9 nodal force and comparison*

In this study, a fully physics-based reduced-order modeling approach for static structural analysis is presented and systematically evaluated. The proposed approach constructs a reduced basis from high-accuracy finite element snapshots and uses a Galerkin projection to efficiently approximate the structural response under varying loading conditions. The methodology was evaluated using independent stochastic loading scenarios, enabling a comprehensive assessment of both computational efficiency and numerical accuracy.

The results clearly demonstrate that the reduced order modeling (ROM) approach achieves an extraordinary reduction in computational cost, providing an average speedup of approximately 4500 times compared to the full-order finite element analysis (FEA) model. Despite this acceleration, the ROM maintains a high level of accuracy in absolute terms, with RMS displacement errors consistently remaining at the 10^{-2} mm scale. Although relative L2 errors increase in cases involving small global displacements, absolute deviations remain limited, confirming that the ROM reliably captures the structure's global deformation behavior.

Shared comparisons for randomly selected representative cases further support the findings, demonstrating strong agreement and spatially uniform, limited error distributions between finite element analysis (FEA) and random model (ROM) displacement fields. These observations demonstrate that the proposed ROM provides a robust and physically consistent approach to structural response under various loading scenarios.

Overall, the developed physics-based ROM strikes an effective balance between accuracy and computational efficiency, making it particularly suitable for real-time simulation, interactive design analysis, parametric studies, and rapid decision support systems. While full-order FEA remains indispensable for final validation and detailed local stress analysis, the proposed ROM serves as a powerful backup model for fast and reliable structural response estimation in iterative engineering workflows.

REFERENCES

Das, O., Gonenli, C., & Das, D. B. (2023). Crack detection in folded plates with back-propagated artificial neural network. Steel and Composite Structures. Retrieved from https://doi.org/10.12989/scs.2023.46.3.319

GÖNENLİ, C. (2022). FOLDED ANGLE DEPENDENT MODAL ANALYSIS OF THE FLAT AND FOLDED PLATES. Uludağ University Journal of The Faculty of Engineering. Retrieved from https://doi.org/10.17482/uumfd.1009101

Gonenli, C., & Das, O. (2021). Location-based effect of decomposition on laminated curved plate structures. Latin American Journal of Solids and Structures. Retrieved from https://doi.org/10.1590/1679-78256671

Hijazi, S., Freitag, M., & Landwehr, N. (2023). POD-Galerkin reduced order models and physics-informed neural networks for solving inverse problems for the Navier–Stokes equations. Advanced Modeling and Simulation in Engineering Sciences. Retrieved from https://doi.org/10.1186/s40323-023-00242-2

Kim, N. H. (2015). Introduction to nonlinear finite element analysis. Introduction to Nonlinear Finite Element Analysis. Retrieved from https://doi.org/10.1007/978-1-4419-1746-1

Meng, C., Yao, H., & Liu, Y. (2025). MFEA-Net: A pixel-adaptive multigrid finite element analysis neural network for efficient material response prediction. Neurocomputing. Retrieved from https://doi.org/10.1016/j.neucom.2025.129657

Reddy, J. N., & Arciniega, R. A. (2004). Advances in Shell Finite Elements. Ecommons. Cornell.Edu.

Santana, P. B., Ferreira, A. J. M., Gomes, H. M., & Tita, V. (2024). A nonlinear finite element analysis of laminated shells with a damage model. Composites Part C: Open Access. Retrieved from https://doi.org/10.1016/j.jcomc.2024.100505

Stabile, G., Hijazi, S., Mola, A., Lorenzi, S., & Rozza, G. (2017). POD-Galerkin reduced order methods for CFD using Finite Volume Discretisation: Vortex shedding around a circular cylinder. Communications in Applied and Industrial Mathematics. Retrieved from https://doi.org/10.1515/caim-2017-0011

Wu, X., Zhang, B., Nielsen, M. P., & Chen, Z. (2023). Neural Network Based Fea sible Region Approximation Model for Optimal Operation of Integrated Electricity and Heating System. CSEE Journal of Power and Energy Systems. Retrieved from https://doi.org/10.17775/CSEEJPES.2022.09040

Yadav, P., & Suresh, K. (2014). Large scale finite element analysis via assembly-free deflated conjugate gradient. Journal of Computing and Information Science in Engineering. Retrieved from https://doi.org/10.1115/1.4028591

Yamaguchi, T., & Okuda, H. (2021). Zooming method for FEA using a neural network. Computers and Structures. Retrieved from https://doi.org/10.1016/j.compstruc.2021.106480

Yu, G., Lou, Y., Dong, H., Li, J., & Jin, X. (2023). A Multilevel Hierarchical Parallel Algorithm for Large-Scale Finite Element Modal Analysis. Computers, Materials and Continua. Retrieved from https://doi.org/10.32604/cmc.2023.037375

Chapter 9

DIGITAL TWINS IN MECHANICAL ENGINEERING: BACKGROUND, APPLICATIONS, AND FUTURE DIRECTIONS

Özden İŞBİLİR [1]

1 Assistant Professor Dr. Özden İŞBİLİR. Karabuk University, Faculty of Engineering and Natural Sciences Department of Mechanical Engineering. E-mail: ozdenisbilir@karabuk.edu.tr
ORCID: 0000-0002-2526-602X

1. Introduction

The advent of Industry 4.0 has fundamentally altered the landscape of mechanical engineering, shifting the focus from purely physical asset management to cyber-physical integration. At the heart of this transformation lies the Digital Twin (DT), a concept that has evolved from its niche origins in aerospace applications to become a cornerstone of modern smart manufacturing and systems engineering. As mechanical systems continue to grow in complexity, incorporating advanced electronics, software, and connectivity, traditional approaches to design, testing, and maintenance are becoming increasingly inadequate. The Digital Twin offers a paradigm shift, providing a dynamic, virtual counterpart to physical entities that enables engineers to simulate, predict, and optimise performance throughout the product lifecycle (Erofeev, Kravchenko, & Kryukov, 2025). This introductory section establishes the definitional boundaries of Digital Twins, traces their historical evolution, distinguishes them from related digital concepts, and outlines their hierarchical classification within the context of mechanical engineering. Figure 1 provides an integrated overview of the fundamental forms of digital representation, their hierarchical organisation within mechanical systems, and the unifying role of the digital thread across lifecycle stages.

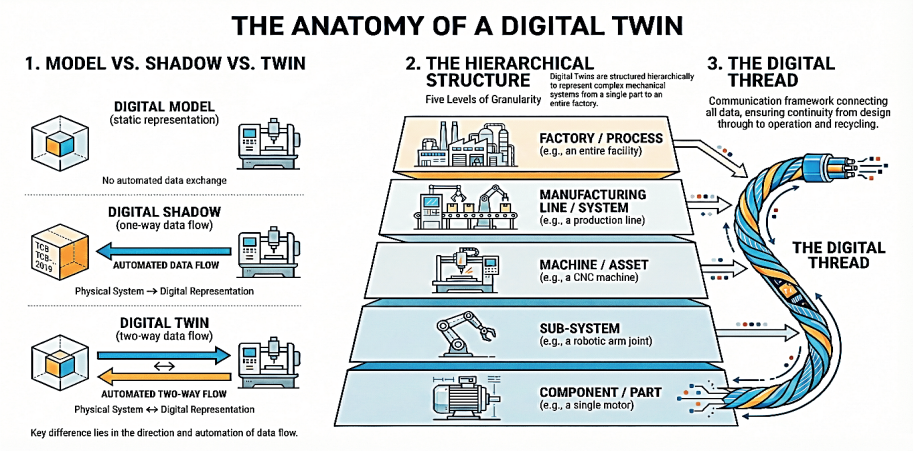

Figure 1: The anatomy of a Digital Twin

1.1. Conceptual Definition and Evolution

The term *Digital Twin* is used widely, but a precise definition is essential for academic clarity. In mechanical engineering, a Digital Twin is best described as a virtual representation of a physical object, system, or process that functions as its digital counterpart in real time (Bellavista & Modica, 2024). Unlike static

digital models, a DT integrates multi-physics, multi-scale, and probabilistic representations with real-time sensor data and historical information to reflect the evolving state of the physical asset (also called a physical twin) accurately.

Although the conceptual foundations were formalised by Michael Grieves in 2002 through his Product Lifecycle Management (PLM) model, which linked a real space, a virtual space, and an information flow, Digital Twin principles predate this terminology (Vohra, 2022). Although the conceptual foundations were formalised by Michael Grieves in 2002 through his Product Lifecycle Management (PLM) model, which linked a real space, a virtual space, and an information flow, Digital Twin principles predate this terminology (Vohra, 2022). The phrase *Digital Twin* was formally introduced in a NASA systems engineering roadmap in 2010, cementing the concept's relevance across aerospace operations (Vohra, 2022).

Since then, the DT has evolved in tandem with Industry 4.0 and the emerging Industry 5.0. No longer confined to aerospace, DTs now support manufacturing, automotive engineering, robotics, and energy systems by improving reliability, enhancing decision-making, and reducing unplanned downtime (Erofeev et al., 2025; Vohra, 2022). They help mitigate undesirable system behaviour and reduce resource waste related to material usage, energy consumption, and time (Patel, Patel, & Patel, 2022). As industrial systems become more autonomous and interconnected, the Digital Twin has become a critical enabler for continuous optimisation and lifecycle intelligence.

1.2. The Taxonomy of Digital Representation

Confusion frequently arises between Digital Twins and other digital artefacts such as CAD models or simulations. In mechanical engineering, these representations differ fundamentally in terms of data integration and information flow. Three primary categories are widely recognised:

- **Digital Model:** A static digital representation of an asset without automated data exchange. Changes to the physical system are not reflected in the model unless they are manually updated, and model modifications do not affect the physical asset (Condori, 2022; Kinnunen, 2024).

- **Digital Shadow:** A digital representation in which data flows automatically from the physical system to the digital entity. The digital state updates in response to physical changes, but there is no reverse influence from the digital domain back to the physical system. This is characteristic of monitoring systems with visualisation but no direct control (Bucaioni et al., 2025; Kinnunen, 2024).

- **Digital Twin:** The most advanced category, defined by automated bidirectional data flow. The digital representation not only mirrors the physical

asset but can also influence it through commands or decision-support outputs. This closed-loop functionality enables real-time optimisation, predictive control, and autonomous behaviour (Bucaioni et al., 2025; Kinnunen, 2024).

This bidirectionality distinguishes the DT from earlier forms of digital engineering and is essential for advanced use cases such as adaptive control, self-optimising machinery, and human–robot collaboration.

1.3. Hierarchical Classification in Mechanical Systems

Mechanical systems are rarely monolithic; they consist of assemblies, sub-assemblies, and discrete components. Consequently, Digital Twins must be structured hierarchically to provide value at different levels of granularity. A comprehensive framework for the Industrial Internet of Digital Twins (IIoDT) identifies five key levels within the manufacturing hierarchy (Sicard et al., 2023):

- **Component/Part Level:** This is the foundational level, representing critical individual components such as motors, bearings, or ball screws. At this level, the DT focuses on mechanical, electrical, and physical characteristics to estimate condition and degradation (Sicard et al., 2023; Vohra, 2022). It is important to note that simple components, such as paper clips or washers, typically do not warrant a DT; instead, DTs are reserved for sophisticated assets where lifecycle information is critical (Vohra, 2022).

- **Sub-System Level:** This level aggregates component twins to represent functional modules, such as a machine tool spindle or a robotic arm's joint system. Analysis at this level might include simulating dynamics to estimate vibration or thermal characteristics based on the combined behaviour of components (Sicard et al., 2023).

- **Machine/Asset Level:** This represents a complete piece of equipment, such as a CNC machine or a conveyor belt. The Machine DT integrates data from sub-systems to provide a holistic view of health, power usage, and operational status, often connected to a centralised data processing centre (Sicard et al., 2023; Vohra, 2022).

- **Manufacturing Line/System Level:** This level encompasses a collection of assets working together towards a production goal. A System DT allows engineers to observe interactions between disparate products and optimise throughput, reliability, and material flow (Sicard et al., 2023; Vohra, 2022).

- **Factory/Process Level:** The highest level of the hierarchy represents the entire production facility or process. It aggregates data from all lower levels to monitor inventory, overall equipment effectiveness (OEE), and enterprise-level performance (Sicard et al., 2023; Vohra, 2022).

1.4. The Role of the Digital Thread

Binding these hierarchical levels and lifecycle stages together is the concept of the *Digital Thread*. The Digital Thread establishes a closed loop that connects physical systems with their virtual counterparts, ensuring data continuity from design and conception through manufacturing, operation, and service, ultimately extending to disposal or recycling (Borole, Borkar, Raut, Balpande, & Chatterjee, 2023c).

In the design phase, physics-based models (such as Finite Element Analysis) serve as the DT prototype. As the asset enters production, manufacturing data is appended to it. During operation, the DT evolves by ingesting real-time sensor data, allowing for predictive maintenance and performance optimisation. Finally, at the end-of-life stage, the DT provides insights for recycling and informs the design of the next generation of products. This continuous flow of information addresses the issue of static data in traditional Product Lifecycle Management (PLM), thereby enhancing efficiency and sustainability (Borole, Borkar, Raut, Balpande, & Chatterjee, 2023a).

2. Modelling, Data Integration, and Computational Frameworks

The realisation of a Digital Twin within mechanical engineering necessitates a sophisticated convergence of high-fidelity modelling, robust data integration architectures, and scalable computational frameworks. Unlike traditional simulation, which is often static and offline, a DT requires a dynamic, bidirectional flow of information between the physical entity and its virtual counterpart. This section dissects the technical anatomy of DTs, categorising the fundamental modelling paradigms, the architectures required for data synchronisation, and the computational strategies that enable real-time performance in complex mechanical systems. Figure 2 illustrates the core technical components that underpin a Digital Twin, highlighting the interplay between multi-physics virtual models, real-time data integration mechanisms, distributed computational infrastructures, and integrated cybersecurity measures.

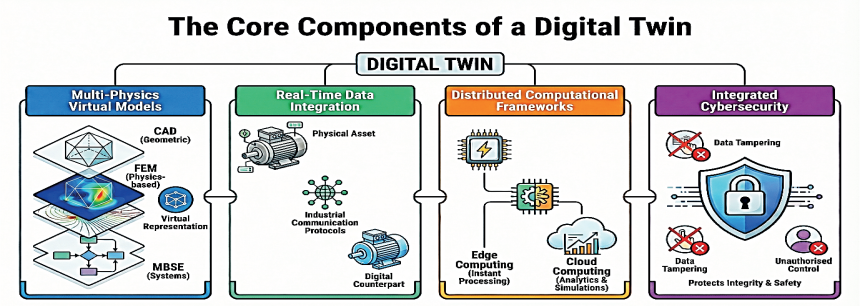

Figure 2: The core components of a Digital Twin

2.1. Modelling Paradigms in Mechanical Systems

The *Virtual System* is the core computational engine of a DT, tasked with mirroring the behaviour of the physical system over time (Santos & Montevechi, 2022). In mechanical engineering, this representation is rarely achieved through a single modelling technique; instead, it requires a multi-scale, multi-physics approach that blends geometric precision with behavioural dynamics.

2.1.1. Geometric and Parametric Modelling

At the foundational level, geometric modelling captures the physical dimensions and spatial constraints of the asset. Tools such as Computer-Aided Design (CAD) provide the static visual representation, but for a DT to be actionable, these models must be parametric. Parametric design allows the model to adjust dynamically based on real-time data or optimisation algorithms (Jiang & Fan, 2025). For instance, in the optimisation of automotive stamping processes, Bézier curves are frequently employed to define complex smooth contours of sheet-metal designed part geometries. A typical parametric curve is defined mathematically as:

$$P(t) = \sum_{i=0}^{n} B_{i,n}(t) P_{i,n} \; for \; 0 \leq t \leq 1$$

where $P(t)$ represents a point on the curve, $B_{i,n}(t)$ is the Bernstein basis polynomial of degree n, and $P_{i,n}$ denotes the Bernstein coefficients. This parametric flexibility allows engineers to evaluate multiple virtual prototypes without incurring physical tooling costs, supporting design-space exploration and process optimisation in forming, machining, and structural design (Jiang & Fan, 2025).

2.1.2. Physics-Based and Phenomenological Modelling

Mechanical systems frequently operate under complex combinations of loading, thermal exposure, and dynamic interactions. Physics-based models, therefore, form an essential part of the DT. The Finite Element Method (FEM) remains the principal technique for simulating stress, strain, deformation, and energy dissipation within solid structures (Jiang & Fan, 2025). Similarly, Computational Fluid Dynamics (CFD) is used to model fluid–structure interactions, heat transfer, and flow fields in systems such as compressors, turbines, and heat exchangers (Poddar, Sanikal, Thakare, & Sharma, 2025).

However, purely physics-based models can be computationally expensive for real-time applications. Consequently, phenomenological models are often employed to manage material damage and fatigue. Unlike micromechanical models, which characterise microstructural features such as crack initiation and growth, phenomenological models describe macroscopic material

behaviour and represent damage accumulation through statistical functions (Erofeev et al., 2025). These models are crucial for predictive maintenance services, as they allow the DT to estimate the Remaining Useful Life (RUL) of components based on cyclic loading conditions (Erofeev et al., 2025).

2.1.3. Model-Based Systems Engineering (MBSE)

The increasing complexity of mechanical–cyber systems necessitates a shift from document-centric to model-centric engineering methodologies. Model-Based Systems Engineering (MBSE) provides a structured framework in which the system model becomes the authoritative reference for requirements, architecture, analysis, and verification (Kinnunen, 2024). Languages such as SysML and Modelica play a central role in MBSE. Modelica, an acausal, equation-based modelling language, is particularly effective for multi-domain modelling in cyber-physical systems (Kinnunen, 2024). It allows motor, gear, actuator, and control models to interact through physical ports, supporting integrated analysis across mechanical, electrical, hydraulic, and thermal domains. This holistic representation is essential for building Digital Twins of mechatronic and automated manufacturing systems.

2.2. Data Integration and Communication Architectures

The performance and reliability of a Digital Twin depend on its ability to capture, synchronise, and transfer data efficiently and securely. The Communication Interface acts as the bridge between the physical system and its digital representation, enabling high-frequency data acquisition, preprocessing, and storage (Borole et al., 2023c).

2.2.1. The ISO 23247 Reference Architecture

The ISO 23247 standard provides a structured framework for implementing Digital Twins in manufacturing environments (International Standard Organisation, 2021). It defines four interlinked entities:

- **Device Communication Entity** – acquires data from Observable Manufacturing Elements (OMEs) via industrial networks and sends commands to actuators.
- **Digital Twin Entity** – contains the modelling, simulation, analytics, and decision-making modules.
- **Cross-System Entity** – governs interoperability, translation, and cybersecurity across heterogeneous systems.
- **User Entity** – interacts with the DT for monitoring, analysis, and control.

This architecture ensures that Digital Twins remain interoperable, modular, and scalable, rather than isolated bespoke solutions.

2.2.2. Communication Protocols and Data Flow

Industrial communication must accommodate multiple requirements: determinism, low latency, high reliability, and semantic interoperability. For high-speed control loops, deterministic industrial Ethernet technologies such as PROFINET, EtherCAT, and EtherNet/IP are preferred due to their low jitter and cycle times (McCormick & Wuest, 2025). For the broader Industrial Internet of Things (IIoT), Message Queuing Telemetry Transport (MQTT) and Open Platform Communications Unified Architecture (OPC UA) are the preferred standards, owing to their publish-subscribe communication models and their support for semantic interoperability (Malik, 2023).

In a typical MQTT architecture, a central broker manages data exchange between clients (DTs and physical assets). A client publishes a topic (e.g., sensor data), and subscribed clients receive the update (Kiangala & Wang, 2025). Discrete system states within a manufacturing process can be represented mathematically using binary variables. For process stage S_i, the state at time *t* may be described as:

$$S_i(t) = \begin{cases} 1, & if\ process\ stage\ i\ is\ active\ at\ time\ t \\ 0, & otherwise \end{cases}$$

Such abstractions allow the DT to track the operational cycle precisely and support the synchronisation of control logic across the virtual and physical domains.

2.2.3. The Digital Thread and Semantic Integration

To enable traceability across the entire product lifecycle, the Digital Thread provides the relational links among design models, manufacturing data, operational logs, and service records (Dozortsev, Agafonov, Slastenov, & Bauli, 2021). To interpret this data meaningfully, Semantic Modelling using Knowledge Graphs (KG) is increasingly adopted. KGs provide a structured, graph-based representation of domain knowledge, linking physical assets (e.g., *CNC Machine*) to their properties (e.g., *Spindle Speed*) and relationships (e.g., *located in*) (Meyers et al., 2022). Semantic integration thus transforms raw data streams into contextualised knowledge suitable for higher-level reasoning, optimisation, and decision support (Meyers et al., 2022).

2.3. Computational Frameworks and Simulation

A Digital Twin must support continuous simulation, data processing, and analytics within real-time or near-real-time constraints. To achieve this, modern DTs rely on distributed computation across edge, fog, and cloud platforms.

2.3.1. Semi-Physical Simulation and Time Synchronisation

Semi-physical simulation (also termed hybrid simulation) integrates virtual models with real hardware signals, a common approach in Hardware-in-the-Loop (HiL) testing. To evaluate future scenarios more quickly than real time, simulation clock acceleration is used. The acceleration rate v can be expressed as:

$$v = \frac{n.\Delta t}{t}$$

where n is the number of simulation clock advances per unit time, Δt is the time step, and t is the real-world time unit (Cheng, Wang, Yang, Dai, & Wang, 2022). This capability is essential for *what-if* analyses, where the DT simulates multiple future scenarios to determine the optimal control strategy before implementing it on the physical asset (Gomes, Oakes, Fitzgerald, & Larsen, 2024).

2.3.2. Co-Simulation via FMI

Complex mechanical systems often require the coupling of heterogeneous models (e.g., a Matlab control model with an ANSYS structural model). The Functional Mock-up Interface (FMI) standard addresses this by encapsulating models as Functional Mock-up Units (FMUs). Co-simulation enables the execution of these FMUs, which represent structural mechanics, control logic, thermal modelling, or system dynamics, together, exchanging data at discrete time steps (Abbiati et al., 2024). This modular architecture enables engineers to construct complex Digital Twins using the most suitable modelling tools for each subsystem, thereby enhancing reusability and maintainability (Abbiati et al., 2024).

2.3.3. Distributed Computing: The Edge-Cloud Continuum

Digital Twin deployments typically span:

- **Edge Computing** handles high-frequency, latency-critical tasks such as anomaly detection, real-time control, or vibration monitoring (Bellavista & Modica, 2024).
- **Cloud Computing** supports computationally intensive workloads such as data analytics, machine learning model training, and fleet-level optimisation (Bellavista & Modica, 2024).
- **Hybrid Frameworks** use orchestration frameworks such as Kubernetes and TOSCA to manage distributed microservices and deploy ML models trained in the cloud onto edge devices for real-time inference (Bellavista & Modica, 2024).

This layered computing continuum enables DTs to balance performance, scalability, and efficiency.

2.3.4. Digital Twin as a Service (DTaaS)

To lower the barrier to entry, particularly for Small and Medium-sized Enterprises (SMEs), the concept of Digital Twin as a Service (DTaaS) has emerged. This platform-based approach allows DTs to be constructed from reusable components (assets, models, data pipelines) rather than being built from scratch (Talasila, Mikkelsen, Gil, & Larsen, 2024). A DTaaS architecture typically includes containers for data processing, model management, and service execution, accessible via web-based dashboards (Talasila et al., 2024). This modularity supports the *composability* of DTs, where a complex system DT is aggregated from smaller, component-level DTs (Sicard et al., 2023).

2.4. Cybersecurity in Computational Frameworks

As DTs increase the connectivity of mechanical systems, they expand the attack surface for cyber threats. A compromised DT may lead not only to data breaches but also to incorrect control commands that could damage mechanical assets or compromise safety. Attack vectors include tampering with simulation or CAD files, sensor spoofing and false-data injection, unauthorised controller access and replay and man-in-the-middle attacks (Poddar et al., 2025).

To mitigate these risks, robust cybersecurity strategies must be integrated into DT architectures. These include encryption (e.g., AES-256 for data at rest and in transit), strong authentication mechanisms (e.g., OAuth 2.0), and the use of digital twins themselves to detect anomalies in network traffic or physical behaviour that indicate a breach (Poddar et al., 2025). For instance, a DT can run parallel simulations to verify if the commands sent to a physical controller will result in safe operational states, acting as a logic-based intrusion detection system (Kulik, Kazemi, & Larsen, 2024).

3. Applications of Digital Twins in Mechanical Engineering

The transition of the Digital Twin (DT) from a conceptual framework to a practical engineering tool is particularly evident within mechanical engineering. As established in earlier sections, a DT enables high-fidelity, real-time synchronisation between physical assets and their virtual counterparts, facilitating predictive, prescriptive, and autonomous capabilities. This section synthesises the principal application domains of DTs across mechanical engineering, including advanced manufacturing, machine tools, robotics, maritime systems, and materials engineering, illustrating how DTs deliver quantifiable improvements in performance, quality, and operational resilience. Figure 3 provides an overview of the principal application domains of Digital Twins in mechanical engineering, highlighting their roles in manufacturing optimisation, predictive maintenance, autonomous system safety, and immersive training.

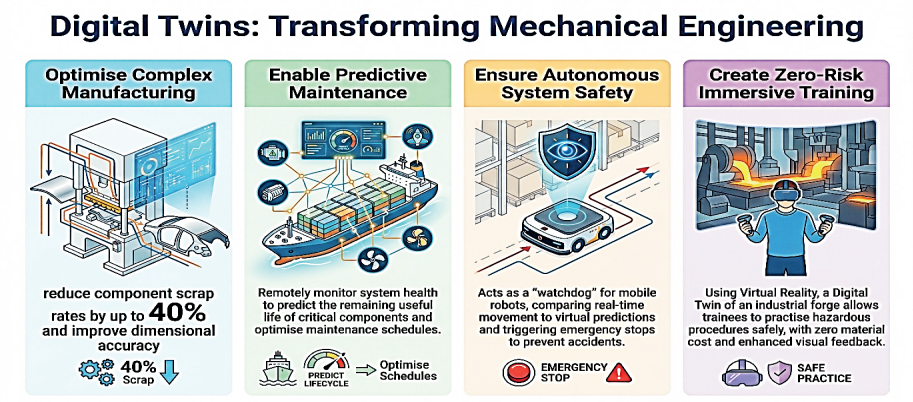

Figure 3: Digital Twins in mechanical engineering

3.1. Advanced Manufacturing Processes

Advanced manufacturing represents one of the earliest and most mature domains for DT adoption. By enabling virtual commissioning, process optimisation, and predictive control, DTs support the shift from reactive to proactive production systems. Applications range from discrete forming operations to full assembly-line synchronisation.

3.1.1. Automotive Stamping and Forming

The automotive sector relies heavily on high-volume forming operations, where dimensional accuracy and material utilisation are critical. Digital Twins have been employed to optimise stamping processes, such as those involving DP980 dual-phase steel components (Jiang & Fan, 2025).

A high-fidelity forming DT typically integrates finite element (FE) simulations representing material behaviour, process physics such as friction coefficients and punch velocities, and optimisation algorithms for parameter tuning. The DT of this process incorporates the material properties (yield strength, tensile strength), friction coefficients, and stamping speeds into a virtual simulation environment (e.g., ABAQUS). By applying multi-objective optimisation algorithms, such as Particle Swarm Optimisation (PSO) or Genetic Algorithms (GA), the DT can iteratively refine process parameters. For instance, the objective function for such an optimisation might minimise the dimensional tolerance range (R_{tol}) and the scrap ratio (S_{ratio}) while maximising tool life (L_{tool}). The optimisation problem can be formulated as:

$$\boxed{min\ f(x) = [R_{tol}(x), S_{ratio}(x)],} \qquad \boxed{\max\ L_{tool}(x)}$$

where x represents the vector of process parameters (e.g., die cushion pressure, punch velocity). Empirical results from such implementations have

shown significant improvements, such as reducing dimensional tolerance from ±0.5 mm to ±0.1 mm and decreasing the scrap rate by up to 40%, demonstrating the value of DTs in process optimisation (Jiang & Fan, 2025).

3.1.2. Assembly Line Synchronisation

For multi-stage manufacturing systems, DTs support system-level synchronisation and virtual commissioning. A representative case is a valve assembly line that incorporates robotic handling, ring pressing, and leakage testing, all under a nominal cycle time of 90 seconds (Malik, 2023).

A comprehensive DT is constructed using:

- **Virtual Devices:** Accurate kinematic models defined in tools like Siemens NX or Tecnomatix Process Simulate.
- **Virtual Controller:** Emulated PLCs (e.g., PLCSim Advanced) that execute the actual automation code.
- **Communication Layer:** Protocols such as OPC UA or MQTT facilitate data exchange between the virtual controller and the simulation model.

This virtual commissioning identifies control logic flaws, task sequence conflicts, or collision risks before physical deployment. Reported benefits include a 20–25% reduction in commissioning time, reduced downtime during start-up, and lower integration costs (Malik, 2023).

3.1.3. Additive Manufacturing

Additive Manufacturing (AM) presents unique challenges due to its thermal complexity, the stochastic nature of powder behaviour, and the difficulty of real-time defect detection. DTs in AM are utilised to predict microstructural formation, residual stresses, and part distortion, which are difficult to measure in real-time (Zhang, Zhou, & Chen, 2022). A DT for AM typically integrates a mechanistic model (simulating melt pool dynamics and solidification), a sensing model (collecting in-situ data from pyrometers or thermal cameras), and a data-driven model (utilising machine learning to correlate sensor data with defect probability) (Zhang et al., 2022).

For example, in Laser Powder Bed Fusion (LPBF), a DT predicts thermal fields and microstructural outcomes, enabling closed-loop adjustments to laser power, scan speed, or hatch spacing. This converts AM from an open-loop to a closed-loop process, improving part consistency and reducing scrap rates (Zhang et al., 2022).

3.1.4. Industrial Forging and Immersive Education

Digital Twins also support training and educational functions in hazardous industrial domains. An immersive DT of an industrial forge replicates a screw-press workplace within Virtual Reality (VR), enabling learners to interact with virtual billets and forge components without exposure to heat or mechanical hazards (Fleury, Baudouin, & Bondesan, 2024). An immersive DT offers;

- visualisation of invisible phenomena such as thermal gradients,
- low-cost repetition of complex procedures,
- real-time haptic or visual feedback on operator actions.

A comparison between the physical forge and its immersive DT is shown in Table 1 (Fleury et al., 2024).

Table 1: Comparison of Physical and Immersive Digital Twin for Forging.

Feature	Physical Forge	Immersive Digital Twin
Safety	High risk (heat, moving parts)	Zero risk
Visibility	Limited to the surface	Cross-sections, thermal gradients visible
Cost	High (energy, material)	Low (computational cost only)
Feedback	Post-process inspection	Real-time visual and haptic feedback

This application demonstrates the DT's capacity to support skill acquisition and safety training in high-risk mechanical environments (Fleury et al., 2024).

3.2. Machine Tools and Equipment

Machine tools are the workhorses of mechanical engineering. DTs at the machine level focus on monitoring health, optimising performance, and predicting failures of critical components, such as spindles, motors, and gears.

3.2.1. Industrial Tool Management (The ITB-A Case)

A clear example of a component-level DT is the handheld battery angle tool (ITB-A) developed by Atlas Copco (Kinnunen, 2024). The DT decomposes the tool into its constituent subsystems, namely gears, planetary stages, an electric motor, and a torque transducer, and utilises a Modelica-based MBSE framework to simulate torque, speed, energy consumption, and wear.

For a planetary gearbox, the cumulative gear ratio G_r is given by:

$$G_r = \prod_{i=1}^{n} \left(1 + \frac{Z_{rim,i}}{Z_{sun,i}}\right)$$

where Z_{rim} and Z_{sun} denote the number of teeth on the gear rim and sun wheel, respectively.

The DT predicts battery performance, usage distribution across tightening cycles, and component wear, enabling optimised maintenance strategies and lifecycle tracking, fully aligned with ISO 23247 DT definitions (Kinnunen, 2024).

3.2.2. Spindle and Cutter Health Monitoring

In CNC machining, the spindle and cutting tools are critical assets. DTs are employed to monitor tool wear and predict *Remaining Useful Life* (RUL). A hybrid DT approach merges physics-based cutting-force models with data-driven techniques using vibration or acoustic-emission signals (Sicard et al., 2023). A virtual sensor can estimate cutting force F_c from motor current and spindle speed, avoiding impractical direct force measurements as follows.

$$F_c = k.I_{motor}.w_{spindle}$$

Deviations between the estimated force and the theoretical force derived from cutting databases can indicate tool wear or breakage. This allows the DT to trigger an emergency stop or adjust feed rates to prevent damage, effectively acting as a supervisory control system (Sicard et al., 2023).

3.2.3. Compressor Manufacturing and Quality Control

In the production of compressor air ends (the core element of a compressor), DTs are used to correlate machining conditions with geometrical quality outcomes. At Atlas Copco Airpower, a Knowledge Graph-based DT links temperature measurements (coolant, machine bed, ambient conditions), CNC machine events and CMM dimensional inspections (Meyers et al., 2022).

The semantic model enables cross-domain analysis, such as identifying whether thermal drift during a specific machining step correlates with deviations in rotor bore geometry. This DT supports root-cause analysis, process stability assessment, and continuous quality improvement (Meyers et al., 2022).

3.3. Robotics and Autonomous Systems

Robotic systems, particularly those operating in dynamic or collaborative environments, benefit significantly from DTs for motion planning, collision avoidance, and synchronised execution.

3.3.1. The Desktop Robotti: Mobile Agricultural Robotics

The *Desktop Robotti* is a scale model of an autonomous agricultural field robot, serving as a testbed for DT technologies. The DT for this system focuses

on parallel operation and runtime monitoring. It employs a co-simulation architecture where a kinematic model (based on bicycle dynamics) runs in parallel with the physical robot (Oakes et al., 2024). The kinematic state of the robot (position x, y, heading ψ) is predicted using inputs of linear velocity (v), steering angle (δ) and the wheelbase (L):

$$\dot{x} = v\cos(\psi), \qquad \dot{y} = v\sin(\psi), \qquad \dot{\psi} = \frac{v}{L}\tan(\delta)$$

The DT compares this predicted state with real-time location data (e.g., from indoor GPS or LiDAR). Significant divergence indicates a fault (e.g., wheel slip, actuator failure) or an environmental anomaly (e.g., collision). This setup allows the DT to act as a *watchdog*, capable of triggering an emergency stop if the physical robot deviates dangerously from its expected path, thereby enhancing safety in autonomous operations (Oakes et al., 2024).

3.3.2. Cooperative Robotic Manufacturing

In collaborative manufacturing cells involving multiple robots, such as a KUKA LBR iiwa and a UR5, Digital Twins provide coordinated control, collision avoidance, and virtual commissioning (Oakes et al., 2024). A central DT Manager ensures bidirectional communication between virtual and physical robots, synchronised trajectory planning, and continuous deviation checking between planned and actual joint movements. This enables safe execution of cooperative tasks, such as part handovers, by validating the entire workflow in the virtual domain before physical deployment (Oakes et al., 2024).

3.4. Energy and Maritime Systems

High-value assets in the energy and maritime sectors operate in harsh environments where physical access is limited. DTs here provide remote monitoring and lifecycle management capabilities.

3.4.1. The Research Vessel Gunnerus

The R/V Gunnerus, a marine research vessel, utilises a DT for decision support and predictive maintenance. The DT integrates a high-fidelity hydrodynamic model of the hull, models of the propulsion system (thrusters) and a power plant model, as well as sensor fusion from onboard GPS, wind sensors, and motion reference units (Oakes et al., 2024). Data transmitted via 4G/5G enables onshore monitoring and supports predictive maintenance by comparing live operating profiles with physics-based degradation models. The DT assists in estimating the Remaining Useful Life (RUL) of thrusters and engines, improving the scheduling of dry-dock inspections and minimising operational disruptions (Oakes et al., 2024).

3.4.2. Power Generation and Gas Turbines

In the power sector, DTs are indispensable for gas turbines and wind farms. A gas turbine's DT might focus on critical components, such as turbine blades, which are subject to extreme thermal and mechanical stresses. Phenomenological models are used to manage material damage, predicting blade fatigue based on operational profiles (start-stop cycles, load variations) (Erofeev et al., 2025).

The DT creates a Digital Thread connecting the design phase (CAD/CAE models) with the operational phase. For instance, if a turbine blade shows signs of premature fatigue, the DT can revert to the design models to simulate the specific operating conditions that caused the damage. This feedback loop informs the design of more robust future components. Cybersecurity is a critical aspect here; as highlighted in recent research, a compromised DT (e.g., via tampered FEA files) could lead to catastrophic failure by masking stress concentrations or overriding safety protocols (Poddar et al., 2025).

3.5. Structural Integrity and Materials Engineering

Digital Twins are increasingly applied to materials engineering, particularly for damage detection, fatigue analysis, and composite manufacturing.

3.5.1. Phenomenological Models for Material Damage

Mechanical engineering relies heavily on understanding how materials degrade under load. DTs integrate phenomenological models, which describe macroscopic material behaviour using statistical functions, to predict damage accumulation (Erofeev et al., 2025). Unlike purely micromechanical models that simulate individual crack growth (computationally expensive), phenomenological models in a DT allow for real-time estimation of fatigue life. These models often employ cumulative damage concepts such as Miner's rule:

$$D = \sum_{i=1}^{k} \frac{n_i}{N_i}$$

where n_i is the number of cycles at a given stress level and N_i is the allowable cycle count before failure.

Such DTs are essential in safety-critical sectors, offering real-time structural health monitoring and early failure prediction (Erofeev et al., 2025).

3.5.2. Composite Manufacturing (Hand Lay-up)

Composite manufacturing involves complex, multi-stage processes where quality depends heavily on operator skill. Composite manufacturing requires

precise control over fibre orientation, resin distribution, and curing cycles. DTs combined with VR environments support training and quality assurance by simulating material deformation and ply stacking, visualising resin flow during vacuum bagging and modelling curing cycles and process-induced distortions (Darejeh, Chilcott, Oromiehie, & Mashayekh, 2025). Table 2 summarises the DT functions used for educational and operational guidance in composite lay-up.

Table 2: Digital Twin functions in Composite Manufacturing Training (Darejeh et al., 2025)

Stage	Physical Action	Digital Twin Function
Material Prep	Cutting fibre sheets	Simulating geometry and nesting to minimise waste
Lay-up	Stacking layers	Visualising fibre orientation and ply sequence
Curing	Vacuum bagging	Simulating resin flow and cure cycle times

While this application is currently educational, it demonstrates the potential for DTs to guide manual manufacturing processes, ensuring that operators adhere to precise specifications required for high-performance composite parts.

4. Challenges, Emerging Trends, and Future Research Directions

Although Digital Twins (DTs) have demonstrated considerable benefits across mechanical engineering, improving process optimisation, quality control, and lifecycle intelligence, their widespread industrial deployment is hindered by a range of technical, operational, and organisational challenges. Moreover, as DTs mature, they intersect with new technological paradigms, including the Industrial Metaverse, cognitive reasoning, and human-centric automation. This section provides a critical examination of the primary limitations facing the implementation of DT. It explores the emerging trends shaping future Digital Twin research within the context of Industry 4.0 and the forthcoming Industry 5.0. Figure 4 summarises the principal challenges currently constraining the deployment of Digital Twins, alongside the emerging trends expected to shape future research and industrial adoption.

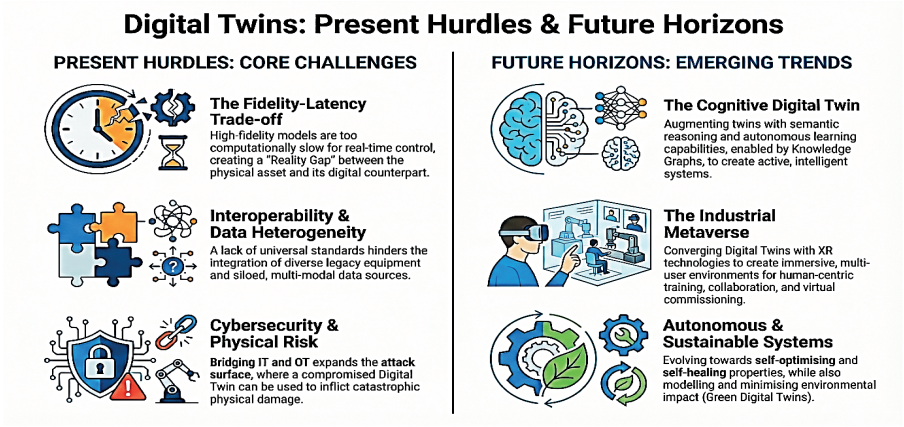

Figure 4: Current challenges and future direction of Digital Twin

4.1. The Fidelity-Latency Trade-off and the Reality Gap

One of the most persistent challenges in Digital Twin engineering is the inherent trade-off between *model fidelity* and *computational latency*. High-fidelity physics-based models, such as Finite Element Analysis (FEA) or Computational Fluid Dynamics (CFD), offer accurate predictions of mechanical behaviour but are often computationally prohibitive for real-time or near-real-time use (Jiang & Fan, 2025; Zhang et al., 2022). In manufacturing systems with sub-millisecond control cycles, the computational load required to run full-resolution simulations can exceed the allowable cycle time, making direct integration infeasible (McCormick & Wuest, 2025).

This mismatch contributes to the so-called *Reality Gap*, the discrepancy between the actual physical state of the system and its digital representation. Factors that widen this gap include modelling assumptions, parametric uncertainties in material behaviour, uncertainties in sensor measurements or sensor noise, and unpredictable environmental disturbances (Larsen et al., 2024). To address this, researchers are increasingly employing *Model Order Reduction (MOR)*, surrogate models, and hybrid approaches combining physics-based constraints with machine learning. However, ensuring that reduced-order models remain valid across the full operating envelope remains an open research challenge, particularly in non-linear, multi-physics environments (Larsen et al., 2024; Pierce, 2024).

Synchronisation poses an additional issue. Industrial communication protocols such as MQTT, despite Quality of Service (QoS) mechanisms, struggle to guarantee the bounded latency required for high-frequency mechanical control (McCormick & Wuest, 2025). For instance, packet loss or

jitter (*J*) in the communication network can lead to surface quality deterioration in milling processes if the jitter exceeds 100 μs (McCormick & Wuest, 2025). The relationship between the update time (*UT*) and the phenomenon response time (*PRT*) must be rigorously optimised to ensure the DT does not induce instability in the physical asset (McCormick & Wuest, 2025).

4.2. Interoperability and Data Heterogeneity

The mechanical engineering ecosystem comprises a heterogeneous mix of legacy equipment, proprietary controllers, and diverse software platforms. A significant barrier to widespread DT adoption is the lack of universal interoperability and standardisation (D'Amico, Addepalli, & Erkoyuncu, 2023). While standards such as ISO 23247 have emerged to define reference architectures for manufacturing DTs, their adoption is inconsistent, and integration with legacy systems remains complex and costly (Kinnunen, 2024; Talasila et al., 2024).

Data heterogeneity represents another significant barrier. Mechanical systems generate multi-modal datasets, including high-frequency sensor data (e.g., vibration, current, thermal readings), static CAD and CAE models, event logs from PLCs and CNC machines and unstructured maintenance reports (Meyers et al., 2022). Integrating these disparate data sources into a unified semantic model is a non-trivial task. Current frameworks often rely on ad-hoc integration methods that are brittle and difficult to scale. The siloed structure of data storage, in which design, manufacturing, and operational data reside in disconnected repositories, inhibits the realisation of a fully integrated Digital Thread that spans the entire product lifecycle (Scheibmeir & Malaiya, 2022; Talasila et al., 2024).

4.3. Cybersecurity and Mechanical Integrity

As DTs bridge the gap between Information Technology (IT) and Operational Technology (OT), they significantly expand the attack surface of mechanical systems. The security risks extend beyond data theft to physical sabotage. A compromised DT can be manipulated to send malicious control commands to the PT, potentially causing catastrophic mechanical failure or safety hazards (Kulik et al., 2024; Poddar et al., 2025).

Specific threats to Computer-Aided Engineering (CAE) workflows have been identified, such as the tampering of FEA mesh files or boundary conditions during transmission. If a cyber-attacker modifies simulation parameters (e.g., lowering mesh density to hide stress concentrations), the DT may falsely validate an unsafe operating condition (Poddar et al., 2025). Risk assessment in this context requires a distinct taxonomy that accounts for mechanical consequences. A risk score *R* can be calculated as:

$$R = P \times S$$

where P is the probability of an attack (e.g., due to unencrypted data transmission) and S is the severity of the mechanical impact (e.g., turbine blade fracture).

Furthermore, common attacks such as Man-in-the-Middle (MitM), Denial of Service (DoS), and False Data Injection (FDI) can disrupt the synchronisation between the DT and PT (Kulik et al., 2024). For instance, a replay attack might feed the DT recorded *normal* sensor data while the physical machine is being driven to failure (Kulik et al., 2024). Mitigating these risks requires robust encryption protocols (e.g., AES-256 for CAE files) and anomaly detection mechanisms capable of identifying deviations between expected physical behaviour and reported sensor data (Kulik et al., 2024; Poddar et al., 2025).

4.4. Emerging Trend: The Cognitive Digital Twin

To address the limitations of current data-driven and physics-based models, the concept of the *Cognitive Digital Twin* (CDT**)** is emerging. CDTs augment traditional DTs with semantic capabilities, reasoning, and autonomous learning, enabling them to understand complex interrelationships and make decisions in unforeseen situations (D'Amico et al., 2023; Larsen et al., 2024).

A key enabler for CDTs is the use of *Knowledge Graphs* (KGs). KGs provide a structured, semantic layer that links heterogeneous data sources (e.g., machine logs, quality measurements, and physics simulations) using domain ontologies. In a use case involving compressor manufacturing at Atlas Copco, a KG-based cognitive twin was employed to link disparate data silos, including temperature sensor data, CNC machine events, and quality measurements. This enabled data scientists to query the system using domain-level concepts rather than low-level database schemas (Meyers et al., 2022). This semantic abstraction enables flexible, ad hoc analysis and reasoning, shifting the DT from a passive observer to an active and intelligent participant in the engineering process.

4.5. Emerging Trend: The Industrial Metaverse and Human-Centricity

The convergence of DTs with Extended Reality (XR) technologies is giving rise to the *Industrial Metaverse*. While often conflated, the metaverse extends the DT concept by providing an immersive, persistent, and multi-user environment where physical and virtual entities interact (Kiangala & Wang, 2025). This trend aligns closely with Industry 5.0, which re-emphasises the role of the human worker, prioritising resilience, sustainability, and human-centricity over pure efficiency (Kiangala & Wang, 2025; Larsen et al., 2024).

In the Industrial Metaverse, DTs serve as the backbone for immersive training, remote collaboration, and *virtual commissioning* of human-robot collaborative cells. For example, operators can interact with a virtual forge or robotic cell via VR headsets to validate safety protocols or learn complex assembly tasks without physical risk (Bellavista & Modica, 2024; Fleury et al., 2024). This human-in-the-loop approach ensures that the DT empowers the workforce rather than replacing it, using visualisation to make complex data comprehensible and actionable (Bohlbro, Macedo, Tola, Esterle, & Larsen, 2024).

4.6. Future Research Directions

The trajectory of DT research in mechanical engineering suggests several critical avenues for future investigation:

1. **Federated Digital Twins and Systems of Systems (SoS):** Future industrial ecosystems will increasingly require interconnected DTs spanning suppliers, factories, logistics, and customers. *Federated DTs* allow autonomous DT nodes to share data selectively and securely across organisational boundaries (Bucaioni et al., 2025). Challenges include governance structures, semantic interoperability, and trust frameworks (Kiangala & Wang, 2025; Talasila et al., 2024).

2. **Physics-Informed Machine Learning (PIML):** PIML approaches embed physical principles (e.g., conservation laws, constitutive relations) into the structure or loss functions of machine learning models (Pierce, 2024; Rojek, Mikołajewski, Dostatni, Cybulski, & Kozielski, 2025). This reduces data requirements, improves generalisability, and ensures physically plausible predictions, making PIML essential for safety-critical mechanical applications.

3. **Autonomous Reconfiguration and Self-X Properties:** Moving beyond monitoring, DTs must evolve to support *autonomous reconfiguration*. This involves equipping DTs with *Self-X* properties (self-monitoring, self-optimising, self-healing) (Esterle, Frasheri, & Larsen, 2024). This requires advanced control architectures such as MAPE-K loops or Belief–Desire–Intention (BDI) agents, allowing the DT to safely modify the physical parameters of a machine (e.g., adjusting heater timing in an incubator) in response to environmental changes or detected faults, closing the loop between virtual cognition and physical action (Esterle et al., 2024; Larsen et al., 2024).

4. **Sustainability and Circular Economy:** DTs must explicitly incorporate sustainability metrics. Future DTs should model not just performance and cost, but also energy consumption, carbon footprint, and material recyclability throughout the asset's lifecycle (Borole, Borkar, Raut, Balpande, & Chatterjee, 2023b). This *Green Digital Twin* will be instrumental

in achieving the sustainability goals of Industry 5.0, enabling manufacturers to optimise for minimal environmental impact alongside mechanical efficiency.

5. **Standardisation of Semantics:** Building on ISO 23247, the development of unified semantic standards, such as Asset Administration Shells (AAS), will be critical for enabling plug-and-play interoperability. Standardised vocabularies and ontologies will ensure that DT components from different vendors (e.g. a DT of a motor from one manufacturer plugs into the DT of a pump from another system) can interact seamlessly (Kiangala & Wang, 2025; Talasila et al., 2024).

In summary, the future of Digital Twins in mechanical engineering lies in their evolution from isolated, static models to interconnected, autonomous, and human-centric systems. Addressing the challenges of latency, security, and interoperability is a prerequisite for unlocking this potential, paving the way for autonomous, resilient, and sustainable mechanical systems.

5. Conclusion

The exploration of Digital Twins (DTs) throughout this chapter has illuminated their status not merely as a technological novelty but as a fundamental paradigm shift within the discipline of mechanical engineering. We have traced the evolution of the Digital Twin from its conceptual origins, rooted in the need to replicate complex aerospace assets, to its current role as a pervasive enabler of Industry 4.0 and the emerging Industry 5.0. This journey reveals that the Digital Twin is the realisation of the long-sought convergence between Operational Technology (OT) and Information Technology (IT), fusing the deterministic rigour of mechanical physics with the probabilistic agility of data science.

The value of a Digital Twin lies not in its graphical fidelity alone, but in its functional interconnectivity. As we have discussed, the distinction between a static Digital Model, a passive Digital Shadow, and a fully active Digital Twin is defined by the flow of data. It is the bidirectional exchange of information, involving the automatic synchronisation of the physical and virtual states, that enables engineers to move beyond retrospective analysis towards proactive control and predictive maintenance. By establishing a continuous Digital Thread, organisations can preserve semantic consistency across the entire product lifecycle, ensuring that insights generated during the operational phase flow directly back into the design and manufacturing phases. This closes the loop on engineering, allowing for products that evolve and improve over time based on real-world usage profiles rather than static design assumptions.

Furthermore, the technological substrates underpinning these systems demonstrate that modern mechanical engineering is becoming increasingly interdisciplinary. The reliance on diverse modelling paradigms, ranging from

geometric and parametric CAD to high-fidelity Finite Element Analysis and Computational Fluid Dynamics, underscores the need for deep domain knowledge. However, the integration of these physics-based models with data-driven approaches, such as machine learning and neural networks, represents a crucial evolution. We have seen that hybrid modelling is often the most pragmatic path forward, balancing the computational expense of high-fidelity simulations with the speed required for real-time edge computing. This balance is critical for bridging the reality gap, ensuring that the virtual entity remains a valid surrogate for the physical asset without inducing unacceptable latency in control loops.

The breadth of applications reviewed, from the micro-scale optimisation of drilling operations to the macro-scale management of maritime vessels and wind farms, underscores the versatility of the Digital Twin. Whether used for virtual commissioning to reduce risks in assembly lines or applied to monitor structural integrity in hazardous environments, the DT functions as a controlled sandbox for innovation and experimentation. It enables engineers to test hypotheses and simulate catastrophic failure modes without incurring physical risk or economic penalties. Yet, as we look to the future, we must remain cognizant of the significant hurdles that still lie ahead. The challenges of interoperability, data heterogeneity, and cybersecurity are not merely technical inconveniences but foundational barriers that require rigorous standardisation and robust security architectures.

Ultimately, as we transition towards Industry 5.0, the role of the Digital Twin will expand to encompass human-centricity and sustainability. The next generation of Cognitive Digital Twins will likely possess greater autonomy, capable of reasoning and self-reconfiguration. However, their primary function will remain the empowerment of the human engineer. By abstracting the complexity of massive data streams into actionable insights, Digital Twins enable us to make more informed, ethical, and sustainable decisions. In doing so, they ensure that the mechanical systems of the future are not only efficient and reliable but also resilient and responsive to the needs of society. The Digital Twin is, therefore, not just a tool for observation, but the central nervous system of modern mechanical engineering.

REFERENCES

Abbiati, G., Gomes, C., Sandberg, M., Kazemi, Z., Hansen, S. T., & Larsen, P. G. (2024). Modelling for digital twins. In J. Fitzgerald, C. Gomes, & P. G. Larsen (Eds.), The engineering of digital twins (pp. 89-127). Cham: Springer International Publishing.

Bellavista, P., & Modica, G. D. (2024). IoTwins: Implementing distributed and hybrid digital twins in industrial manufacturing and facility management settings. Future Internet, 16(65). https://doi.org/10.3390/fi16020065

Bohlbro, C. H., Macedo, H. D., Tola, D., Esterle, L., & Larsen, P. G. (2024). Visualisation in a digital twin context. In J. Fitzgerald, C. Gomes, & P. G. Larsen (Eds.), The engineering of digital twins (pp. 175-188). Cham: Springer International Publishing.

Borole, Y., Borkar, P., Raut, R., Balpande, V. P., & Chatterjee, P. (2023a). Digital twin and IoT. In Digital twins:Internet of things, machine learning, and smart manufacturing (pp. 39-48). Berlin, Boston: De Gruyter.

Borole, Y., Borkar, P., Raut, R., Balpande, V. P., & Chatterjee, P. (2023b). Digital twin use cases and industries. In Digital twins: Internet of things, machine learning, and smart manufacturing (pp. 87-114). Berlin, Boston: De Gruyter.

Borole, Y., Borkar, P., Raut, R., Balpande, V. P., & Chatterjee, P. (2023c). What is digital twin? Digital twin concept and architecture. In Digital twins:Internet of things, machine learning, and smart manufacturing (pp. 1-16). Berlin, Boston: De Gruyter.

Bucaioni, A., Eramo, R., Berardinelli, L., Bruneliere, H., Combemale, B., Khelladi, D. E., . . . Wimmer, M. (2025, March 31 – April 02). Multi-partner project: A model-driven engineering framework for federated digital twins of industrial systems (MATISSE). [Conference proceeding] 2025 Design, Automation & Test in Europe Conference (DATE), Lyon, France.

Cheng, K., Wang, Q., Yang, D., Dai, Q., & Wang, M. (2022). Digital-twins-driven semi-physical simulation for testing and evaluation of industrial software in a smart manufacturing system. Machines, 10(5), 388. https://doi.org/10.3390/machines10050388

Condori, P. P. C. (2022). Digital twin in development of products. In M. Vohra (Ed.), Digital twin technology: Fundamentals and applications (pp. 205-218): Wiley-Scrivener Publishing.

D'Amico, R. D., Addepalli, S., & Erkoyuncu, J. A. (2023). Industrial insights on digital twins in manufacturing: Application landscape, current practices, and future needs. Big Data and Cognitive Computing, 7(3), 126. https://doi.org/10.3390/bdcc7030126

Darejeh, A., Chilcott, G., Oromiehie, E., & Mashayekh, S. (2025). Virtual reality and digital twins for mechanical engineering lab education: Applications in composite manufacturing. Education Sciences, 15(11), 1519. https://doi.org/10.3390/educsci15111519

Dozortsev, V., Agafonov, D., Slastenov, I., & Bauli, E. (2021, April 14-16). Digital twins in industrial process engineering. [Conference proceeding] 5th International Science Fiction Prototyping Conference (SCIFI-IT'21), Ghent, Belgium.

Erofeev, M. N., Kravchenko, I. N., & Kryukov, M. V. (2025). Integration of digital twins in mechanical engineering: Information support, modeling, and management of the product life cycle. Journal of Machinery Manufacture and Reliability, 54(2), 210-215. https://doi.org/10.1134/s1052618824701747

Esterle, L., Frasheri, M., & Larsen, P. G. (2024). Autonomous reconfiguration enabled by digital twins. In J. Fitzgerald, C. Gomes, & P. G. Larsen (Eds.), The engineering of digital twins (pp. 345-362). Cham: Springer International Publishing.

Fleury, S., Baudouin, C., & Bondesan, P. (2024, June 10-13). Immersive digital twins of an industrial forge in engineering education. [Conference proceeding] 20th International CDIO Conference, Tunis, Tunisia.

Gomes, C., Oakes, B. J., Fitzgerald, J., & Larsen, P. G. (2024). Foundational concepts for digital twins of cyber-physical systems. In J. Fitzgerald, C. Gomes, & P. G. Larsen (Eds.), The engineering of digital twins (pp. 45-63). Cham: Springer International Publishing.

Jiang, Q., & Fan, J. (2025). A study of digital twins in simulating and improving mechanical manufacturing processes. SCIENTIFIC BULLETIN Series D: Mechanical Engineering, 87(3), 263-276. Retrieved from https://www.scientific-bulletin.upb.ro/rev_docs_arhiva/rezf8e_536710.pdf

Kiangala, K. S., & Wang, Z. (2025). An inceptive approach for designing simple digital twins and industrial metaverse process frameworks for small manufacturing I5.0 environments using Node-RED. The International Journal of Advanced Manufacturing Technology, 140, 2245–2268. https://doi.org/10.1007/s00170-025-16434-6

Kinnunen, P. (2024). Standardizing excellence: ISO-defined digital twins in industrial applications : Enhancing the management of industrial tools through model-based systems engineering. (Master Student thesis). Retrieved from http://urn.kb.se/resolve?urn=urn:nbn:se:kth:diva-359224

Kulik, T., Kazemi, Z., & Larsen, P. G. (2024). Security and privacy-related issues in a digital twin context. In J. Fitzgerald, C. Gomes, & P. G. Larsen (Eds.), The engineering of digital twins (pp. 313-344). Cham: Springer International Publishing.

Larsen, P. G., Fitzgerald, J., Gomes, C., Woodcock, J., Basagiannis, S., Ulisse, A., . . . Oakes, B. J. (2024). Future directions and challenges. In J. Fitzgerald, C. Gomes, & P. G. Larsen (Eds.), The engineering of digital twins (pp. 363-386). Cham: Springer International Publishing.

Malik, A. A. (2023, December 10-13). Simulation based high fidelity digital twins of manufacturing systems: an application model and industrial use case. [Conference proceeding] 2023 Winter Simulation Conference (WSC), San Antonio, TX, USA.

McCormick, M. R., & Wuest, T. (2025). An evaluation of industrial communication and time-series classification performance for predictive process control digital twins in smart Manufacturing and Industry 4.0. [Unpublished manuscript].

Meyers, B., Noten, J. V., Lietaert, P., Tielemans, B., Hristov, H., Maes, D., & Gadeyne, K. (2022, June 22-24). Knowledge graphs in digital twins for manufacturing-lessons learned from an industrial case at Atlas Copco Airpower. [Conference proceeding] 10th IFAC Conference on Manufacturing Modelling, Manage-

ment and Control (MIM 2022), Nantes, France.

Oakes, B. J., Zhang, H., Hatledal, L. I., Feng, H., Frasheri, M., Sandberg, M., . . . Gomes, C. (2024). Case studies in digital twins. In J. Fitzgerald, C. Gomes, & P. G. Larsen (Eds.), The engineering of digital twins (pp. 257-310). Cham: Springer International Publishing.

Patel, A. K., Patel, A., & Patel, K. M. (2022). An insight to digital twin. In M. Vohra (Ed.), Digital twin technology: Fundamentals and applications (pp. 33-46): Wiley-Scrivener Publishing.

Pierce, C. G. H. F. Z. K. K. (2024). Calibration of models for digital twins. In J. Fitzgerald, C. Gomes, & P. G. Larsen (Eds.), The engineering of digital twins (pp. 129-146). Cham: Springer International Publishing.

Poddar, S., Sanikal, V., Thakare, S., & Sharma, N. (2025). Mechanical engineering integrity in Industry 4.0 & cybersecurity protocols for CAE-based digital twins. International Research Journal of Engineering and Technology (IRJET), 12(3), 918-923.

Rojek, I., Mikołajewski, D., Dostatni, E., Cybulski, J., & Kozielski, M. (2025). Personalization of AI-based digital twins to optimize adaptation in industrial design and manufacturing. Applied Sciences, 15(15), 8525. https://doi.org/10.3390/app15158525

Santos, C. H. d., & Montevechi, J. A. B. (2022). Digital twins architecture. In Z. Lv & E. Fersman (Eds.), Digital twins: Basics and applications (pp. 1-12). Cham: Springer International Publishing.

Scheibmeir, J., & Malaiya, Y. (2022). Social media perspectives on digital twins and the digital twins maturity model. In Z. Lv & E. Fersman (Eds.), Digital twins: Basics and applications (pp. 73-99). Cham: Springer International Publishing.

Sicard, B., Butler, Q., Kosierb, P., Wu, Y., Ziada, Y., & Gadsden, S. A. (2023, September 16-17). IIoDT: Industrial internet of digital twins for hierarchical asset management in manufacturing. [Conference proceeding] 2023 IEEE International Conference on Artificial Intelligence, Blockchain, and Internet of Things (AIBThings), Mount Pleasant, MI, USA.

International Standard Organisation (2021). ISO 23247: Digital twin framework for manufacturing. Retrieved from https://www.iso.org/

Talasila, P., Mikkelsen, P. H., Gil, S., & Larsen, P. G. (2024). Realising digital twins. In J. Fitzgerald, C. Gomes, & P. G. Larsen (Eds.), The engineering of digital twins (pp. 225-256). Cham: Springer International Publishing.

Vohra, M. (2022). Overview of digital twin. In M. Vohra (Ed.), Digital twin technology: Fundamentals and applications (pp. 1-18): Wiley-Scrivener Publishing.

Zhang, L., Zhou, W., & Chen, X. (2022). Digital twins and additive manufacturing. In Z. Lv & E. Fersman (Eds.), Digital twins: Basics and applications (pp. 27-35). Cham: Springer International Publishing.

Chapter 10

SOLAR CHIMNEY SYSTEMS AND THE INVESTIGATION OF EFFICIENCY INCREASE IN A SMALL SYSTEM USING COMPUTATIONAL FLUID DYNAMICS METHODS[1]

Faruk KÖSE[2]

Ousmane DIALLO[3]

1 This publication is derived from master's thesis entitled "An Analysis of a Small-Scale Solar Chimney System Using Computational Fluid Dynamics Methods" conducted by Ousmane Diallo, under the supervisor of Prof. Dr. Faruk KÖSE, Konya Technical University, Institute of Graduate Studies, Department of Mechanical Engineering.

2 Prof. Dr., Konya Technical University, Faculty of Engineering and Natural Sciences, Department of Mechanical Engineering, Konya/Türkiye, Orcid: 0000-0003-2171-9148, fkose@ktun.edu.tr, kosefaruk@gmail.com.

3 Mech. Engineer MSC., Ardi Elektrik San. ve Tic. Ltd. Şti. Şemsipaşa Mah. 17. Sok. No: 15/6 Gaziosmanpaşa/İstanbul, Orcid: 0009-0003-5183-7329, ousmanediallo293@gmail.com, contact@ardielektrik.com.

1. INTRODUCTION

The use of renewable energy sources has become inevitable because of both global population growth and environmental protection goals. Energy demand has increased significantly due to rapidly increasing industrialization. Finding sustainable solutions that do not harm the environment is essential to meet this demand. Prioritizing the use of renewable energy is a globally accepted approach in the face of increasingly serious environmental problems. Due to its low cost and easy accessibility, solar energy production stands out as one of the most common and high-potential methods among renewable energy sources. Generating electricity using solar chimneys is one of the important application areas of renewable energy technologies. A solar chimney power plant consists of a turbine that uses airflow, an air collector that collects solar radiation, and a central chimney that generates electricity from the airflow. The absorption of solar energy by the collector changes the density of the air, initiating a convective flow. The turbine converts this airflow into electrical energy. Solar chimneys are one of the thermal methods that utilize solar energy.

1.1. History of Solar Chimney Systems and Their Applications Worldwide

Theoretically, although the first application of a solar chimney power plant began in the 1980s, the idea was first adopted as a smoke jack by Leonardo Da Vinci between the 1450s and 1500s. However, the Spanish engineer Isidoro Cabanyes was the first to propose generating energy using solar chimneys in 1903. In 1926, Professor Bernard Dubos developed the idea of solar power plants built on a mountainside in North Africa, considering the modern definition of solar chimney systems. Robert Lucier filed a comprehensive patent application in 1975, which was approved in 1981 after researchers reviewed it. In 1982, Jörg Schlaich, along with a German team, built a prototype in Manzanares, Spain, that was 200 m high and had a maximum power output of 50 kW. Numerous solar chimney power plants worldwide have attracted the attention of researchers since the production of the first prototype (Cuce et al., 2022). Below, some solar chimney designs are given in chronological order (1982-2020) in Figure 1.1. In this way, a) a solar chimney designed by Leonardo da Vinci (1452-1519) (Pastohr, 2004), b) a futuristic representation of a solar chimney presented by Günther in 1931 (Gün, 2013), c) and d) solar chimney test facilities established in Manzanares, Spain in 1982-1983 and in Australia in 1997 (Maia et al., 2019), and e) a solar chimney established on the Tehran University campus (Fadaei et al., 2018). f) A photograph of a slanted solar chimney designed and constructed at Konya Technical University (Güzel, 2019) is given. In addition, a solar chimney with a height of 7.92 m, a collector diameter of 9.15 m, and a chimney inlet

diameter of 2.28 m was built in Florida, USA in 1997 (Gün, 2013). Experimental solar chimney prototypes have been established at Isparta Süleyman Demirel University (Koyun, 2006), in Damascus, the capital of Syria (Kalash et al., 2013), and in India (Mokrani et al., 2024). Table 1.1 provides a history of solar chimney systems established up to 2021.

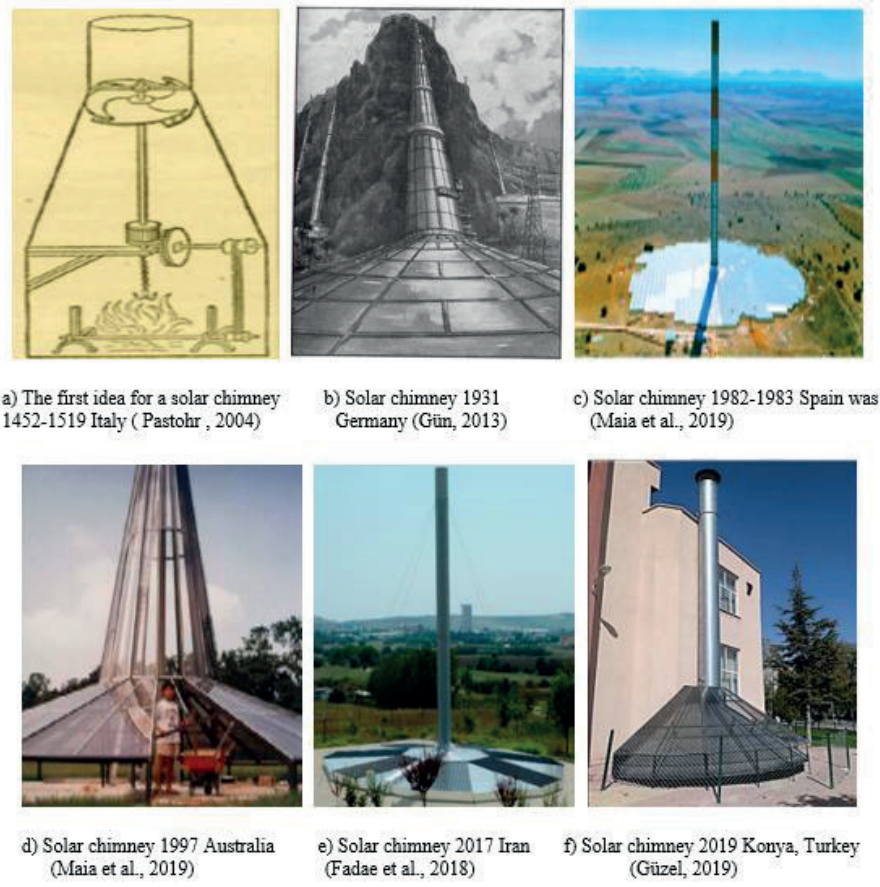

Figure 1.1. Images of solar chimneys in chronological order (a, b, c, d, e, f)

2. LITERATURE REVIEW

Schlaich et al. (2005) studied the theory, economics and storage of solar chimneys. The study presents the results of the design, construction and operation of a 50-kW prototype built in Spain in 1982-1983.

Koyun (2006) completed his doctoral thesis by establishing a solar chimney system with a diameter of 1.2 metres, a height of 15 metres, and a

collector diameter of 16 metres. He also analysed the system using the Ansys Fluent programme.

İçel (2012) established a solar chimney system with a 15-metre-high and 0.8-metre-diameter chimney at Adıyaman University campus and conducted experimental studies related to his thesis.

Padki and Sherif (1999) developed a simple analytical model to make predictions about the production of solar chimney systems, demonstrating that the analytical model's predictions were highly consistent with those of the differentiating model.

Rangel et al. (2016) achieved a power output of 78 kW at a rotational speed of 58 rpm using a turbine with 12 main blades and 18 adjustable blades, in which the output power was adjusted by changing the blade angles in solar chimney systems.

Güzel (2019) conducted experiments for his thesis by installing a solar chimney with a 6.4 m collector in the shape of an inclined semicircle and a chimney height of 8 m at the Faculty of Engineering and Natural Sciences at Konya Technical University.

In his thesis study, Ünal (2019) conducted research on increasing turbine efficiency by setting up a test system with 5-bladed turbines featuring NACA0015, NACA2415, and NACA4415 profiles at 3 different pitch angles in the solar chimney system established at the Mechanical Engineering Department of Konya Technical University. In the study, the highest efficiency was achieved with the NACA 4415 profile at a pitch angle of 40°.

Ayadi et al. (2018) constructed a prototype chimney using solar energy at the Sfax National Engineering School and conducted power enhancement studies with four different turbines with diameters of 90, 120, 140 and 150 mm.

In his thesis study, Büyüklüoğlu (2014) conducted experiments by constructing four different turbine blades with Clark Y, Fx66196v, NACA4415 and NACA23012 profiles to determine the turbine blade profile used in a prototype solar chimney system. The study determined that the Fx66196v profile had the highest CL and CL/CD values.

Kasaeian et al. (2017) presented a basic mathematical model to determine the flow through a solar chimney turbine. They performed a 3D Computational Fluid Dynamics (CFD) simulation of the turbine blades of a Manzanares solar power plant prototype. The CFD simulation was validated

by comparing it with experimental data obtained from the Manzanares solar power plant. Then, a simulation was performed with 12 CFDs showing the effects of turbine rotational speed on the number of turbine blades, collector diameter, and chimney height. The five-bladed turbine showed a maximum output of 91 kW. At 80 rpm, the outlet velocities were 9.5 m/s, 13.7 m/s, and 17.5 m/s at chimney heights of 100 m, 200 m, and 300 m, respectively.

Santos Bernardes (2004) states that solar chimney technology offers significant advantages among alternative systems for using solar energy in electricity production. The losses occurring in a solar chimney system and the approximate amount of electrical energy that can be obtained as a result are shown in Figure 2.1.

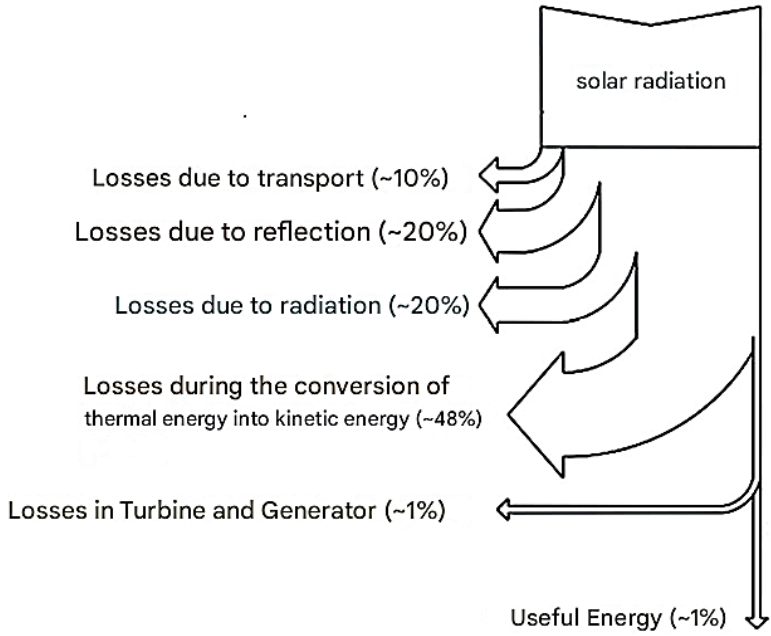

Figure 2.1. Energy flow in solar chimneys (Santos Bernardes, 2004)

3. WORKING PRINCIPLES AND BASIC COMPONENTS OF A SOLAR CHIMNEY SYSTEM

Solar chimneys are thermal systems designed to generate electricity from solar energy. They operate in a manner significantly different from conventional thermal systems. The three fundamental physical aspects of this system are chimney draught, the greenhouse effect, and kinetic energy transfer. Solar radiation heats the air within the collector, creating air movement inside the collector. At the same time, the vertical chimney at the center of the collector discharges the air into the external environment. The turbine and generator located at the inlet section of the chimney are turned by the accelerated air, generating electricity. Figure 3.1 details the operation of the solar chimney (Köse, 2018).

3.1. Basic Components of a Solar Chimney System

A solar chimney system basically consists of the following:

- Collector (glass or covered with permeable foil),
- Chimney,
- One or more turbines,
- Generator

Figure 2.2 shows the general energy conversion steps for a solar chimney

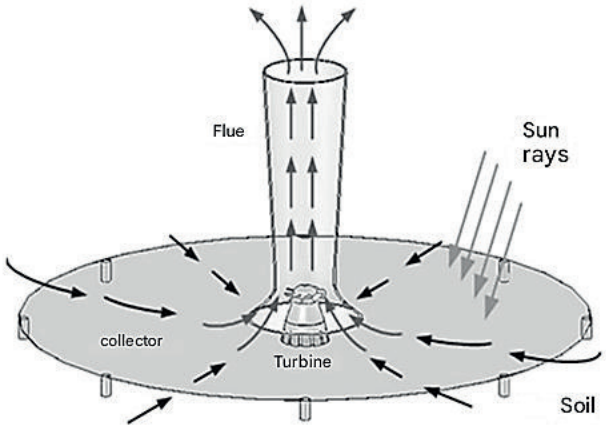

Figure 3.1 Basic working principle of a solar chimney (Köse, 2018)

3.1.1. Collector

The collector is the most important part of the solar chimney and transmits the rays from the sun to the surrounding air. The surface can be covered with glass or foil with high light transmittance. The height from the ground increases towards the chimney, which is the centre of the solar chimney, and is lower in the side inlet area. This prevents the air flow velocity from increasing too much, thereby preventing increased friction loss. At the same time, the air is directed into the chimney with minimal loss. The collector surfaces must transmit sunlight well. The inclined solar chimney collector measured in the study is shown in Figure 3.2.

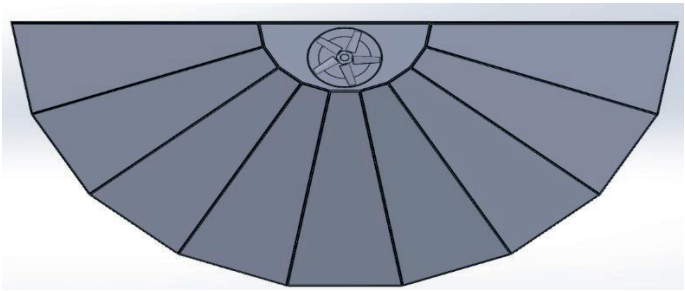

Figure 3.2. Top view of the designed inclined collector

3.1.2. The effect of chimney height on air flow and efficiency

The chimney, the most important part of the system, draws the hot air formed under the collector cover. It works like the pressure pipe of a hydraulic system and has very little friction loss. As the collector temperature rises and the chimney capacity increases, the air temperature and capacity of the collector also rise proportionally. The chimney is one of the most important components of the system. The rise of heated air in the collector is primarily directly related to ΔT (temperature increase) and the volume of the chimney (chimney diameter and height).

Equation 2.1 below is provided for calculating the pressure difference ΔP_{tot} (İçel, 2012).

$$\Delta_{P_{tot}=g.\int_O^H (\rho_a-\rho_{chim.}).dH} \quad [\text{Pa}] \qquad (2.1)$$

g : Gravitational acceleration [m/s^2]

H : Chimney height [m]

ρ_a : Ambient air density [kg/m^3]

$\rho_{chim.}$: Chimney air density [kg/m^3]

The higher the chimney height, the greater the system efficiency and the more energy it produces. The effect of chimney height on electricity generation is shown in Figure 3.3. The chimney converts thermal energy into kinetic energy. Coarse materials such as concrete, aluminium, sheet metal and steel are generally preferred. If the chimney to be constructed is longer than the system capacity, various safety measures must be taken (Ünal, 2019).

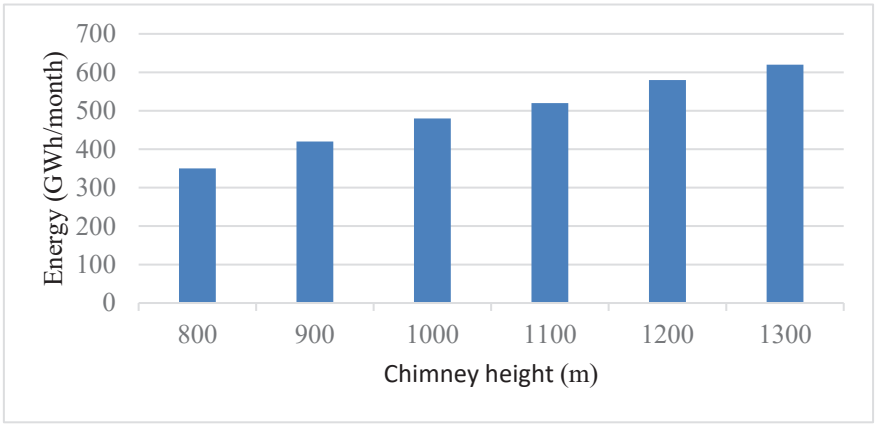

Figure 3.3. Effect of stack height on electricity generation (Gün, 2013)

3.1.3. Working principle of the turbine used in solar chimneys

This system converts kinetic energy into mechanical energy and then into electrical energy. Unlike wind turbines, turbines used in solar chimneys operate on a speed-step basis rather than a pressure-step basis. Compared to velocity-graded turbines, these turbines generate more power per unit rotor surface area. It has been discovered that they can produce approximately ten times more energy than turbines of the same diameter. Figure 3.4 shows how the turbine blades are mounted on the rotor. The turbine is usually located immediately after the collector outlet at the bottom of the chimney. It should

be easily accessible in case of modification or malfunction. Solar chimney turbines can be placed around the collector, at the chimney inlet or outlet in large systems.

Figure 3.4. Solar chimney turbine blades mounted on the rotor (Ünal, 2019)

4. CFD ANALYSIS OF SOLAR CHIMNEY SYSTEM

In this study, a previously designed and tested solar chimney was installed in the Engineering and Natural Sciences Faculty building at Konya Technical University. Theoretical analysis and Computational Fluid Dynamics (CFD) Fluent simulation tests were performed on this solar chimney. Both the theoretical analysis and the CFD simulation were performed using the monthly average data for Konya's meteorological weather conditions for 2024. Irradiance values and ambient temperatures were considered. The theoretical analysis was performed using the average monthly data for air flow velocity at the chimney inlet ranging from 1 m/s to 5 m/s.

4.1. Theoretical Analysis of the Solar Chimney System

Energy balance for a control volume is instantaneous (Çengel et al., 2008).

$$\frac{dE_{CV}}{dt} = \dot{Q} - \dot{W} + \sum_{in} \dot{m}\left(h + \frac{V^2}{2} + gz\right) - \sum_{out} \dot{m}\left(h + \frac{V^2}{2} + gz\right) \quad (4.1)$$

Here;

E_{CV}:: total energy of the control volume (internal + kinetic + potential)

$\dot{Q}$: heat energy [W]

$\dot{W}$: work output [W]

m: mass flow rate, h: specific enthalpy (J/kg), V: velocity (m/s), z: height-dependent potential term.

4.1.1. Theoretical calculations for the solar chimney

This theoretical analysis was based on monthly meteorological data for the province of Konya for the period up to 2024, and the values obtained are presented in Table 4.1 (Anonymous, 2025e). The maximum chimney velocity is calculated using the expression (4.2) obtained using the Boussineq equation in free convection (İçel, 2012).

$$V_{chim,maxs} = \sqrt{2.g.H\frac{\Delta T}{T_{ambient}}} \quad [\mathrm{m/s}] \tag{4.2}$$

In this way;

H (m): Chimney height

ΔT (K): It shows the increase from the ambient temperature to the collector outlet (chimney inlet) temperature.

$T_{ambient}$(K): Ambient temperature

The vacuum effect in the chimney due to density-related ΔP_{total} and the buoyancy force caused by the difference in air density increase as the collector heats up. When the total pressure and chimney gas pressure are equal depending on temperature and density ΔP_{total}, $\Delta P_{presure}$ the following equation (4.2) is given (İçel, 2012).

$$\Delta P_{total} = \rho_{air}.g.H_{chim.}\frac{\Delta T}{T_{ambient}} \tag{4.2}$$

Here, the following are determined: air density ρ_{air}(kg/m² m^3), chimney height $H_{chimney}$ (m), and ambient temperature $T_{ambient}$(K). The air density inside the chimney can be calculated in equation (4.3), and then the collector outlet temperature T_{exit} (K) can be found in the formula of the density equation and is given below.

$$\rho_c = \rho_a - \frac{\Delta P_{total}}{g.H} \qquad [kg/m^3] \qquad (4.3)$$

Here, was calculated according to the ambient temperatures $\rho_c$based on meteorology in the history between 1929-2024. For Konya 2024 monthly average solar radiation and ambient temperature, with collector efficiency at 50%, the calculated flue air flow velocity, temperature and pressure difference for the system, and turbine power values are given in Table 4.1.

Table 4.1. Chimney air flow velocity, temperature and pressure difference, and turbine power values, for collector efficiency 50%, the monthly average solar radiation and ambient temperature in Konya in 2024

Months	I (W/m^2)	$T_{ambient}$ (℃)	Chimney Velocity, V (m/s)	ΔT (K)	$\Delta p_{chim.}$ (Pa)	Turbine power P_t (W)
January	133	1	1.05	2.87	0.94	0.15
February	192	1.5	1.14	3.43	1.24	0.22
March	246	5.6	1.24	4.11	1.44	0.28
April	296	11.1	1.32	4.74	1.60	0.33
May	371	15.9	1.42	5.60	1.83	0.40
June	438	20.2	1.56	6.81	1.94	0.47
July	483	23.6	1.61	7.36	2.05	0.51
August	467	23.4	1.59	7.19	2.01	0.49
September	400	18.8	1.51	6.37	1.84	0.43
October	304	12.9	1.38	5.19	1.57	0.33
November	221	6.5	1.24	4.10	1.29	0.25
December	133	1.8	1.05	2.88	0.94	0.15

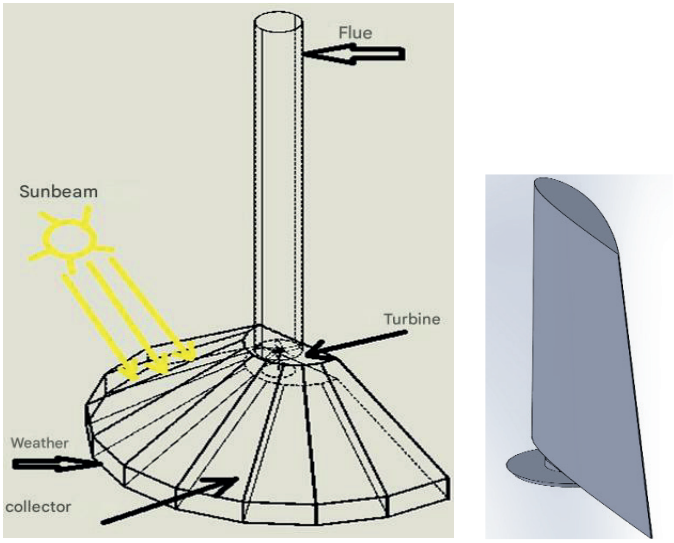

Figure 4.1. A solar chimney designed in SOLIDWORKS and the 3D solid modelling of the NACA4415 turbine blade in Solidworks

The 3D solid modelling of the solar chimney and NACA4415 turbine blade designed in SOLIDWORKS is shown in Figure 4.1. The blade drawing coordinates for the selected blade profile types are transferred to a three-dimensional solid modelling programme. The blade is 25 cm long, with a lower chord of 9.6 cm and an upper chord of 6.72 cm. Each profile type is drawn at a blade angle of 10°. NACA4415 was selected from three different NACA-type blade profiles, and all CFD analysis was performed on NACA4415.

4.2. CFD Method Analysis for Increasing Solar Chimney Efficiency

Computational Fluid Dynamics (CFD) simulation is used in the field of fluid mechanics to solve flow and heat transfer problems in a computer environment. Here, modern techniques are applied for the solution of fluid dynamics equations, preprocessing, and postprocessing. The CFD process is divided into three main groups (Figure 4.2).

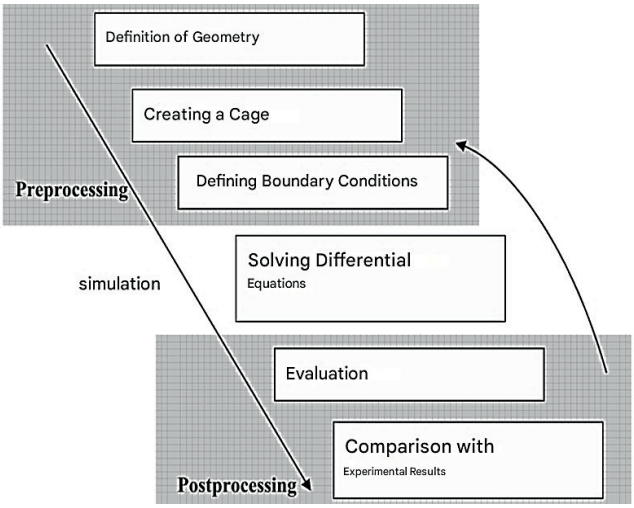

Figure 4.2. General HAD simulation steps (Janicka, 2004)

In the HAD model, the collector surface material was glass and the chimney was aluminium, and their physical properties were entered into the system. The simulation types used were DNS (Direct Numerical Simulation), LES (Large Eddy Simulation) and RANS (Reynolds-averaged Navier-Stokes simulation). In the HAD method used in this study, the RANS-based turbulence model standard k-ε was applied.

4.2.1. Geometry creation and mesh generation method and calculation in ANSYS Chimney

Physical quantities were first included by the HAD programme. Then, the mesh structure was created according to the desired accuracy, and the input and output parameters of the system were defined. Figure 4.3 shows the mesh of the solar chimney. An element size of 0.03 m was used to create the mesh. For the analyses, the mesh was increased by 1,540,197, and the inputs and outputs were determined. An element size of 0.015 m was used to create the mesh. For the analysis, the mesh was increased by 1,607,140, and the inputs and outputs were determined. The air inlets and outlets were determined, and the chimney material was defined as aluminium, the collector top as glass, and the collector bottom as sheet metal.

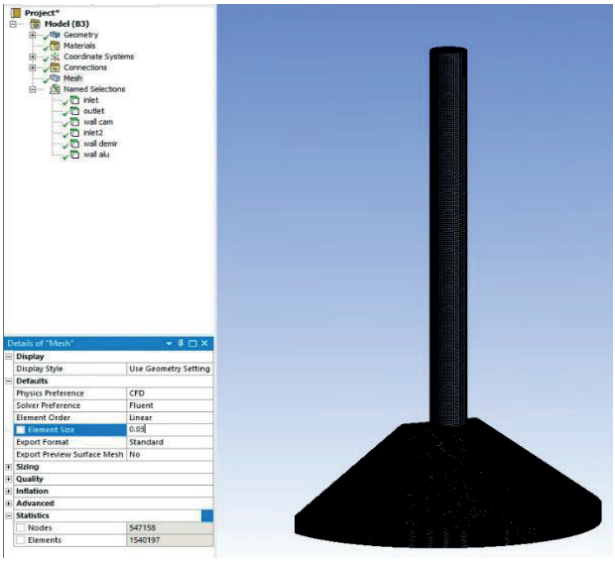

Figure 4.3. Number of meshes created in the solar chimney

4.2.2. Modelling and numerical solution method

The flow in the solar chimney was calculated using the numerical solution of the compressible, stable, symmetric, 2-dimensional Reynolds-averaged Navier-Stokes (RANS) equations. Due to the stable flow, there are no time-dependent terms. In this study, the k- ε turbulence model was used as the standard wall model for turbulence. The aim is to determine that the flow inside the chimney is continuous and how the air density changes. The selection screen related to this process is shown in Figure 4.4 below.

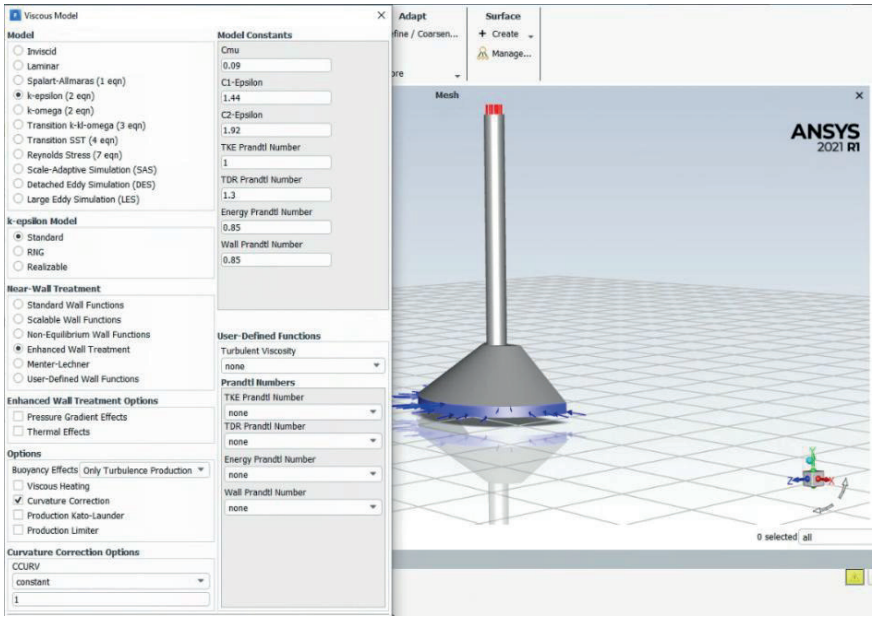

Figure 4.4. k-ε modelling process solution

4.2.3. Definition of border conditions

To start the simulation process, each component of the system must meet the initial conditions. The collector inlet is set to its highest temperature based on the experimental results. The initial values are shown in Table 4.2. Characteristics of the collector (glass) surface and grounding materials is Table 4.3.

Table 4.2. Program start and end conditions

Parameters	Type	Value
Chimney Surface	Wall (Aluminium)	Chimney A = 0.385 $^{m^2}$
Collector Surface (Glass)	Wall (Semi-Transparent)	H = 5.8 $^{W}/_{m^2K}$; A_{koll}=0.385 m ^{2} $C_{p(glass)}$ =750 J/kg.^oC
Collector Inlet	Velocity inlet	$C_{p(air)}$ =1005 J/kg.K ; g= 9.81 m ^{2}/s $V_{baca;gir} = 1m/s - 5\,m/s$

Table 4.3. Characteristics of the collector (glass) surface and grounding materials

Material properties	Collector (Glass) surface
Absorption coefficient	0.004
Transmission coefficient	0.92
Density (kg/ m^3)	ϱ=2500
Specific heat (J/kgK)	750
Thermal conductivity (W/mK)	0.78
Emissivity	0.9

Initially, the standard values for the basic physical properties of the fluid (air) – density 1.14 kg/m³, specific heat capacity 1005 J/kgK, thermal conductivity 0.0242 W/mK, and viscosity 1.789 x 10^{-5} kg/ms – were entered into the Chimney program. The theoretical analysis showed the portion of the airflow velocity at the collector inlet to be entered in the CFD simulation, and k-ε was defined as the solution. The analyses were performed by entering the collector inlet airflow velocity at specific intervals between 0.11 and 0.53.

In the Chimney program, the incident solar radiation on the collector surface is entered as 467 W/m² and the collector thickness as 0.004 m. After model selection, the system starts solving. When the mass flow rate of air entering the collector is equal to the mass flow rate of air exiting, the number of iterations for the analysis is determined. The model solution method is determined, and the analysis begins. After entering the mass flow rates obtained from theoretical calculations using average monthly data into the ANSYS Chimney program, the airflow at the chimney inlet is calculated.

4.3. Theoretical Analyses and HAD Chimney Results

The results of Computational Fluid Dynamics (CFD-Chimney) simulations were compared with theoretical assessments made using long-term meteorological data for Konya until 2024, and a high degree of agreement was shown.

The findings showed that the overall system performance was significantly affected by changes in the air inlet velocity at the opening of the chimney. The airflow behaviour, pressure distribution, and thermal properties within the chimney were investigated in detail for inlet velocities of 1 m/s, 2 m/s, 3 m/s, 4 m/s, and 5 m/s. Although the rate of improvement decreased at higher velocities, both theoretical and ANSYS chimney studies demonstrated

that increasing the inlet velocity improved the system's mass flow rate and energy conversion efficiency.

Considering all factors, combining theoretical and HAD assessments with long-term meteorological data allows us to comprehensively understand how well solar chimneys perform in the Konya climate. This result demonstrates how solar chimneys can be a successful renewable energy source in regions with similar weather conditions. Table 4.4 shows the monthly average solar radiation, ambient pressure, and ambient temperature values for Konya province in 2024 (Anonymous, 2025f).

Table 4.4. Monthly average solar radiation, external air pressure and temperature data for Konya province in 2024.

Months	I (W/ m^2)	P (kPa)	Environment (°C)
January	133	89.9	1
February	192	99.8	1.5
March	246	99.7	5.6
April	296	99.7	11.1
May	371	99.8	15.9
June	438	89.7	20.2
July	483	89.6	23.6
August	467	89.7	23.4
September	400	89.9	18.8
October	304	90.2	12.9
November	221	90.1	6.5
December	133	90	1.8

4.3.1. Results of the theoretical analysis of the solar chimney system.

The three main components of a solar energy system are the collector, the chimney, and the turbine. When sunlight strikes the surface of the collector, the air heats up and temperatures change. As the heated air rises through the chimney, its density decreases, and it is converted into mechanical energy. The turbine converts this energy into electrical energy.

In this study, theoretical calculations were performed using average monthly meteorological data for the year 2024 for Konya province. In the calculations, air flow velocities at the chimney inlet were chosen as 1 m/s, 2 m/s, 3 m/s, 4 m/s, and 5 m/s, respectively, and the collector inlets were calculated as 0.11 m/s, 0.21 m/s, 0.32 m/s, 0.42 m/s, and 0.53 m/s. The

theoretically calculated results are presented below both in tabular and graphical form.

Table 4.5 show how the efficiency of a solar chimney is affected by a combination of temperature difference and airflow velocity inside the collector when the chimney inlet velocity is 1 m/s via solar radiation.

Table 4.5. Monthly average radiation for a chimney inlet air velocity of 1 m/s ΔT_{koll}. collector and system efficiencies

Months	I (W/ m^2)	ΔT_{koll} (K)	Collector efficiency (%)	System efficiency (%)
January	133	0.01	0.11	0.00
February	192	0.01	0.12	0.00
March	246	0.04	0.35	0.01
April	296	0.07	0.57	0.02
May	371	0.10	0.64	0.02
June	438	0.13	0.61	0.02
July	483	0.15	0.63	0.02
August	467	0.15	0.65	0.02
September	400	0.12	0.62	0.02
October	304	0.08	0.57	0.02
November	221	0.04	0.41	0.01
December	133	0.01	0.19	0.01

Table 4.6 show how the efficiency of a solar chimney is affected by a combination of temperature difference and airflow velocity inside the collector when the chimney inlet velocity is 5 m/s via solar radiation.

Table 4.6 . Average monthly radiation for a chimney inlet air velocity of 5 m/s ΔT_{koll}. collector and system efficiencies

Months	I (W/ m^2)	ΔT_{koll} (K)	Collector efficiency (%)	System efficiency (%)
January	133	0.16	13.24	0.38
February	192	0.24	15.25	0.43
March	246	0.89	43.73	1.23
April	296	1.77	70.65	1.94
May	371	2.53	79.48	2.15
June	438	3.22	75.74	2.02
July	483	3.76	79.24	2.09
August	467	3.73	81.40	2.14
September	400	2.99	77.73	2.08

October	304	2.05	71.87	1.96
November	221	1.04	50.90	1.42
December	133	0.29	23.79	0.68

One of the most important variables directly affecting the efficiency of solar chimney systems is chimney height. Since the efficiency of a solar chimney depends on its height, and in this analysis the chimney height is 8 m, the chimney efficiency was calculated as 0.03%. Table 4.7 shows the efficiencies of the solar chimney collector calculated for chimney inlet velocities of 1-5 m/s according to the average monthly meteorological data for Konya in 2024.

Table 4.7. Collector efficiencies calculated for chimney inlet velocities of 1, 2, 3, 4, 5 m/s based on monthly average meteorological data for Konya in 2024

Months	**1 m/s**	**2 m/s**	**3 m/s**	**4 m/s**	**5 m/s**
January	0.11	0.85	2.86	6.78	13.24
February	0.12	0.98	3.29	7.81	15.25
March	0.35	2.80	9.45	22.39	43.73
April	0.57	4.52	15.26	36.17	70.65
May	0.64	5.09	17.17	40.69	79.48
June	0.61	4.85	16.36	38.78	75.74
July	0.63	5.07	17.12	40.57	79.24
August	0.65	5.21	17.58	41.68	81.40
September	0.62	4.97	16.79	39.80	77.73
October	0.57	4.60	15.52	36.80	71.87
November	0.41	3.26	10.99	26.06	50.90
December	0.19	1.52	5.14	12.18	23.79

As shown in Table 4.7, according to the average monthly meteorological data for Konya in 2024, increasing the air velocity at the chimney inlet also increases the air flow velocity in the collector, thus improving the collector's efficiency.

4.3.2. Numerical analysis of a solar chimney system with ANSYS Chimney

In this study, the values obtained from theoretical calculations, such as collector inlet and outlet temperature, collector inlet airflow velocity, mass flow rate, and average monthly solar radiation data, were entered into the ANSYS chimney program to calculate the airflow velocity in the chimney.

In this study, theoretical calculations were performed using monthly average meteorological data for Konya province in 2024. In the ANSYS chimney analysis, after entering the air flow velocities at the chimney inlet to the collector as 0.11 m/s, 0.21 m/s, 0.32 m/s, 0.42 m/s and 0.53 m/s respectively, the chimney inlet velocities were calculated as 0.10 m/s, 0.20 m/s, 0.30 m/s, 0.40 m/s and 0.50 m/s respectively. Figure 4.5 shows the temperature behaviour inside the collector and the contours of the inlet temperature and the maximum outlet temperature.

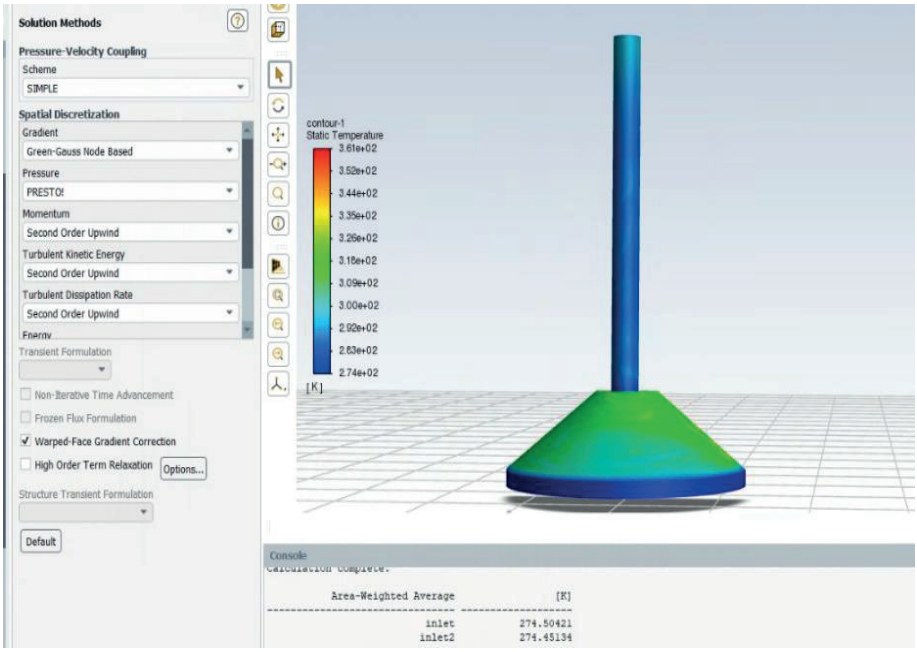

Figure 4.5. Temperature contour formed inside the solar chimney at the collector inlet of 0.11 m/s

The theoretically calculated results are presented below both in tabular and graphical form. Table 4.8 show how the efficiency of the solar chimney is affected by a combination of temperature difference and air flow velocity inside the collector when the solar radiation enters the collector at a velocity of 0.11 m/s.

Table 4.8. Collector and system efficiencies found in Ansys Chimney analysis for Konya meteorological average monthly solar radiation inlet of 0.11 m/s in 2024.ΔT_{coll} ile

Months	I (W/ m^2)	ΔT_{koll} (K)	Collector efficiency (%)	System efficiency (%)
Fireplace	133	0.01	0.09	0.00
February	192	0.01	0.10	0.00
March	246	0.03	0.30	0.01
April	296	0.06	0.48	0.01
May	371	0.09	0.53	0.01
June	438	0.11	0.51	0.01
July	483	0.14	0.56	0.01
August	467	0.14	0.58	0.02
September	400	0.11	0.52	0.01
October	304	0.07	0.48	0.01
November	221	0.04	0.34	0.01
December	133	0.01	0.16	0.00

Table 4.9 shows how the efficiency of a solar chimney is affected by a combination of temperature difference and air flow velocity inside the collector when the solar radiation enters the collector at a velocity of 0.53 m/s.

Table 4.9. Collector and system efficiencies found in Ansys Chimney analysis for Konya meteorological average solar radiation inlet at 0.53 m/s in 2024.ΔT_{koll} ile

Months	I (W/ m^2)	ΔT_{koll} (K)	Collector efficiency (%)	System efficiency (%)
January	133	0.14	11.17	0.32
February	192	0.21	13.00	0.37
March	246	0.80	37.34	1.05
April	296	1.59	60.05	1.65
May	371	2.29	68.31	1.85
June	438	2.86	63.35	1.69
July	483	3.40	68.10	1.79
August	467	3.37	69.96	1.84
September	400	2.71	66.94	1.79
October	304	1.85	61.19	1.67
November	221	0.93	43.42	1.21
December	133	0.26	20.34	0.58

In this study, using monthly average meteorological data for Konya province for the year 2024, the collector inlet velocities obtained in theoretical calculations for solar chimneys, ranging from a minimum of 0.11 m/s to a maximum of 0.53 m/s, were analysed using Ansys Chimney analysis, and the data presented in Table 4.10 below are given.

Table 4.10 for collector inlet velocity of 0.11 m/s $V_{chim,inl}$ and $\dot{m}$ Columns 3 and 4 are designed for a collector inlet velocity of 0.53 m/s. $V_{bchim,inl}$ and $\dot{m}$ Columns 5 and 6 show monthly average data

Months	I (W/ m^2)	$V_{chim,inl}$ (m/s)	$\dot{m}$ (kg/s)	$V_{chim,inl}$ (m/s)	$\dot{m}$ (kg/s)
January	133	0.95	0.42	4.75	2.09
February	192	0.95	0.46	4.72	2.30
March	246	0.94	0.45	4.72	2.27
April	296	0.95	0.45	4.74	2.23
May	371	0.94	0.44	4.75	2.20
June	438	0.94	0.39	4.71	1.93
July	483	0.96	0.39	4.75	1.93
August	467	0.96	0.39	4.75	1.93
September	400	0.94	0.39	4.76	1.97
October	304	0.94	0.40	4.74	2.01
November	221	0.94	0.41	4.74	2.05
December	133	0.95	0.42	4.75	2.08

This study theoretically and numerically (HAD–Chimney) analyses a solar chimney system using average monthly meteorological data for Konya in 2024.

- HAD simulations and theoretical analyses have generally shown agreement with each other.
- Increasing the airflow velocity (1–5 m/s) increased the mass flow rate and energy conversion efficiency at the chimney inlet. However, the rate of increase decreased as the speed increased.
- HAD simulations show the temperature and velocity distributions in the chimney in detail, and these analyses have yielded results very close to theoretical calculations.
- As a general conclusion of this thesis, it has been determined that solar chimney-based electricity generation systems are suitable for the meteorological values and climate of Konya, and the results obtained are consistent with other similar studies in literature.

In this study, using the average monthly meteorological data for May 2024, the highest collector efficiency was obtained at 68.3% and the system efficiency at 1.85% when the collector inlet velocity was 0.53 m/s. The findings are consistent with studies in literature.

REFERENCES

Anonymous, 2025e, https://en.tutiempo.net/ultraviolet-index/selcuklu.html .

Anonymous, 2025f, https://www.mgm.gov.tr/veridegerlendirme/il-ve-ilceler-istatistik.aspx?m=KONYA .

Arslan, T., 2011, Electricity generation under laboratory conditions using a solar chimney: Model study, *Institute of Science* .

Atit, K., 2009, Analysis of flow in solar chimney for an optimal design purpose.

Ayadi, A., Driss, Z., Bouabidi, A. and Abid, MS, 2018, Effect of the turbine diameter on the generated power of a solar chimney power plant, *Energy & Environment* , 29 (5), 822-836.

Balijepalli, R., Chandramohan, V. and Kirankumar, K., 2017, Performance parameter evaluation, materials selection, solar radiation with energy losses, energy storage and turbine design procedure for a pilot scale solar updraft tower, *Energy Conversion and Management* , 150, 451-462.

Buyukluoğlu, Ö. F., 2014, Investigation of optimum turbine blade profile by using CFD method to increase the efficiency of a solar chimney prototype.

Çalışkan, M., 2014, Axial flow fan design, *Institute of Science* .

Cao, F., Li, H., Zhao, L., Bao, T. and Guo, L., 2013, Design and simulation of the solar chimney power plants with TRNSYS, *Solar Energy* , 98, 23-33.

Çengel, YA, Cimbala, JM and Engin, T., 2008, Fluid mechanics: fundamentals and applications, Güven Kitabevi, p.

Cuce, E., Cuce, PM, Carlucci, S., Sen, H., Sudhakar, K., Hasanuzzaman, M. and Daneshazarian, R., 2022, Solar chimney power plants: a review of the concepts, designs and performances, *Sustainability* , 14 (3), 1450.

Fadaei, N., Kasaeian, A., Akbarzadeh, A. and Hashemabadi, SH, 2018, Experimental investigation of solar chimney with phase change material (PCM), *Renewable energy* , 123, 26-35.

Chimneynt, 2003, CHİMNEYNT 6.1 User's Guide, Vol. 1-2-3. .

Fluri, TP and von Backström, TW, 2008, Comparison of modeling approaches and layouts for solar chimney turbines, *Solar Energy* , 82 (3), 239-246.

Gannon, AJ and von Backström, TW, 2003, Solar chimney turbine performance, *J. Sol. Energy Eng.* , 125 (1), 101-106.

Gün, AR, 2013, Analysis and evaluation of the feasibility of horizontal solar chimney systems, *Institute of Science* .

Güzel, MH, 2019, Design, installation and testing of a micro solar chimney power system with inclined collectors, *Graduate Education Institute* , *Konya Technical University, Konya* .

Haaf, W., Friedrich, K., Mayr, G. and Schlaich, J., 1983, Solar chimneys part I: principle and construction of the pilot plant in Manzanares, *International Journal of solar energy* , 2 (1), 3-20.

İçel, Y., 2012, Investigation of electricity generation efficiency from solar chimney energy systems with different fin diameter models, *Institute of Science* .

Janicka, J., 2004, Ein Program zur Beschreibung technischer und reaktiver Strömungen, Technische Universität Darmstadt, 25 p.

Kalash, S., Naimeh, W. and Ajib, S., 2013, Experimental investigation of the solar collector temperature field of a sloped solar updraft power plant prototype, *Solar Energy* , 98, 70-77.

Kasaeian, A., Mahmoudi, AR, Astaraei, FR and Hejab, A., 2017, 3D simulation of solar chimney power plant considering turbine blades, *Energy Conversion and Management* , 147, 55-65.

Köse, F., 2018, Comparison of Solar Chimney Power Systems with PV and Wind Power Systems, *Academic Platform-Journal of Engineering and Science* , 6 (3), 121-129.

Koyun, A., 2006, Investigation of energy production with solar chimneys. SDÜ, *Institute of Science, PhD Thesis, 142 pages, Isparta* .

Maia, CB, Silva, FV, Oliveira, VL and Kazmerski, LL, 2019, An overview of the use of solar chimneys for desalination, *Solar Energy* , 183, 83-95.

Mokrani, OBEK, Ouahrani, MR, Sellami, MH and Segni, L., 2024, Experimental investigations of hybrid: geothermal water/solar chimney power plant, *Energy Sources, Part A: Recovery, Utilization, and Environmental Effects* , 46 (1), 15474-15491.

Padki, M. and Sherif, S., 1999, On a simple analytical model for solar chimneys, *International journal of energy research* , 23 (4), 345-349.

Pastohr, H., 2004, Thermodynamische Modellierung eines Aufwindkraftwerkes, *Dissertation, Weimar, Bauhaus-Universität Weimar, 2004* .

Rangel, LP, Contessi, BA, Copes, TA, Alberto, P. and Ropelato, K., 2016, Advances in solar chimney turbine modeling, *Mecánica Computacional* , 34 (14), 897-915.

Santos Bernardes, MA d., 2004, Technische, ökonomische und ökologische Analyse von Aufwindkraftwerken, *Zugl.: Stuttgart, Univ., Diss., 2004* .

Schlaich, J. r., Bergermann, R., Schiel, W. and Weinrebe, G., 2005, Design of commercial solar updraft tower systems—utilization of solar induced convective flows for power generation, *J. Sol. Energy Eng.* , 127 (1), 117-124.

Tan, F. and Dede, AE, 2024, The impact of turbulence models and design parameters on solar chimney power plant efficiency: A CFD study, *International Journal of Energy Studies* , 9 (3), 399-422.

Üçgül, İ. and Koyun, A., 2010, Experimental investigation of solar chimney design parameters and performance, *Pamukkale University Journal of Engineering Sciences* , 16 (3), 255-264.

Ünal, RE, 2019, Turbine design, fabrication and testing for a micro solar chimney, *Graduate Education Institute* , Konya Technical University, Konya.

Chapter 11

INVESTIGATION OF THE EFFECT OF PCM LAYERED WALL POSITION ON INDOOR THERMAL CONDITIONS

Başak METİN[1]
Halil BAYRAM[2]

1 Master's Student Başak Metin, Mechanical Engineering Department, Graduate School of Natural and Applied Sciences, ORCID: 0009-0006-5423-7515
2 Assoc. Prof. Dr. Halil Bayram, Amasya University, Engineering Faculty, Mechanical Engineering Department, ORCID: 0000-0002-4664-3883

INTRODUCTION

Phase change materials (PCM) are materials that store a large amount of heat during phase change and release the stored energy when needed. They are frequently used in energy systems. PCMs should be selected considering the thermophysical properties of the system and material, cost, applicability, and availability. These materials are divided into two categories in some building applications: active systems and passive systems (Zare & Mikkonen, 2023). A test room with two windows has been built to examine the thermal performance of the ceiling panels, due to the innovative approach of the S23 salt hydrate, which has a melting point of 23°C, for passive thermal energy storage systems. The test room is constructed with brick walls and a ceiling thickness of 15 cm, with a total of 15 cm coated with plaster and paint. A plastic encapsulation method was used to prevent the abrasive effect of the PCM-containing panel. With the integration of the panels, phase separation was observed despite the reduction in heating and cooling loads. To prevent this, it was recommended to reduce the panel sizes and select climate conditions compatible with the thermophysical properties of PCM (Velasco-Carrasco et al., 2020). Applications that provide energy efficiency in buildings are developing worldwide. An original wall structure integrated with a night sky radiator and PCM has been proposed. By utilizing the latent heat storage feature of PCM, active and regular heat control is achieved to save energy. In a comparative study conducted with and without PCM integration, it was found that the innovative system reduced the average temperature on the inner surface by 1.6°C compared to the traditional system, with decreases in cooling load ranging from 37.8% to 57.8%, and reductions in energy consumption ranging from 15.7% to 24.1% (Yan et al., 2020). Although lightweight buildings have advantages such as modularity, easy portability, and cost-effectiveness, their low thermal mass is one of the biggest problems. They cannot maintain indoor thermal comfort over long periods. In such cases, PCMs have different application techniques for areas like floors, ceilings, walls, windows, flooring, bricks, plaster, etc., and for building materials (Marín et al., 2016). A study conducted in 2024 concluded that when an PCM insulation layer is placed in the middle of the lightweight building envelope, it reduces the amplitude of thermal fluctuations by a factor of 2-13 when 4% paraffin is used volumetrically in a 100 mm polyurethane foam wall (Nizovtsev & Sterlyagov, 2024). When examining the thermal behavior of the integrated new system consisting of a capsule-encased PCM wall placed inside a pipe and a night sky emitter, it has been shown that the design results

in a decrease of 0.4–0.7 °C in the internal surface temperature, a reduction of up to 53% in the internal surface heat flux, and a 16.1% decrease in cooling energy demand. As a result, it has been considered an effective design for low-energy building applications (Yan et al., 2021).

The effects of lightweight coating panels containing PCM on building energy efficiency and thermal comfort, compared to cement plaster, have been examined through numerical simulations and validated with experimental data. It has been shown that panel thickness and phase transition temperature are decisive factors influencing system performance. The optimal condition provided up to a 25.1% reduction in cooling load with a thickness of 3.0 cm and a phase transition temperature of 29°C. Additionally, the application of optimal lightweight coating panels reduces the annual thermal discomfort duration by up to 6% in non-conditioned buildings, while decreasing annual cooling energy by 22.1% to 50.3% and reducing CO_2 emissions by up to 63.5% in conditioned buildings. It has been concluded that coating panels offer an effective solution for sustainable building design (Al-Absi et al., 2025). PCMs are very effective in preventing sudden temperature fluctuations indoors and ensuring thermal comfort. The heat transfer of PCM-integrated concrete has been numerically studied and modeled. PCM, which is found in walls and roofs, has a melting temperature of 21°C and a thickness of 10 mm, and has provided the most efficient results (Mohseni & Tang, 2021).

A polymer-paraffin-based PCM that prevents leakage has been integrated into hollow floor elements. To increase the effectiveness of the PCM, it was placed in a ring shape inside a panel with cylindrical voids. It was found that when the PCM fill rate is 50% or higher, the amplitude of temperature fluctuations on the opposite surface decreases to one-third. Additionally, to define the effective amount of PCM in hidden heat storage, a new performance indicator called PCM activity was proposed, and it was determined that the optimal fill rate is 50% (Royon et al., 2014). In space systems, the intense power consumption of electronic components can lead to overheating and performance issues. Oscillating heat pipes can increase heat transfer rates and transfer heat like a radiator panel, but their thermal capacities are limited. A hybrid radiator panel created by integrating PCMs into oscillating heat pipes has been examined. For the system, the effects of PCM types such as octadecane, gallium, and octadecane-aluminum composite (volumetric ratio of 90% octadecane, 10% aluminum) at power levels of 1 kW, 3 kW, and 10 kW, with PCM thicknesses ranging from 0.001 to 0.01 meters, on transient

temperature rise have been investigated. It has been supported that it can be effectively used through design volume-mass optimization (Shrestha, 2022). A storage unit containing 9 and 13 kg of stearic acid was placed in a panel radiator suitable for operating conditions of 75/65 °C, and its charge-discharge behavior was evaluated. The standard thermal output of panel radiators with storage units was more limited compared to traditional panel radiators. According to energy efficiency results, 9 kg of stearic acid proved to be more efficient in the panel radiator (Erkek & Güngör, 2013). A life cycle assessment was conducted for three cabins in a building constructed in Spain. The climate control of the cabin areas was managed with a heat pump and electric radiator. The study analyzed whether the energy consumptions for the cabins and the energy savings during the operation phase of PCM-produced components were balanced. It has been demonstrated that SP-25 A8 salt hydrate shows approximately 75% lower production impact compared to RT-27 paraffin, thereby reducing the global impact and increasing the benefits of PCM usage (De Gracia et al., 2010). The effects of different cities on the thickness (1, 2, 3, 4, 6, and 8 cm), the position within the wall (outer side, inner side, and middle), and the internal wall temperature of PCM types (RT-27, RT-31, RT-42, RT-35HC, RT-44HC, and lauric acid) were compared under Aswan climate conditions in Egypt during the summer season. ANSYS 2020 R1 simulation was used for two-dimensional thermal analysis. Among the PCMs examined, RT-35HC has the highest thermal performance, and the optimal PCM position was chosen to be 1.5 cm from both the interior and exterior of the wall (Anter et al., 2023).

MATERIALS AND METHODS

In this study, a room measuring 2.5 × 3 × 3.5 meters, heated by a panel radiator (0.6 × 1 meter), was modeled and used in three-dimensional, transient CFD analyses. The effect of a 10 mm-thick modeled PCM layer, whose thermophysical properties are given in Table 1, on indoor temperature distributions was examined for different room walls. Additionally, the effect of PCM usage was analyzed under the same conditions without PCM (Case 0).

Table 1. The Thermophysical Properties of The Model

Material	Phase-transition temperature [°C]	Phase change latent heat [kj/kg]	Thermal conductivity [W/(mK)]	Specific heat [J/(kgK)]	Density [kg/m^3]
PCM	20-22	200	0.2	2000	800
Air	-	-	0.0242	1006.43	1.225
Glass wool	-	-	0.035	1220	40
Gypsum board	-	-	0.33	1050	1050

The room used in the numerical study is subject to boundary conditions that place it on the top floor at the corner of a building. The room layout is schematically shown in Figure 1.

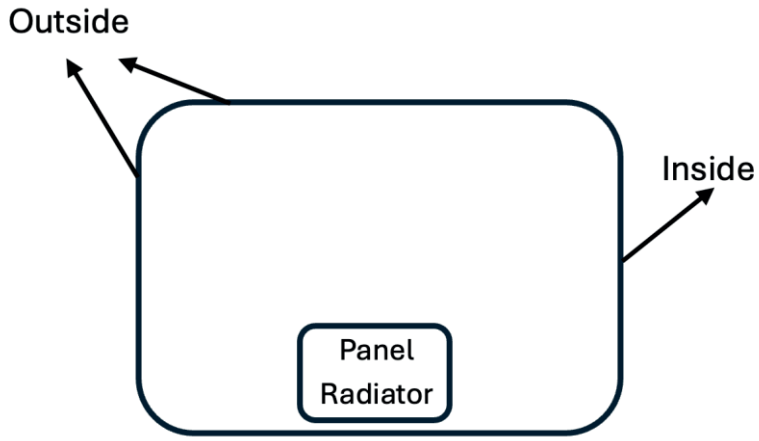

Figure 1. Schematic view of the modelled room

Three walls have been equipped with PCM layers, and an attempt has been made to determine the most suitable placement of these layers. The outdoor environment has been maintained at 4°C throughout all analyses. The indoor environment has been kept constant at 14 °C. Wall 1 (Case 1) and Wall 2 (Case 2) are in direct contact with the outdoor environment.

In the model developed for CFD analyses, the layers outside the room are, in order, gypsum board, PCM, and glass wool. The thicknesses of the gypsum board and glass wool layers are selected as 5 mm and 30 mm, respectively.

The thermophysical properties of these materials are detailed in Table 1. The solid model view created for Case 2 is shown in Figure 2.

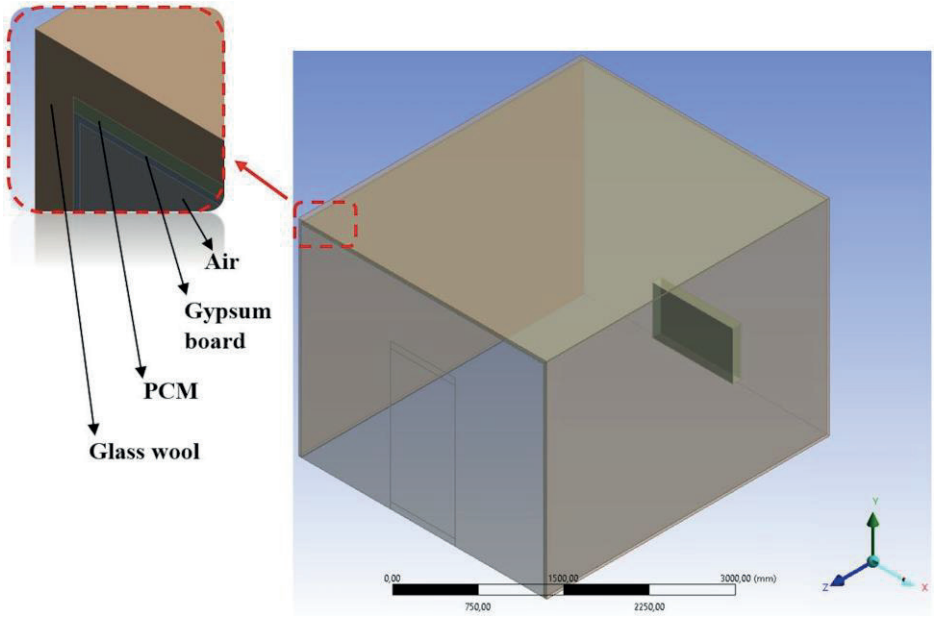

Figure 2. The view of the CAD model (Case 2)

In the CFD model, the floor, the wall on which the panel radiator is located, and the wall directly opposite the door are treated as adiabatic to isolate the effect of the PCM-layered wall. A heat-transfer coefficient of 1 W/(m^2K) has been assigned to Walls 1 and 2, which are in contact with the external environment. The solidification and melting model has been activated for the phase change of PCM. For Wall 3, a heat-transfer coefficient of 1 W/(m^2K) has been specified, accounting for its interaction with the indoor environment. The iterations at each time step continued until the residuals of the continuity and momentum equations were below 10^{-4} and the residual of the energy equation was below 10^{-8}.

The numerical studies were conducted using the ANSYS-Fluent software package. The analyses were performed for approximately two hours under constant external ambient temperature conditions. The total number of mesh elements in the created models is approximately 1 million. The mesh structure of the case without PCM, which is referred to as the reference study, is shown in Figure 3.

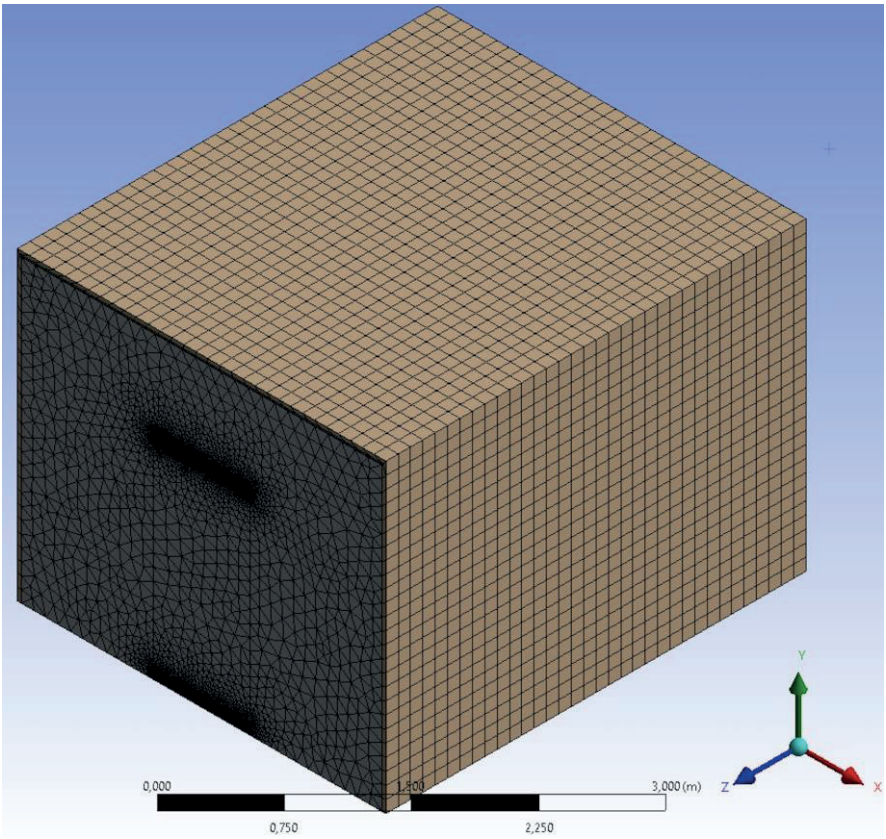

Figure 3. Isometric View of The Mesh Structure

RESULTS AND DISCUSSIONS

In this study, the effects of PCM application in LBW wall buildings, which exhibit greater indoor temperature variations due to their lower thermal mass than conventional brick wall buildings, were numerically examined. The effects of a 10 mm-thick PCM layer applied to different wall regions of the room in the numerical model on indoor temperature variations were examined. Using the results from the numerical study, changes in the average indoor temperature, the distribution of indoor temperature and velocity, and the liquid-fraction rate of the PCM layer were determined.

Figure 4 shows the temperature distributions on the cross-section taken from the center of the room at different time steps. Overall, it can be observed that the temperature distributions are quite similar at all examined time steps, both when the PCM is placed on the ceiling (Case 1) and when the PCM is placed

on the right wall of the room (Case 2). Additionally, in both cases, the heat from the panel radiator rose to the ceiling area of the room due to natural convection, and then moved toward the door area, which has a lower temperature. As the air cooled, it directed downward. However, when looking at the values taken in this section, the temperature values in Case 1 are more fluctuating and lower compared to the other case. Especially in the ceiling area, due to the PCM layer absorbing heat, lower temperature values were observed near the floor of the room. In Case 2, these fluctuations are almost nonexistent. The reason for this is that the PCM layer is placed on the right wall of the room, and in this case, lower temperature values are observed near the left wall of the room.

Time [minute]	Case 1	Case 2
		
30		
60		
90		

120	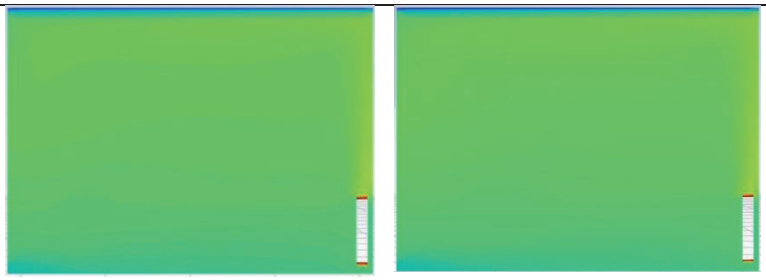

Figure 4. The temperature distribution on the cross-section of the room

When examining the velocity distributions obtained from the analyses, it was observed that the distributions formed during the first 30 minutes did not change significantly in subsequent stages (Figure 5). An airflow of approximately 0.21 m/s, originating from natural convection through the panel radiator toward the room door, is observed in both cases. In Case 1, where PCM is added to the ceiling area, higher-velocity regions are observed in the central regions of the room. The air velocities in these regions were approximately 0.1 m/s. In Case 2, where the PCM layer is integrated into the right wall, lower velocities were observed in the middle of the room due to heat trapping within the wall. The highest velocity value in the vortex region formed in the middle of the room is around 0.07 m/s. Additionally, although the velocity distributions changed little over time in Case 1, the values gradually increased until the end of the analysis in Case 2.

Time [minute]	**Case 1**	**Case 2**
30	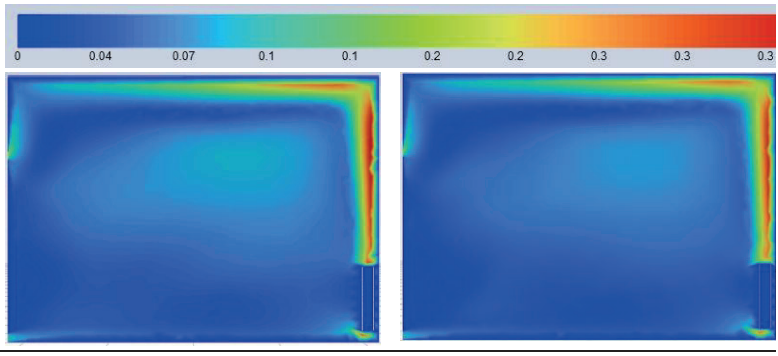	

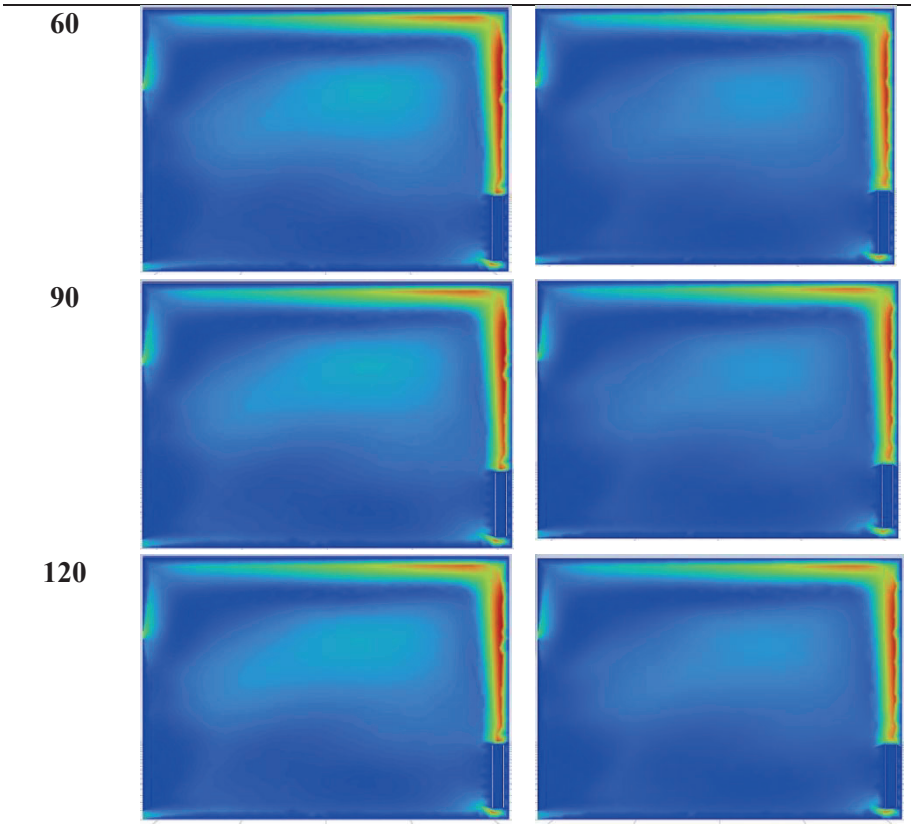

Figure 5. The velocity distribution on the cross-section of the room

The average indoor air temperature values used in the analyses were obtained at different time steps for both cases containing PCM and the reference case without PCM (Table 2). The temperature values in Case 0, which is the case without PCM, were higher by 1.87°C to 3.07°C compared to the temperature values in Case 1, and by 1.25°C to 2.13°C compared to those in Case 2. These temperature differences are due to the complete transfer of heat from the panel radiator into the indoor environment. In other cases, a portion of the heat from the heat source has been absorbed by the PCM. Additionally, when examining the liquid fraction values of the PCM layer (Table 3), the melting rate of the phase-changing material has increased over time. In Case 1, only about 3% of the PCM layer melted during the first 30 minutes. In Case 2, this value remained only around 1%. One hour after the analysis began, it was observed that a 10% PCM layer had melted in Case 1. When the PCM layer is on the right wall, only about 4% of it is melted. During the 90th and 120th minutes of the analysis, while the PCM layer was at its peak, approximately 16% and

27% of it had melted, respectively. The rising hot air from the natural convection significantly contributed to the melting of the PCM layer in the ceiling area. However, when the heated air moved in a parallel manner rather than directly, only about 15% melting was achieved even after two hours.

The indoor air temperature increased in both Case 1 and Case 2, but relatively small increases in temperature were observed due to the rise in the melting rate of the PCM layer. The reason for both the increase in the melting rate of the PCM and the relatively low increase in room temperature over time is thought to be due to the gypsum board layer between the room and the PCM layer, which also stores some heat, as well as the heat absorption occurring in the unheated areas of the room.

Table 2. Average temperature values of the air volume of the room

Time [minute]	Temperature [°C]		
	No PCM	Tavan	Right wall
30	18.94	17.07	17.69
60	19.51	17.15	17.98
90	20.32	17.25	18.19
120	20.36	17.32	18.37

Table 3. Liquid fraction ratios of the PCM layer

Time [minute]	Liquid fraction ratio [-]		
	No PCM	Tavan	Right wall
30	-	0.03	0.01
60	-	0.10	0.04
90	-	0.16	0.08
120	-	0.27	0.15

CONCLUSIONS

In this study, the effects of adding PCM layers to various building walls, which are increasingly used due to their advantages, were numerically examined. Within this scope, a 10 mm-thick PCM layer was added to the ceiling and the right wall of the room that interacts with the external environment. Under the same boundary conditions, both the effects of PCM use and the impact of the PCM layer's placement were investigated. In Case 2, the temperature distribution varies between 17.7°C and 18.4°C. It can be

observed that the temperature distributions at all time steps examined are similar in both cases: when the PCM is mounted on the ceiling (Case 1) and when the PCM is placed on the right wall of the room. Additionally, in both cases, heat from the panel radiator rises toward the room ceiling due to natural convection, then moves toward the door area, which has a lower temperature. As the air cools, it flows downward. It was observed that the PCM layer in the ceiling absorbs heat, resulting in lower temperatures near the floor of the room.

In Case 0, the average indoor air temperature ranged from approximately 19°C to 20.5°C. In Case 1, these values varied minimally, ranging from approximately 17°C to 17.3°C. Among the liquid fraction values, the case with greater melting (Case 1) exhibited lower indoor temperatures. Given that our goal is for the PCM layer to absorb heat from the heat source and subsequently release it, the ceiling area is more effective. In Case 1, at the end of the analysis, 27% of the PCM layer had melted, and the average indoor air temperature was measured at 17.32°C. In the absence of PCM, the average indoor air temperature at the end of the analysis was approximately 3°C higher. However, in Case 2, the PCM layer trapped relatively little heat, and only 15% of it had melted by the end of the analysis. The indoor air temperature of the room was observed to be relatively lower by 2°C compared to the situation without PCM. When these results are examined, it is concluded that the preferred placement of the PCM layer within the room is more suitable on the ceiling area rather than on the side walls. However, it should also be taken into account that the thickness of the PCM layer must be appropriately selected, considering the heat input durations, so that the entire PCM can melt during the day and then release the stored heat afterward. In future studies, it is planned to investigate the effects of placing the PCM layer on the ceiling, which increases the heat transfer surface area, versus placing it on the wall.

REFERENCES

Al-Absi, Z. A., Asif, M., & Hafizal, M. I. M. (2025). Numerical investigation and parametric analysis of PCM-based lightweight panels for wall's exterior cladding. *Case Studies in Thermal Engineering, 65*, 105654.

Anter, A. G., Sultan, A. A., Hegazi, A. A., & El Bouz, M. A. (2023). Thermal performance and energy saving using phase change materials (PCM) integrated in building walls. *Journal of Energy Storage, 67*, 107568.

De Gracia, A., Rincón, L., Castell, A., Jiménez, M., Boer, D., Medrano, M., & Cabeza, L. F. (2010). Life cycle assessment of the inclusion of phase change materials (PCM) in experimental buildings. *Energy and Buildings, 42*(9), 1517–1523.

Erkek, T. Ü., & Güngör, A. (2013). Experimental performance evaluation of PCM thermal storage in a panel radiator.

Marín, P. E., Saffari, M., de Gracia, A., Zhu, X., Farid, M., Cabeza, L. F., & Ushak, S. (2016). Energy savings due to the use of PCM for relocatable lightweight buildings passive heating and cooling in different weather conditions. *Energy and Buildings*. https://doi.org/10.1016/j.enbuild.2016.08.007

Mohseni, E., & Tang, W. (2021). Parametric analysis and optimisation of energy efficiency of a lightweight building integrated with different configurations and types of PCM. *Renewable Energy*. https://doi.org/10.1016/j.renene.2020.12.112

Nizovtsev, M. I., & Sterlyagov, A. N. (2024). Effect of phase change material (PCM) on thermal inertia of walls in lightweight buildings. *Journal of Building Engineering, 82*, 107912.

Royon, L., Karim, L., & Bontemps, A. (2014). Optimization of PCM embedded in a floor panel developed for thermal management of the lightweight envelope of buildings. *Energy and Buildings, 82*, 385–390.

Shrestha, A. (2022). *Numerical simulation and design of hybrid oscillating heat pipe–phase change materials for radiator panel* (Doctoral dissertation).

Velasco-Carrasco, M., Chen, Z., Aguilar-Santana, J. L., & Riffat, S. (2020). Experimental evaluation of thermal energy storage (TES) with phase change materials (PCM) for ceiling tile applications. *Future Cities and Environment, 6*.

Yan, T., Gao, J., Luo, Y., & Yu, J. (2020). Performance evaluation of a PCM-embedded wall integrated with a nocturnal sky radiator. *Energy, 210*, 118412.

Yan, T., Li, J., Gao, J., Xu, X., & Yu, J. (2021). Model validation and application of the coupled system of pipe-encapsulated PCM wall and nocturnal sky radiator. *Applied Thermal Engineering, 194*, 117057.

Zare, M., & Mikkonen, K. S. (2023). Phase change materials for life science applications. *Advanced Functional Materials, 33*(12), 2213455.

Chapter 13

SHAPE MEMORY POLYMER COMPOSITES

Sakine KIRATLI[1]

1 Asst.Prof.Dr. Çankırı Karatekin University, Engineering of Faculty, Department of Mechanical Engineering, Çankırı, Türkiye
ORCID ID: 0000-0001-6292-5605

1. Introduction

The materials sector continues to develop rapidly in today's world. While traditional metal materials remain indispensable in many areas, composites have spread across a wide range of applications. Composite materials are primarily notable for their high rigidity, high strength, and lightness. Various types of composite materials are designed to meet different requirements depending on their application. In this context, shape memory materials, which belong to the smart materials class, are integrated into composites.

When certain environmental stimuli such as heat, magnetism, electricity, humidity, etc. are detected, smart materials react by changing chemically or physically and then reverting to their initial state when the stimuli are eliminated **[1]**. The discovery of these materials has brought about a major transformation in many sectors, including the construction industry, the aviation industry, and the maritime industry. The focus switched to shape memory materials when Swedish researcher Arne Olander discovered the shape memory effect in gold-cadmium alloys in 1932. Special materials known as shape memory materials (SMMs) change shape in response to a particular stimulus and then remember their original shape **[1]**. Figure 1 depicts a schematic illustration of the shape memory process.

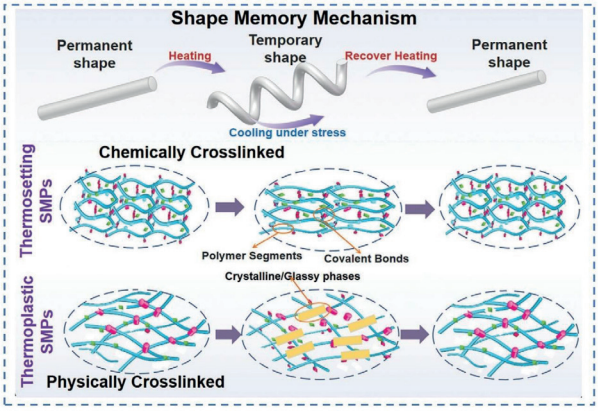

Figure 1. *Shape memory mechanism* [2]

Shape memory materials can undergo plastic deformation and then revert to their original configuration when a certain external stimulus is triggered **[3]**. Superelasticity in alloys and viscoelastic behavior in polymers are phenomena frequently encountered under specific conditions. Moreover, the shape memory effect has broad applicability across numerous sectors, ranging from aerospace engineering to advanced medical device technologies. **[4]**. The following stimuli are covered in this article: light (photosensitive materials), heat (thermosensitive materials), tension/pressure (mechanosensitive

materials), pH change/solvent/moisture (chemically-sensitive materials), and electric current/voltage (electrosensitive materials) **[5]**.

Shape memory materials (SMMs) can be divided into four major categories: magnetic shape memory alloys (MSMAs), shape memory ceramics (SMCs), shape memory polymers (SMPs), and shape memory alloys (SMAs). These multifunctional materials can be used in actuator systems, structural health monitoring systems, self-healing applications, etc. **[6]**. Alloys with the ability to retain their original shapes are known as shape memory alloys. Martensite and austenite are the two crystal microstructure types found in these systems. The material is known as thermoelastic martensite because of its very loosely packed crystal microstructure at low temperatures. The material's well-packed crystal structure, known as austenite, is a hexagonal lattice at high temperatures **[7]**. Shape memory alloys are a type of SMA that exhibits ferromagnetic properties. When exposed to a strong enough magnetic field, a SMA element undergoes twin reorientation and twin boundary movement in its microstructure, changing in size and shape **[8]**. Shape memory polymers are substances that, in addition to temperature, can change back into their original, permanent shape when exposed to light, electricity, magnetic fields, microwaves, water, or other solutions. But the majority of SMPs are susceptible to heat **[9]**.

When an external stimulus is applied, a family of smart materials called shape memory polymers (SMPs) has the unique ability to deform greatly before returning to its original shape **[10]**. In recent years, there has been a lot of interest in the field of study due to the unique properties of shape memory alloys (SMPs) compared to shape memory alloys (SMAs). Among the most noteworthy features of SMPs in contrast to SMAs are biodegradability, ease of processing, low density, increased recoverable strain, adjustable transition temperature, multiple shape recovery capabilities, and low cost **[11]**.

To create shape-memory polymers (SMPs), different reinforcing phases, including metals, glass, and carbon, can be mixed into composites in various ways. These techniques include particle reinforcements and fiber reinforcement techniques including continuous and short fiber reinforcements. SMPs can display distinct response characteristics, increased shape memory effects under a range of stimuli, and improved mechanical properties by combining multiple reinforcing phases **[12]**.

An overview of shape memory materials and a particular class of them shape memory polymer composites is given in this book chapter. The core ideas, manufacturing processes, and technical uses of shape memory polymer composites are highlighted. The paper concludes with a presentation of these materials' different limits and future prospects.

2. Shape Memory Polymers (SMPs)

One class of intelligent materials that can react actively to outside stimuli is called shape memory polymers (SMPs) **[13]**. In the rubber state, they show remarkable huge deformation capacity and superb flexibility, while in the glass state, they exhibit excellent strength and hardness. The shape memory effect states that when heated above the glass transition temperature (Tg), they can undergo significant deformation to take on a desired shape; when the temperature drops below Tg, they will recall this transitory shape. SMPs also provide exceptional performance in harsh conditions, lightweight characteristics, and shock-free operation. As a result, SMPs are used in a variety of industries, including biomedicine, smart drive systems, and aerospace **[14,15]**. Space reflectors are widely used in space telescopes, remote sensing cameras, space antennas, and other spacecraft equipment **[16]**. As space technology has advanced, space reflectors' aperture, surface sensitivity, and light weight have become more important due to the high resolution and high communication capabilities of spaceflight equipment **[17]**.

The same external stimuli can cause SMPs to revert to their original shape. Different kinds of shape memory materials that react to heat, electricity, magnetic fields, microwaves, humidity, and light have been created by researchers. The most common stimulus for SMPs is heat activation, which has been thoroughly investigated **[18]**. Fiber reinforcements have been introduced to SMPs to strengthen their weak mechanical characteristics and increase their structural performance **[19]**.

Numerous functioning SMPs with remarkable shape memory effect (SME) have been created thus far. These cutting-edge smart materials include epoxy-based SMPs, cyanate, styrene, and polyurethane (PU) **[20]**. Cyanate thermoset resin is a very thermally stable material with a glass transition temperature (Tg) of up to 400°C. Furthermore, because of their low hygroscopicity and low dielectric loss, cyanate-based polymers are a suitable material for wave transmission, electronic circuit boards, dielectric coatings, and aeronautical applications **[21]**. The low Tg of styrene-based SMPs makes them attractive for low-temperature applications **[22]**. Polyurethane SMPs have a Tg range of about room temperature. Injection, extrusion, and blow molding are methods for shaping thermoplastic PU SMPs into the required shape. They are crucial for biomedical applications because of their low deformation temperatures **[23]**.

3. Shape Memory Polymer Composites (SMPCs)

Shape memory polymer composite (SMPC) is a type of smart material that may be momentarily fixed by an external force and then return to its original shape when exposed to specific stimuli (such as solutions, temperature, magnetic, or electricity) **[24]**. SMPC shares properties with traditional fiber-reinforced composites, such as low weight, high specific modulus, and specific

strength, in addition to deformability, high recovery rate, and recovery force. As an innovative material for the upcoming generation of space-deployable structures, it has shown a great deal of potential. Numerous SMPC-based constructions, including booms, solar panels, hinges, and related parts, have been created **[25]**. A visual representation for both SMP and SMPC production and application is shown in Figure 2.

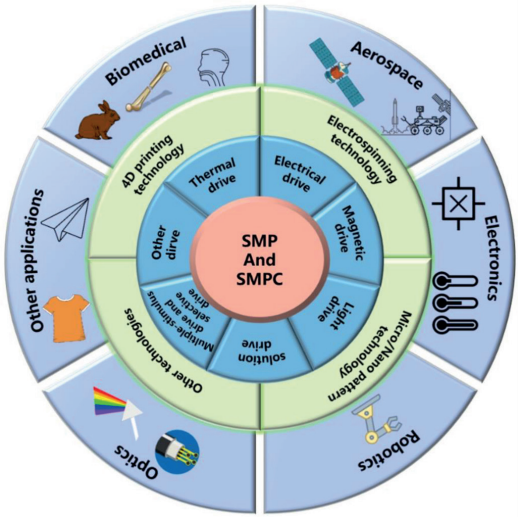

Figure 2. *Production methods and application areas for SMP and SMPC* **[12]**

Carbon nanotubes, graphene, boron nitride, nanokil, and many other nanoparticles are used as fillers in composites. These fillers significantly affect the bonds within the polymer, thereby improving its properties. Additionally, continuous fiber reinforcement such as glass, carbon, and basalt is used in areas where high mechanical strength is required. Depending on the application, various reinforcements are used in the manufacture of shape-memory composites.

Shape memory polymer composites (SMPCs) offer innovative solutions in many engineering fields by going beyond conventional composite materials thanks to their numerous functional properties, such as programmable shape change and lightness. In particular, SMPCs are most intensively researched in the biomedical, aerospace, electronics, and optics fields, which have the highest application potential.

Thus far, fiber-reinforced SMPCs have mostly been developed for space exploration applications. The main disadvantages of conventional structures constructed of conventional materials, such as weight, high cost, and enormous volume consumption, can be solved by using lightweight smart SMPC components. The space environment consists of thermal cycles, high-

energy protons, high vacuum, ultraviolet light, atomic oxygen radiation, and other associated components. Material deterioration, structural or component damage, reduced system dependability, and even a shorter spacecraft operational life might result from materials exposed to the space environment without shielding. Therefore, it is necessary to evaluate the materials' ability to survive space radiation **[26]**. Due to their ongoing exposure to variations in solar light, spacecraft typically experience alternating temperature shifts **[27]**. The ability of materials used in space applications to withstand both high and low temperatures as well as temperature fluctuations between these extremes is known as thermal cycling. The mechanical, thermal, and physical characteristics of materials or components can all be directly impacted by thermal cycling.

Additionally, the idea of using SMPCs can be applied to difficult civil applications to boost construction productivity. For busy cities where time and space are crucial, prefabricated modular construction is the perfect, quickly evolving building technology. The distribution and transportation of bulky, heavy prefabricated modules have grown to be major disadvantages despite their obvious advantages **[28]**. Furthermore, constructing footbridges in isolated locations and over difficult terrain takes a lot of work, time, and money.

Compared to other materials, just 11% of flexible materials have become a desirable platform with great promise for design and biological applications including cell management and smart medications **[29]**. When SMPs are subjected to light or electricity, they can rapidly regain their previous shape. The biggest benefit of SMP is its versatility. When SMP reaches the transition point (Tg), it turns rubbery. Hardness and storage modulus rise with decreasing temperature **[30]**. SMP has an unbreakable synergy that allows it to change shape without losing its original form because it is a fixed and reversible phase. The fixed phase's function in maintaining and returning the polymer to its initial state prevents polymer flow distortion. This fixed phase has a greater glass transition temperature (Tg). Common external triggers include light and electric fields. In addition, a controlled or voluntary chemical reaction is a mechanism responsive to internal inputs **[31]**. Tools for minimally invasive surgery are one example of new biomedical applications where SMP can be helpful.

4. Manufacturing Methods

The performance of shape memory polymer composites is closely linked to their composite components, namely the matrix and reinforcement. Simultaneously, the specified attributes are also significantly impacted by the production method utilized to combine these components. Several factors are critical in the production process for SMPCs. The most fundamental

requirement is the preservation of shape memory behavior. At the same time, a good manufacturing process ensures the functional activation of properties by providing mechanical integrity with strong bonding. Manufacturing methods for composites are examined under two headings: traditional methods and additive manufacturing.

Traditional SMPC production involves a shape-memory polymer matrix containing continuous or chopped fibers or particles at the nano or micro scale. The polymer matrix is reinforced with both fibers and particles. Hand lay-up, vacuum bagging, vacuum infusion, resin transfer molding (RTM), and hot pressing are the most commonly used production techniques. These methods, in particular, enable the achievement of a balanced fiber-matrix ratio, which is important for composites **[32]**. These methods are reliably preferred in the manufacture of structural elements with various geometries because they provide high mechanical strength and maintain shape memory performance. However, the production of complex geometries creates certain limitations in traditional methods **[33]**.

In order to get around the drawbacks of conventional techniques, there has been a recent move toward additive manufacturing techniques, which provide production flexibility. 3D and 4D manufacturing techniques are becoming more and more popular. However, 4D printing techniques allow for the preservation of shape memory effects. 4D printing has recently become an intriguing development of regular 3D printing since technology allows for the creation of intelligent objects that can easily change their shape over time in response to a specific stimulus **[34]**. Direct ink writing (DIW), digital light processing (DLP), stereolithography (SLA), and fused filament fabrication (FFF/FDM) are a few of the additive manufacturing techniques frequently used in 4D printing applications **[35]**. Figure 3 shows a schematic illustration of 4D production techniques.

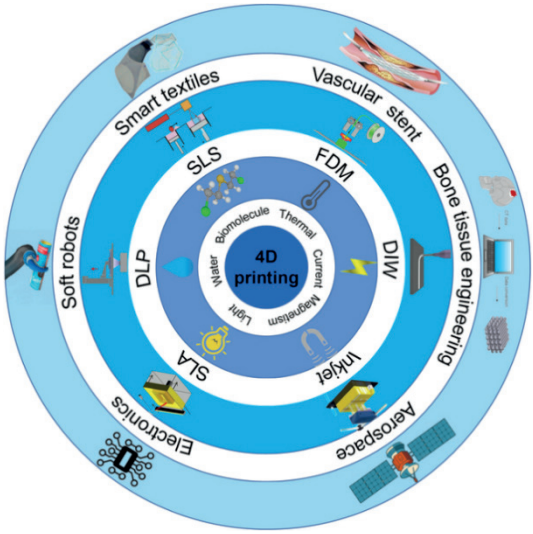

Figure 3. *4D production methods* [**34**]

In 4D printing, various structures can be directly encoded through the structural modeling process, providing greater design freedom for 4D printed objects. The capacity of printed things to change shape over time is one of the advantages of 4D printing. Simple printing is possible for products, and 4B printing enables the creation of intricate shapes without wasting material on the support structure. Therefore, thanks to controlled anisotropy, designs suitable for shape changes can be easily achieved for complex products **[36]**.

Studies in the literature have determined that shape memory properties can be achieved in materials with different characteristics using 4D printing methods. In this context, materials with various glass transition temperatures and cross-linking densities have been tested, yielding successful results. Consequently, a wide range of industries, including construction, agriculture, electronics, smart furniture, textiles, biomedical devices, soft robotics, and aviation, could benefit from the use of 4D printing technology **[35]**.

Additive manufacture of shape-memory structures is referred to as 4D printing technology, a fast emerging new field of study. There are numerous potential uses for 4D printed structures in biomedical science, flexible electronics, aircraft, and photosensitive gadgets. 4D printing is an appealing method for incorporating smart materials into structural fabrication when compared to conventional additive manufacturing technologies. One benefit of 4D printing is that it may create buildings that change shape over time **[37]**. Form memory hydrogels, form memory polymers, shape memory alloys, and liquid crystal elastomers are examples of smart materials for 4D printing. SMPs are among these materials that have garnered more attention recently because of their massive, reversible deformation capabilities, ease

of processing, and inexpensive cost. 4D printed buildings can revert to their original forms in response to one or more external stimuli, such as heat, light, water, electricity, or magnetic fields **[37]**.

Because of customized implant devices and medical needs, 4D-printed SMPs and structures are especially important in biomedical science. Cell culture, tissue engineering scaffolds, tracheal stents, medication transporters, and implant devices are examples of possible 4D structures. 4D-printed implant devices provide distinct advantages in clinical operations, such as biodegradability, reduced invasiveness, remote intervention techniques, and contactless control, because of the shape-changing and recovery qualities of SMPs **[38]**.

5. Conclusion and Future Perspective

Shape memory polymer composites (SMPCs), which hold a unique place in the broader category of shape memory materials, are covered in detail in this chapter with regard to their underlying mechanisms, material constituents, manufacturing processes, and engineering uses. When fiber and particle reinforcements are added, the unique characteristics of shape memory polymers such as their high deformation capacity, low density, adjustable transition temperature, and multi-stimulus sensitivity allow for the creation of functional systems that go beyond the capabilities of traditional composite materials. In this regard, SMPCs are unique as active and flexible engineering components in addition to being structural load-bearing elements.

Research in the literature demonstrates that when the right kind of reinforcement and production technique is chosen, SMPCs can preserve both their mechanical integrity and shape memory performance. While additive manufacturing and, in particular, 4D printing technologies are causing a major paradigm shift in the creation of structures with complex geometries that can change shape over time and in response to stimuli, traditional composite production techniques continue to be reliable in applications requiring high mechanical strength. By allowing material design and function to be programmed simultaneously, these technologies greatly increase the range of applications for SMPCs.

According to recent research, SMPCs have enormous potential in a variety of multidisciplinary fields, such as flexible electronics and smart structures, minimally invasive implants in the biomedical field, deployable structures in space and aerospace applications, and modular and portable systems in civil engineering. However, challenges including cost-effectiveness, scalable production, performance stability in multiple shape memory cycles, and resistance to long-term environmental effects continue to be important research subjects that are essential for the widespread industrial application of these materials.

In the future, the creation of multi-stimulus and multi-functional SMPC systems, the improvement of nano and hybrid reinforcement techniques, and the attainment of more accurate control over 4D printing procedures are thought to be crucial components for advancement in this discipline. It is anticipated that shape-memory polymer composites will be at the core of intelligent and sustainable structural solutions created by the combined efforts of materials science, manufacturing technologies, and application-oriented engineering disciplines.

References

[1] Arun, D.I., Chakravarthy, P., Arockia Kumar, R., & Santhosh, B. (2018). *Shape memory materials*. CRC Press.

[2] Luo, L., Zhang, F., Wang, L., Liu, Y., & Leng, J. (2024). Recent advances in shape memory polymers: multifunctional materials, multiscale structures, and applications. *Advanced Functional Materials*, *34*(14), 2312036.

[3] Finlayson, T.R. (2023). The contributions by Kazuhiro Otsuka to "Shape Memory and Superelasticity": A Review. *Shape Memory and Superelasticity*, *9*(2), 217-230.

[4] Huang, W.M., Ding, Z., Wang, C.C., Wei, J., Zhao, Y., & Purnawali, H. (2010). Shape memory materials. *Materials Today*, *13*(7-8), 54-61.

[5] Sun, L., Huang, W.M., Ding, Z., Zhao, Y., Wang, C.C., Purnawali, H., & Tang, C. (2012). Stimulus-responsive shape memory materials: A review. *Materials & Design*, *33*, 577-640.

[6] Abavisani, I., Rezaifar, O., & Kheyroddin, A. (2021). Multifunctional properties of shape memory materials in civil engineering applications: A state-of-the-art review. *Journal of Building Engineering, 44,* 102657.

[7] Baitab, D.M., Majid, D.L.A.H.A., Abdullah, E., & Hamid, M. (2018). A review of techniques for embedding shape memory alloy (SMA) wires in smart woven composites. *International Journal of Engineering Technologies, 7(4),* 129-136.

[8] Jokinen, T., Ullakko, K., & Suorsa, I. (2001, August). Magnetic shape memory materials-new possibilities to create force and movement by magnetic fields. In ICEMS'2001. Proceedings of the Fifth International Conference on Electrical Machines and Systems (IEEE Cat. No. 01EX501) (Vol. 1, pp. 20-23). IEEE.

[9] Lv, H., Leng, J., Liu, Y., & Du, S. (2008). Shape-memory polymer in response to solution. *Advanced Engineering Materials, 10(6),* 592-595.

[10] Liu, Y., Du, H., Liu, L., & Leng, J. (2014). Shape memory polymers and their composites in aerospace applications: a review. *Smart Materials and Structures*, *23*(2), 023001.

[11] Cabanlit, M., Maitland, D., Wilson, T., Simon, S., Wun, T., Gershwin, M. E., & Van de Water, J. (2007). Polyurethane shape-memory polymers demonstrate functional biocompatibility in vitro. *Macromolecular Bioscience, 7(1),* 48-55.

[12] Liu, Y., Wang, L., Liu, Y., Zhang, F., & Leng, J. (2024). Recent progress in shape memory polymer composites: Driving modes, forming technologies, and applications. *Composites Communications, 51,* 102062.

[13] Mu, T., Liu, L., Lan, X., Liu, Y., & Leng, J. (2018). Shape memory polymers for composites. Composites Science and Technology, 160, 169-198.

[14] Santo, L., & Quadrini, F. (2017). Shape memory materials from epoxy matrix composites. In Smart Polymer Nanocomposites: Energy Harvesting, Self-He-

aling and Shape Memory Applications (pp. 303-320). *Cham: Springer International Publishing.*

[15] Roh, J.H., & Bae, J.S. (2017). Softenable composite boom for reconfigurable and self-deployable structures. *Mechanics of Advanced Materials and Structures, 24(8),* 698-711.

[16] Lin, W.C., Chang, S.T., Yu, Z.R., Lin, Y.C., Ho, C.F., Huang, T.M., & Chen, C.H. (2014). Comparing optical test methods for a lightweight primary mirror of a space-borne Cassegrain telescope. *Measurement Science and Technology, 25(9),* 094014.

[17] Chen, P.C., Saha, T.T., Smith, A.M., & Romeo, R.C. (1998). Progress in very lightweight optics using graphite fiber composite materials. *Optical Engineering, 37(2),* 666-676.

[18] Meng, Q., & Hu, J. (2009). A review of shape memory polymer composites and blends. *Composites Part A: Applied Science and Manufacturing, 40(11),* 1661-1672.

[19] Emmanuel, K.D.C., Herath, H.M.C.M., Jeewantha, L.H.J., Epaarachchi, J.A., & Aravinthan, T. (2021). Thermomechanical and fire performance of DGEBA based shape memory polymer composites for constructions. *Construction and Building Materials, 303,* 124442.

[20] Xin, X., Liu, L., Liu, Y., & Leng, J. (2019). Mechanical models, structures, and applications of shape-memory polymers and their composites. *Acta Mechanica Solida Sinica, 32(5),* 535-565.

[21] Xie, F., Liu, L., Gong, X., Huang, L., Leng, J., & Liu, Y. (2017). Effects of accelerated aging on thermal, mechanical and shape memory properties of cyanate-based shape memory polymer: I vacuum ultraviolet radiation. *Polymer Degradation and Stability, 138,* 91-97.

[22] Tandon, G. P., Goecke, K., Cable, K., & Baur, J. (2009). Durability assessment of styrene-and epoxy-based shape-memory polymer resins. *Journal of Intelligent Material Systems and Structures, 20(17),* 2127-2143.

[23] Tobushi, H., Hayashi, S., Hoshio, K., & Ejiri, Y. (2008). Shape recovery and irrecoverable strain control in polyurethane shape-memory polymer. *Science and Technology of Advanced Materials, 9(1),* 015009.

[24] Tan, Q., Li, F., Liu, L., Liu, Y., & Leng, J. (2023). Effects of vacuum thermal cycling, ultraviolet radiation and atomic oxygen on the mechanical properties of carbon fiber/epoxy shape memory polymer composite. *Polymer Testing, 118,* 107915.

[25] Li, F., Liu, L., Lan, X., Zhou, X., Bian, W., Liu, Y., & Leng, J. (2016). Preliminary design and analysis of a cubic deployable support structure based on shape memory polymer composite. *International Journal of Smart and Nano Materials, 7(2),* 106-118.

[26] Huang, Z.M. (2000). Strength formulae of unidirectional composites including thermal residual stresses. *Materials Letters, 43(1-2),* 36-42**.**

[27] Azimpour-Shishevan, F., Akbulut, H., & Mohtadi-Bonab, M. A. (2020). Effect of thermal cycling on mechanical and thermal properties of basalt fibre-reinforced epoxy composites. *Bulletin of Materials Science, 43(1),* 88.

[28] Ferdous, W., Bai, Y., Ngo, T.D., Manalo, A., & Mendis, P. (2019). New advancements, challenges and opportunities of multi-storey modular buildings–A state-of-the-art review. *Engineering structures, 183,* 883-893.

[29] Oladapo, B.I., Zahedi, S.A., Ismail, S.O., & Olawade, D.B. (2021). Recent advances in biopolymeric composite materials: Future sustainability of bone-implant. *Renewable and Sustainable Energy Reviews*, *150*, 111505.

[30] Ploszajski, A.R., Jackson, R., Ransley, M., & Miodownik, M. (2019). 4D printing of magnetically functionalized chainmail for exoskeletal biomedical applications. *MRS advances, 4(23),* 1361-1366.

[31] Raad, J., & Parvin, A. (2020). Iron-based shape memory alloy and fiber reinforced polymers rods for prestressed NSM strengthening of RC beams. *Engineering Structures, 207*, 110274.

[32] Bhanushali, H., Amrutkar, S., Mestry, S., & Mhaske, S.T. (2022). Shape memory polymer nanocomposite: a review on structure–property relationship. *Polymer Bulletin*, *79*(6), 3437-3493.

[33] Emmanuel, K.D.C., Jeewantha, L.H.J., Herath, H.M.C.M., Epaarachchi, J.A., & Aravinthan, T. (2023). Shape memory polymer composite circular and square hollow members for deployable structures. *Composites Part A: Applied Science and Manufacturing*, *171*, 107559.

[34] Yan, S., Zhang, F., Luo, L., Wang, L., Liu, Y., & Leng, J. (2023). Shape memory polymer composites: 4D printing, smart structures, and applications. *Research*, *6*, 0234.

[35] Khalid, M.Y., Arif, Z.U., Noroozi, R., Zolfagharian, A., & Bodaghi, M. (2022). 4D printing of shape memory polymer composites: A review on fabrication techniques, applications, and future perspectives. *Journal of Manufacturing Processes*, *81*, 759-797.

[36] Lalegani Dezaki, M., & Bodaghi, M. (2023). Sustainable 4D printing of magneto-electroactive shape memory polymer composites. *The International Journal of Advanced Manufacturing Technology*, *126*(1), 35-48.

[37] Cortés, A., Cosola, A., Sangermano, M., Campo, M., González Prolongo, S., Pirri, C.F., ... & Chiappone, A. (2021). DLP 4D-printing of remotely, modularly, and selectively controllable shape memory polymer nanocomposites embedding carbon nanotubes. *Advanced Functional Materials*, *31*(50), 2106774.

[38] Zhang, F., Wang, L., Zheng, Z., Liu, Y., & Leng, J. (2019). Magnetic programming of 4D printed shape memory composite structures.

Chapter 13

THE EFFECT OF RADIATOR PANEL SURFACE TEMPERATURE ON INDOOR TEMPERATURE VALUES OF LIGHT WALL BUILDINGS WITH PCM LAYER

Başak METİN[1]
Halil BAYRAM[2]

1 Master's Student Başak Metin, Mechanical Engineering Department, Graduate School of Natural and Applied Sciences, ORCID: 0009-0006-5423-7515
2 Assoc. Prof. Dr. Halil Bayram, Amasya University, Engineering Faculty, Mechanical Engineering Department, ORCID: 0000-0002-4664-3883

INTRODUCTION

Increasing environmental concerns are driving greater efficiency in the use of existing energy sources and a shift toward more environmentally friendly ones. Especially in enclosed spaces such as residential and commercial buildings, substantial energy is consumed to achieve thermal comfort. The use of panel radiators plays a huge role in meeting the heating needs of these enclosed spaces (Bayram & Koç, 2023; Sevilgen & Kilic, 2011). Classifications are based on the temperature range of the hot water entering the panel radiators. If the supply water temperature is between 75–90°C, the heating system is called a high-temperature system. When the supply temperature is 55°C, the system is classified as a medium-temperature heating system. When the temperature is set to 45°C or 35°C, the systems are referred to as low-temperature and very-low-temperature systems, respectively (Ganter et al., 2016; Eijdems et al., 2000).

Existing buildings are generally constructed from brick, and such materials have relatively high thermal mass. However, today, the use of lightweight building walls (LBWs), which are increasingly popular due to their quick construction and lightweight nature, have relatively low thermal masses. For this reason, they respond quickly to temperature changes, which can lead to indoor temperature fluctuations. Consequently, this can reduce thermal comfort within and create undesirable thermal conditions for occupants (Liu et al., 2021). In such buildings, using Phase Change Material (PCM) can reduce the load on heating or cooling systems, thereby improving energy efficiency, and also help prevent undesirable conditions such as indoor temperature fluctuations, contributing to the achievement of thermal comfort conditions (Hou et al., 2022). Studies on the use of PCMs in buildings with LBW have focused on parameters such as the position of the PCM layers, phase change temperature, thickness, latent heat, specific heat, thermal conductivity, and density. In a study in which a PCM layer was added, it was concluded that this addition increased thermal energy efficiency, reduced internal temperature fluctuations, and resulted in an approximately 7-hour increase in delay time (Hou et al., 2021). In another study conducted within this scope, PCM-based lightweight wall (LW) panels were installed on the exterior and interior surfaces of the test chamber. It was observed that in the interior placement, the delay time values increased by approximately 3 to 4 hours compared to the exterior placement. As a result, they concluded that placing this installation in areas closer to the interior environment is more advantageous in terms of thermal efficiency (Yang et al., 2018). In an experimental study which in hollow bricks were filled with PCM material to create a simulation model, it was observed that the delay time value increased from approximately 4 hours to about 9 hours (Gao et al., 2020). In another

study related to adding PCM as a passive method to improve thermal efficiency, analyses were conducted using a gypsum board layer integrated with PCM in the simulation program called Apache. As boundary conditions, the effects of alternative thermal conductivity and different ventilation rates under hot air conditions were examined. It was stated that the phase change temperature value is optimally 22°C (Kendrick & Walliman, 2007). In another study, the use of PCM in portable LBWs was investigated for its potential to achieve significant energy savings under heating and cooling conditions. The researchers also noted that optimizing the PCM melting point is an essential factor (Marin et al., 2016).

In this study, as seen from the conducted literature review, the relationship between PCM usage in LBW buildings and the surface temperature of panel radiators was numerically examined to improve both energy efficiency and indoor thermal comfort conditions.

MATERIALS AND METHODS

Panel radiators are widely used to meet the heating demands of many enclosed spaces, such as residential and commercial buildings. In this study, a simplified Type-22 model panel radiator with dimensions of 0.6 × 1 m was used. The purpose of simplifications is to reduce the solution time in CFD studies, which is significantly increased by detailed surface modeling. The 3D CFD model was created under transient regime conditions. To represent the surface temperature of this panel radiator for medium and low-temperature systems, the temperatures were fixed at 60°C and 40°C, respectively, during the analyses. There is no water flow through the panel radiator, and in the CFD model, only the surface temperature boundary condition was defined for the radiator.

The panel radiator is mounted in a room measuring 2.5 × 3 × 3.5 meters, and the analyses were conducted within this room. A 5-mm-thick gypsum board layer was applied to the room ceiling. On top of this layer, a 10 mm thick phase change material (PCM) layer with a phase change temperature range of 20-22°C was applied. The thermophysical properties of these materials used in the numerical study are detailed in Table 1. A door is placed directly opposite the room surface where the panel radiator is located. On the lower and upper edges of the door, surfaces with a thickness of 8 mm are defined for the intake and exhaust of clean air, respectively. No additional insulation material has been modeled on the top surface of the PCM, and this surface is considered adiabatic. The other surfaces of the room are assumed to have insulation coating on the outside, and different heat transfer coefficient boundary conditions have been applied accordingly. A heat transfer coefficient of 2 W/(m^2K) was defined for the wall surface where the radiator

is located. For the other remaining surfaces of the room (the left, right, and bottom walls, as well as the wall at the door side), a heat transfer coefficient of 1 W/(m^{2}K) was defined. To model the radiative heat transfer within the room, the discrete ordinate radiation model was used.

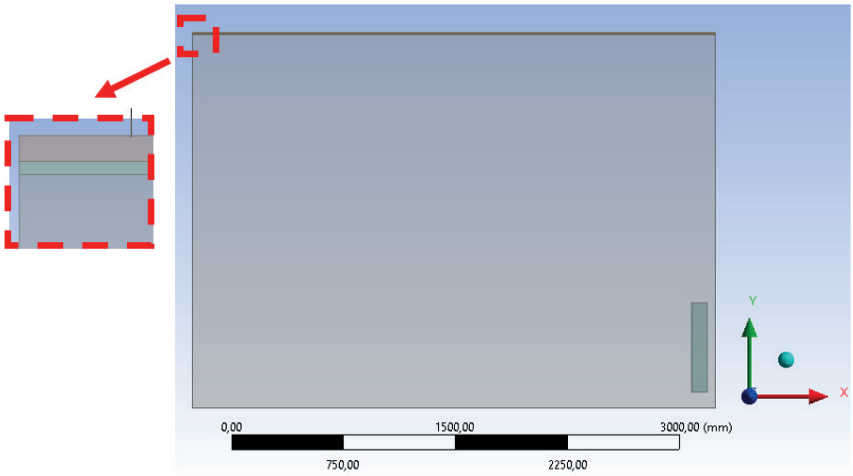

Figure 1: The view of the CFD model

Table 1. The thermophysical properties of the materials in the analyses

Material	**Phase-transition temperature**	**Phase change latent heat**	**Thermal conductivity**	**Specific heat**	**Density**
	[°C]	**[kj/kg]**	**[W/(mK)]**	**[J/(kgK)]**	**[kg/m^3]**
PCM	20-22	200	0.2	2000	800
Air	-	-	0.0242	1006.43	1.225
Gypsum board	-	-	0.33	1050	1050

The PCM layer installed on the room ceiling absorbs heat during phase change and subsequently releases it, thereby contributing to indoor thermal comfort. To model this phase change in the numerical study, a solidification & melting model was employed. Additionally, according to the coordinate system shown

in Figure 1, gravity in the -y direction was also included in the numerical model. The initial temperature was set to 14°C for all cell zones. The work carried out under the temporary regime conditions has been continued for 2 hours. Iterations at each time step continued until the residuals of the continuity and momentum equations fell below 10^{-4}, and the energy equation residual fell below 10^{-8}. The mesh structure of the numerical study consists of approximately 1 million elements (Figure 2). Additionally, the ANSYS-Fluent software package was used.

Additionally, a traditional model without PCM added has been developed to observe the effects of using the PCM layer. Analyses were conducted using this model with the boundary conditions applied in other analyses.

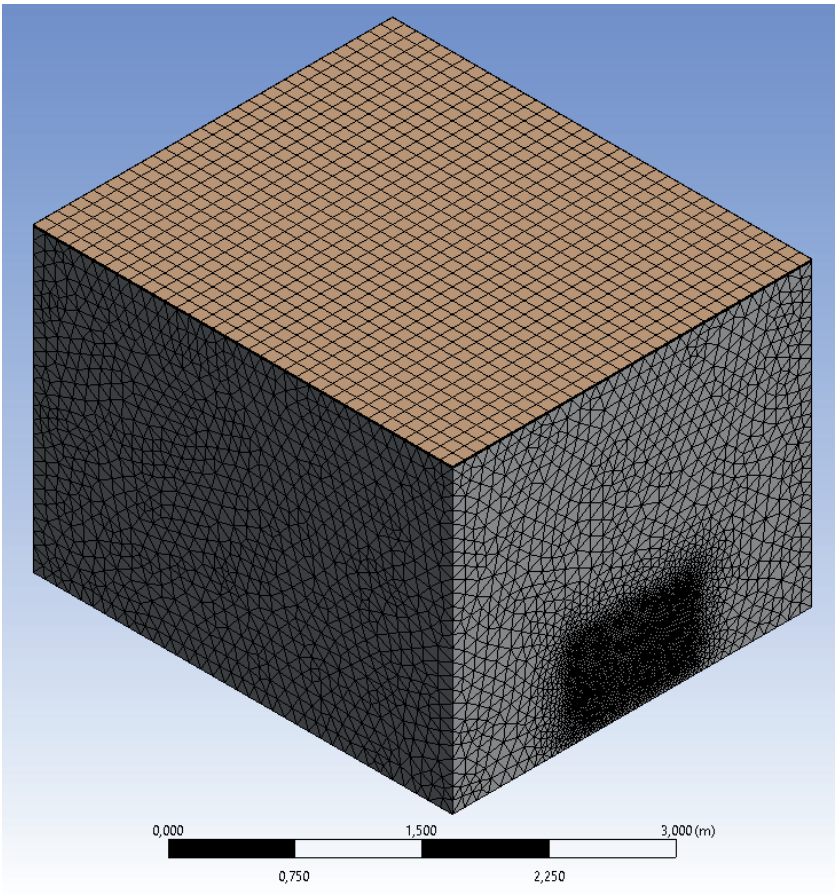

Figure 2: Isometric View of The Mesh Structure

RESULTS AND DISCUSSIONS

In this study, CFD analyses were performed in a test room heated by a panel radiator with a 10 mm-thick PCM layer in the ceiling area, under different surface-temperature boundary conditions for the panel radiator. The surface temperature distribution at the room cross-section, the average air temperature within the room, and the liquid-fraction ratios of the PCM layer will be presented in detail.

A surface that passes through the center of the room was defined for the analyses. The distributions of air temperature values on this surface were examined for all cases (Figure 4-7). Additionally, the average air temperature values inside the room are detailed in Table 2.

First, the results of Case 0, which does not have a PCM layer added to the ceiling and has a panel radiator surface temperature of 60°C, were examined (Figure 4). When the distributions here are analyzed, during the first half hour, the temperature distribution within the room shows higher values in the panel radiator area. The average air temperature in the room was also found to be 25.07°C from the analyses. The other areas of the room have a noticeably lower temperature distribution. Looking at the temperature distribution in the first hour, the temperature wave on the panel radiator has relatively spread to other parts of the room. The air heated by the panel radiator has risen due to the density difference and has moved toward the cooler areas of the room. The warm air approaching the door then directed downward. As a result, a hot air dome has formed between the panel radiator and the door. This dome-shaped distribution is most clearly observed in the temperature distribution at the end of the first hour. It was not visible during the first half-hour because the room did not warm up sufficiently. By the end of the second hour, the temperature distribution in the room had become relatively uniform, and this dome distribution had become quite small. At the end of the first hour, the average air temperature in the room was 26.82°C. In the final state of the analysis, the hot air wave in the room has gradually spread. 27. An average air temperature of 27.82°C was obtained at this time step. Additionally, in all three cases, it can be observed that the temperature values at the lower part of the door where fresh air enters the room are lower than those in other areas.

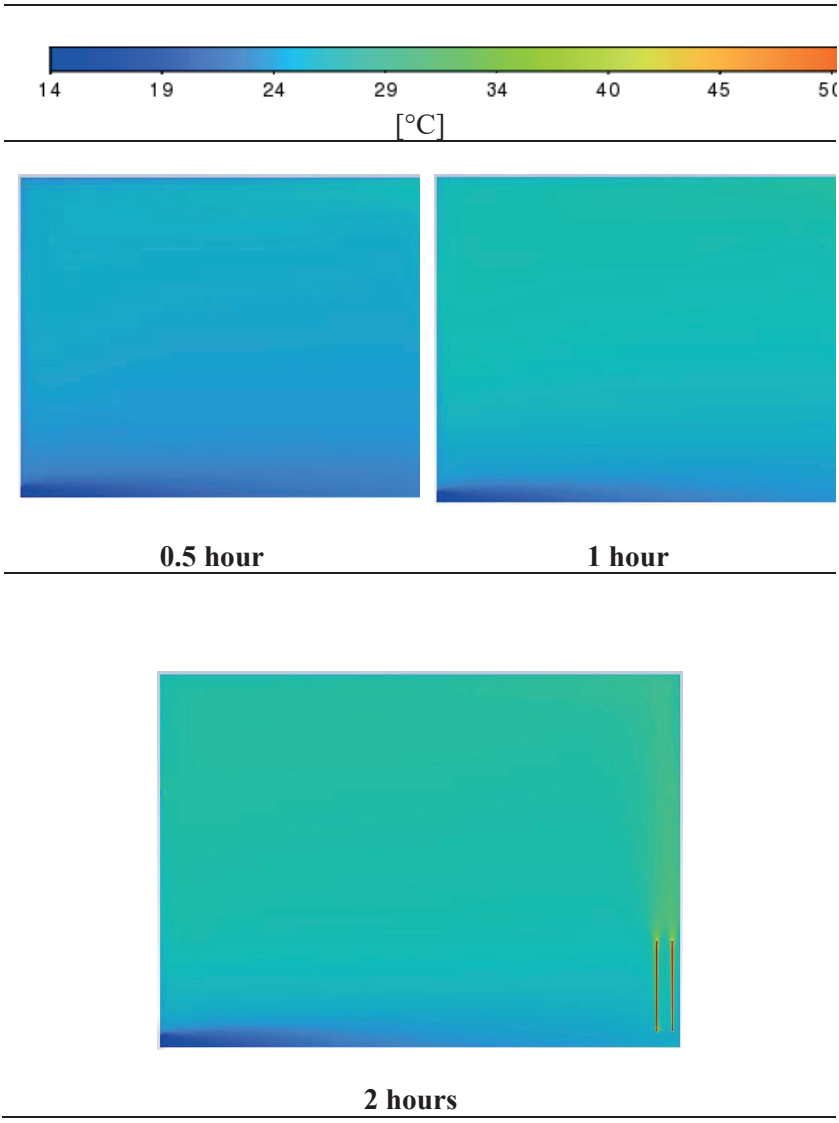

Figure 4. Temperature distribution on the cross-section of the room model (Case 0)

The temperature distribution results for Case 1, where the panel radiator surface temperature is set to 40°C and a 10 mm thick PCM layer is placed in the ceiling area of the room, are shown in Figure 5. The temperature distributions here are relatively low due to both the low surface temperature value and the PCM layer in the ceiling area also absorbing some heat. It is observed that the rising of the heated air in the panel radiator area and the paths it follows within the room are not significantly different from the

situation in Case 0. The change of liquid fraction values in the PCM layer over time is detailed in Table 3. Here, almost no phase change is observed after the first half hour. During this time step, the average air temperature in the room is 21.38°C. After the first hour, the liquid fraction value in the PCM layer is 0.06. By the end of the analysis, the liquid fraction value is 0.025, indicating that no noticeable melting has occurred. Additionally, the average temperature values of the room at the end of the first and second hours were calculated as 22.31°C and 22.61°C, respectively. As can be seen from both these values and the temperature distributions in Figure 5, there was not much change in the temperature distribution within the room during these two time steps. The reason for this is thought to be that the heat coming from the panel radiator is stored by the PCM layer.

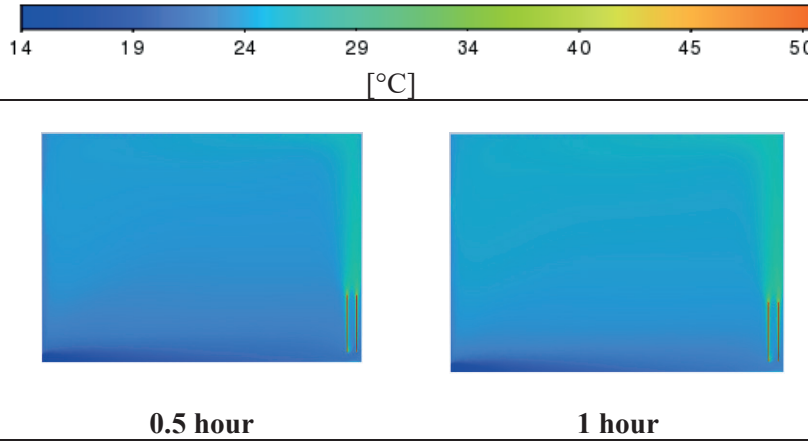

0.5 hour **1 hour**

2 hours

Figure 5. Temperature distribution on the cross-section of the room model (Case 1)

When examining the results of the situation where the panel radiator surface temperature is 50°C (Case 2), similar results to those in Case 1 were obtained (Figure 6). During the first half-hour period, the room started to warm up relatively. The heat transfer to the PCM layer began almost at the end of the first hour, coinciding with the heating of the gypsum board layer, which is the layer of the room in contact with the air. At the end of the first and second hours, the average air temperature in the room was measured as 23.24°C and 23.47°C, respectively. The liquid fraction values at these time steps were calculated as 0.011 and 0.043, respectively.

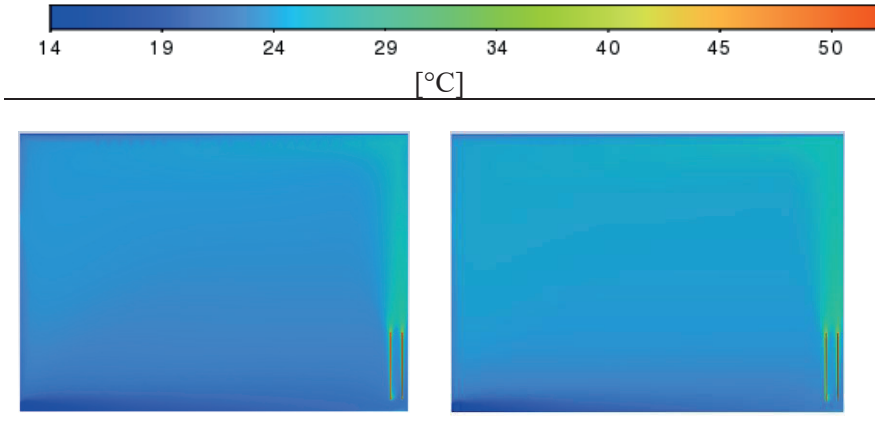

Figure 6. Temperature distribution on the cross-section of the room model (Case 2)

The results for the case where the maximum surface temperature of the panel radiator is 60°C (Case 3) are shown in Figure 7. Overall, the temperature distributions have been similar since the PCM layer started melting. On the other hand, the boundary conditions for the panel radiator here are the same as in Case 0. The addition of the PCM layer caused the average room temperature to decrease from 25.07°C to 23.10°C after half an hour. The approximately 2°C decrease observed here is due to energy storage from PCM melting. In other time steps, it caused temperature drops of about 2.7°C and 3.4°C.

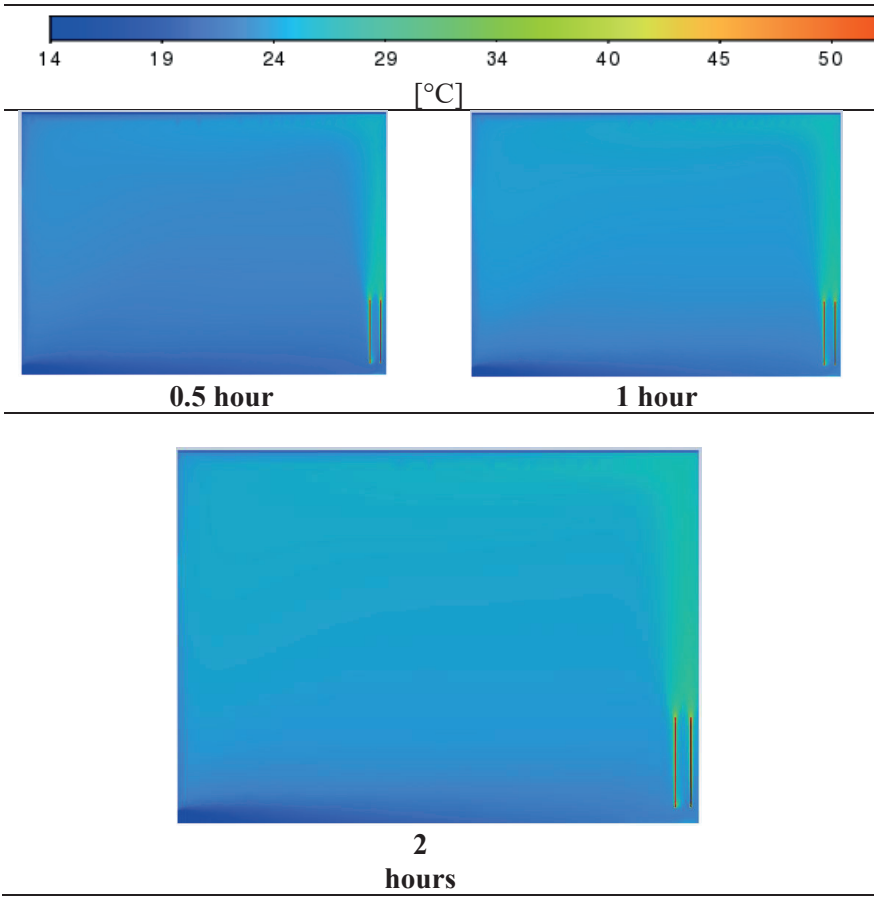

Figure 7. Temperature distribution on the cross-section of the room model (Case 3)

Table 2. The average temperature values of the air volume of the room[°C]

	Case 0	Case 1	Case 2	Case 3
0.5 hour	25.07	21.38	22.21	23.10
1 hour	26.82	22.31	23.24	24.16
2 hours	27.82	22.65	23.47	24.45

Table 3. The average liquid fraction values of the PCM layers

	Case 0	Case 1	Case 2	Case 3
0.5 hour	-	0.001	0.003	0.007
1 hour	-	0.06	0.011	0.018
2 hours	-	0.025	0.043	0.076

CONCLUSIONS

This study examined the effect of using phase change materials, whose usage is increasing, in buildings with LBW (Lightweight Building Wall) structures. The analysis was conducted numerically using a room model heated by a panel radiator measuring 2.5*3*3.5 meters. CFD analyses were performed under transient conditions for a duration of two hours. When evaluating the results obtained from the analyses, it was observed that the air near the surface of the panel radiator heats up and rises through natural convection, moving toward the relatively cooler areas of the room. Subsequently, the cooled air descends back toward the floor of the room. In cases where there is no uniform temperature distribution within the room, unwanted temperature fluctuations have occurred due to the rising and falling air distribution. Especially in these low thermal mass LBW-built buildings, changing outdoor conditions cause both temperature fluctuations and vertical temperature differences inside. To prevent these unwanted situations, a PCM layer has been installed in the room ceiling. As a result, the temperature fluctuations within the room are significantly reduced compared with the case without PCM. Additionally, when examining temperature distributions from the moment the PCM layer

begins to melt, a homogeneous distribution within the room has been observed, and the vertical temperature differences have decreased. However, it should be known that for the PCM layer to fully release the stored energy from the heat source that meets the heating needs of the room, very good insulation must be applied to the outside of the PCM layer. Additionally, the PCM layer should be able to completely melt while the heat source is in operation and then fully release the stored energy afterward. In the cases presented in this study, Case 1 and Case 2, the desired level of melting could not be achieved in the PCM layer due to the relatively low surface temperatures of the panel radiator. The design, placement, and appropriate selection of the heat source for the PCM layer are of critical importance. Future studies aim to conduct a 72-hour experiment that will include day and night variations.

REFERENCES

Bayram, H., & Koc, N. (2023). Experimental investigation of the effects of add-on fan radiators on heat output and indoor air temperature. *Case Studies in Thermal Engineering*, 50, 103432.

Eijdems, H. H. E. W., Boerstra, A. C., & Op't Veld, P. J. M. (2000). Low temperature heating systems: Impact on iaq, thermal comfort and energy consumption. vol. *Annex*, 37.

Ganter, N., Holmberg, S., & Pitsch, S. (2016). Achieving better thermal comfort and energy savings by low-temperature heating.

Gao, Y., He, F., Meng, X., Wang, Z., Zhang, M., Yu, H., and Gao, W. (2020). Thermal behavior analysis of hollow bricks filled with phase-change material (PCM). *Journal of Building Engineering*, 31, 101447.

Hou, J., Meng, X., and Dewancker, B. J. (2021). A numerical study on the effect of phase-change material (PCM) parameters on the thermal performance of lightweight building walls. *Case Studies in Construction Materials*, 15, e00758.

Hou, J., Huang, Y., Zhang, J., Meng, X., & Dewancker, B. J. (2022). Influence of phase change material (PCM) parameters on the thermal performance of lightweight building walls with different thermal resistances. *Case Studies in Thermal Engineering*, 31, 101844.

Kendrick, C., and Walliman, N. (2007). Removing unwanted heat in lightweight buildings using phase change materials in building components: simulation modelling for PCM plasterboard. *Architectural Science Review*, 50(3), 265-273.

Liu, Z. A., Hou, J., Meng, X., & Dewancker, B. J. (2021). A numerical study on the effect of phase-change material (PCM) parameters on the thermal performance of lightweight building walls. *Case Studies in Construction Materials*, 15, e00758.

Marin, P., Saffari, M., de Gracia, A., Zhu, X., Farid, M. M., Cabeza, L. F., and Ushak, S. (2016). Energy savings due to the use of PCM for relocatable lightweight buildings passive heating and cooling in different weather conditions. *Energy and Buildings*, 129, 274-283.

Sevilgen, G., & Kilic, M. (2011). Numerical analysis of air flow, heat transfer, moisture transport and thermal comfort in a room heated by two-panel radiators. *Energy and buildings*, 43(1), 137-146.

Yang, L., Qiao, Y., Liu, Y., Zhang, X., Zhang, C., and Liu, J. (2018). A kind of PCMs-based lightweight wallboards: Artificial controlled condition experiments and thermal design method investigation. *Building and Environment*, 144, 194-207.